VELOCITY, VORTICITY AND TURBULENCE MEASUREMENTS IN THE SURF ZONE

By

Kessie Govender

Submitted in partial fulfilment of
the requirement for the Degree of
Doctor of Philosophy
in the department of Physics,
University of Natal,
Durban

Durban
January 1999

Dedicated to my family.

Preface

The author hereby declares that this thesis represents his own original and unaided work except where specific acknowledgement is made by name or in the form of a reference. This thesis has not been submitted to any other university for degree purposes.

Acknowledgements

The work presented here would not have been possible without the assistance of many individuals and organisations. Foremost, I am greatly indebted to Prof M.J. Alport from the Dept. of Physics, University of Natal, and Dr G.P. Mocke from the CSIR, Stellenbosch, for their direction and guidance during the course of this work and also for their concerns stretching beyond the normal call of duty.

I wish to thank the workshop staff in the Dept. of Physics for their efforts in the construction of experimental items.

I also wish to acknowledge the assistance provided by the staff of CSIR, Stellenbosh, especially to the Model Hall workers, too numerous to mention here, for maintaining the wave flume and the wave generator.

Acknowledgements is also due to the CSIR, FRD and the University of Natal for their financial contributions.

Abstract

The coastal regions of the world play a significant role with regards to social and economic development, and with the ever increasing human activities along the coast, it has become necessary to understand and protect this vast resource. This requires a thorough understanding of the hydrodynamic processes that occur in the surf zone as a result of wave breaking. Laboratory investigations form an essential part of unravelling any physical process. It is the aim of this thesis, therefore, to investigate via laboratory measurements, the hydrodynamics of plunging and spilling waves in the surf-zone with the view to obtaining greater physical insight and also to obtain real data for model validation purposes. To achieve the above goal it was also necessary to develop new measuring techniques that were suitable for surf zone application, since conventional water level and fluid velocity measuring devices perform poorly in the presence of wave breaker related aeration, a common feature in the surf zone.

The experimental investigation of processes occurring in the surf zone was carried out using a plane beach in a 20 m long wave flume. Both spilling and plunging waves are considered. The measurement of the spatial and temporal fluid velocities, water level and aeration area was accomplished using digital video imaging and analysis techniques in conjunction with particle image velocimetry.

The diagnostic equipment, employed for the measurement of water levels, consists of a monochrome video camera connected to a video cassette recorder (VCR) and to a video frame grabber residing in a PC. The video machine is used for mass storage of video data and easy replay of the experiment. The frame grabber is used to digitise and grab a sequence of video frames. The frame grabber can accept a video signal directly from the camera or from the VCR during playback. Fluid velocities were measured using a non-interlaced digital CCD camera connected direct to a frame grabber residing in a pentium PC. Thus, images were stored direct to the hard disk.

Water level measurements were performed with the aim of measuring wave heights as well

as the mean water level set-down prior to wave breaking and the subsequent set-up in the surf zone. A time series of wave evolution was obtained by tracking the air-water interface along a vertical line of pixels at a fixed horizontal position in the video image. This method has the advantage of being non intrusive, and is considered more reliable than some of the more traditional techniques employed in the surf zone. Mean water levels were measured every 0.1 m along the measurement section of the flume, which is approximately 8 m in length.

The spatial and temporal particle velocities were measured initially by tracking individual neutrally buoyant particles. This technique is referred to as particle image velocimetry (PIV). More extensive measurements were later accomplished using digital cross correlation techniques, referred to as digital correlation image velocimetry (DCIV). A longitudinal section of the flume was illuminated with a sheet of light and the flume was seeded with neutrally buoyant particles. Velocities are then estimated by tracking individual seeds or a group of seeds in consecutive video frames. The velocity flow field was measured at the break point and in the surf zone. The average and turbulent velocities are estimated through phase ensemble-averaging. The undertow current and shoreward mass flux are derived from the flow field through averaging over the wave phase. A sensitivity analysis on this data is done to ensure statistical convergence.

The measured velocity flow fields were analyzed and compared with linear wave theory and measurements made using Laser Doppler anemometry (LDA). The turbulent structures generated in the surf zone are investigated through the computation of the phase ensemble-averaged turbulence intensities and vorticity. The vorticity of the averaged flow field is computed and analyzed. The time averaged Reynolds stress and the turbulent kinetic energy is also computed. The Reynolds stress near the bed is shown to increase almost linearly with distance above the bed. Spectral analysis of the spatial velocities was used to obtain estimates of the scale lengths, and a comparison with the Kolmogorov frequency scaling law in the equilibrium region of the spectrum was also performed.

The measurement of the aeration/roller geometry for spilling and plunging waves was accomplished using the video techniques used for water level measurements. The normalised

wave roller area, in spilling waves, is shown to be nearly constant through the inner surf-zone, increasing slightly in the middle of the surf-zone. The roller slope tends to show a decreasing trend in the surf zone.

Contents

List of symbols and abbreviations

A_r	aeration/roller area
c	wave celerity
d	distance, still water depth
d_s	diameter of the Airy disk
E(k)	energy spectrum
f	frequency
g	gravitational acceleration
h	mean local water depth
h_b	mean water depth at break point
h_0	mean water depth near the wave generator
H_b	wave height at breakpoint
H_0	deep water wave height
I	intensity
k	turbulent kinetic energy, wavenumber
l	length scale
m	lens magnification
N	sample length
p	pressure
p_0	atmospheric pressure
R_{ij}	cross correlation of velocity components u_i and u_j
S_{ij}	mean rate of strain
s_{ij}	fluctuating strain rate
t	time
Δt	sampling time
T	wave period, exposure time
u	horizontal velocity component in the direction of wave propagation
u'	turbulent horizontal velocity component in the direction of wave propagation
u'_{rms}	rms value of u'
u_i	velocity component in cartesian tensor form
v	horizontal velocity component perpendicular u
v_x	velocity component along the x coordinate
v'	turbulent horizontal velocity component perpendicular to u
v'_{rms}	rms value of v'
w	vertical velocity component
w(x)	exposure weighting function
w'	turbulent vertical velocity component
w'_{rms}	rms value of w'
x	horizontal coordinate axis parallel to the wave flume
x_b	location of the breakpoint along the x-axis
y	horizontal coordinate axis perpendicular to the direction of wave propagation
z	vertical coordinate axis
z_t	elevation of trough level above the bed
ε	energy dissipation rate
η	vertical coordinate of water level with respect to the still water line
θ	phase

λ	wavelength
ν	kinematic viscosity
μ	molecular viscosity
ξ	mean waterlevel
ρ	density
σ_{ij}	stress tensor
τ_{ij}	Reynolds stress tensor
ϕ	phase
ω	radian frequency, vorticity
$<.>$	phase ensemble-average operation
$\overline{.}$	time-averaging operation
CCD	charge coupled device
CSIR	council for scientific and industrial research
CIV	correlation image velocimetry
DCIV	digital correlation image velocimetry
DPIV	digital particle image velocimetry
FFT	fast fourier transform
FM	frequency modulation
LDA	laser doppler anemometry
MWL	mean water level
NSE	Navier-Stokes Equation
PC	personal computer
PIV	particle image velocimetry
PSF	point spread function
Re	Reynolds number
SWL	still water level
TKE	turbulent kinetic energy
VCR	video cassette recoder

wave roller area, in spilling waves, is shown to be nearly constant through the inner surf-zone, increasing slightly in the middle of the surf-zone. The roller slope tends to show a decreasing trend in the surf zone.

Contents

List of symbols and abbreviations

A_r	aeration/roller area
c	wave celerity
d	distance, still water depth
d_s	diameter of the Airy disk
E(k)	energy spectrum
f	frequency
g	gravitational acceleration
h	mean local water depth
h_b	mean water depth at break point
h_0	mean water depth near the wave generator
H_b	wave height at breakpoint
H_0	deep water wave height
I	intensity
k	turbulent kinetic energy, wavenumber
l	length scale
m	lens magnification
N	sample length
p	pressure
p_0	atmospheric pressure
R_{ij}	cross correlation of velocity components u_i and u_j
S_{ij}	mean rate of strain
s_{ij}	fluctuating strain rate
t	time
Δt	sampling time
T	wave period, exposure time
u	horizontal velocity component in the direction of wave propagation
u′	turbulent horizontal velocity component in the direction of wave propagation
u'_{rms}	rms value of u′
u_i	velocity component in cartesian tensor form
v	horizontal velocity component perpendicular u
v_x	velocity component along the x coordinate
v′	turbulent horizontal velocity component perpendicular to u
v'_{rms}	rms value of v′
w	vertical velocity component
w(x)	exposure weighting function
w′	turbulent vertical velocity component
w'_{rms}	rms value of w′
x	horizontal coordinate axis parallel to the wave flume
x_b	location of the breakpoint along the x-axis
y	horizontal coordinate axis perpendicular to the direction of wave propagation
z	vertical coordinate axis
z_t	elevation of trough level above the bed
ε	energy dissipation rate
η	vertical coordinate of water level with respect to the still water line
θ	phase

λ	wavelength
ν	kinematic viscosity
μ	molecular viscosity
ξ	mean waterlevel
ρ	density
σ_{ij}	stress tensor
τ_{ij}	Reynolds stress tensor
ϕ	phase
ω	radian frequency, vorticity

$\underline{<.>}$	phase ensemble-average operation
$\bar{.}$	time-averaging operation

CCD	charge coupled device
CSIR	council for scientific and industrial research
CIV	correlation image velocimetry
DCIV	digital correlation image velocimetry
DPIV	digital particle image velocimetry
FFT	fast fourier transform
FM	frequency modulation
LDA	laser doppler anemometry
MWL	mean water level
NSE	Navier-Stokes Equation
PC	personal computer
PIV	particle image velocimetry
PSF	point spread function
Re	Reynolds number
SWL	still water level
TKE	turbulent kinetic energy
VCR	video cassette recoder

CHAPTER 1

INTRODUCTION

The oceans play a significant role in terms of maintaining certain environmental and ecological balances. A complex interaction occurs between the ocean and the atmosphere that results in the present climatic conditions. In the modern world the oceans have began to play an ever more important socio-economic role with regards to transportation, recreation, land reclamation, dispersion of waste water and off-shore industrial activities to name a few. Thus there is a need to understand the dynamics of the oceans in order to evaluate the long term impact of natural and human activities in the ocean. The part of the ocean that is most dynamic is the region dominated by breaking waves and is referred to as the surf zone. The surf zone plays a vital recreational role and with the ever increasing human habitation along the coastline, it is imperative that protection and preservation of the state of the beaches and coastline is ensured. Thus, the measurement of surf zone physical parameters such as waves, fluid velocities, undertow currents and turbulence intensities will be the focus of this thesis. These measurements will assist in the quantification and modelling of the processes occurring in the surf-zone and these models in turn will assist in predicting phenomena such as beach erosion and coastline changes.

Physical processes

One of the most visible feature of the ocean is the presence of surface waves. These waves are generated offshore either by the interaction of the wind with the surface or by earthquakes or submarine landslides. The most common source of waves is undoubtedly the interaction of wind with the ocean surface. The actual mechanism involved in the air-sea interaction is still under intense study. Initially, ripples are created that grow in size and propagate in various directions, and a fair proportion of these deep water waves move towards the coastline where they are dissipated spectacularly in the form of breaking waves. These breaking waves have been the delight of many a surfer, beach-lover and even scientists. However, beneath that surface beauty lurks a power that can wreck havoc with the coastline and coastal structures.

In deep water the power of the waves is barely noticed by ships and boats, which simply bob up and down in sympathy with the wave passing beneath them. As the wave approaches the shallow, sloping region of the coast, it begins to slow down and there is a corresponding increase in the height of the waves and steepening of the front face of the wave, until a point is reached when the crest of the wave becomes unstable and breaking occurs. The breaking results in the generation of large amounts of turbulence and the creation of currents in the surf zone, such as rip currents, undertow currents and longshore currents. The turbulent fluid causes the suspension of sediments and these are then transported away by the current, resulting in erosion of the beach and shoreline. The water action, together with the suspended sediments, form a very abrasive mixture that is responsible for the weathering of natural and man-made structures.

With regard to beach erosion and sediment transport, there is in some cases a natural balance between the process of erosion and deposition. In one instance sediment may be removed and transported to another location and in another instance the process may be reversed. The improper positioning of man-made coastal structure can upset this natural balance, resulting in permanent erosion at one location and permanent deposition at another location. Thus, a thorough understanding of the hydrodynamic processes in the surf-zone can remove a lot of the guess-work in coastal design and provide a more realistic picture of the long term morphological changes. There has been significant advancements in our understanding of the

surf-zone through experimental and theoretical studies. It is instructive to briefly review some of the work done to date, the techniques employed and their short- comings.

Theoretical developments

Hydrodynamics are well described by the Navier-Stokes equation (NSE). This equation together with the boundary condition at the surface results in a highly nonlinear problem and a general analytical solution is not possible yet. In practice various approximation are then applied to simplify the NSE. For example, in solving the NSE for deep water waves, the boundary condition at the surface and the convective acceleration terms are linearised, resulting in solutions that are well known (*Le Mehaute,1976; Lighthill, 1978, Whitham, 1974*).

In shallow water it is necessary to employ dimensional analysis to decide which terms are small enough to be neglected. The NSE equation can then be shown to lead to the non-linear shallow water equations (NSWE) and the Boussinesq equation (*Peregrine, 1975*). These equations are based on depth averaged quantities and are not capable of providing detailed velocity flow fields. These equations are used however to predict the surface wave characteristics, such as the mean wave profile and the mean water level. Wave breaking is incorporated into the Boussinesq equation by the inclusion of a dissipation term when the wave slope exceeds a critical value (*Schaffer et al, 1992; Schaffer et al, 1993*). A more phenomenological approach in studying the mean quantities in the surf-zone, such as mean wave heights, wave set-down and set-up, results in a set of differential equations that can be solved numerically (*Svendsen, 1978*).

The theoretical analysis of turbulence is accomplished by representing all quantities in the NSE as the sum of a steady component and a fluctuating component. Substitution in the NSE and computing the time average results in a set of differential equations describing the mean and fluctuating parts of the flow (*Tennekes and Lumley, 1972*). It can be shown that the equation for the mean flow has the contribution of a stress, called the Reynolds stress. The measurement and modelling of the Reynolds stress term in the surf-zone is therefore the subject of intense study.

Existing experimental measurements

Due to the highly non-linear nature of the processes occurring in the surf-zone, it is necessary to rely heavily on experimental measurements to provide some insight to the problem at hand. Visual observations of the movements of the air bubbles created during wave-breaking, indicate the creation of horizontal and oblique vortices (*Nadaoka, 1988*) and high levels of turbulence. It is believed that most of the turbulence is generated in the roller that is formed on the front face of the wave. In a comprehensive review of the existing turbulence measurements, *Mocke(1998)* finds that most measurements have been performed using Laser Doppler Anemometry (LDA), an interferometric technique, and measurements are available mostly for position below the trough level (*Stive, 1980*). Some improvements to the conventional LDA have been made using fibre optics (*Hino et al, 1984; Nadaoka, 1989; Ting and Kirby, 1994,1995,1996*). These measurements tend to confer that there are high levels of turbulence in the upper part of the water column. *Ting and Kirby(1994)* have shown that spilling and plunging waves have different turbulence transport characteristics. They maintain that in spilling waves turbulence is transported seawards, and landwards in a plunging wave. Experiments in a natural surf-zone using hot-film measuring techniques and random waves have also been done (*George et al, 1994*). More details on existing surf zone measurements will be provided in chapter 2.

Despite the large number of surf-zone measurements, there is still a lack of data in the crests of the wave, where high levels of aeration are present. There is also some question about the validity of LDA and hot-film measurements in the surf zone, in general. These methods are sensitive to the presence of air bubbles, resulting in signal drop-out. In the surf zone the air bubbles can reach regions well below the trough levels. The signal drop-out in these measurements can create havoc with the turbulence intensity measurements. The conventional techniques also provide only a point measurement in space.

Imaging techniques

Traditionally, the time series of the surface wave is measured using partially submerged resistance or capacitance wave gauges. In order to measure the time series over a large area, it is necessary to use a number of gauges or alternatively to make measurements sequentially using a single gauge. This can be a tedious exercise and conceivably gauges can interfere

with the local flow behaviour. The performance of these gauges in the surf zone is also often unreliable due to the highly aerated water and rapid evolution of the air-water interface.

The fluid velocity is usually measured using either a mechanical propeller, electromagnetic flow meters, hot wire anemometer or laser doppler anemometry (LDA). LDA is an interferometric technique that provides a velocity measurement at a single point and has sufficient frequency resolution in turbulent flows. None of the above techniques can however provide an instantaneous snapshot, that is, a spatially extended synoptic view of the flow field. Secondly, LDA systems in particular are labour intensive to set up and the equipment required is costly. The conventional LDA also fails due to signal dropout when there is a large concentration of air bubbles in the measurement area, such as in the surf zone, although this problem has been alleviated somewhat through the use of fibre optics (*Hino et al, 1984*).

Recently there has also been a growing interest in the use of imaging techniques to measure wave parameters in the laboratory and in the ocean. A number of researchers have reported on the measurement of water surface elevation using specular reflection of the water surface (*Krishnan et al, 1974; Jahne et al, 1994*). This type of measurement is suitable for the study of the spectral-wavenumber characteristics of waves in a model hall and at sea. There has also been a serious interest in the application of optical techniques to the measurement of velocities within a breaking wave (*Quinn et al, 1995*) and in the surf zone (*Govender et al, 1996; Craig et al, 1996; Chang et al, 1996*).

In this thesis we set out to develop new measuring techniques to overcome the limitation imposed by the conventional methods (*Govender et al, 1998*) and to provide new experimental data to validate and supplement existing data (*Govender et al, 1996, 1997; Alport et al,1998; Govender et al, 1999*). The limitations of the conventional measuring instruments in the surf zone has created a need for alternative methods that are more suitable in this region. The use of video techniques has been shown to have many promising advantages and there is a growing interest in the application of video techniques to measurements in fluid mechanics. The early applications of imaging techniques were film-based (e.g. *Bijker et al, 1974, Dimotakis et al, 1981*) and these involved tracking the images

of particles in fluids, that were illuminated by a laser sheet, with the view to estimating fluid velocities. The analysis of the images were done optically using speckle analysis(*Erf, 1980*). With the proliferation of digital electronic equipment and digital signal processing techniques, most of the film-based recording and processing techniques have been superseded by CCD imaging cameras and digital processing (*Adrian, 1991; Fincham et al, 1997; Govender et al, 1998; Hesselink, 1988; Tokumaru et al, 1995; Willert and Gharib, 1991*). There has also been an interest in the use of optical and video techniques to measure the surface elevation of waves in fluids (*Krishnan et al,1974; Jahne et al, 1994; Govender et al, 1996, 1998*). It will be shown in this thesis that digital video techniques can provide a versatile set of diagnostic tools for the study of surf zone behaviour.

Thesis layout

In Chapter 2 the basic definitions and hydrodynamic concepts are reviewed. These include the concepts of translation, rotation and deformation of fluid elements. The mass and momentum flux, and the radiation stress are also reviewed. The equations describing the motion of a fluid element is presented together with their linearised solutions. This is followed by a qualitative description of wave breaking and the processes occurring in the surf zone. Turbulence theory is reviewed together with existing LDA measurements of turbulence in the surf zone.

A description of the experimental facility and the diagnostic equipment is given in Chapter 3. The experimental setup, dimension of the wave tank and measurement positions are also described.

The experimental techniques that were developed to measure the time series of the surface wave and the fluid velocity flow fields using video techniques are discussed in Chapter 4. A general discussion is presented and describes the choice of various instruments and digital analysis techniques. This includes a description of the various stages of the development of the technique, which incorporated a range of measurement and analysis techniques. The time series of the wave surface was measured using keograms and the fluid velocities were measured using digital particle image velocimetry and digital correlation image velocimetry.

In Chapter 5 results of the temporal measurement of the surface wave along the surf-zone are presented for a 0.9 Hz spilling and 0.4 Hz plunging waves. The computation of the mean wave height and water levels is also presented for the above cases. The comparison with time series of water levels obtained from wave gauges is presented. Keograms, consisting of sequential slices of the grey scale images, were used to measure the roller area and slope.

The measurement of the velocity flow fields in a 0.9 Hz spilling wave and 0.4 Hz plunging waves, using digital correlation image velocimetry, is presented in Chapter 6. Significantly, it is possible to make velocity measurements well into the aerated region of the waves. The velocity undertow is computed from the phase ensemble-averaged velocity flow fields. This chapter includes a sensitivity analysis of the influence of sample and bin sizes on the convergence of the mean and rms velocities. The imaged data is compared with similar results reported in the literature.

The turbulence analysis of the velocity data presented in Chapter 6 is examined in Chapter 7. The computation of the turbulent intensities, or the rms values of the fluctuating velocity components, using phase ensemble-averaging is presented. The time-averaged turbulence intensities and Reynolds stress are computed from the phase ensemble-averaged turbulence intensities. It will be shown that the turbulence intensities increase rapidly from the bed upwards, reaching a maximum just above the trough level and decreasing thereafter. The Reynolds stress near the bed increases almost linearly with distance above the bed. The analysis of the phase ensemble-averaged vorticity and the spectral analysis is also presented in Chapter 7.

CHAPTER 2

BASIC CONCEPTS AND THEORY

In this chapter the definition of standard variables and hydrodynamic concepts are reviewed. The equations describing the motion of a fluid element is presented followed by the linear theory of surface waves. The breaking of waves on sloping beaches and the resulting processes occurring in the surf zone are reviewed. The theory of turbulence is examined via the Reynolds decomposition of the terms in the Navier-Stokes equation, and the significance of the resulting Reynolds stress is highlighted. A detail examination of some selected measurements of turbulence in the surf zone is also presented.

2.1 Introduction

The basic concepts of hydrodynamics and the description of standard variables used in coastal and surf zone literature are described in this chapter. The continuity and the Navier-Stokes equations of motion describing the motion of the fluid flow and their approximate linear solutions are presented. This is followed by a discussion on the wave breaking process as deep water waves approach a sloping beach. The development of the equations describing turbulent fluid motion is presented, followed by a review of existing turbulence measurements in the surf zone.

The equations of motion of a fluid element is obtained by applying the conservation of mass and the balance of forces. This results in the equation of continuity and the Navier-Stokes equation(NSE). The Navier-Stokes equation is highly nonlinear due to the convective acceleration terms. The nonlinear nature of the NSE and the free surface boundary condition makes analytical solution to the NSE very difficult, if not impossible. In cases where the viscous forces are negligible the Navier-Stokes equation reduces to the Euler equation. If the flow is considered irrotational, then a velocity potential function together with a linearised free surface boundary condition can be employed to obtain a linear solution to the Euler equation.

Deep water waves moving towards a sloping beach begin to slow down. This is accompanied by an increase in wave height and a lowering of the mean water level, referred to as set-down. At a critical wave height breaking occurs. The condition for breaking is dependent on the wave height, wavelength and the beach slope. The overturning of the wave results in the formation of a roller that rides on the front face of the wave. The breaking results in the generation of horizontal and oblique eddies and large amounts of turbulence.

The theory of turbulence is analyzed by decomposing the variables in the Navier-Stokes equation into a mean and fluctuating part, and computing ensemble averages results in a set of equation describing the mean flow, mean kinetic energy and turbulent kinetic energy. These equations contain the Reynolds stress term. Existing measurements of turbulence intensities and the time-averaged quantities are presented.

2.2 Hydrodynamic concepts

The orientation of the coordinate system and symbols commonly used in the study of water waves is illustrated in Figure 2.1 below. The positive x-axis extends in the direction of wave propagation, while the positive y and z axis extend in horizontal and vertical directions perpendicular to the direction of wave propagation. The distance between the still water line (swl) and the bed is represented by d and the displacement of the water surface with respect to the swl is represented by η. The wave height, H, is the vertical distance between the wave trough and crest. The fluid velocities in the x, y and z directions are represented by u, v and w , respectively.

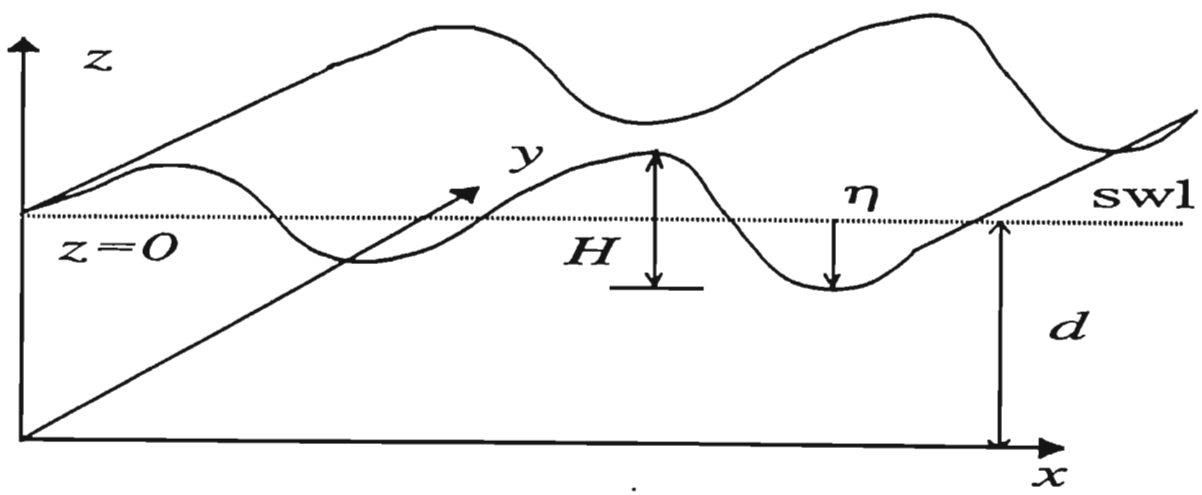

Figure 2.1: Coordinate axes and symbolic notation.

The total acceleration of a fluid element consists of a local and convective acceleration terms, that is:

$$\boldsymbol{a}=\frac{d\boldsymbol{u}}{dt}=\frac{\partial \boldsymbol{u}}{\partial t}+\frac{\partial \boldsymbol{u}}{\partial x}\frac{\partial x}{\partial t} \tag{2.1}$$

where $\boldsymbol{u}=(u,v,w)$ and $\boldsymbol{x}=(x,y,z)$.

The local acceleration is the acceleration, as function of time, at a point as the fluid passes through it, and the convective acceleration is the acceleration of a fluid element with respect to change in position. It is the convective acceleration that is responsible for the deformation, rotation and the straining of fluid elements.

Other important concepts are the mass and momentum flux, and the radiation stress.
The mass flux in the x-direction is defined as:

$$M=\int_0^z \rho u(z)dz \tag{2.2}$$

and the momentum flux as:

$$F_t=\int_0^z \rho u(z)^2 dz \tag{2.3}$$

where ρ is the density of water.

The radiation stress (*Longuet-Higgins, 1964*), which is the rate of flow of momentum, is given by:

$$\begin{aligned} S_{xx} &= \overline{\int_{-d}^{\eta}(p+\rho u^2)dz} - \int_{-d}^{0} p_0 dz \\ S_{yy} &= \overline{\int_{-d}^{\eta}(p+\rho v^2)dz} - \int_{-d}^{0} p_0 dz \\ S_{xy} &= \overline{\int_{-d}^{\eta}\rho uv dz} \end{aligned} \tag{2.4}$$

S_{xx} and S_{yy} are the rate of flow of momentum across the planes perpendicular(x=constant) and parallel(y=constant) to the direction of wave propagation, while S_{xy} is the rate of flow of x-momentum across the plane y=constant.

Using the results of linear wave theory, to be discussed next, the radiation stresses in 2D non- breaking deep water waves are:

$$
\begin{aligned}
S_{xx} &= E\left(\frac{2kd}{\sinh(2kd)}+0.5\right) \\
S_{yy} &= E\left(\frac{kd}{\sinh(2kd)}\right) \\
S_{xy} &= 0
\end{aligned}
\tag{2.5}
$$

where d is the local water depth, k is the wavenumber and E is the energy of the wave. This simplifies to:

$$
\begin{aligned}
S_{xx} &= 0.5\ E\ (\textit{deep water}\quad) \\
S_{xx} &= 1.5\ E\ (\textit{shallow water}) \\
S_{yy} &= 0.5\ E\ (\textit{shallow water})
\end{aligned}
\tag{2.6}
$$

2.3 Linear wave theory

The motion of a fluid element is obtained by applying the conservation of mass and Newton's laws resulting in the equation of continuity:

$$\nabla . \boldsymbol{u} = 0 \tag{2.7}$$

and the Navier-Stokes equation:

$$\frac{\partial \boldsymbol{u}}{\partial t} + \boldsymbol{u}\nabla . \boldsymbol{u} = \nabla(p + \rho g z) + \mu \nabla^2 \boldsymbol{u} \tag{2.8}$$

The terms on the left hand side represent the local and convectional acceleration terms. The first term on the right represents the sum of the hydrostatic and dynamic pressure force, while the second term represents the viscous force. This equation is highly nonlinear due to the convective acceleration terms. In situations were the viscous force is small, the NSE reduces to the Euler equation which is still nonlinear due to the convective acceleration term. The ratio of the viscous term to the convective term is used as measure of the relative strengths of the viscous and convective term. This ratio, estimated using the length scale, l, the velocity scale, u, of the process, and the kinematic viscosity of the fluid, ν,results in the Reynolds number: $Re = ul/\nu$. The Reynolds number is often used to quantify the transition between laminar and turbulent flows

If the fluid flow is irrotational(i.e. $\nabla \times \boldsymbol{u}=0$), then a linear solution to the Euler equation can be obtained using a velocity potential function, ϕ, such that $\boldsymbol{u}=\nabla\phi$, together with the linearised free surface boundary condition. This results in the following expressions for the potential function, particle velocities and dispersion relation (*Le Mehaute, 1976*):
The potential function is given by:

$$\phi=-a\frac{\omega}{k}\frac{\cosh k(d+z)}{\sinh kd}\cos(\omega t-kx) \tag{2.9}$$

where a is the amplitude of the wave($a=H/2$), d is the local water depth, k is the wavenumber and ω is the radian frequency.

The velocities components are then obtained using $\boldsymbol{u}=\nabla\phi$:

$$u=a\omega\frac{\cosh k(d+z)}{\sinh kd}\sin(\omega t-kx) \tag{2.10}$$

$$w=a\omega\frac{\sinh k(d+z)}{\sinh kd}\cos(\omega t-kx) \tag{2.11}$$

and the dispersion relation is:

$$\omega^2=kg\tanh(kd) \tag{2.12}$$

If the wavelength, L, is very much less than d, then the above equation reduces to $\omega^2=kg$, and in shallow water, where L is very much greater than d, $(\omega/k)^2=gd$. Thus in shallow water the speed of the wave is a function of the depth.

The energy per unit horizontal area of the wave is:

$$E=\frac{1}{8}\rho g H^2 \tag{2.13}$$

2.4 Surf zone processes

Figure 2.2 shows a schematic illustration of the processes occurring as offshore waves propagate towards a beach. Deep water waves propagating towards a sloping beach begin to slow down, accompanied by a corresponding increase in wave height, referred to as shoaling. There is also a corresponding lowering of the mean water level, referred to as set-down. Further increase in wave height occurs as the wave moves up the beach, until a point is reached at which breaking occurs. Beyond the breakpoint, the wave height decreases and the mean water level begins to rise. The region immediately beyond the breakpoint is called the transition region. Here the mean water level remains fairly constant.

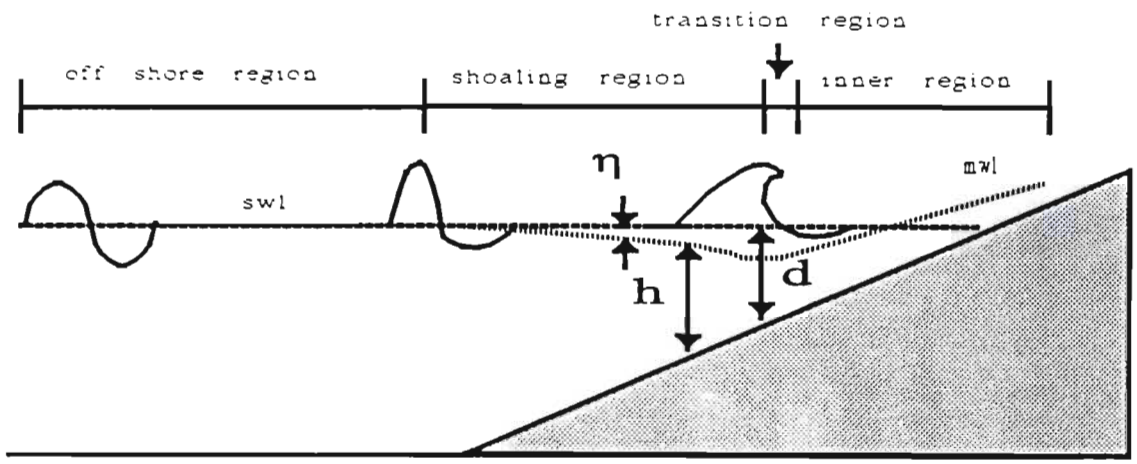

Figure 2.2: Schematic illustration of shoaling, wave breaking, set-down and set-up of the mean water level.

The notation described in Section 2.1 also applies to the surf zone with the following additions. A subscript *o* implies wave conditions offshore, that is far away from the beach, while variables with a subscript *b* signify conditions at the break point. Further, $\overline{\eta}$ denotes the mean water level with respect to the still water line and h refers to the local mean water depth.

Breaking water waves are classified as spilling, plunging or surging according to the way in which they break (*Galvin, 1968*). In a spilling wave a volume of fluid near the top of the crest slides down the front face of the wave at the break-point, and in a plunging wave there is a curling of the wave front at the break-point, forming a jet of water. The surging breaker develops like a plunging wave but their bases surge up the beach before the crest can plunge. The spilling and plunging wave, which are the most dominant wave types, have very different actions on the sediment transport (*Ting and Kirby, 1994*). Measurements involving waves in the surf zone are therefore placed in these two categories.

The breaking of waves results in the formation of a roller that rides on the front face of the wave, and moves forward with same speed as the wave. The water mass in the roller is also rotating about a horizontal axis that is parallel to the wave-front, thus creating a huge amount of turbulence and shear stress at the front face of the wave. A sequence of images showing the wave breaking and roller formation is shown in Figure 2.3. The top three images in Figure 2.3 shows the steepening and curling of the wave-front forming a jet of water that moves forward. The middle three images show the collapsing of the top of the wave and the subsequent splash-up and formation of the resulting roller. The last three images show the final stages in the roller formation. The penetration of aeration into the lower and rear of the wave is also visible.

When considering the water motion subject to the action of waves, from a Eulerian point of view, there is always a shoreward mass flux between the trough and crest, and there is a return current below the trough level (*de Vriend*). In breaking waves these effects are enhanced. In non-breaking waves the mass flux equals $\rho E/c$, where c is the phase speed of the wave and E is wave energy per unit horizontal area. The undertow in breaking waves is driven by an effective surface stress which is proportional to D/c, where D is the wave energy dissipation rate due to breaking.

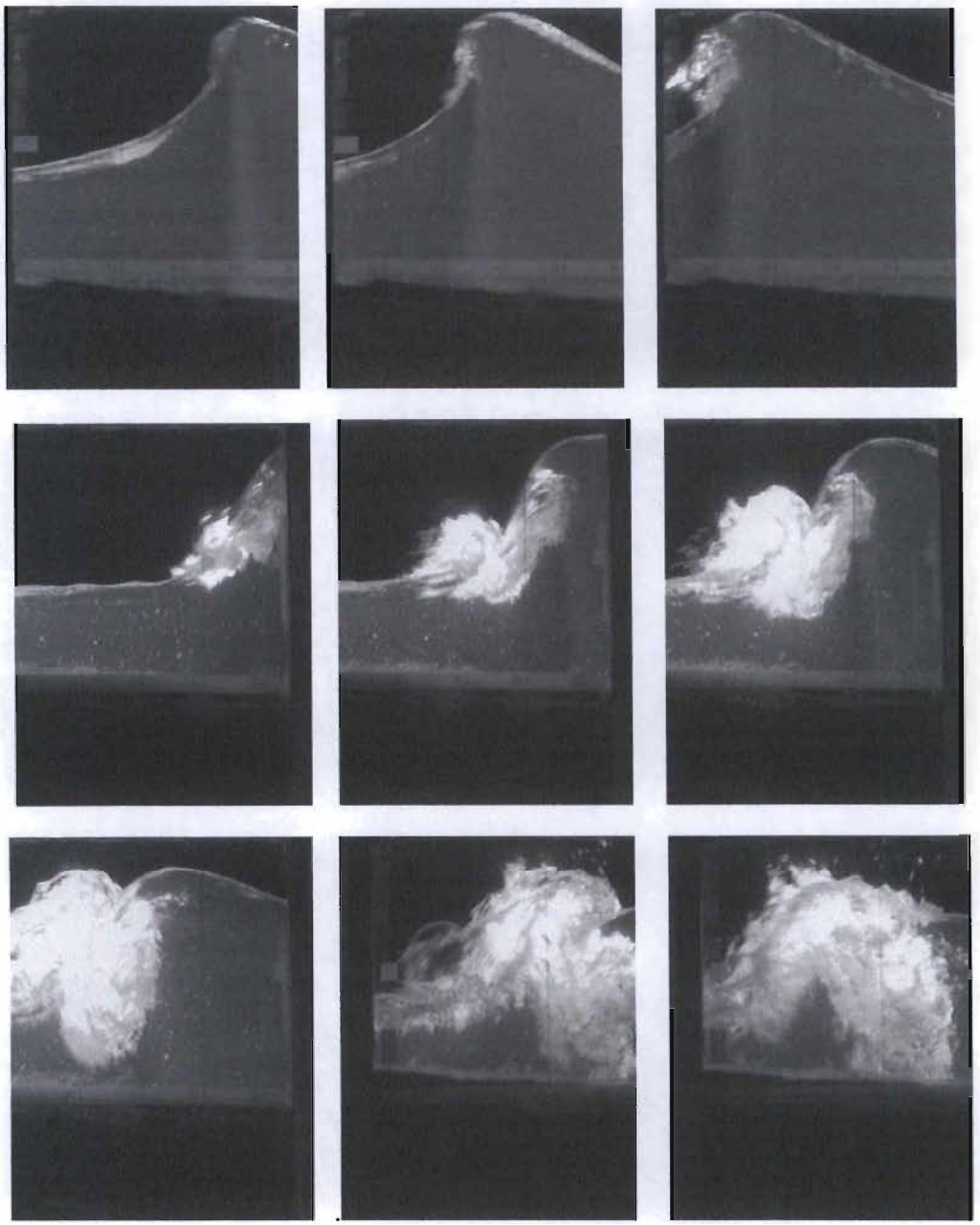

Figure 2.3: Images of a wave approaching breaking and the formation of the roller that rides on the front face of the wave. Images are arranged in rows with the wave propagating from right to left. The bottom three images also show the penetration of aeration into the lower part of the wave. These images were obtained using the setup to be described in Chapter 3.

Wave breaking criterion

The stability of waves in deep water is characterised by the ratio of the wave height, H, to the wavelength, L. A theoretical maximum value of the steepness was found by *Miche(1944)* to be:

$$\left(\frac{H}{L}\right)_{max} = \frac{1}{7}\tanh\frac{2\pi d}{L} \qquad (2.14)$$

In deep water Equation 2.14 reduces $(H_0/L_0)=1/7$ and this occurs when the crest angle is 120^0. In shallow water Equation 2.14 reduces to (H/L)=0.9.

The earliest criterion for the breaking of waves in shallow water is by *McCowan(1894)*, as reported by *Dean and Dalrymple(1991)*, who related the breaking wave height to the local water depth as follows:

$$H_b = \kappa\, d_b \qquad (2.15)$$

where κ is an empirical constant and a value $\approx$ 0.74 has been used, although field measurements indicate that κ ranges from 0.5 to 0.9. More recently, the criterion for breaking has been derived to be (*Weggel, 1972*):

$$\frac{H_b}{d_b} = b_m - a_m\frac{H_b}{gT^2} \qquad (2.16)$$

where H_b is wave height at breaking, d_b is water depth at breaking, m is the beach slope, T is the wave period, g is the gravitational acceleration, and

$$a_m = 43.8[1.0 - e^{-19m}]$$

$$b_m = 1.56/[1.0 + e^{-19.5m}]$$

Energy dissipation in breaking waves

The energy dissipation in progressive waves have been computed by comparing the broken waves in the surf zone to that of a periodic bore (*Le Mehaute, 1962*), and is given by:

$$D = \frac{\rho g h H^3}{T(4h^2 - H^2)} \qquad (2.17)$$

where H is the wave height, h is the local water depth and T is the wave period.

The energy dissipation in a random field (*Battjes and Jansen, 1978*) as been studied by assuming a Rayleigh probability distribution of wave heights. In shallow water, the Rayleigh distribution is truncated above a maximum wave height, H_m, that can be sustained in a given depth of water. In shallow water $H_m=\gamma h$, where γ is an adjustable parameter to cater for the effects of beach slope and random waves has been used by *Battjes and Jansen (1978)*. At any position along the beach the wave energy dissipation, D_w, is based on the fraction of broken waves, Q_b and is given by:

$$D_w \sim \frac{1}{4} Q_b \bar{f} \rho g H^2{}_m \tag{2.18}$$

where $\overline{f}$ is the mean frequency of the random waves.

Wave roller properties

The energy of the roller, E_r, can be defined as follows (*Svendsen, 1984*):

$$E_r = \frac{1/2 m_r c^2}{L} = \rho \frac{Ac^2}{2L} = \rho \frac{Ac}{2T} \tag{2.19}$$

where m_r is the roller mass, L is the wavelength, c is the wave propagation speed and ρ is the fluid density.

Estimates of the roller area by *Svendsen(1984)* using hydrofoil measurements by *Duncan(1981)* resulted in the following:

$$A = 0.9H^2 \tag{2.20}$$

More recently (*Dally and Brown, 1995*) have attempted to theoretically estimate the roller area in the surf zone, based on a depth-integrated and time-averaged energy balance equation that contains contribution from both the organised wave motion and the roller.

The energy, D_r, dissipated by the roller as a result of shear stress, τ_s, between the roller and the underlying wave can be described (*Fredsoe and Deigaard,1992*) by:

$$D_r = -\tau_s c = \beta \rho g \frac{A}{T} \tag{2.21}$$

where $\tau_s = \rho g A \beta / l_r$ and β is the roller slope and l_r is the roller length (see figure below).

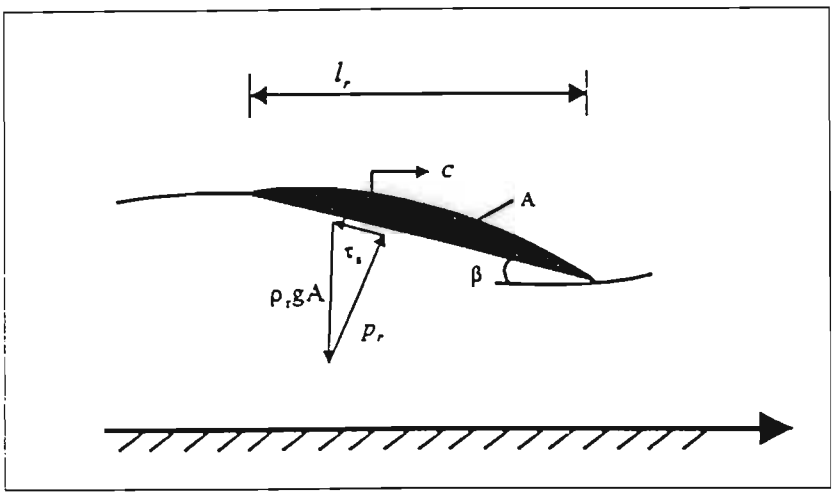

Figure 2.4: Roller configuration (*Fredsoe and Deigaard, 1992*).

Mean water level

The changes to the mean water levels can be described in terms of radiation stress, S_{xx}. The balance of momentum is then given by:

$$\frac{\partial \overline{\eta}}{\partial x} = -\frac{1}{\rho g(d+\overline{\eta})}\frac{\partial S_{xx}}{\partial x} \tag{2.22}$$

where d is the depth below the swl and $\overline{\eta}$ is the mean water level.

As the waves move from the open sea towards the shore, it encounters the shoaling area where S_{xx} increases primarily due to the increase of energy, which is a consequence of the decrease of the phase speed of the waves as the water becomes shallower. In this shoaling area $\overline{\eta}$ decreases, because $\partial\overline{\eta}/\partial x \propto -\partial S_{xx}/\partial x$. The horizontal particle velocity, however, will increase. This can be shown by taking the shallow limit of Equation 2.10 and noting the fact that the wave amplitude increases in the shoaling region.

Longuet-Higgins and Stewart(1962) have integrated Equation 2.22, using Equation 2.5 and the fact that seaward of the breakpoint the energy flux of the wave is constant, to obtain the following expression for the mean water level:

$$\overline{\eta} = -\frac{1}{8}\frac{H^2 k}{\sinh(2kh)} \tag{2.23}$$

Beyond the breakpoint, there is a strong energy dissipation and decrease in wave height resulting in a negative gradient in the radiation stress as the waves moves upon the beach. This negative gradient in radiation stress results in the increase in mean water level, called set-up.

2.5 Turbulence

Reynolds Decomposition

The motion of the fluid flow is described by the Navier-Stokes equation, discussed in Section 2.3, and it is re-examined here in order to further describe the effects of turbulence. With the view to making the above expansion more compact and in keeping with the notation used in most, if not all, treatments of turbulence, cartesian tensor notation will be used in this chapter. An equation with index i implies that there are three equations corresponding to the three coordinates of 3D space, and repeated index in any term implies the summation over all values of that index.

The equations of motion for an incompressible fluid are the momentum and continuity equation. The momentum equation is given by:

$$\frac{\partial u_i}{\partial t} + u_j \frac{\partial u_i}{\partial x_i} = \frac{1}{\rho}\frac{\partial}{\partial x_j}\sigma_{ij} \tag{2.24}$$

σ_{ij} is the stress tensor and represents the stresses acting on all sides of a fluid element. The stress tensor can be written in terms of the pressure and the rate of strain as follows:

$$\sigma_{ij} = -p\delta_{ij} + 2\mu s_{ij} \tag{2.25}$$

where μ is the molecular viscosity and s_{ij} is the rate of strain given by:

$$s_{ij}=\frac{1}{2}\left(\frac{\partial u_i}{\partial x_j}+\frac{\partial u_j}{\partial x_i}\right) \tag{2.26}$$

The Navier-Stokes equation can now be derived by using the equation of continuity and the above equations to give:

$$\frac{\partial u_i}{\partial t}+u_j\frac{\partial u_i}{\partial x_j}=-\frac{1}{\rho}\frac{\partial p}{\partial x_i}+\nu\frac{\partial^2 u_i}{\partial x_j \partial x_j} \tag{2.27}$$

where ν is the kinematic viscosity and is equal to μ/ρ.

In the case of turbulent flows, it is customary to decompose the flow into its mean and fluctuating components, a technique first applied to fluid mechanics by *Osborne Reynolds(1894)* and is therefore referred to as the Reynolds decomposition. Thus the velocity, pressure and rate of strain are represented as follows:

$$u_i=<u_i>+u_i',\ p=<p>+p',\ s_{ij}=<s_{ij}>+s_{ij}' \tag{2.28}$$

The bracketed letters represent the ensemble-averaged components and the acute denotes the fluctuating part. Substituting the above into Equation 2.27 and noting that the mean of the fluctuating parts are zero, results in the following equation for the mean flow:

$$\frac{\partial<u_i>}{\partial t}+<u_j>\frac{\partial<u_i>}{\partial x_j}=-\frac{1}{\rho}\frac{\partial<p>\delta_{ij}}{\partial x_j}+\frac{1}{\rho}\frac{\partial 2\mu<s_{ij}>}{\partial x_j}-\frac{\partial<u_i'u_j'>}{\partial x_j} \tag{2.29}$$

Thus, the equation describing the motion of the mean flow cannot be obtained simply by substituting mean quantities into the Navier-Stokes equation; there is a contribution by turbulence to the mean flow. The equation describing the mean flow now has additional unknowns in the form of $<u_i'u_j'>$. These terms form the Reynolds stress tensor which has nine components of which only six are independent of each other (the tensor is symmetric). The above decomposition now has more unknowns than equations, resulting in what is known

as the closure problem. In order to solve these equations it is therefore necessary to find expressions to model the Reynolds stresses. These expressions are often determined using empirical data. Methods of modelling the Reynolds stresses will be examined later.

Since the mean values of the fluctuating components are zero, it is difficult to analyze the influence of the mean flow on the turbulence. It is therefore best to examine the kinetic energies of the mean and turbulent flows. The equation of the kinetic energy of the mean flow is:

$$\frac{\partial}{\partial t}\left(\frac{1}{2}<u_i><u_i>\right)+<u_i>\frac{\partial}{\partial x_j}\left(\frac{1}{2}<u_i><u_i>\right)=\frac{\partial}{\partial x_j}\left(-\frac{<p>}{\rho}<u_j>+2\nu<u_i><s_{ij}>-<u_i'u_j'><u_i>\right) \quad (2.30)$$
$$-2\nu<s_{ij}><s_{ij}>+<u_{,i}'u_j'><s_{ij}>$$

where $<s_{ij}>$ is the mean strain rate given by:

$$<s_{ij}>=\frac{1}{2}\left(\frac{\partial<u_i>}{\partial x_j}+\frac{\partial<u_j>}{\partial x_i}\right) \quad (2.31)$$

The first three terms on the right hand side of Equation 2.30 are due to the action of pressure, transport of mean flow energy by viscous stresses, and transport of mean flow energy by Reynolds stresses, respectively.

The equation of the turbulent kinetic energy, k, is given by:

$$\frac{\partial k}{\partial t}+\frac{\partial<u_j>k}{\partial x_j}=-\frac{\partial}{\partial x_j}\left(\frac{1}{\rho}<u_j'p'>+<u_j'k'>-2\nu u_i's_{ij}'\right) \quad (2.32)$$
$$-<u_i'u_j'><s_{ij}>-2\nu<s_{ij}'s_{ij}'>$$

where $k=1/2<u_i'u_i'>$, $k'=1/2(u_i'u_i')$ and s_{ij}' is the fluctuating strain rate given by:

$$s_{ij}'=\frac{1}{2}\left(\frac{\partial u_i'}{\partial x_j}+\frac{\partial u_j'}{\partial x_i}\right) \quad 2.33$$

The first three terms on the right hand side of Equation 2.32 are due to the work by the pressure gradient, transport by turbulent velocity fluctuations and transport by viscous stresses, respectively. The last two terms are due to the work associated with deformation. Notice the term $-<u_i'u_j'><s_{ij}>$ occur with opposite sign in the equation for the mean and turbulent flows. This term serves to exchange energy between the mean flow and turbulence. The last term in Equation 2.32 is the work due to the deformation by viscous stresses and it is always a drain of energy.

Thus, from the above equations an estimate of the rate of production, P, and dissipation, ε, of turbulent energy can be obtained as follows:

$$\begin{aligned} P &= -<u_i'u_j'><s_{ij}> \\ \varepsilon &= 2\nu<s_{ij}'s_{ij}'> \end{aligned} \tag{2.34}$$

P and ε can be in local equilibrium, however, in most cases the energy is produced at one point, transported and dissipated at another point in space or time as described by Equation 2.32.

Vorticity dynamics

The vorticity is the curl of velocity vector field and is given in tensor notation as:

$$\omega_j = \delta_{ijk}\frac{\partial u_k}{\partial x_j} \tag{2.35}$$

where δ_{ijk} is the alternating tensor (0 for any two indices being equal, +1 for any even number of permutations, and -1 for any odd permutations).

It is instructive to examine the how the vorticity influences the Navier-Stokes equation. By rearranging terms in Equation 2.27 and using the equation of continuity, Equation 2.27 can be rewritten as:

$$\frac{\partial u_i}{\partial t} = -\frac{\partial}{\partial x_i}\left(\frac{p}{\rho} + \frac{1}{2}u_j u_j\right) + \delta_{ijk} u_j \omega_k - \nu \delta_{ijk} \frac{\partial \omega_k}{\partial x_j} \tag{2.36}$$

If the flow is irrotational, that is, $\omega_k = 0$, then the above equation reduces to the Bernoulli equation. The term $\delta_{ijk} u_j \omega$ is crucial to turbulence theory. It is analogous to the Coriolis force that would appear if the system were rotating with an angular velocity.

The equation describing the vorticity dynamics is obtained by computing the curl of the Navier-Stokes equation. The time evolution of the vorticity field is then given by:

$$\frac{\partial \omega_i}{\partial t} + u_j \frac{\partial \omega_i}{\partial x_j} = \omega_j s_{ij} + \nu \frac{\partial^2 \omega_i}{\partial x_j \partial x_j} \tag{2.37}$$

The term $\omega_j s_{ij}$ represents amplification and rotation of the vorticity by the strain rate. The second term on the right represents the effects of viscous diffusion. The vortex stretching is considered to be the most important contributor to vorticity production in turbulent flows. The concept of vortex stretching is depicted in Figure 2.5. A fluid element under the influence of a linear strain (Figure 2.5(a)) will be stretched in the direction of strain and its cross section in the plane perpendicular to the strain will become smaller. Extending this argument to vortices, those vortices whose axes are aligned with direction of strain will become smaller in cross-section, while those vortices with axes perpendicular to the direction of strain will become larger (*Frost and Moulden, 1977*). The above description provides some insight into the manner in which energy is extracted from the shear due to the mean flow and transferred to the large scale vortices, and from the large scale vortices to smaller scale vortices.

Turbulence measurement in the surf zone

A brief review of existing measurements of turbulence in the surf zone has already been presented in Chapter 1. Details, including test conditions and results, of some of these works will be presented here. A comprehensive review of published measurements is presented in *Mocke(1998)*. Most of the measurements have been made using LDA.

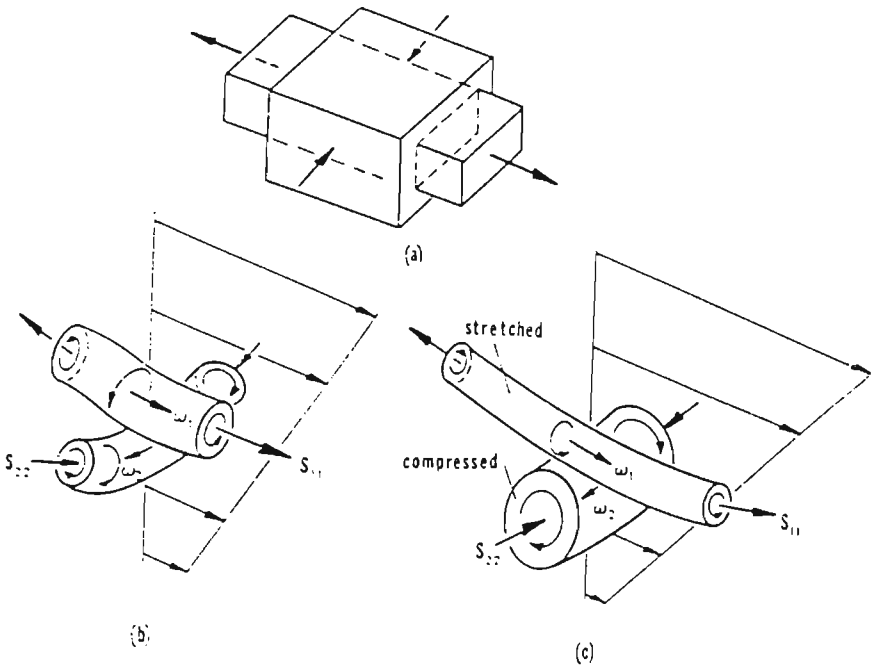

Figure 2.5: Concept of vortex stretching (*Frost and Moulden, 1977*).

One of the earliest turbulence measurements was conducted by *Stive(1980)* on spilling (test 1) and plunging(test 2) waves, breaking on a 1:40 slope beach. Measurements of turbulence intensities in a plunging wave as reported in *Stive(1980)* is shown in Figure 2.6. Due to signal drop-out, no measurements are available in the aerated region of the crests. Peak turbulence intensities in the order of 10-12 cm/s are found to occur near the trough level within the crest.

The measurement of the time-averaged turbulent kinetic energy by a number of researchers for the case $h/h_b \sim 0.7$, as extracted from *Mocke(1998)*, is shown in Figure 2.7. Since only two components of the velocities were measured, it is not possible to measure directly the turbulent kinetic energy, but this quantity is estimated using the relation:

$$k = 1.33\frac{1}{2}(<u'_{rms}>^2 + <w'_{rms}>^2)$$

This relation is based on the assumed relative magnitudes of the velocity components derived from measurements in a plane wake.

The results in Figure 2.7 shows that measurements are available mostly for vertical positions of $z/h < 0.8$. The measurements by *Stive(1980)* and *Ting & Kirby(1994)* are very similar,

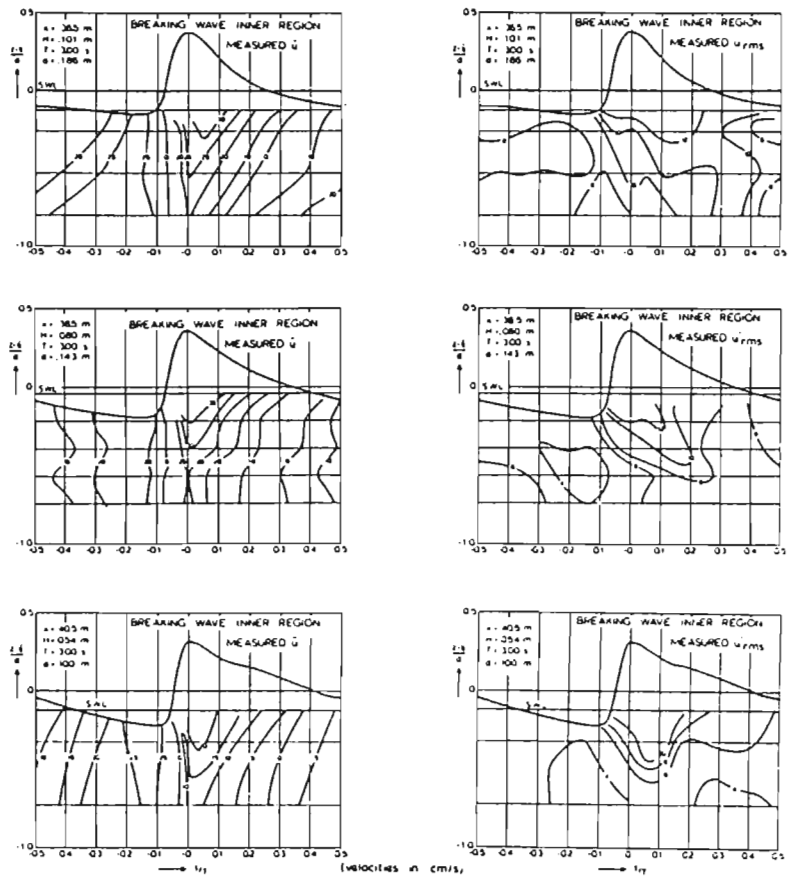

Figure 2.6: Measured horizontal periodic and turbulent velocities (cm/s) of *Stive(1980)* test 2 (plunging wave), over the wave period.

being grouped close together. The field measurements of *George et al.(1994)*, under random waves, are seen to be very much lower. Most of the measurements also show a decreasing trend with respect to distance below the trough level. The measurements by *Okaysau(1989)* shows a rapid increase near the trough level. This is the first indication of higher turbulent kinetic energy in the crest of the waves and confirmation and extension of this result will be shown in Chapter 7.

The phase ensemble-averaged vorticity computed by *Nadaoka(1989)* using the equation:

$$<\omega> = \frac{\partial <u>}{\partial z} - \frac{\partial <w>}{\partial x}$$

is shown in Figure 2.8. There is a marked peak in vorticity at the front face of the wave near the toe of the roller, while there is lower vorticity in the rear of the wave. This suggests that the vorticity is generated at the front face of the wave.

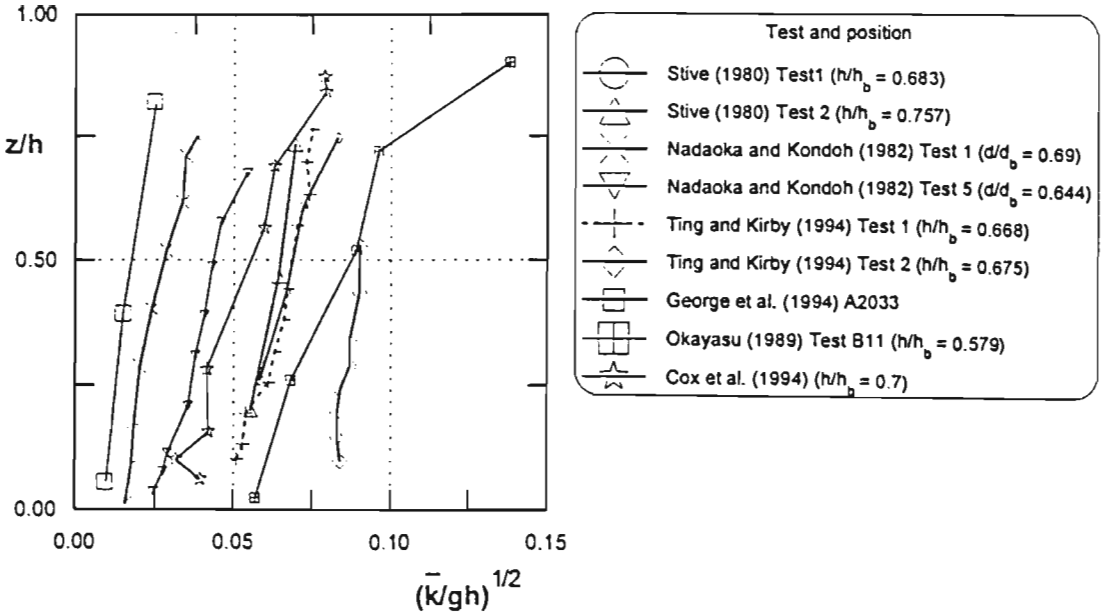

Figure 2.7: Comparison of time averaged turbulent kinetic energy of *Stive(1980), Nadaoka and Kondoh(1982), Ting & Kirby(1994), George et al.(1994)* and *Okayasu(1989)*, taken from a compilation by *Mocke(1998)*.

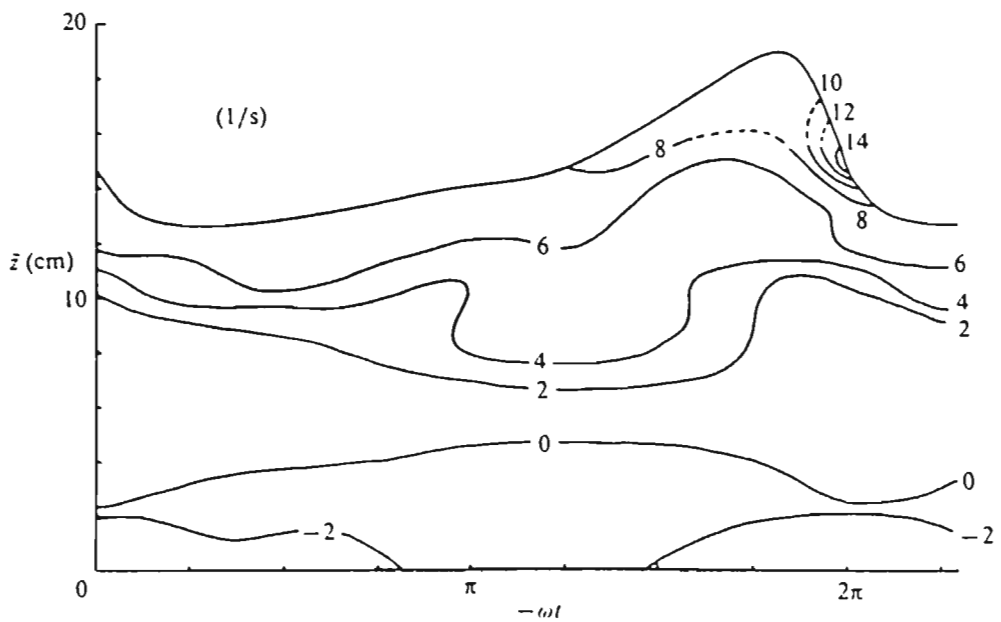

Figure 2.8:Phase ensemble-averaged vorticity $<\zeta>$ (*Nadaoka et al, 1989*)

2.6 Summary

The basic definitions of variables and hydrodynamic concepts have been reviewed. The equations of water waves and their approximate solution of the potential function, particle velocities and the dispersion relation have been presented. The breaking of waves on a sloping beach and the resulting processes have been reviewed. The criterion for wave breaking has been shown by some theories to depend on the wave height, the wavelength and the beach slope. The theory of turbulence has been examined and existing measurements in the surf zone have been reviewed. Most measurements so far have been accomplished using LDA and are available for positions below the approximate trough level. Measurements of the turbulent kinetic energy show a decreasing trend with distance below the trough level.

CHAPTER 3

EXPERIMENTAL FACILITY AND DIAGNOSTICS

A description of the experimental setup including the wave tank, diagnostic equipment and observation procedure used for the measurement of the time series of the water level and velocity flow fields is given.

3.1 Introduction

The variation of the water level and velocity flow fields, in spilling and plunging waves, were investigated in a laboratory surf zone using digital imaging and analysis techniques. A CCD camera was used to image the wave including illuminated suspended seed particles. The images were stored on tape and also directly onto a PC hard disk. Individual video frames were digitised using a frame grabber residing in the PC. The description of the wave tank and the experimental arrangement of the diagnostic equipment for the above purposes are described in this chapter.

Water levels

Measurements of water levels were accomplished by tracking the image of the air water interface in consecutive video frames. Here the wave was viewed from the side, with the camera located approximately at the still water line level and approximately 2 m from the flume. Various arrangements of camera position, lighting and background colour were investigated. Initially, the camera was placed below the still water line level, looking upwards at the under surface of the wave, and a white board was place at the rear of the wave tank. This arrangement resulted in the image of the water, including aeration, to be dark and whilst the region above the wave appeared white, facilitating easy detection of the air-water interface. In later experiments a black background was employed together with overhead lighting. This arrangement resulted in only the meniscus and aeration to be visible, facilitating measurement of the wave roller geometry as well as water levels.

Flow fields

The measurement of the velocity flow fields was accomplished by tracking the displacement of an image of a single seed particle or a group of particles over a known time interval. These particles were illuminated using a light sheet and early analysis involved tracking individual particle images in consecutive video frames. Initially, the light source was placed below the bed in a cut-out section midway across the flume. This arrangement necessitated much laborious repositioning of the light source each time the measurement position was moved. Furthermore, very few or no particles were visible in the crests of the waves, due to them being obscured by the aeration present there. The light source was subsequently moved closer the tank wall but ($\sim$ 10 cm) away from the side boundary layer. This resulted

in only a marginal improvement, since particles did not stay in the light sheet long enough for them to appear in two consecutive frames. Thus, progress using the individual tracking of images in consecutive frames was painfully slow. It was then decided to investigate more automated methods of image analysis together with a higher seeding density and at the same time improve on the sampling frequency associated with standard video format, which is 25 Hz. This resulted in the use of cross correlation techniques to track a group of seeds and improvements in the sampling frequency was accomplished using a progressive scan camera and appropriately strobing the light sheet. To further streamline the measurement process the light source was mounted on a base that could be translated on a pair of rails located above the wave tank. The wave was thus illuminated from above.

3.2 The Experimental Facility

The experiments described in this thesis were conducted in a glass walled 2D wave flume in the Coastal Engineering Laboratory, CSIR, Stellenbosch, South Africa. The flume is 21 m long, 1 m deep and 0.7 m wide. The glass walls provided easy optical and visual access to the processes occurring within the interior of the flume. The flume is also fitted with a well supported artificial beach, made of plywood, on which breaking of waves occurred. Figure 3.1 shows a picture of the flume. The wave generator, which is not visible in the photograph, is located at the extreme right in Figure 3.1. Figure 3.2 shows the wooden beach, having a plane slope 1:20, in the flume. The dark under surface (due to total internal reflection) of a wave is clearly visible in Figure 3.2. This high contrast of the air-water interface was exploited in the measurement of the time series of the water level. Figure 3.3 shows an overhead view of the flume.

Figure 3.1: Overall view of the wave flume.

Figure 3.2: Close-up view of the flume showing the wooden 1:20 plane beach.

The waves were generated by means of two paddles (or wave boards) which consists of a flat rectangular board hinged at the bottom and driven in tandem by servomotors motors connected to a waveform generator. The frequency and amplitude of the waveform generator determined the corresponding parameters of waves in the flume. It has been reported that the generation of waves by means of a wave board tends to lead to the generation of free harmonics (*Hulsbergen, 1978*).

The vertical profile of the horizontal velocity component of the water particles immediately adjacent to the paddle differs from that of the wave in an equivalent depth of water. This difference in velocity can create harmonics that travel with a speed different from that of the main wave and are therefore called free harmonics. Free harmonics are a severe problem, especially, with piston type wave board, since here the horizontal velocity at the wave board is constant over the depth, whereas in deep water the horizontal velocity of the water particle, under the action of waves, is zero at the bottom and maximum at the surface. In order to make accurate measurements of the wave set-down and set-up it is necessary to ensure that these free harmonics are kept to a minimum. The presence or absence of these free harmonics was ascertained from the frequency-wavenumber spectral measurements of waves in the deep water section of the flume. More details on this issue will be given in the chapter on water level measurements.

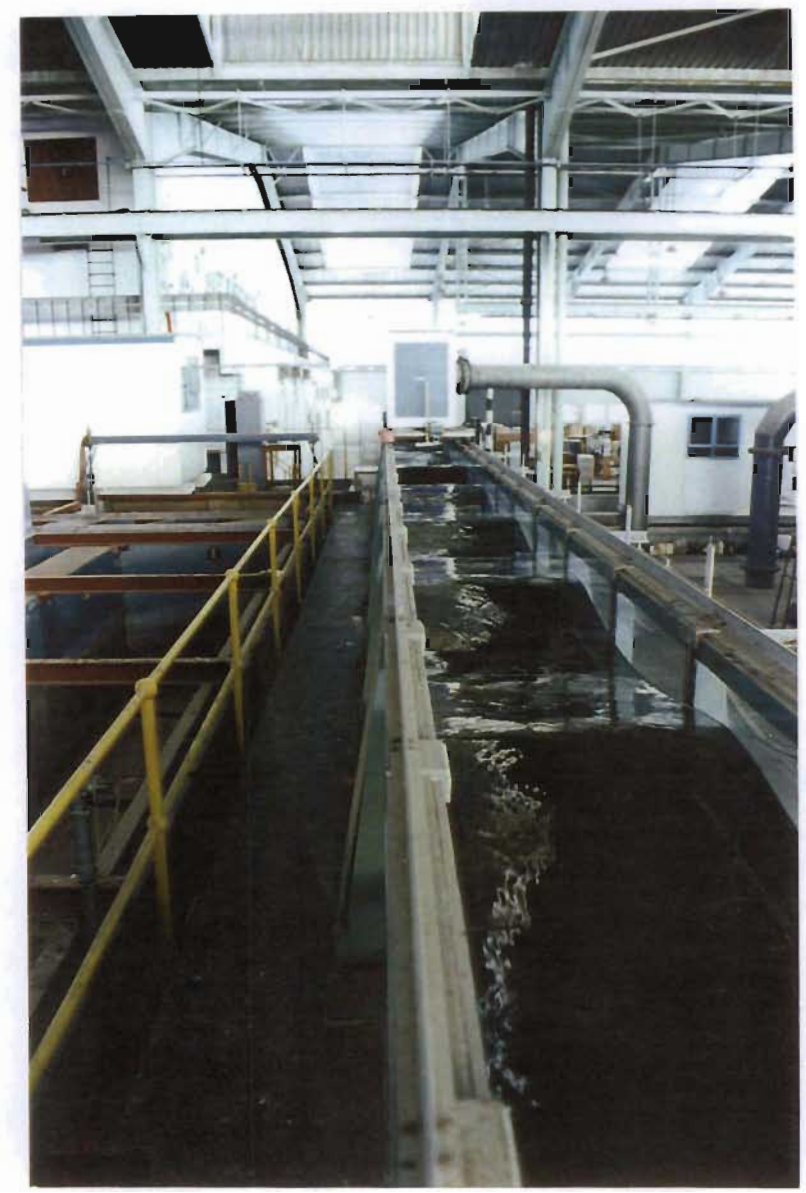

Figure 3.3: Overhead view of the flume.

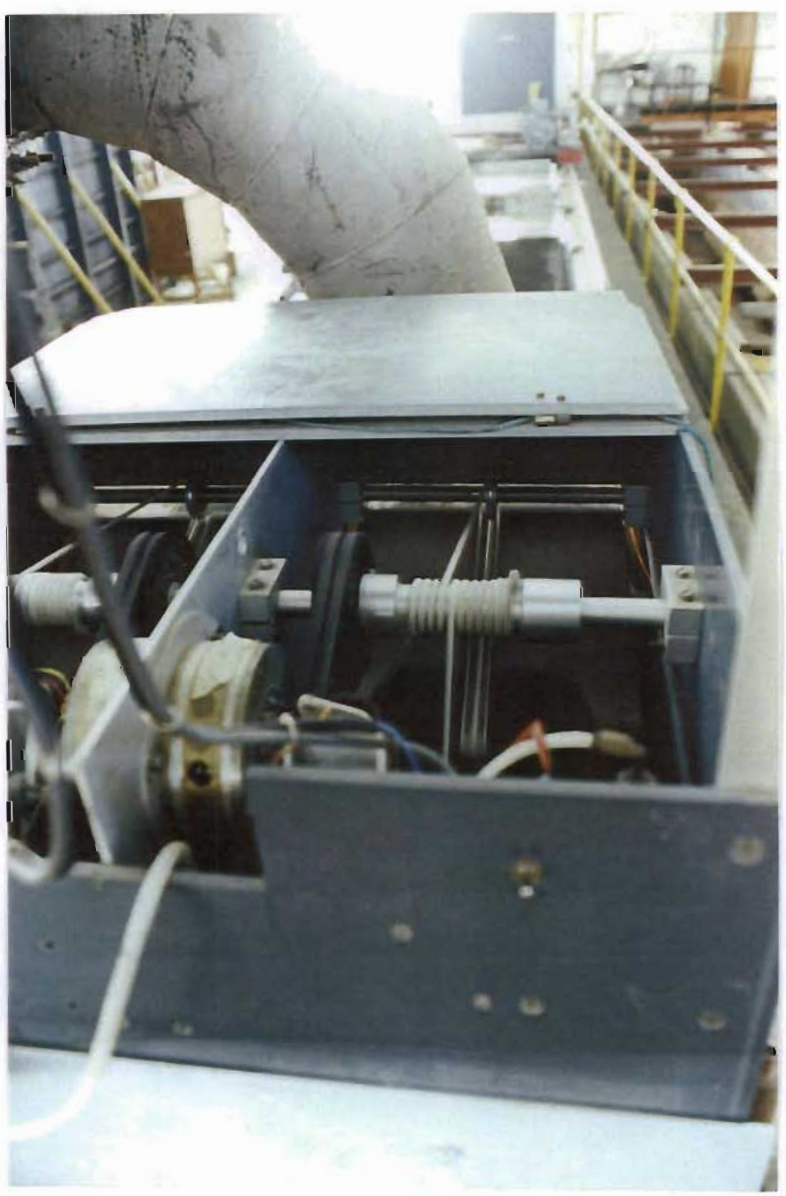

Figure 3.4: Photo of the wave generator mechanics.

Figure 3.5: Front view of wave paddles.

3.2 Flume Dimensions and measurement positions

The dimensions and measurement positions along the flume are given in Figure 3.6. The beach consists of an initial section of slope 1:12 and followed by a section having a slope of 1:20, where wave-breaking occurred. Water level measurements were performed at intervals of approximately 0.1 m over the experimental section, and the velocity flow fields were measured at the four stations indicated below (labelled 1-4).

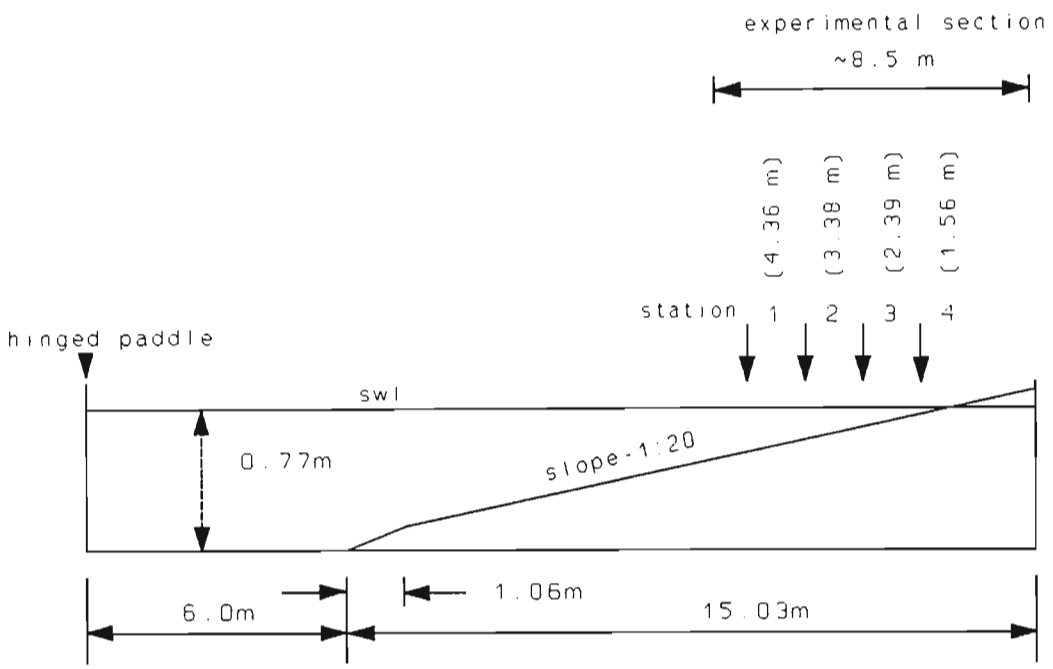

Figure 3.6: Flume dimensions and measurement positions. Water levels were measured every 10 cm over the experimental section, and velocities were measured at stations 1-4, located 4.36, 3.38, 2.39 and 1.56 m from the still water mark on beach.

Table 3.1: Location of the measurement stations, with respect to the still water mark on beach, and their corresponding still water depths, d. (a more comprehensive table will be provided in Chapter 6).

Station	1	2	3	4
Distance (m)	4.36	3.38	2.39	1.56
d (m)	0.218	0.169	0.12	0.078

3.3 Experimental setup and diagnostic equipment

Water level measurements

The time series of the wave surface was obtained by measuring the instantaneous water level from a sequence of video images of the wave recorded at positions along the length of the flume. The measurement of these levels was accomplished using the setup shown in Figure 3.7. The flume was viewed from the side using a monochrome, Videotronic CCD camera and the wave was illuminated from above using a 500 watt lamp. A corresponding photograph of this arrangement is shown in Figure 3.8. A black backdrop was also placed at the rear of the flume. This arrangement enhances the image of the meniscus, formed at the water-glass interface, as well as the aerated region at wave breaking.

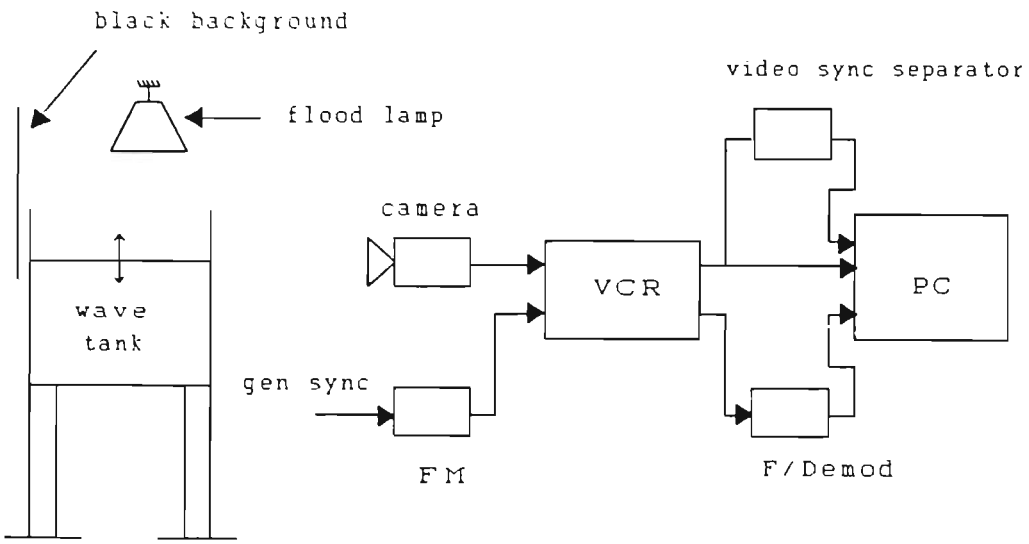

Figure 3.7: Experimental arrangement and setup of the diagnostic equipment for water level measurements.

The images of the wave were recorded onto video tape and analysed on playback using digital methods. The composite video signal from the camera was connected to a Mitsubishi VCR and the output from the VCR was connected to a SE100 Video-Blaster frame grabber residing in a PC. The video frame synchronising pulse, derived from the composite video signal, was connected to the parallel port of the PC and is used to synchronise the capture

of images on PC and the switching of memory banks on the frame grabber. Thus, water levels were measured at a sampling rate equal to the frame update rate.

Another synchronising pulse, from the wave generator, was recorded on the video tape using the audio channel of the VCR. This signal was first encoded onto a (~8 kHz) FM (frequency modulation) carrier signal prior to recording. It is used as a reference when comparing the phase relationship of time series of water level measured at different locations and also in the phase ensemble-averaging of the velocity flow fields. Measurements of the velocity flow field will be discussed in the next section.

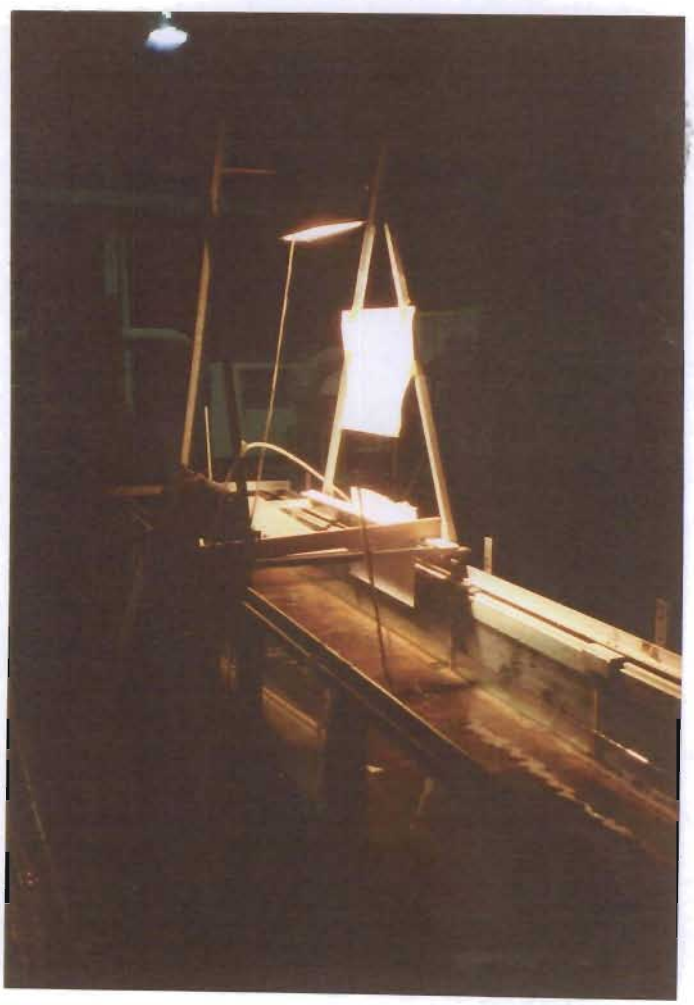

Figure 3.8: Photo of the over-head lighting arrangement used during water level measurements. The overhead light was mounted on a trolley that could be translated on a pair of rails attached to the top of the flume.

The Creative Labs SE100 frame grabber was used for the measurement of water levels and for the initial measurement of the velocities and deserves some description. Figure 3.9 below depicts the memory configuration of the SE100 as viewed from the PC expansion bus. This card is a colour frame grabber. The digitised colour image is stored in memory in the YUV format. The Y represents the image intensity of each pixel, and, the U and V represent the colour difference components. The Y signal has twice the spatial resolution of the colour signals, i.e. one set of UV is associated with two Y values. The method of computing the YUV parameters is as follows:

$Y=0.3R+0.59G+0.11B$

$U=(B-Y)0.56$

$V=(R-Y)0.7$

where R, G, B are the red, green and blue intensity levels of each pixel.

For the application at hand only the Y values are used.

The SE100 was mapped into the high memory space of the PC in order to have fast access of the entire video memory. The SE100 appears as ordinary memory to the PC and accesses it as such. The intensity values are read on the fly, that is, while the SE100 is updating the video memory. Software to access high memory was developed using a GNU, 32 bit C compiler.

The SE100 is a consumer grade frame grabber and is thus relatively inexpensive, however, it does have one major limitation. The video images from most cameras are based on the standard TV image format (details of this will be given in the next chapter), that is, each video frame consists of two interlaced fields, an even and an odd field. The fields are continuously updated at twice the frame rate. The SE100 digitises only one of these fields. The implication of this is that there is a reduction in the vertical spatial resolution of the digitised image and it is not possible, using this particular frame grabber, to capitalise on the higher field update rate.

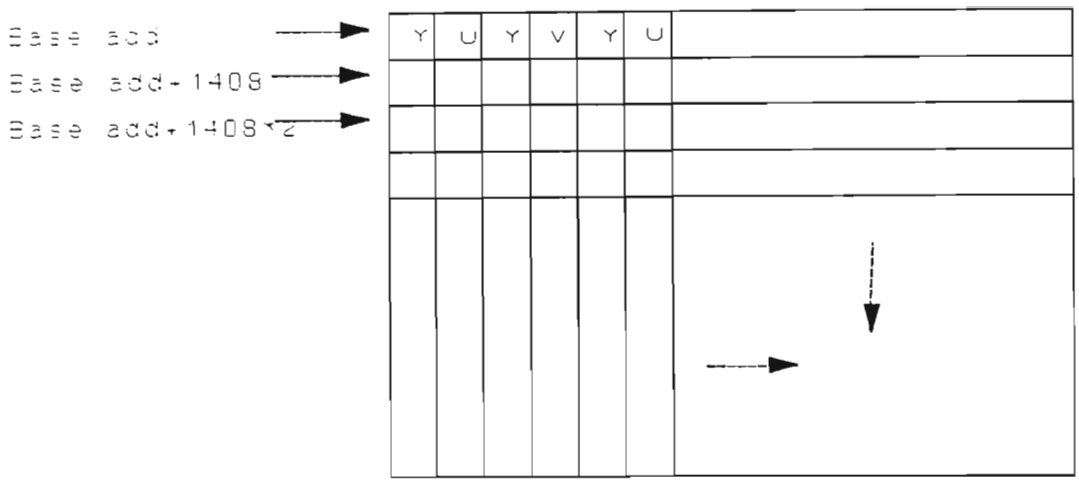

Figure 3.9: Memory map of the Creative Labs SE100 frame grabber within the PC (Base address in hexadecimal was E0D00000h).

Velocity flow field measurements

Early measurements of the velocity flow fields of the waves were accomplished using the setup of the diagnostics shown in Figure 3.7. A longitudinal section of the flume was illuminated with a laser sheet and seeded with neutrally buoyant particles. A 5 mW semiconductor laser diode was used to generate the laser light and a cylindrical lens was used to form a sheet. The laser diode and cylindrical lens was encased in a watertight enclosure and installed within a cutout section of the bed. Figure 3.10 shows the watertight enclosure used to contain the laser diode and cylindrical lens. The velocity of the neutrally buoyant particles were then estimated by tracking the images of individual seeds in consecutive video frames.

To enable the capture of two consecutive video frames, the SE100 was modified with the addition of more memory and switching logic. Figure 3.11 shows a picture of the modification with additional memory being piggy-backed onto existing memory and logic control on a separated board. The switching of memory banks was controlled by the PC via the parallel port. This modification allows the capture of two images displaced 40 ms apart.

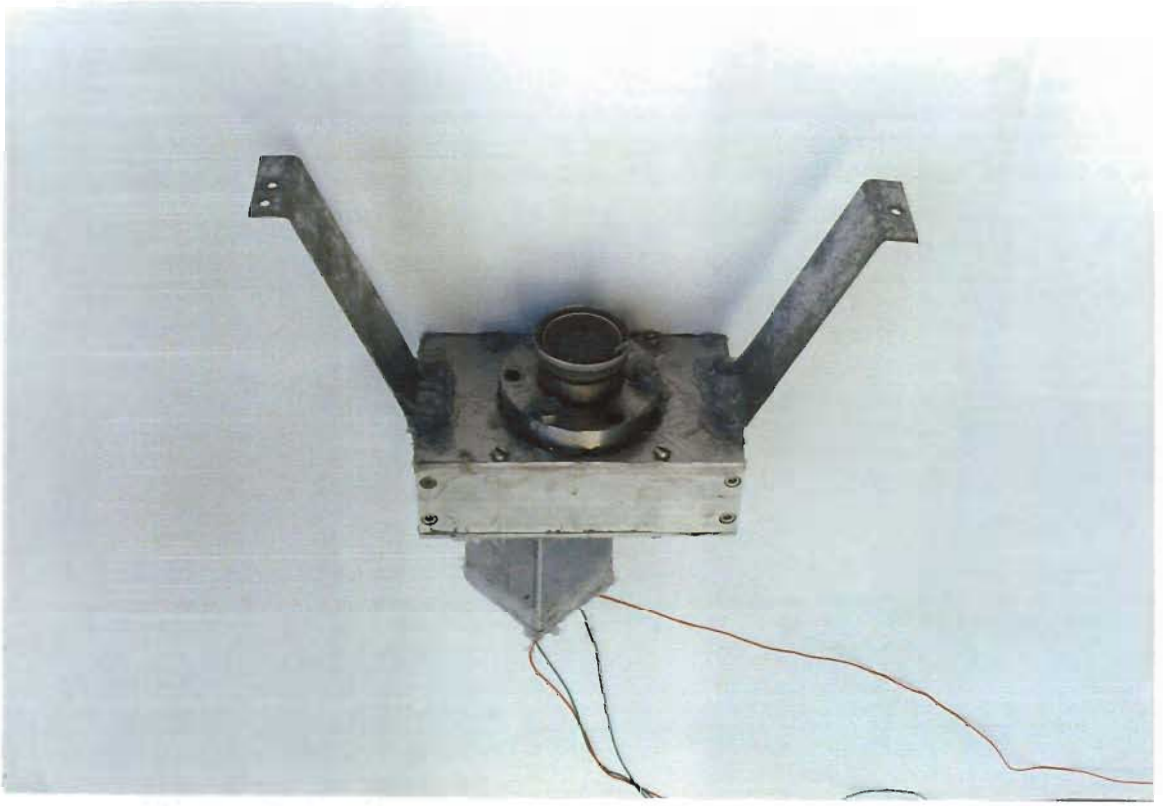

Figure 3.10: Watertight enclosure containing laser diode and cylindrical lens assembly.

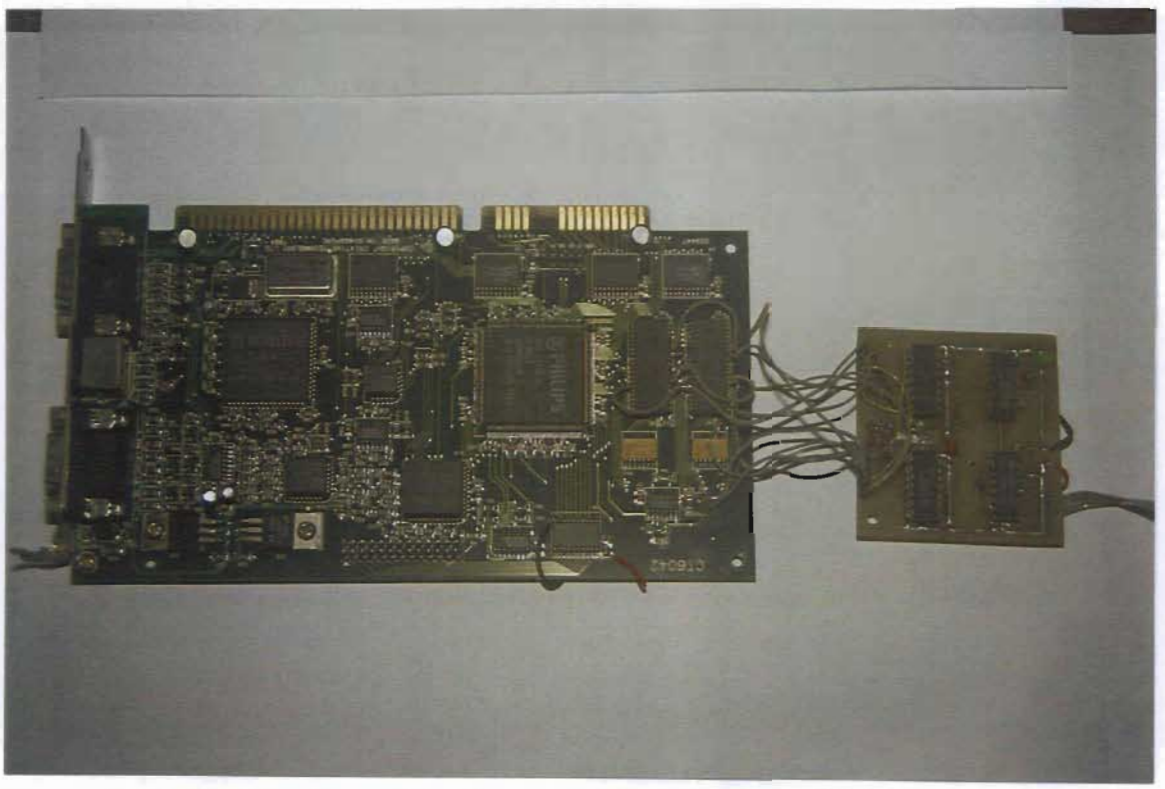

Figure 3.11: Modification of the frame grabber showing additional memory and logic switching control.

It was possible, using the experimental setup and diagnostic equipment as described above, to video an area of approximately 24 cm x 24 cm. This resulted in an effective pixel resolution of 12 pixels/cm and a minimum sampling time of 40 ms, corresponding to a maximum sampling frequency of 25 Hz. In order to obtain shorter sampling times it is necessary to employ strobing techniques.

The highly refined velocity measurements presented in the latter part of this thesis were obtained using a method of strobing and employing a non-interlaced digital camera and a digital frame-grabber. This experimental arrangement is shown in Figure 3.12. A longitudinal section of the flume was illuminated with a rectangular beam of light, called a light sheet(see Figure 3.12). Images of the neutrally buoyant particle and the structure, formed by the bubbles in the aerated region of the wave, were recorded directly onto the hard disk in the PC using a progressive scan Pulnix CCD camera, TM9701, connected to a Imaging Technologies digital frame grabber residing in a 155 MHz pentium PC. The velocity flow field was then estimated using 2D cross-correlation techniques.

The light sheet in Figure 3.12 was produced using a system of triggered stroboscopes and formed into a sheet using a pair of collimating slits. Two banks of stroboscope were used and light flashes a few microsecond apart were obtained by triggering the first bank followed by the second bank. In order to obtain the necessary illumination intensity each bank consists of two stroboscopes that were triggered in parallel. Figure 3.13 shows a picture of the light box containing the stroboscopes.

The progressive scan camera provided full frame images without interlaced fields, thus, giving a higher spatial resolution. The Pulnix camera has a built-in analogue to digital and a digital to analogue converters, thus providing both analogue and digital outputs. The camera also has an external reset facility. Figure 3.14 shows a high level timing diagram of the camera. During each frame time the CCD face plate is exposed and at the same time the image from the previous frame time is digitised and made available. The Pulnix camera is equipped with an internal frame-buffer, and it is this buffer that allows the double acquisition as the first image is quickly transferred into the buffer before readout, freeing the CCD for the next image. Upon receiving an external reset signal the camera immediately discharges

the CCD face-plate and begins the exposure of a new frame. This feature is used to capture images of the wave at a precise point within the wave period, a feature that is necessary for performing phase ensemble-averaging of the velocity flow fields. That is, the instantaneous flow field of a small section of the wave, at a particular wave phase, is computed using images captured at the wave phase in question for a number of wave cycles.

It is feasible, using the setup shown in Figure 3.12, to obtain pairs of video images that are displaced in time by only a few microseconds, while still working with the standard video format. This is achieved as follows: The video frame rate for the Pulnix camera is 30 Hz, thus a video frame is available every 16 ms . The camera shutter is kept open for the entire frame time and the light sheet is strobed at the end of one frame time and then again at the beginning of the next frame time. Although the CCD face-plate is exposed for the entire frame time, the scene is only illuminated during the time that the light sheet is flashed, thus a pair of video images separated by a few microseconds apart are available. Any other sampling time, from a few microseconds to multiple frame times, is also possible. Thus it is possible to obtain a much higher temporal resolution, typically 1-500 kHz, than possible with the standard video format.

High sampling rates are desirable, especially in the crest of the wave were high turbulent velocity are present. It will be shown in the next chapter, that it is possible to obtain velocity estimates well into the aerated region of the wave using the high sampling rate together with the cross-correlation method of analysis.

The synchronisation of the camera, stroboscopes and the acquisition of images were under software control. The software for this purpose was written and compiled using MICROSOFT C for WINDOWS 95 and the analysis of the images were performed using software developed for IDL[1], an image processing package.

1 Interactive Data Language (http:\\rsinc.com)

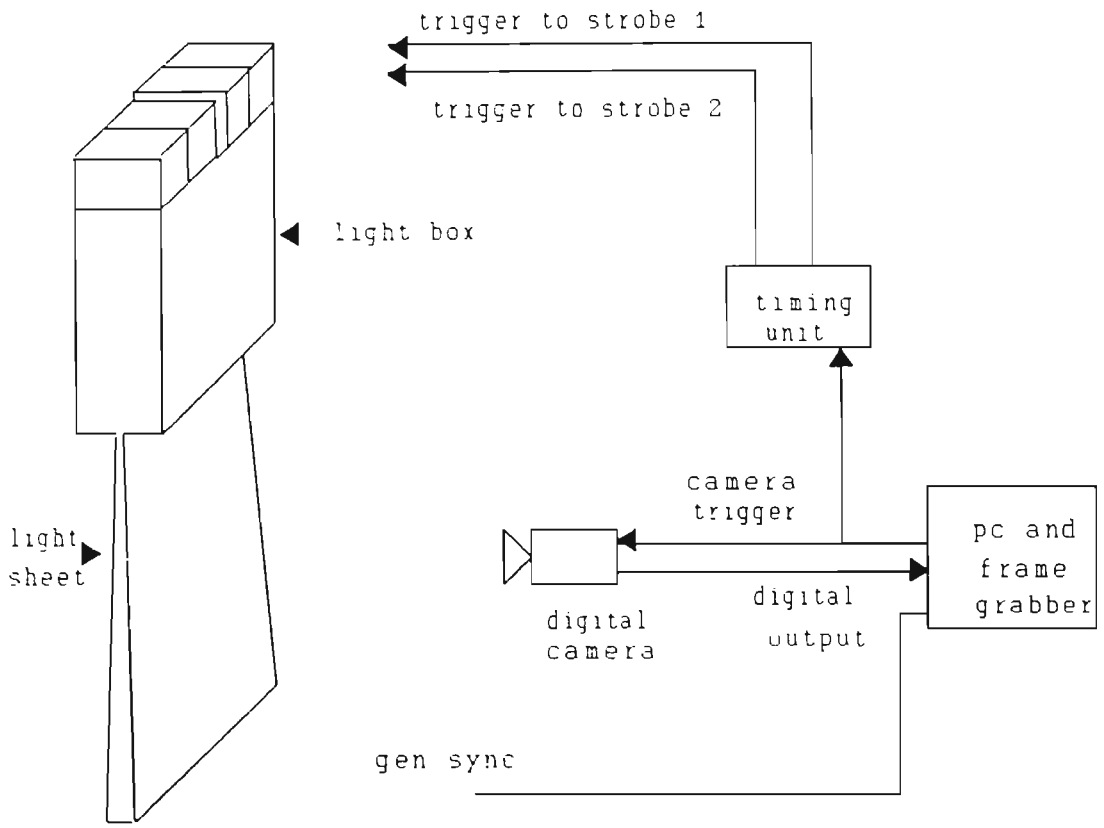

Figure 3.12: Experimental setup for the measurement of velocity flow fields of waves in the surf zone using digital correlation image velocimetry.

Figure 3.13: Light box containing stroboscopes, configured as two banks and each bank containing two stroboscopes.

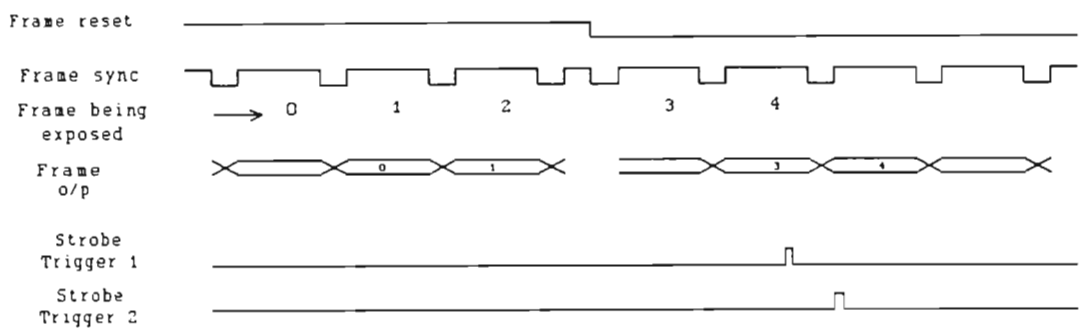

Figure 3.14: Timing diagram of the Pulnix camera as used in the DCIV setup. All frames are down loaded at the frame rate, but images in frame 3 and 4 are displaced in time by a fraction of the frame period, as a result of the strobing.

3.4 Summary

The experimental facility, experimental setup and diagnostics equipment were described. Details of the flume dimensions and measurement position along the flume were given. Digital video imaging and recording techniques were used to measure the surface wave and the velocity vector field within the wave. The time series of the wave is obtained by measuring the instantaneous water level. The velocity flow fields in the waves were measured by tracking the displacement of neutrally buoyant particles and the aeration structure over a know time interval. Water elevations were measured over the last 8 m of the flume and velocity measurement were conducted at four positions, located 4.36, 3.38, 2.39 and 1.56 m from the still water mark on the beach, in the surf zone. Important issues related to the experimental facility and diagnostics have been highlighted and will be discussed further in the chapters to follows. It is now appropriate to examine the method of extracting the necessary information from the video image. This is the subject of the next chapter.

CHAPTER 4

TECHNIQUES FOR FLUID VELOCITY AND WATER LEVEL MEASUREMENTS USING VIDEO IMAGERY

The application of digital particle image velocimetry (DPIV) and digital correlation image velocimetry (DCIV) to the measurement of the velocity flow field of breaking water waves in a two dimensional wave flume is described. The basic optical aspects are reviewed with regards to particle position estimation and significant features of the system components are described. The estimation of particle velocities is accomplished by exploiting the construction of a TV image and by the use of strobing techniques. Improvements in spatial resolution are achieved by using sub-pixel position estimation. The measurement of the time series of the water elevation is also discussed. A keogram is generated from a recording of the wave, from which the time series is extracted by tracking the evolution of the air-water interface. Measurement of the roller area of a plunging wave, an important parameter for mass and momentum flux determinations, is also extracted using the keogram concept.

4.1 Introduction

In this chapter we describe the measurement of the time series of the surface wave and the velocity flow field of waves in a laboratory surf zone using digital image and analysis techniques developed by author and co-workers (*Govender et al, 1998*).

The application of imaging techniques to experiments in fluids has increased in popularity in recent years due to the advancement in digital technology. The figure below illustrates the major components of an imaging system, consisting of the object plane, the camera lens and the image plane. The object plane will contain the physical object and the image plane will contain the focused image of the object. The position of the object and image planes are governed by the simple relation $1/d_0+1/d_1=1/f$, where f is the focal length of the camera lens, and d_0 and d_1 are the position of the object and image planes, respectively, with respect to the lens.

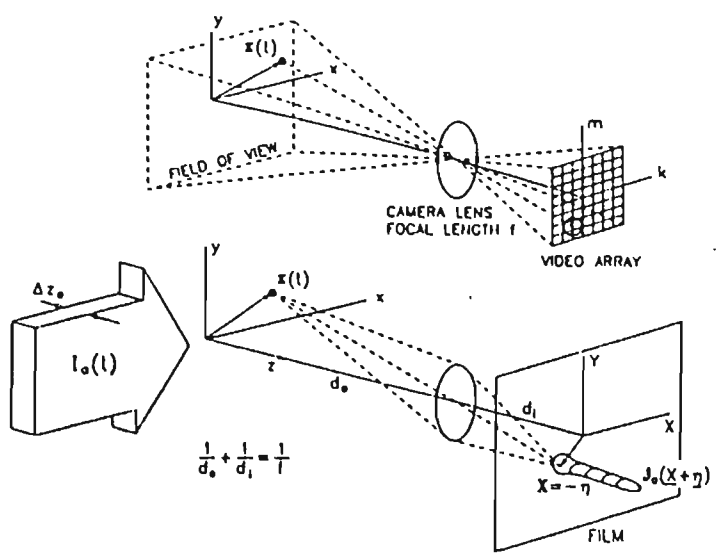

Figure 4.1: Geometry of the imaging system. (Top) Video recording, (bottom) photographic recording (*Adrian, 1991*).

Early application of imaging systems in fluid mechanics utilised photographic film to record the image formed at the image plane. A transformation exists that transforms positions in the object plane, xy plane, to the image plane, XY plane.

Modern systems, however, employ a sensor array consisting of charge coupled devices (CCD) arranged in a rectangular array. In this case a sampled version of the image is obtained. Each sample is then referred to as a pixel. Position in the image plane will then be in terms of pixels. The intensity of each pixel is then digitised and is represented as a binary value. The entire image is then represented as matrix of numbers.

Measurements of object motion then involves tracking the object in the image plane and, by suitable transformations, determine the motion of the object in the object plane. The DPIV technique involves capturing the instantaneous image of a large number of submerged neutrally buoyant seeds at two or more time instances. The velocity is then computed using the displacements that these particles have incurred over the known time intervals. This clearly requires the existence of particles to be imaged in the field of view, and a method of recording and processing these images. There are essentially two types of possible image analysis techniques; In situations where the density of seed particles are low, individual tracking of particle images is required, whilst in cases of high seed densities, 2D cross correlation techniques are employed to track the image of a group of particles. Both these techniques are described here.

In the past, most PIV systems have used photographic film for image recording and optical methods for processing. This provides a high spatial resolution measurement of particle positions. Current CCD camera technology on the other hand, does not provide a high spatial resolution. Typically, a consumer grade CCD face plate has a resolution of $\approx$ 760 x 680 pixels. However, a significant improvement in spatial resolution can be achieved by the appropriate choice of seed particle size, exposure times, and the use of sub-pixel position estimation techniques. This digital version of PIV has certain advantages over the film based method, such as reduced cost and real time processing of the data. The spatial resolution is also bound to improve with advancements in image sensor technology.

Section 4.2 provides details of velocity measurements in the surf zone using DPIV. Here the discussion is centred around the choice of various system components and the method of analysing the images using individual particle tracking and 2D cross correlation techniques. It is also shown that it is possible, using high sampling rates and the cross correlation method of analysis, to use the bubbles created during breaking to form the necessary structure for tracking purposes. This is certainly a breakthrough, since there is to date a scarcity of velocity measurements in the highly aerated region of a breaking wave. Results of phase averaged and instantaneous velocity flow fields for a spilling and plunging wave, respectively, are provided.

We also report here on a method for measuring the time series of water elevation suitable for studying wave propagation in a 2D wave flume. This method involves imaging the wave from the side and exploiting the gradient in the grey level intensity of the image across the air-water interface. The time series at a particular position is obtained by first generating a keogram from a video recording of the wave. This technique is also used to estimate the size of the roller formed in the bore of the wave during breaking. The concept of keograms and the method of extracting the time series of the wave are explained in Section 4.3.

4.2 Velocity measurement using particle image velocimetry (PIV)

As mentioned in the Introduction, PIV involves the tracking of suspended seed particles. This implies observing the position of the particles at two or more time instances. The velocity, v, of the i^{th} particle at position $x=(x,y)$ is then

$$v(x,\theta)=\frac{x(t+\Delta t)-x(t)}{\Delta t} \tag{4.1}$$

The phase, θ, is required in order to bin the velocity estimate with respect to the wave phase. For the technique to be effective, there are a number of inter-related issues that need to be addressed. The choice of one component can seriously effect the performance of other components in the system. Figure 4.2 shows a schematic view of the experimental setup.

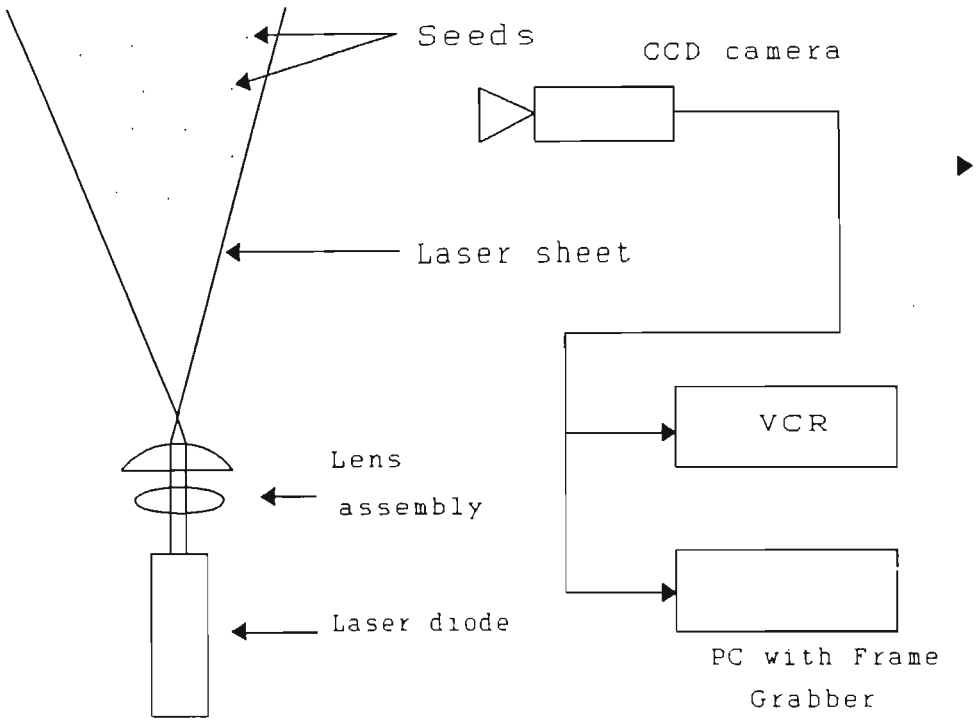

Figure 4.2:: Experimental arrangement for the measurement of fluid velocities using particle image velocimetry.

The light sheet is used to illuminate those particles that are within the focal plane of the camera. The composite video output of the CCD camera is connected to a Video Cassette Recorder (VCR) and also to a PC containing a digital frame grabber card. In most PIV applications a laser is used as a source for the light sheet, however, in applications where the coherent properties of a laser is not essential, it is possible to use ordinary white light. The following issues are of importance when setting up a PIV system:

1. Optical considerations,
2. Choice of seed particles,
3. Laser source characteristics,
4. Video processing equipment, and
5. The analysis of the images.

We will examine each of the above items with application to surf zone measurements.

A. Optical Considerations

The geometry of the optical system and the focusing lens determines the position of the object and image planes. The object plane will in this case coincide with the plane of the laser sheet. The video sensor array is located in the image plane. The distance from the lens to the image plane is typically 4 to 16 mm. The object distance will be in the range of a few centimetres to a few metres. The sensor array consists of a matrix of charge coupled devices (CCD). Most commercial devices have approximately 760 x 680 pixel elements on the die having overall dimensions of 7 mm x 5 mm. This results in a pixel spacing of 12 μm. The rate at which images are captured gives an upper bound to the system's temporal resolution. This will be discussed at length in a later section.

The image of a point source in the object plane is an Airy distribution consisting of a bright central region, the Airy disk, with a number of concentric dark and bright rings. The Airy disk, which is referred to as the point spread function (PSF), has a diameter given by (*Adrian and Yao, 1985*):

$$d_s = 2.44(M+1)f^{\#}\lambda \tag{4.2}$$

where $f^{\#}$ is the f number of the camera lens, λ is the wavelength of the light and M the magnification of the camera. Most CCD cameras with a sensor array such as that described above typically have a magnification that is less than or equal to one.

In order to understand the impact of sampling the image via the CCD array it is necessary to evaluate the optical processes occurring at the sensor. Consider the image intensity of the point source at the image plane of the lens to be $I(x,t)$ in W/m^2. The point spread function can be approximated by a gaussian function:

$$I(x,y) = C\exp(-2\frac{(x-a)^2+(y-b)^2}{\sigma}) \tag{4.3}$$

where the width and height are characterised by the parameters, σ, and, C, respectively, and (a,b) represents the offset from the origin. The exposure then is given by:

$$\varepsilon(x) = \int_0^T I(x,t)dx \tag{4.4}$$

where T is the exposure time.

Now if the point source is moving to the right with velocity $v=(v_x, v_y)$ we write for the image intensity:

$$\begin{aligned} I(x,t) &= I(x-v_x t, y-v_y t) \\ &= C \exp\left(\frac{-2(x-a-v_x t)^2+(y-b-v_y t)^2}{\sigma}\right) \end{aligned} \tag{4.5}$$

and the exposure thus being:

$$\begin{aligned} \varepsilon(x,y) &= \int_0^T I(x-v_x t, y-v_y t)dt \\ &= \int_0^T C \exp\left(\frac{-2(x-a-v_x t)^2+(y-b-v_y t)^2}{\sigma}\right)dt \end{aligned} \tag{4.6}$$

Thus, there is a smearing out of the instantaneous PSF during the integration time.

The image of a moving particle can also be viewed as a convolution between the point spread function and an aperture function. This can be easily seen by considering only the x-dependence of the integral in Equation 4.6, using the substitution $s=v_x t$, to give:

$$\varepsilon(x) = \int_{-\infty}^{\infty} w(x)I(x-s)ds \tag{4.7}$$

where

$$w(x)=\begin{cases} 1/v_x \;\; for \;\; x_i \le x \le x_i + v_x T \\ 0 \qquad otherwise \end{cases} \qquad (4.8)$$

and v_x =particle velocity, T =exposure time, x_i = initial particle position and $I(x)$ is the one-dimensional point spread function. Equations 4.7 and 4.8 shows that the intensity due to a moving particle is inversely proportional to its velocity. The exposure of an hypothetical particle, having a PSF given by Equation 4.3 with σ= 10.0 and C=1.0 and moving to the right with a velocity v=1.0 pixels/s, is computed using Equation 4.7 for three different exposure times. The result is shown in Figure 4.4.

From Figure 4.4 it can be seen that the image will retain most of its gaussian characteristics for exposures less than some critical value. The image will have a flat top for exposures above this critical exposure. For very much shorter exposures, the height of the gaussian is attenuated. This behaviour is exploited in sub-pixel resolution estimation discussed later.

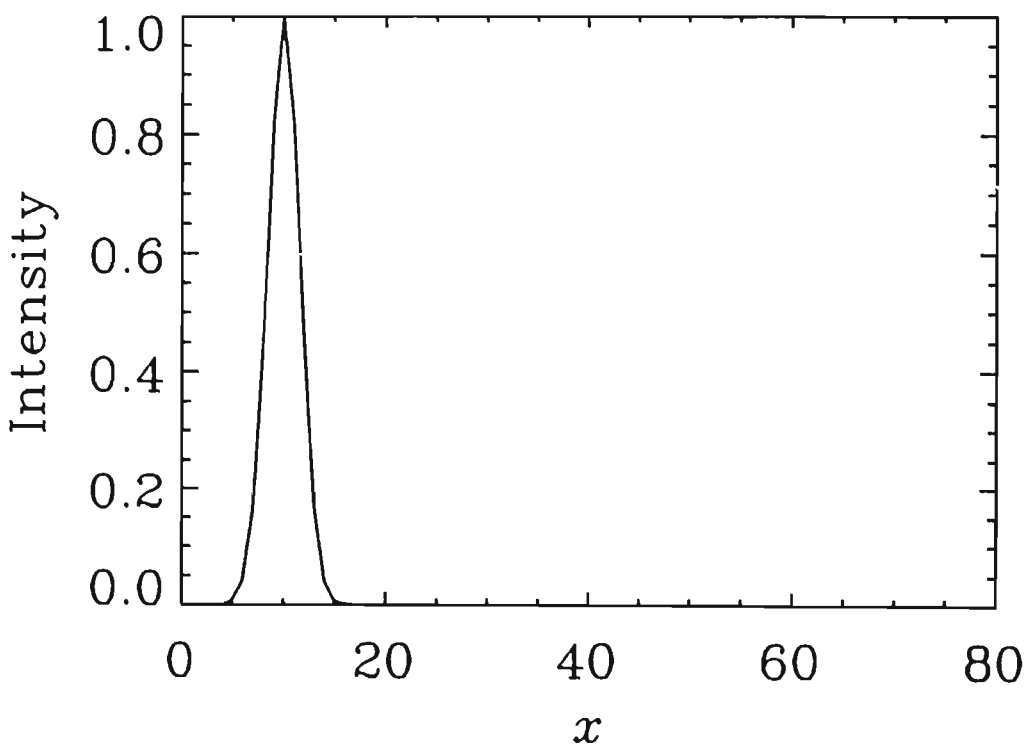

Figure 4.3: Point spread function of an hypothetical particle.

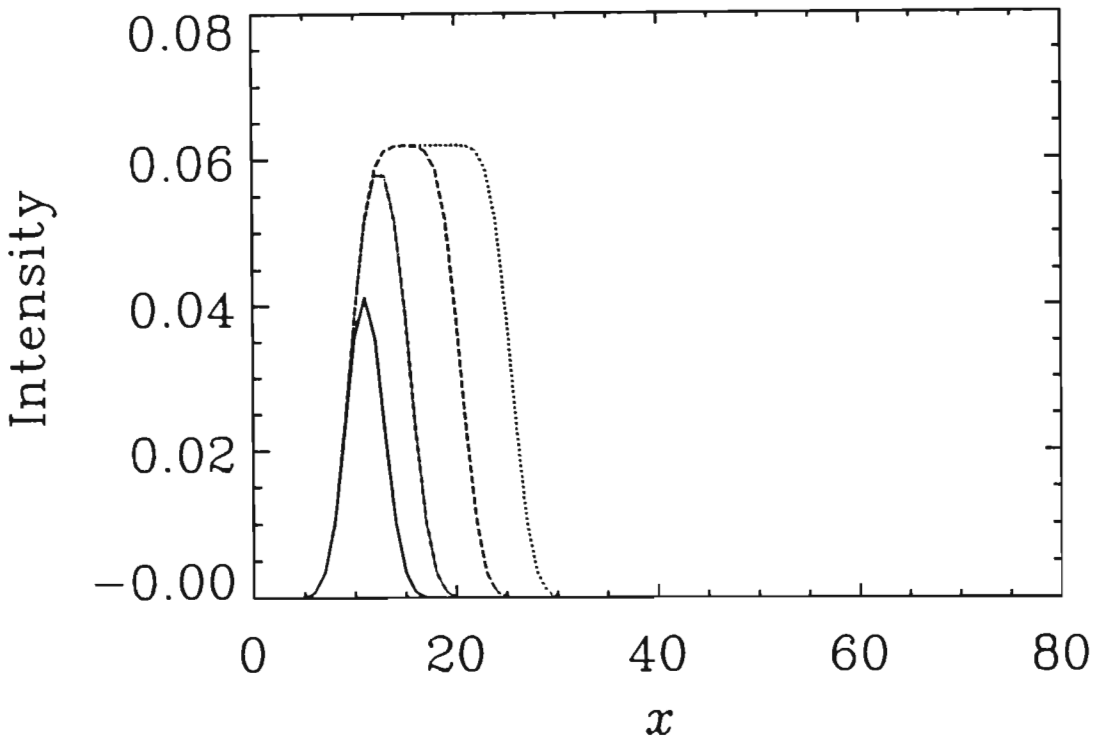

Figure 4.4: Exposure for a particle, with PSF given in figure 4.3, moving to the right. The solid, dash-dotted, dashed and dotted lines represent exposures $T_1 < T_2 < T_3 < T_4$.

B. Seed Particles

Most PIV systems to date have been used in gas dynamics and other flow regimes where the velocity field is to a large extent deterministic and predominately two dimensional. In these instances a few snapshots are essentially all that is required. In gas dynamics, one is dealing with very high velocities and the seed particles should possess dynamic properties similar to the gas under test. This puts a limit on the maximum seed particle size, typically a few microns in diameter. This small particle size then requires the use of a high power laser source, typically a few watts.

The surf zone, however, has a completely different character. Firstly, the processes occurring are highly turbulent. Statistical techniques are therefore required, implying long observation times in order to extract average and rms quantities. Furthermore, because there is a net onshore mass and momentum towards the beach due to breaking in the region above the wave trough there results a net reverse offshore flow (undertow) below the approximate

trough level. This implies that a given volume of water never stays in a fixed region for long. This in turn implies that seed particles added to the water in a particular region will eventually move out, some ending up on the beach and some accumulating at the breakpoint. Therefore a constant supply of particles is required in order to maintain a constant seed density at the point of observation. Thirdly, air bubbles are a characteristic feature of wave breaking in the surf zone. These appear as white patches or streaks in the image which obscure the seed trajectories. It will be shown later that it is possible, using correlation techniques, to determine the velocity flow field by tracking the structure created by the presence of bubbles.

It was discovered, after experimenting with a number of macroscopic particles, that un-expanded polystyrene beads, which were heated in water at a temperature of around 86° C for approximately 30 seconds, were most suitable. These partially expanded beads, approximately 0.8 mm in diameter, function well as seed particles since they are almost neutrally buoyant and their white matt surface makes them good point source scatterers.

C. Laser characteristics

The laser optical power output and frequency are dictated by the seed size, and the spectral response of the camera. Blue/green lasers are most suitable for transmission in water, since these incur the least attenuation. Since these are usually gas lasers, they are not so easily available in compact form. On the other hand red lasers are more compact, and available in a variety of lasing materials, i.e., HeNe, ruby and semiconductor diode lasers.

A 633 nm laser is closely matched to the human eye's response, but these tend to be more expensive. Monochrome video cameras typically have a broader spectral response, thus making it feasible to use a less expensive, longer wavelength, laser. In this particular case a 5 mW, 670 nm semiconductor laser diode was used in conjunction with a monochrome CCD camera having a sensitivity of 0.005 lux. The compactness of the diode laser allows for it to be installed in the bed of the flume, encased in a water tight container.

The generation of a laser sheet of light is easily accomplished using a system of cylindrical lenses. A single cylindrical lens will generate a V shaped laser sheet having a fan angles of

5 -30°.

D. Video Processing Equipment

Some of the essential features of the camera have already been highlighted. A large CCD sensor array is required for good spatial resolution. A camera with a high sensitivity and spectral response that is matched to the image is also desirable.

The images from the camera can be recorded on video tape or stored on hard disk in digital form. In the latter case, the camera output is connected direct to a frame grabber residing in a PC for digitising and storage. The video tape is a high density storage medium and allows for the cost effective archiving of large volumes of raw experimental video data. The video tape, however, does suffer from wear and tear and is subject to stretching, resulting in the distortion of images. There are certain essential features which must be considered when selecting a frame grabber for a PIV application. The frame grabber should operate without significant sampling jitter and should digitise both the even and odd fields of each video frame.

The digitised images can then be analysed using any one of the image processing packages available commercially such as IDL[1]. Typically, each frame is saved in BMP format as a separate file. These files are then read in and converted into binary data arrays by IDL for analysis.

E. Analysis Procedure for low seed density applications

The preferred method of estimating the seed velocity from the captured images is dependent on the density of seed particles. For very high seed densities, where the image of the seeds in two consecutive frames overlap, correlation analysis is usually used and this method will be discussed later. For very low seed densities tracking of individual seed is required. In this section discussion will pertain to the low seed density regime and two methods for tracking particle positions in this regime are described. As will be discussed below there are three possible sampling rates that can be achieved, viz., 20 ms using even/odd field analysis, > 20 ms where the images are separated by multiples of the frame period, and < 20 ms where a laser strobes the seeds during a single frame period.

1 Interactive Data Language.

Frame analysis

The frame analysis method exploits the underlying structure of the PAL TV format. A single TV image consists of a frame that is made up of an even and odd field. These fields are interlaced on the screen to provide a picture of reasonable definition whilst at the same time minimising the transmission bandwidth requirements. The picture is continuously updated with the even and odd fields being alternatively displayed at a rate of 50 Hz. Thus the time interval between consecutive even and odd fields is 20 ms.

Thus, from a single frame, it is possible to extract either the even or odd fields of the particle by selecting the even and odd lines respectively. By correctly matching particles with nearest neighbours, the displacement of each particle can be determined. If particle velocities are small then it is necessary to make observations over a longer time interval. In this case we could observe particle position in two fields separated by an integral number of field time periods.

The duration of the integration time of the light on CCD face plate during each field will determine the shape of the images of the particles. Clearly, short time exposures will freeze the seed images which will then appear as dots, while long exposures result in streaks. This additional streak length information is useful in finding matching pairs of particles, since the particles in each pair should have a streak of similar length and angle of inclination.

Figures 4.5 (a) and (b) show examples of streaked seed images appearing in two consecutive even fields. It can be seen that not every particle in the first image can unambiguously form a pair with its partner in the second image. This can be more clearly seen by subtracting the second image from the first, as is shown in Figure 4.5(c). In this subtracted image, the images of seeds from the first image, labelled A_1, B_1, C_1, D_1 and E_1, appear white, while those from the later image, labelled A_2, B_2, C_2, D_2 and E_2, appear black. The reasons why there is no matching seed for some of the images may be explained in the following way.

Although the flow field in the surf zone is predominantly two-dimensional there is a measure of three dimensionality, particularly in turbulent regions. The velocity component perpendicular to the laser sheet is, however, a lot smaller than those in the plane of the sheet.

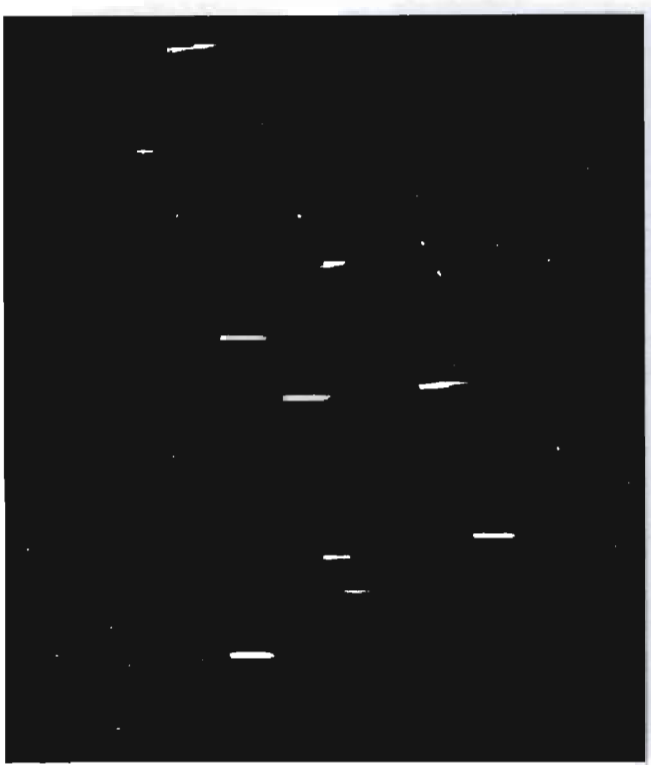

(a)

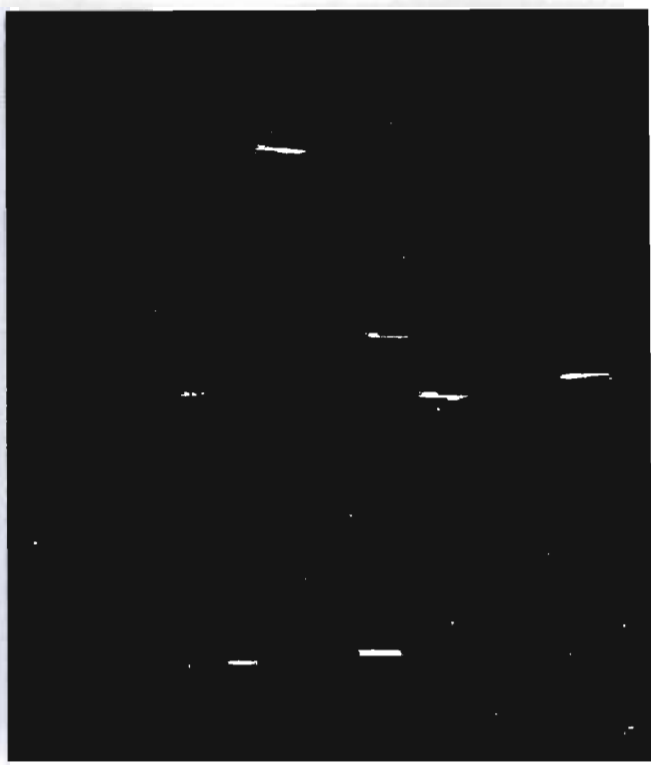

(b)

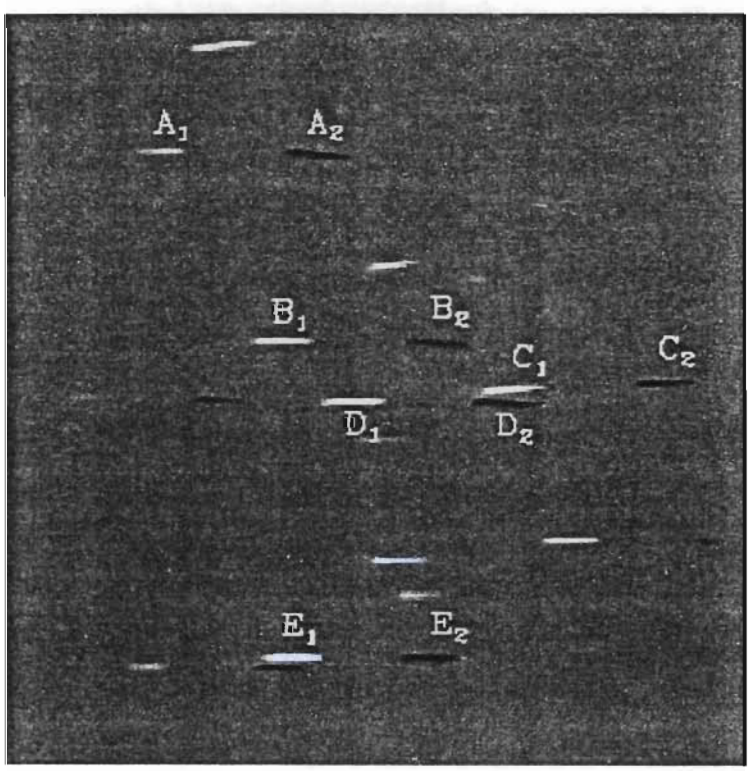

(c)

Figure 4.5: (a) First image of particle streaks, (b) second image of particle streaks and (c) image resulting from subtracting the second image from the first, matching pairs are labelled A-E with subscripts denoting the original image in which they occur.

Figure 4.6 depicts the geometry of the laser sheet and the motion of a seed. In order to find a matching pair, a particle needs to remain in the sheet for one field/frame period, τ. This then restricts the measurement to those particles with $v_y < (d-y_i)/\tau$, where v_y is the component of velocity perpendicular to the sheet and y_i is initial position of the particle. Those particles with $v_y \geq (d-y_i)/\tau$ will not stay in the sheet long enough for them to appear in two consecutive fields/frames. Thus the reason why some seeds are in the first image and not in the second, or visa versa, is because they enter or leave the sheet within the field/frame period. Also, particles with very high velocities, travel greater distances, thus making it more probable that they leave the sheet which in turn makes it difficult to find matching pairs. The absence of complete seed pairs in Figure 4.5(c) does illustrate one of the limitations of velocity estimation using field tracking. The design of the light sheet and analysis of the images should therefore be done in the light of the above discussion.

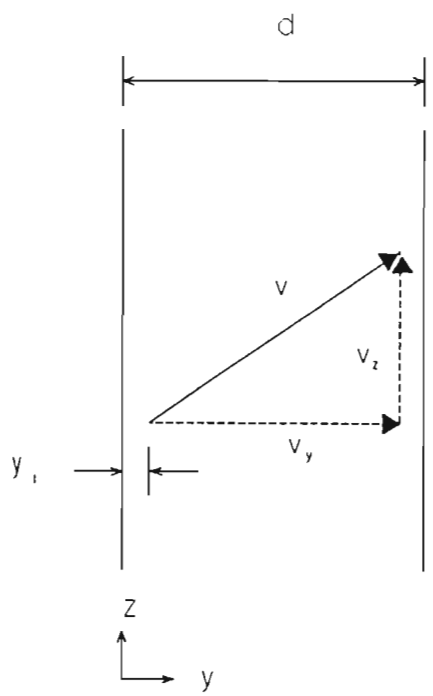

Figure 4.6: Geometry of the laser sheet and particle motion. d is the width of the sheet, y_i is the initial position of particle, and v_y and v_z are the components of velocity in the y and z directions, respectively.

Laser strobing

When the component of velocity perpendicular to the laser sheet becomes large, such as in the turbulent region during the breaking of a wave, then the frame analysis procedure

discussed above fails due to the fact that sufficient particles do not stay in the laser sheet long enough. In this case it is necessary to observe the position of the particle over a shorter time interval. This can be accomplished by strobing the laser sheet within each TV field. Since the laser is strobed a number of times during one field scan, it is necessary to ensure that the electronic shutter is open during the whole field period. Using a symmetric strobe, without any other prior knowledge about the velocity field, results in an unavoidable 180° ambiguity with respect to the direction of the observed velocity. The coded strobe technique offers a way of removing this ambiguity by varying the length of the strobe pulses. There are various methods to accomplish this (*Adrian, 1991*). The directional ambiguity is completely removed if at least three different strobe lengths are repeatedly generated and the particle does not experience a sufficiently high acceleration in a single frame period and thus cause the illuminated particle track to masquerade as a different pulse length. Another potential problem is that, although the particle is being illuminated by a long pulse, its track may appear as a short one if it enters or exits the sheet while it is being illuminated. In order to reduce errors caused by particles crossing the sheet boundary, it thus helps to select those particle images that have at least four tracks. Figure 4.7 shows the chosen pulse lengths where the pulse to be τ, 2τ and 3τ.

Strobing of the laser is accomplished by mechanically rotating a slotted disc in the path of the laser beam. Modern laser diodes can be strobed electrically. This can be an advantage, since strobing can be synchronised with the TV field scan rate and is much more accurate in controlling pulse lengths. In either case the image of the moving particle under strobed illumination is then a series of broken streaks; the length of each segment being dependent on both the pulse length and the seed's velocity. The direction of motion can be inferred by examining the sequence of the line segments. If the particle image spans only a few pixels on the CCD sensor, due to its low velocity, then it might become difficult to distinguish difference between lengths. A way around this difficulty is to use the fact that each strobed line segment is created using different effective time exposures. This results in the peak intensity of each strobed segment being proportional to the pulse duration, thus the ordering of the peak pixel intensities of each line segment can be used as an alternative coding scheme to resolve the directional ambiguity. Figure 4.8 shows a surface plot of the grey scale intensity variation of the strobed image of a single seed. On examining the middle two peaks

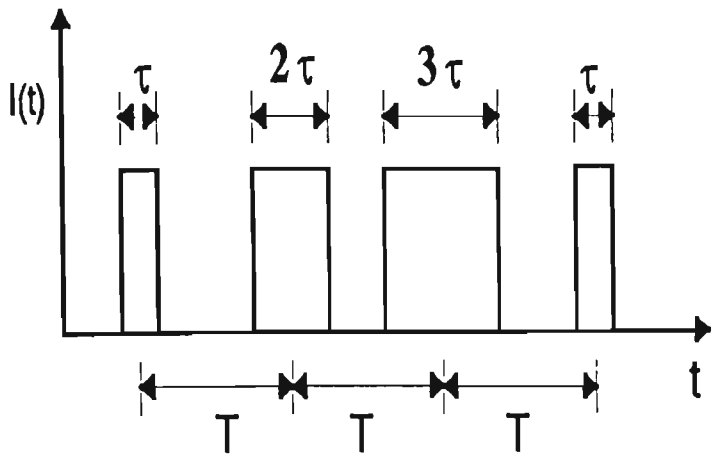

Figure 4.7: Schematic diagram of the coded strobe sequence.

in Figure 4.8, it can be seen that the intensity of one is approximately twice the other. We thus conclude that these two middle pulses correspond to the first two pulses in Figure 4.7. Since the shorter pulse in Figure 4.7 occurs first, we can be sure that particle in Figure 4.8 was moving to the left. It is clear that the width and peak intensity of the two outer peaks may not be reliable since the particle may have been entering or leaving the sheet during these times.

Using the chosen laser pulse widths and assuming typical seed velocities, the particle image travels only a few pixels between flashes. An estimate of the seed position using only the peak intensity value will thus result in the particle position being accurate to within half a pixel, resulting in an uncertainty in the velocity of up to 50%. This uncertainty clearly decreases for higher seed velocities. In order to decrease this uncertainty, it is necessary to estimate particle positions with sub-pixel resolution.

Sub-pixel Resolution

Estimation of the position of point source using peak intensity gives the position accurate to within $\pm$ 0.5 of the pixel separation. In terms of object distance, this accuracy will depend

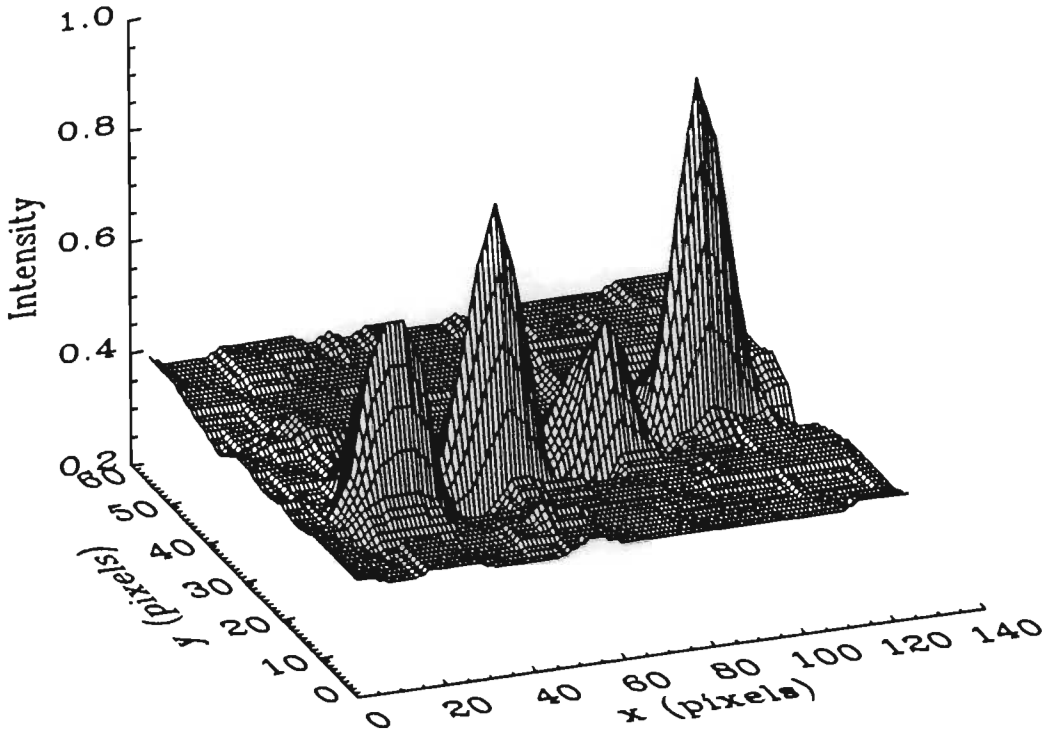

Figure 4.8: Grey scale intensity variation of a single particle illuminated by a coded strobe pulse.

on the size of the CCD array and the magnification of the lens. In our application, the pixel separation in the object plane was 0.8 mm/pixel over a field of view of 200 mm x 200 mm.

Examining the intensity distribution of the strobed images as shown in Figure 4.8, it can be seen that each strobed image of the seed has an approximate gaussian shape. One possible method of improving on position accuracy is to determine the coordinates of all points exceeding a predetermined intensity level around a particular peak, and computing an average position. This can at least improve the estimate to less than half a pixel spacing. A more accurate method is to employ a least square gaussian curve fit to the intensity profile in the x (horizontal) and y (vertical) directions about each peak. The coordinates of the peak can then be determined using the fitted curves. Alternatively, the intensity in the x and y directions can be interpolated using the following algorithm: The intensity profile in horizontal and vertical direction about the peak is Fourier transformed using an FFT of length N_1, where N_1 is sample length of the intensity profile. The spectrum is then zero padded to a length N_2 , $N_2 > N_1$, and the inverse Fourier transform computed using an inverse FFT of length N_2 to give the interpolated intensity profile in the respective directions.

An interpolation factor of N_2/N_1 is achieved. In our application an interpolation factor of 64/1 was used. We will refer to this form of interpolation as the Fourier interpolation method. This method approaches the ideal reconstruction of an analogue signal from its digital samples (*Oppenhiem and Schaffer, 1990*). A peak search using the interpolated intensity profile in the x and y direction gives the position of the peak accurate to within the interpolated pixel spacings.

F. Analysis Procedure for high seed density applications

In cases where high seed densities are present it is more beneficial to employ cross correlation techniques (*Craig et al., 1996, Chang et al., 1996*) to track the image of a group of seeds in consecutive frames or fields, since this technique allows for greater automation. This type of analysis is commonly referred to as Digital Correlation Image Velocimetry (DCIV). Correlation techniques involve finding matching structure between two images and therefore requires high seed densities. The presence of unmatching seeds or seed patterns between images simply contributes to noise. Provided the signal-to-noise ratio of the matching structures is large enough, then the peak of the computed cross-correlation function is a good estimate of the displacement of that particular structure.The cross correlation can be computed in the spatial domain by explicit evaluation of the 2D cross correlation function (*Fincham and Spedding, 1997*) or in the spectral domain by computing the cross spectral density function and transforming back into the spatial domain using the 2D FFT (*Willert and Gharib, 1991*).

The cross correlation of the images in the Fourier domain are performed as follows: Each image frame is sub-divided into smaller 32 × 32 pixel sub-images, and transformed into the Fourier domain using a 2D FFT algorithm. This FFT of a sub-image in the first frame is multiplied by the conjugate of the FFT of the corresponding sub-image in the second frame, which is then transformed back into the spatial domain as given in equation 4.9 below.

$$\begin{aligned} R_{fg}(u,v) &= F(u,v).G^{*}(u,v) \\ r_{fg}(m,n) &= FFT^{-1}\{R_{fg}(u,v)\} \end{aligned} \tag{4.9}$$

where $F(u,v)$ is the Fourier transform of the sub-image, $f(m,n)$, in the first video frame, $G^*(u,v)$ is the conjugate of the Fourier transform of the corresponding sub-image, $g(m,n)$, in the second frame, and $r_{fg}(m,n)$ is the computed 2D cross correlation function of the sub-images. The intensity profile along the x and y direction about the peak in the computed cross correlation is then interpolated using the Fourier interpolation method. The displacement of each sub-image is thus estimated to within the interpolation factor, i.e. typically 1/64, of the original pixel spacing.

When using 2D FFT algorithms, it is beneficial to use sub-images having sizes that are powers of two. This, however, does not necessarily preclude the computation of the displacement of a sub-image whose dimensions are not a power of two. This is achieved as follows: Typically a smaller sub-image from the first frame, say 12 x 18 pixels, about some point (k,l), is selected. This odd-sized sub-image is then adjusted, such that it has a zero mean, and then zero padded in the horizontal and vertical direction to a size of 32 x 32 pixels, resulting in a border of zero intensity around the original 12 x 18 pattern box. The search area, that is the corresponding region in the second frame where a match with the sub-image in the first frame is likely to occur, can be a full 32 x 32 sub-image centred at (k,l) in the second frame. The co-ordinates of the peak in the resulting cross correlation are then the displacement of the original 12 $\times$ 18 pattern box. The zero padding does not influence the cross correlation result. In fact, the zero padding eliminates some of the problems associated with implementing cross correlation using the FFT, such as wrap around (*Oppenhiem and Schaffer, 1990*).

Since the cross correlation technique requires two separate images, we are therefore limited by the 20 ms(40 ms) sampling time associated with field (or frame) update rate of a conventional CCD camera. However, it is possible to obtain pairs of images separated by a few microseconds while still using video frame update rate by using a non-interlaced progressive scan camera and appropriately strobing the light sheet. The essential steps in determining the velocity flow field using the cross correlation technique is as described above except that the image capture configuration was changed in order to achieve sampling times smaller than the frame update rate.

The experimental setup used for DCIV is similar to that shown in Figure 1, except for the following changes; A strobe light is used as a source for the light sheet and a non-interlaced progressive scan digital camera, connected to a frame grabber, was used to record images directly to the hard disk. The non-interlaced camera provides a high spatial resolution, 764 x 468 pixels, and by strobing the light sheet at the end of one frame time and then again at the beginning of the next frame time, it is possible to obtain pairs of images with sampling times ranging from a few microseconds to a few milliseconds while still using the normal frame update rate. Since the sequence of the images is known, the 180 degree directional ambiguity,usually associated with multiple strobing during a single frame time, is removed.

The above cross correlation method was used to measure the velocity flow field of a 0.4 Hz plunging wave and 0.9 Hz spilling wave breaking on a 1:20 slope beach, and having deep water wave heights of 11 cm and 16 cm, respectively.

Figures 4.9(a) and (b) shows a pair of images of the crest of the plunging wave approximately 50 cm beyond the break point. The images are displaced 0.826 ms apart.

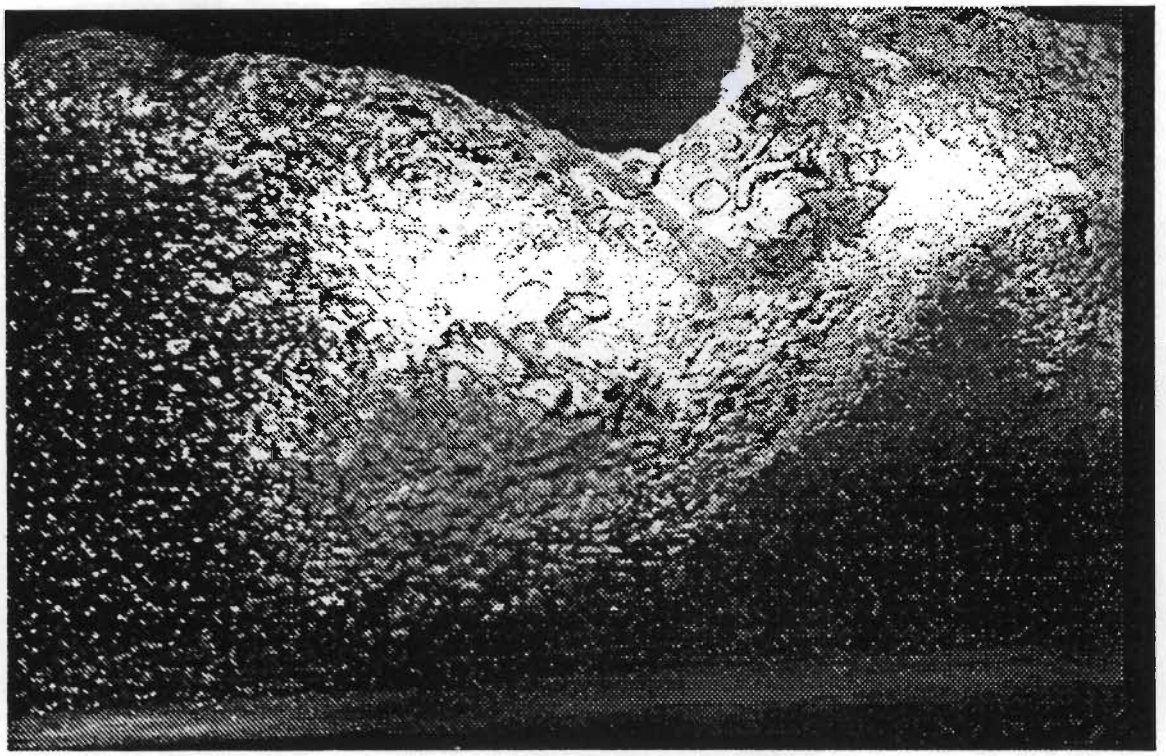

Figure 4.9:(a) First image of the crest of a plunging wave in the surf zone.

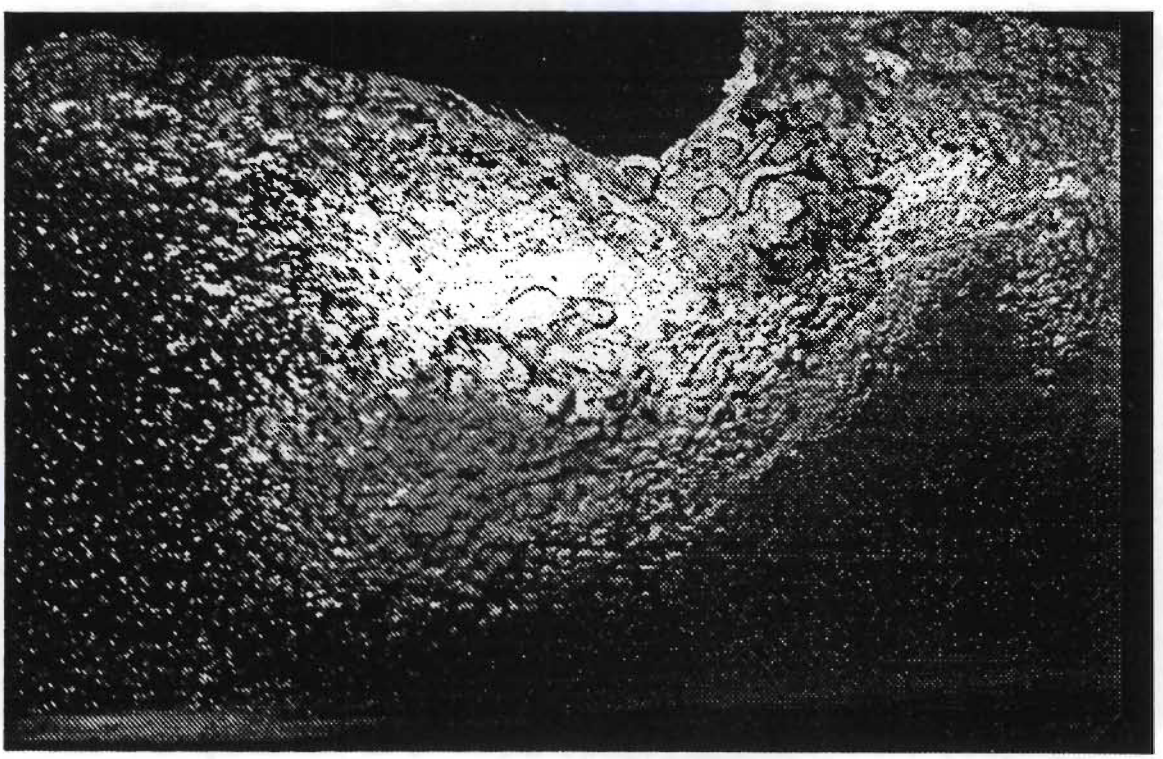

Figure 4.9:(b) Image of the crest of the same plunging wave in (a) captured 0.826 ms later.

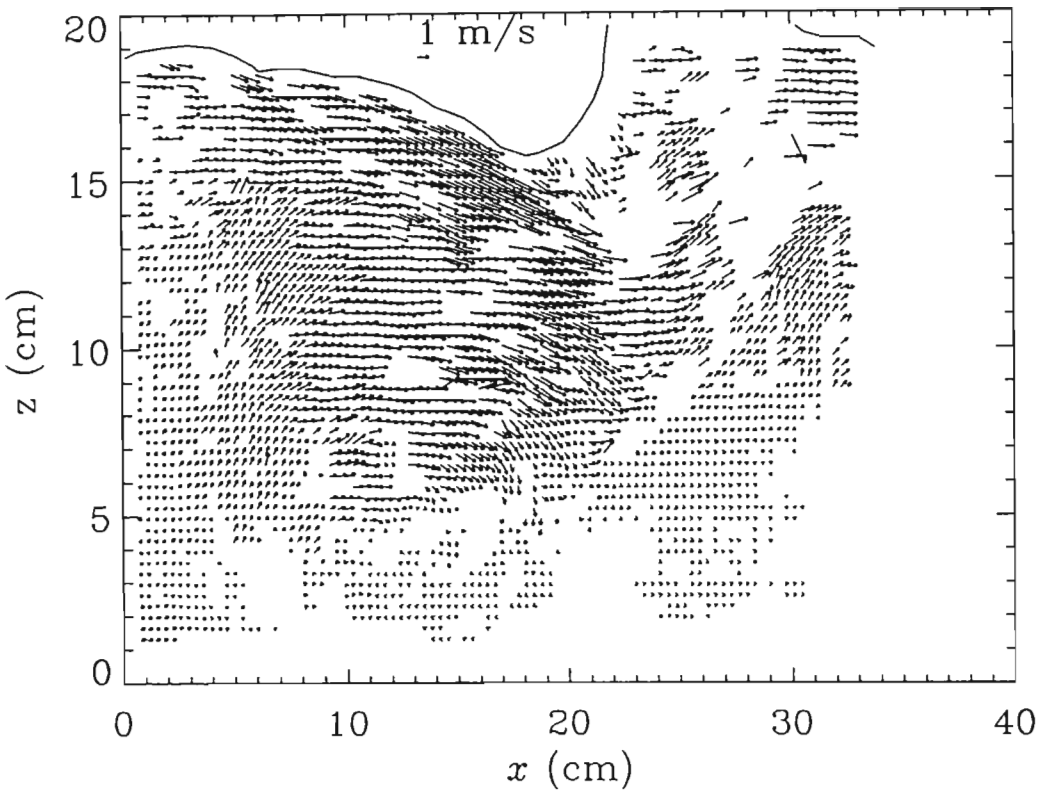

Figure 4.9:(c) Instantaneous velocity field computed using 2D cross correlation of images in (a) and (b).

These images show a scene containing both bubbles resulting from the wave breaking, and polystyrene seed particles. By overlaying the two images, it can be seen that the structure of corresponding portions of the two images persists for the duration of sampling time with very little distortion. The calculated velocity vector field for the above image pairs is shown in Figure 4.9(c). There is maximum flow velocity ($\sim$ 3 m/s) near the surface of the wave, whilst near the bottom, the velocity is almost zero. The formation of a large eddy in the centre of both images and in the vector field is evident. As the rise velocity of the air bubbles in this highly turbulent flow regime is negligible in comparison to the velocity components of the flow, it is thus possible to obtain a detailed flow pattern well into the aerated region of the wave using the air bubbles to create the necessary structure. In the past, some researchers (*Craig and Thieke, 1998*) have gone to great lengths to remove the effects of the air bubbles in order to highlight particulate matter that has been deliberately added to the flow. This appears not to be necessary for the flow regime under discussion. In streamline laminar flow, however, it would be necessary to obtain an estimate of the bubbles rise velocity and apply the necessary correction to the flow field. The sampling time is determined by satisfying the competing criteria of requiring a persistent bubble structure as

well as a measurable displacement.

4.3. Water Level Measurements

Measurement and Analysis

To obtain a time series measurement of the water level, the wave flume was imaged from the side with the camera located at the still water line level and the wave illuminated from above. A black backing sheet was placed behind the flume and used as a backdrop. This arrangement allows the air-water interface to be identified by locating the sharp transition in the vertical lines of grey scale intensity. The camera was also mounted on a base that could be translated on a set of rails parallel to the flume.

The procedure for extracting the time series was as follows: At each position along the flume a video recording of the wave was made. A single vertical line of pixels at a fixed position was then extracted from a sequence of images. These vertical samples were then stacked side by side to create a new image, called a keogram. This procedure is depicted in Figure 4.10. Figures 11(a) and (b) show examples of keograms of a wave, before and after breaking, respectively.

A robust cross correlation algorithm was developed to determine the position of the air-water interface. The transition point was enhanced by cross correlating the vertical grey-scale intensity profile with the edge detection function shown in Figure 4.12. The resulting cross correlation was a signal with an easily found peak at the transition point. The width w1 and w2, and the amplitude a1 and a2 of the cross correlating function were adjusted to maximise the value of the resulting peak at the transition.

The keogram technique was also used to measure the geometry of the roller and the aerated region of the wave in the surf zone. This was achieved by first forming a phase averaged keogram of the wave and demarcating the high intensity region which was identified as being the roller or aerated region.

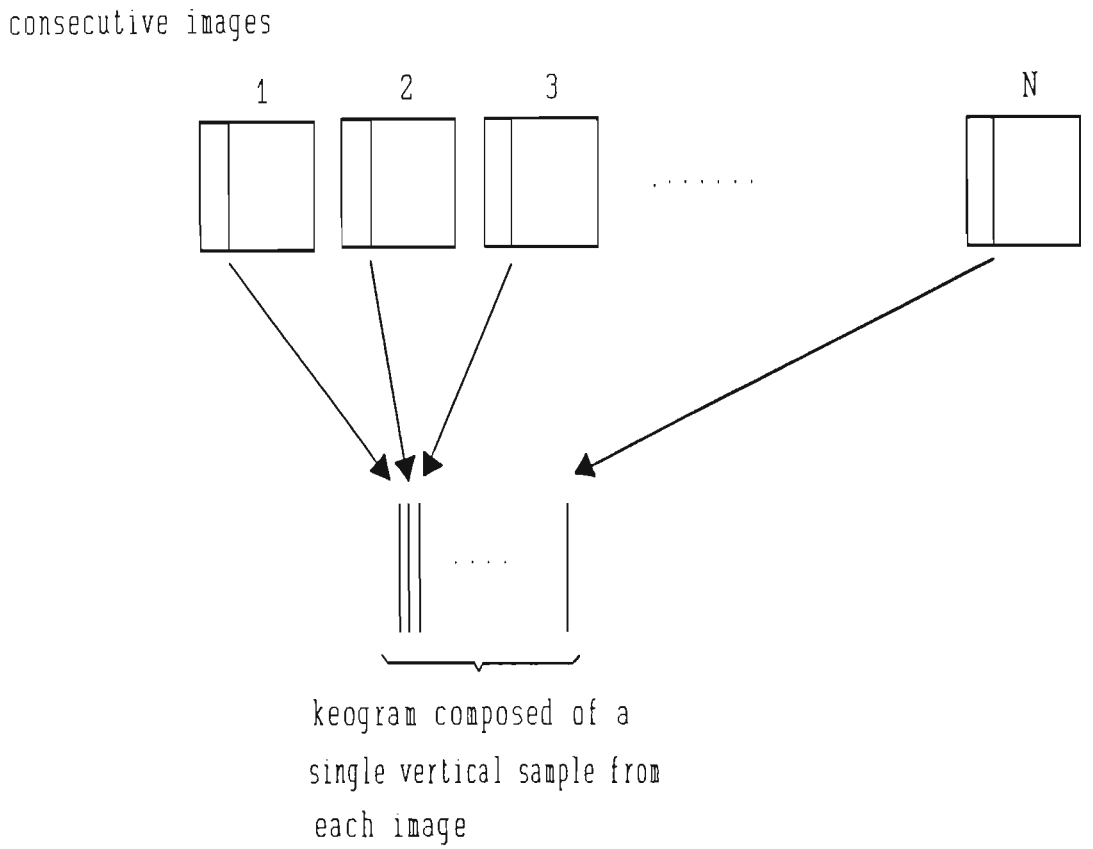

Figure 4.10:The generation of a keogram from a sequence of video images for the measurement of the time series of the water levels in a 2D wave flume.

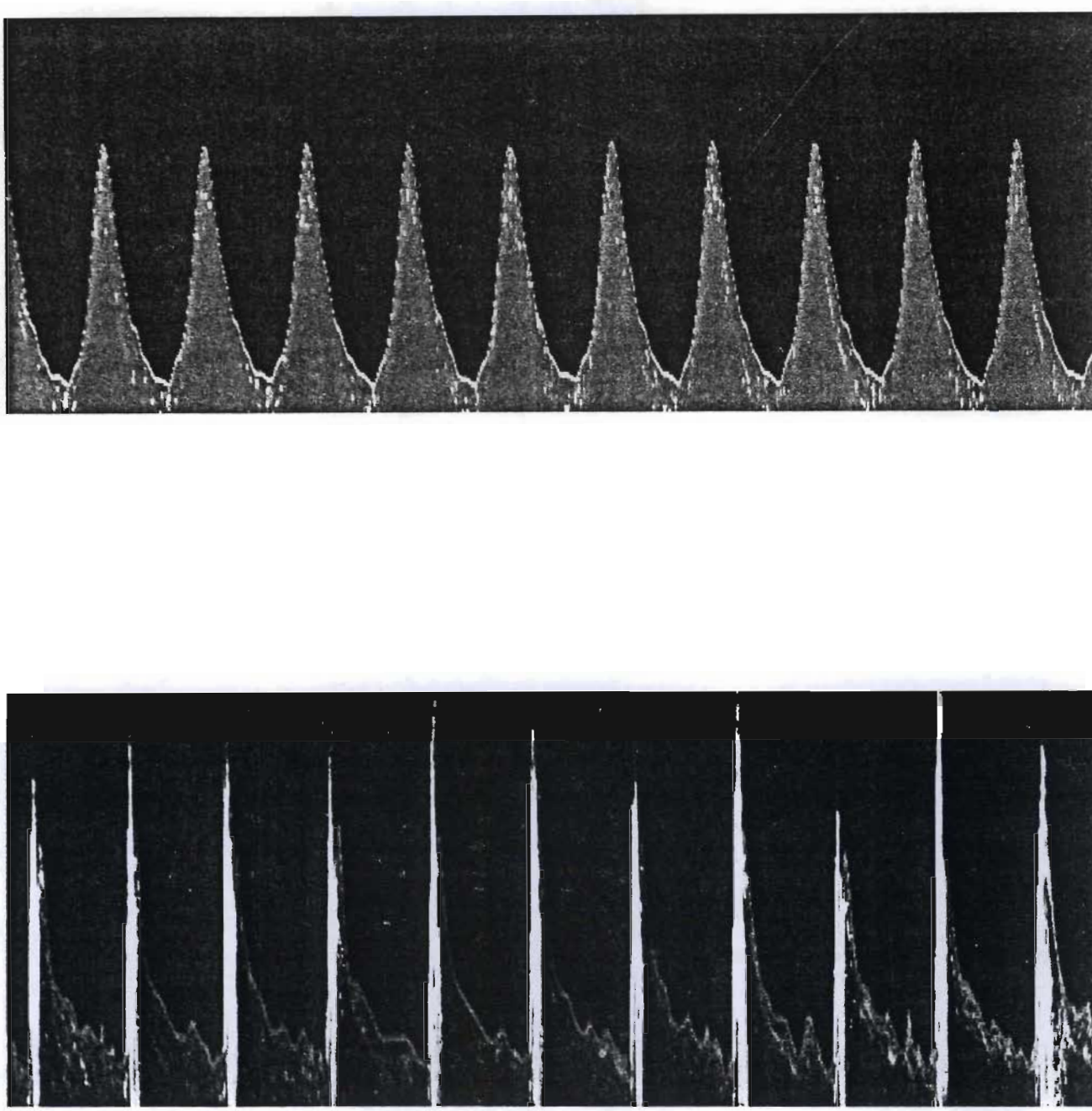

Figure 4.11: Examples of keograms of waves (top) before and (bottom) after breaking. The vertical and horizontal distances in the keogram represent height in image cordinates and time increments, respectively.

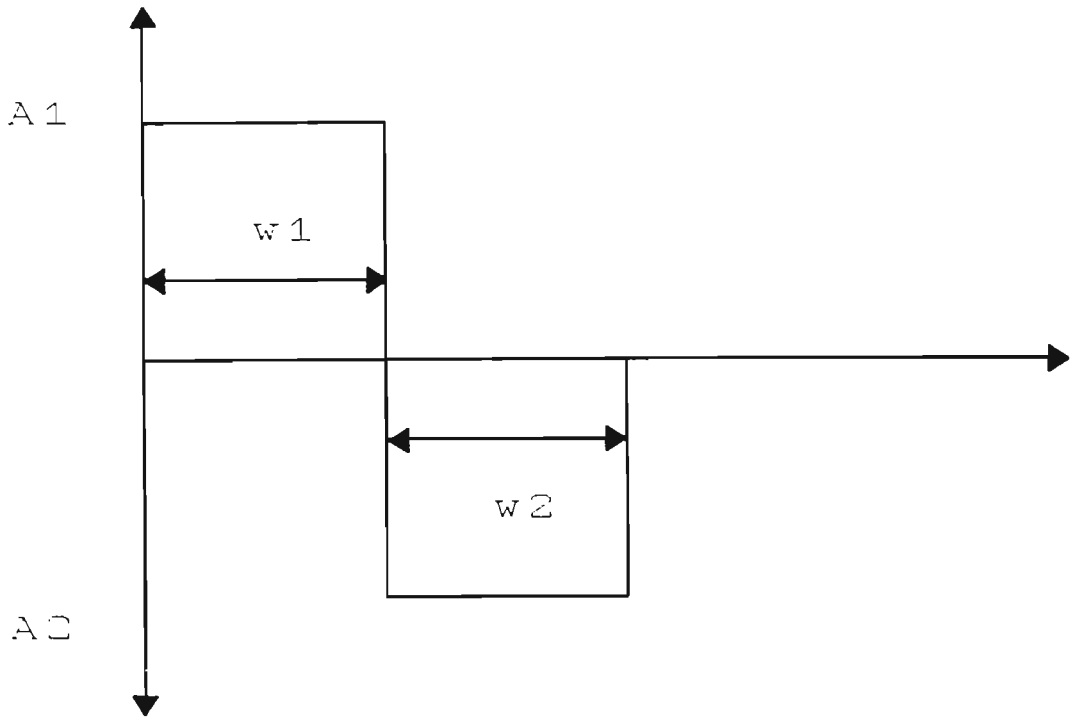

Figure 4.12: Example of an edge detecting function. The width w1 and w2, and amplitude A1 and A2 are adjusted to suit the application.

Extensive results of time series of water-levels measurement and aeration measurement are provided in the next chapter, together with resistive wave-gauge comparisons.

4.4. Summary

The measurement of the velocity flow fields in a laboratory surf zone using digital particle image velocimetry is demonstrated. The choice and operation of various components in the system were highlighted. In order to implement the sub-pixel estimation techniques described, it is necessary for the particle image to span a few pixels. Velocity estimation was accomplished by observing the position of seed particle at two or more time instances. The particle positions were sampled at the TV field/frame update rate. Higher effective sampling rates were accomplished by strobing the laser sheet within each field time. The direction of particle motion was determined by noting the sequence of the images in the field/frame analysis and by the use of pulse coding the laser. Higher sampling rates were achieved using a non-interlaced progressive scan camera and strobing the light sheet. This setup together with the cross correlation method of analysis was used to measure the instantaneous velocity

vector field in the highly aerated crest of a plunging wave.

The measurement of time series of the water level in a 2D flume using video techniques was also discussed and demonstrated. The time series of the wave was extracted from a keogram generated at fixed positions along the flume. The measurement of the roller area of waves in the surf zone is also possible using keogram technique.

A number of techniques suitable for measuring the velocity flow field and water levels of waves in the surf zone have been described and demonstrated. It has been shown that by using particle image velocimetry and correlation image velocimetry techniques it is now possible to obtain velocity measurements well into the aerated region of the wave. The calibration and sensitivity analysis of the video techniques will be presented within the context of surf zone measurements in Chapters 5 and 6. More comprehensive analyses using the techniques, including using the data for computational model validation, will be presented in Chapters 5, 6 and 7.

CHAPTER 5

WATER LEVEL AND AERATION MEASUREMENTS

The external properties of waves breaking on a beach are investigated through the measurement of time series of the water level along the length of the flume. These effects include the set-down and set-up of the mean water level, and the decay of the wave height as the wave propagates across the surf zone. A measurement of the aeration/roller geometry, including the aerated roller area and slope, is also made. The experimental set-up and method of measuring the time series of water level using the keogram concept is discussed. The computation of the frequency wavenumber spectrum of the surface waves in the flume, using two probes and an array of probes, is discussed. The measurements of the mean water levels and wave heights for a spilling and plunging wave is presented.

5.1 Introduction

The oscillation of the water surface is one of the more visible aspects of water wave propagation and it has been one of the first parameters to be investigated. Early measurements of the wave period and height and wavelength were measured by seamen who noted the wave period by observing the bobbing of their ships, and the wavelength and wave height were measured using markings on the side of the ships. These early measurements were restricted mainly to deep water waves and were useful for shipping purposes. There is now a large body of knowledge pertaining to deep water waves. These waves are also well described by a set of near linear equations and so attention is now being directed towards areas involving nonlinear phenomena and turbulence. The surf zone is one of them.

Wave propagation just outside the surf-zone is characterised by shoaling of the wave height and set-down of the mean water level as it approaches the shoreline. Breaking then occurs when the height reaches some critical value. The formation of the roller, a body of water that rides on the front face of wave, occurs. There is also a setting-up of the mean water level. The surf zone is thus characterised by processes that are nonlinear and turbulent, rendering any deterministic analytic analysis almost intractable. One is therefore forced to use a statistical approach when dealing with measured quantities in the surf. Analytical techniques then provide prediction of the average quantities. Pre-breaking conditions have been studied fairly intensely, one of the earliest measurements of the shoaling and set-down of the mean water level was conducted by *Inman and Bowen(1962)*, and the shoaling and set-down characteristics have been explained theoretically using radiation stress theory (*Longuet-Higgins, 1964*). A promising analytical model that is currently being pursued is the Boussinesq equation describing the propagation of surface waves using depth integrated quantities (*Schaffer et al, 1992; Schaffer et al, 1993*).

The surf zone is further complicated by the entrainment of air bubbles during the breaking process. This makes measurement of certain internal and external properties of the wave difficult. Traditionally, the water levels are measured using resistance or capacitance wave gauges. The behaviour of these gauges in the surf zone is somewhat unreliable.

The presence of the air bubbles, however, allows us to visualise and measure some of the

macroscopic features of the wave in the surf zone. In the sections to follow we examine specifically the highly aerated region created at the front face of the wave during breaking. This region constitutes the roller which moves forward with the wave. The slope of the front face of the wave is also measured. These parameters are important inputs in the Boussinesq model as applied to breaking waves (*Schaffer et al, 1992; Schaffer et al, 1993*)and to wave height decay models (*Svendsen, 1984*).

We report here on the measurement of the water levels in the surf zone for two types of waves, viz., 0.9 Hz spilling and 0.4 Hz plunging wave, using the keogram techniques discussed in the previous chapter. The time series of the wave is obtained from the keograms of the wave at a number of positions along the flume. The comparison of the time series of the surface wave with those obtained using resistance wave gauges are also presented. The magnitude of the free-harmonic and reflected waves is ascertained via the computation of the frequency-wavenumber spectrum of the waves in the deep water section of the flume. Two methods of measuring the frequency-wavenumber spectrum are discussed, viz, two probe and a probe array. It will be shown that only the probe array is capable of separating the wavenumber components in the spectrum for waves having identical frequencies but different wavenumbers. The wave height and mean water level is computed using the time series of the wave at positions along the flume. The keogram technique is also used to measure the roller area and wave slope. The roller area is measured by demarcating the high intensity area using different intensity thresholds.

5.2 Experimental conditions and procedures

The water levels were measured at intervals of approximately 0.1 m over the entire surf zone. Table 1 below summarise the characteristics of the waves used in the experiments.

Table 4.1: Wave characteristics

wave type	H_0 (m)	d_0 (m)	f (Hz)	T (s)	L_0 (m)	H_b (m)	h_b (m)
spilling	0.16	0.77	0.9	1.11	2.04	~0.16	0.218
plunging	0.11	0.77	0.4	2.5	6.87	~0.175	0.156

H_0 is the deep water wave height, f is the wave frequency, T is the wave period, L_0 is the deep water wavelength and H_b the wave height at the breakpoint.

The method of measuring the time series of the wave will be briefly described here, more details can be found in the previous chapter and *Govender et al.(1998)*. The flume was imaged from the side using a black and white Videotronic CCD camera connected to a Mitsubishi VCR and also to a SE100 Video Blaster frame grabber residing in a PC. The wave was also illuminated from above using a 500 watt flood lamp and a black backing sheet was placed behind the flume. This arrangement enhances the image of the meniscus and aeration. A two minute recording of the wave was made at each measurement position along the flume. The recorded images of the wave were digitised using a SE100 video blaster frame grabber. A keogram of the wave was generated at each position by extracting a single vertical line of pixel intensity values from consecutive video images. These vertical pixel intensity values were then stacked side by side creating a new image called a keogram. The time series of the wave was then determined by identifying and locating the coordinates of the air water interface in the keogram. The validation and comparison of this method of measuring the time series of the water level with data from wave gauges is presented in the next section. This method of measuring water levels is adopted throughout this thesis.

5.3 Comparison with wave gauge

The majority of water level measurements conducted in the past have been accomplished using resistance (e.g. *Stive, 1980*) and capacitance (e.g. *Ting and Kirby, 1994*) wave gauges,

and the behaviour of these devices in non-breaking waves are well understood. There is, therefore, a level of confidence associated with these types of measurements. A pertinent exercise, therefore, is a comparison of time series of water levels obtained using wave gauges and the video technique.

The time series of the water level was measured simultaneously using the video camera and a resistance wave gauge located within the view of the camera. Measurements were performed at three positions along the flume for each wave case, corresponding to deep water, pre-breaking and in the surf zone. The analogue signal from the wave gauge was modulated onto a 8 kHz carrier signal and recorded onto the video tape using the audio channel of the VCR. The wave gauge signal was later extracted through a reverse process. Thus simultaneity of measurement is ensured.

Figures 5.1 and 5.2 show the keogram and the resulting time series for the 0.9 Hz and 0.4 Hz wave measured in the deep water section of the flume. It is clear from Figures 5.1(b) and 5.2(b) that the wave gauge output and the video results are almost indistinguishable. The comparison in the surf zone, however, is not so simple.

Figures 5.3 and 5.4 show the results of water level measured in the surf zone for the 0.9 Hz and 0.4 Hz wave, respectively. In the time series of the spilling wave, Figure 5.3, the wave gauge signal differs from the video result particularly in the crest and trough regions of the wave. This is clearly understandable since there is a lot of aeration in the crest, resulting in a low electrical conductivity of the water. However, the general trend in wave height variation from one cycle to the next, as is visible in the keogram and the resulting time series from the video, is also present in the wave gauge signal. In the time series of the plunging wave, Figure 5.4, there is a one to one correspondence between the keogram and the resulting time series. The wave gauge signal on the other hand does not show any variation in the wave height from cycle to cycle.

Thus, it is clear that in non breaking waves the video and the wave gauge are capable of measuring water level with comparable accuracies. In the surf zone, however, it is evident that the wave gauge is sensitive to the percentage of aeration present in the crest of the waves

and in some cases like that for the plunging wave the behaviour of the wave gauge is unpredictable. The video on the other hand measures the actual water surface including the aerated water as well. This does imply that the video technique will also record splashups that are still attached to the water surface. Splashups that are disconnected from the water surface does not pose a problem as there is still an identifiable transition of intensity across the air water interface. The effects of splashups can be partially removed by smoothing the resulting time series using a digital moving average filter.

The video technique, however, does have a number of advantages. It is a non-intrusive means of measuring the time series of water level and therefore does not interfere with local flow behaviour. The equipment is also not subjected to corrosion problems associated with wave gauges. The video technique is also less sensitive to drift, that is, the variation of steady state conditions within the equipment. It is also possible, through the selection of suitable threshold techniques, to separate the measurement of the solid body water and the aerated water.

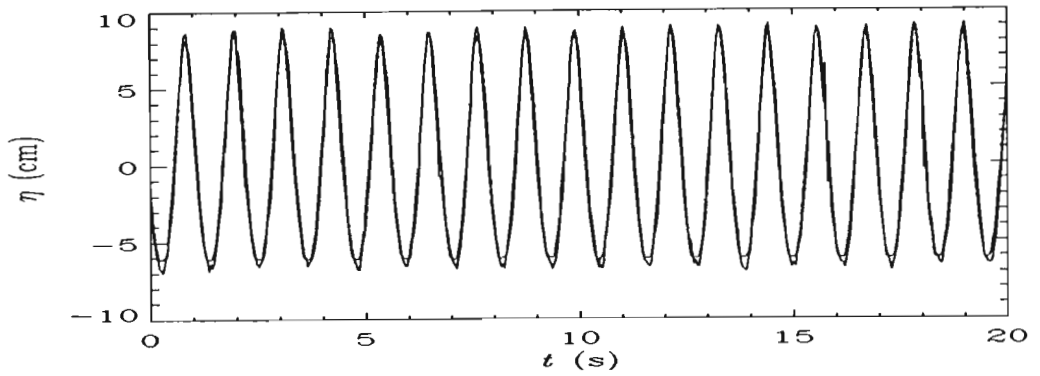

(a)

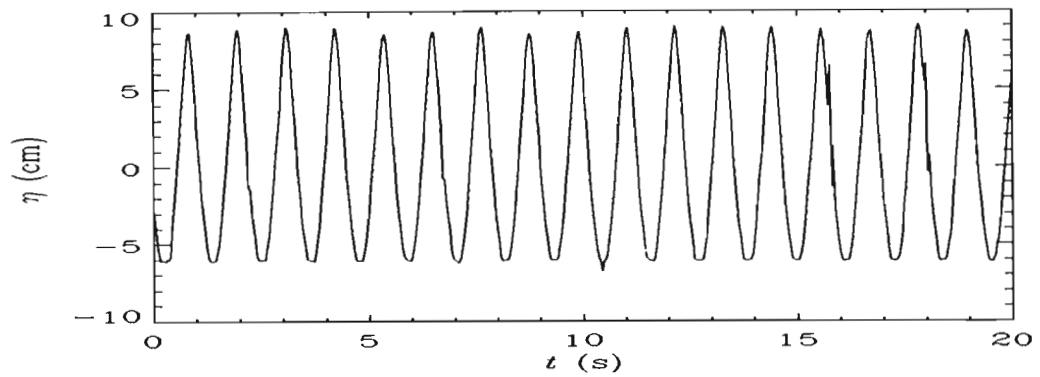

(b)

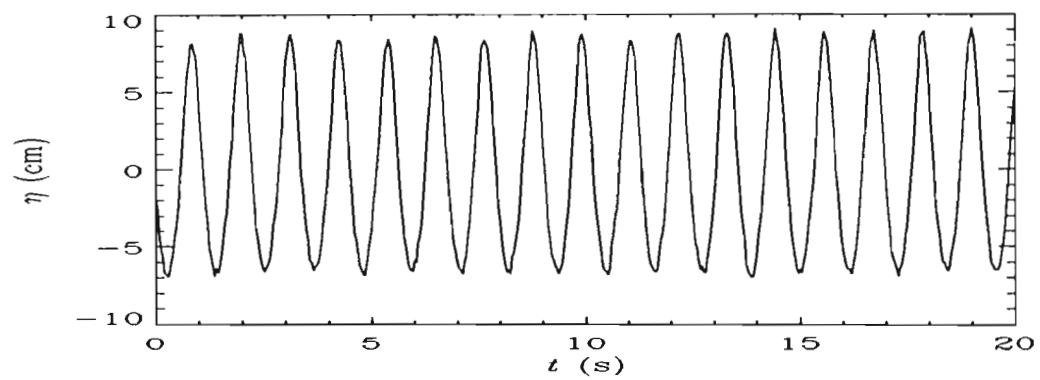

(c)

Figure 5.1: Time series of water level for a 0.9 Hz spilling wave: (a) overlay of both wave gauge and video results, (b) video time series and (c) wave gauge result. These data were measured in the deep water end of the flume.

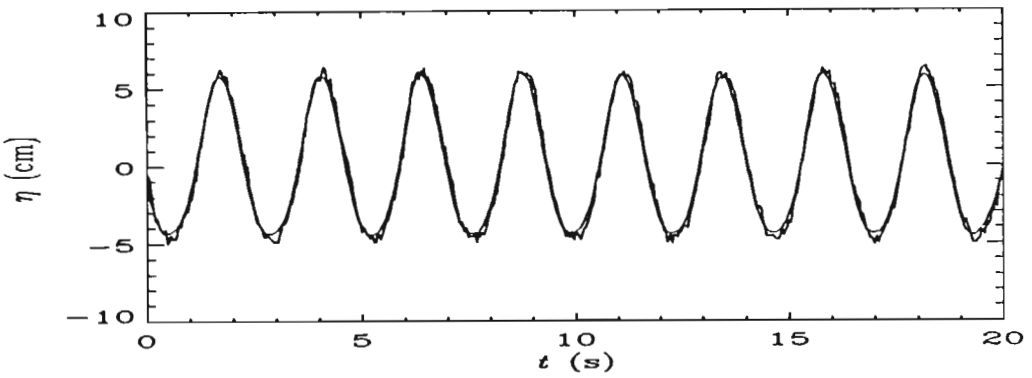

(a)

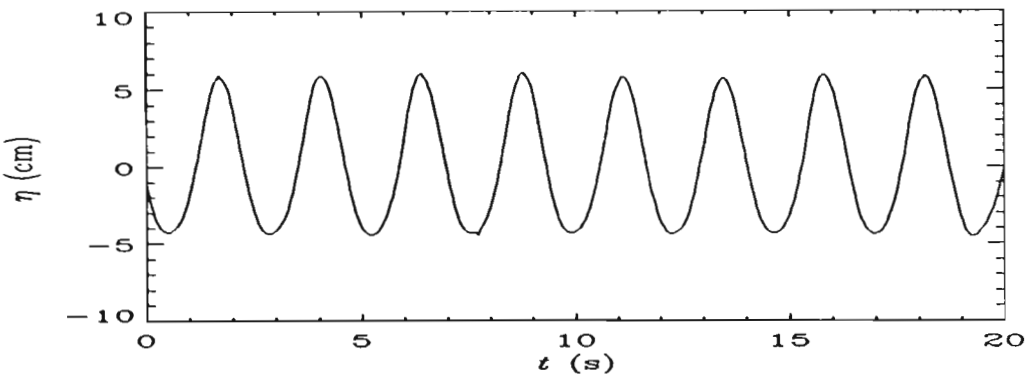

(b)

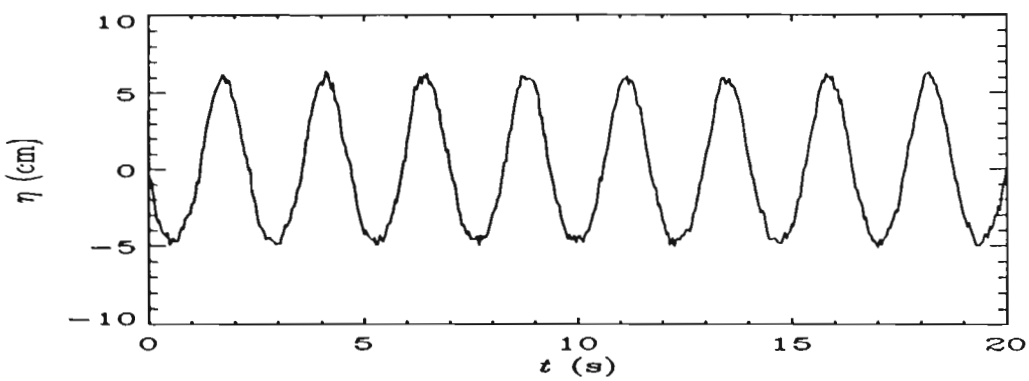

(c)

Figure 5.2: Time series in the deep end of flume for the 0.4 Hz plunging wave:(a) overlay of video and wave gauge results, (b) video time series, (c) wave gauge result.

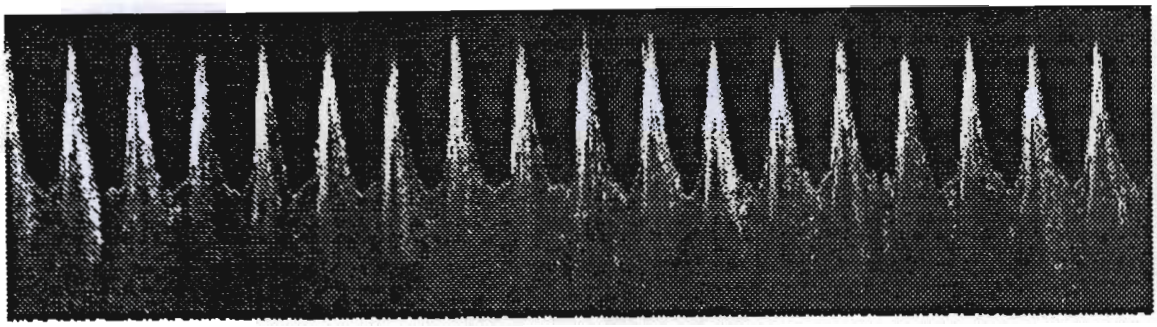

(a)

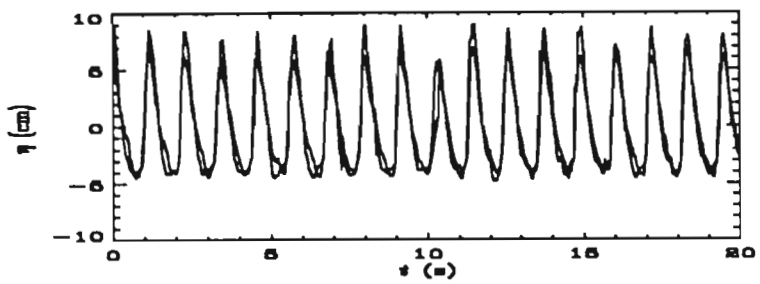

(b)

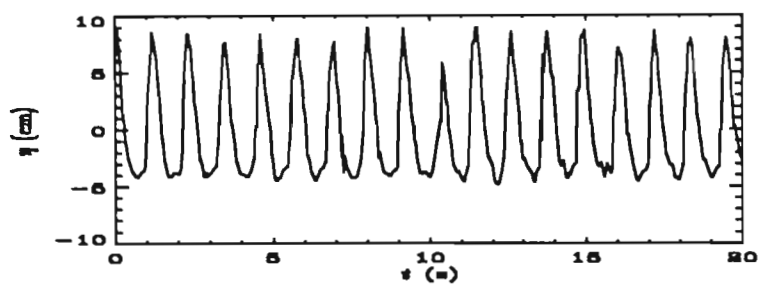

(c)

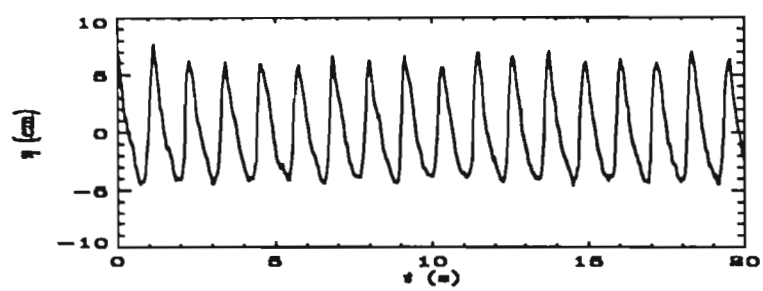

(d)

Figure 5.3: Time series of waterlevel measured in the surf for the 0.9 Hz spilling wave; (a) keogram of the wave, (b) overlay of video and wave gauge measurement, (c) Video measurement, and (d) wave gauge measurement.

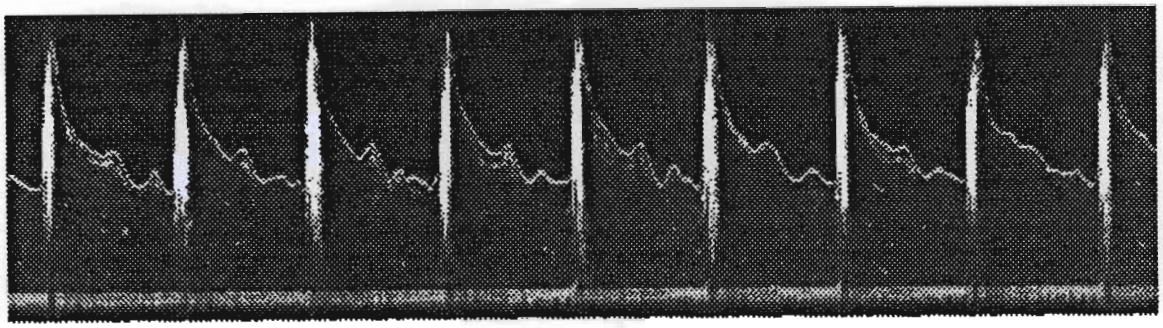

(a)

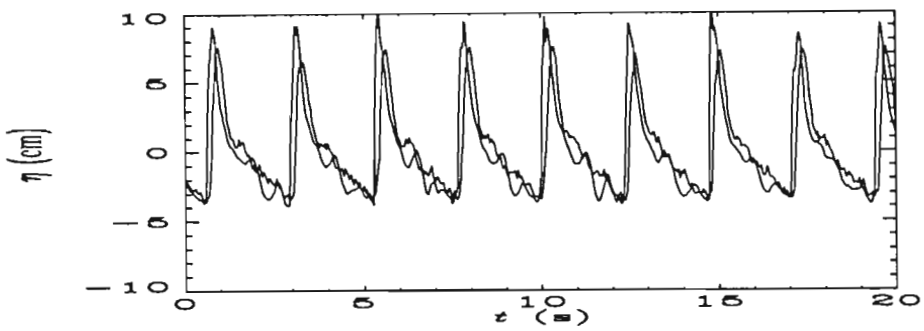

(b)

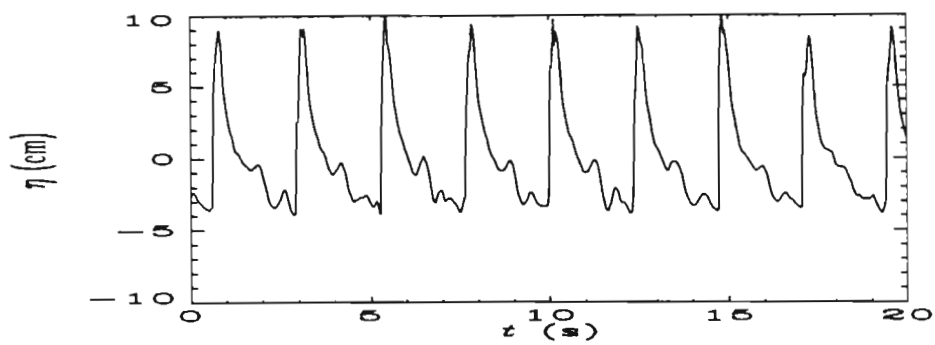

(c)

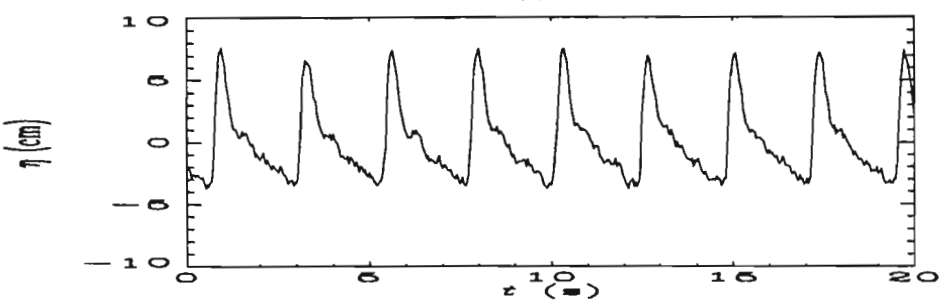

(d)

Figure 5.4: Time series of waterlevels measured in the surf for the 0.4 Hz plunging wave; (a) keogram of the wave, (b) overlay of video and wave gauge measurement, (c) Video measurement, and (d) wave gauge measurement.

5.4 Frequency-wavenumber measurement

Associated with the time series of the surface wave is the frequency-wavenumber spectrum. The wave-number spectrum is used to estimate the phase velocity and wave length of the frequency components present in the surface wave. The wave number spectrum is also used to determine the presence or absence of reflected and free harmonics waves. Two methods of measuring the wave number spectrum, viz. two probe method and a virtual probe array, are presented below.

Two probe method

The time series of the surface wave is measured simultaneously at two positions a known distance, d, apart, using gauges or the video technique. Let these time series be denoted as $x(t)$ and $y(t)$, respectively. In order to estimate the wavenumber spectrum, it is necessary to determine the time lag or phase difference between the frequency component present in the signal $x(t)$ with those in $y(t)$. This can be easily done using the cross spectral density function as follows:

$$S_{xy}(\omega) = X(\omega).Y(\omega)$$

where $X(\omega)$ and $Y(\omega)$ are the Fourier transform of the signals $x(t)$ and $y(t)$, respectively. The wavenumber is then given by:

$$k(\omega) = \theta(\omega)/d$$

where $\theta(\omega)$ is obtained by writing $S_{xy}(\omega)$ in polar form as $S_{xy}(\omega) = |S_{xy}(\omega)| exp(i\theta(\omega))$, with $\theta(\omega) = Im(S_{xy}(\omega))/Re(S_{xy}(\omega))$. If the surface wave is stochastic in character then the average cross spectral density spectrum using a number of realisations of x and y is computed. The wavenumber spectrum is then computed using the average cross spectral density function.

In situations where there are two waves of the same frequency but propagating in opposite directions with amplitudes A_1 and A_2, the two probe method is not capable of separating these two wavenumber components but gives single component with an average wavenumber, $A_1k_1+A_2k_2$. If A_1 and A_2 are equal, then a standing wave is created and the two probe method gives a wavenumber equal to zero, since there is no phase difference between the signals x and y. Thus the two probe method is not suitable for measurements were there is a large reflected component or waves of identical frequency but differing wavenumbers. In this case it is necessary to use an array of probes to estimate the frequency-wavenumber spectrum.

Virtual probe array

It is instructive to consider, the temporal and spatial variation of the water surface when there are one or more wavenumber components present in the flume. In the case of a single component, with frequency f and wavenumber k, propagating from left to right, the surface has sinusoidal profile at any instant in time. However, since the wave is moving, all points on the surface oscillates with frequency f, and amplitude A, but have a linearly increasing phase with respect to distance along the flume. Since the amplitude and frequency are constant, the wavenumber can be determined by measuring the rate at which the phase varies using a simple two probe measurement. If there are a number of components having unique frequencies and wavenumbers, the frequency-wavenumber spectrum can estimated by analysing the phase-distance relationship of each component using the two probe method.

Now consider two waves having identical frequencies but having different wavenumbers, of opposite signs, that is, propagating in opposite directions. The resulting pattern is then an oscillation of the water surface with common frequency but there is a sinusoidal variation in the amplitude and the phase of the oscillation over the length of the flume. If the amplitudes of each components are equal, then a standing wave results and all points on the water surface oscillate with identical phase. In order to separate the surface into the true wavenumber components it is necessary to examine the variation of the amplitude and the phase of each frequency component in space. In the case where there are many different frequencies, it is first necessary to separate the frequency components at each point and then examine the amplitude variation of each frequency component in space. This can be achieved using an equidistant array of probes positioned along a portion of the length of the flume. Let the signal received at each probe be $y_i(t)$, where $i=1,2..N$. We create a matrix with the columns representing the time samples of each probe. Each column is then Fourier transformed, decomposing each probe signals into its frequency components. This is followed by taking the Fourier transform of each row. The resulting matrix is then the frequency - wavenumber spectrum, with rows representing frequency and columns representing wavenumber. The above algorithm is illustrated below.

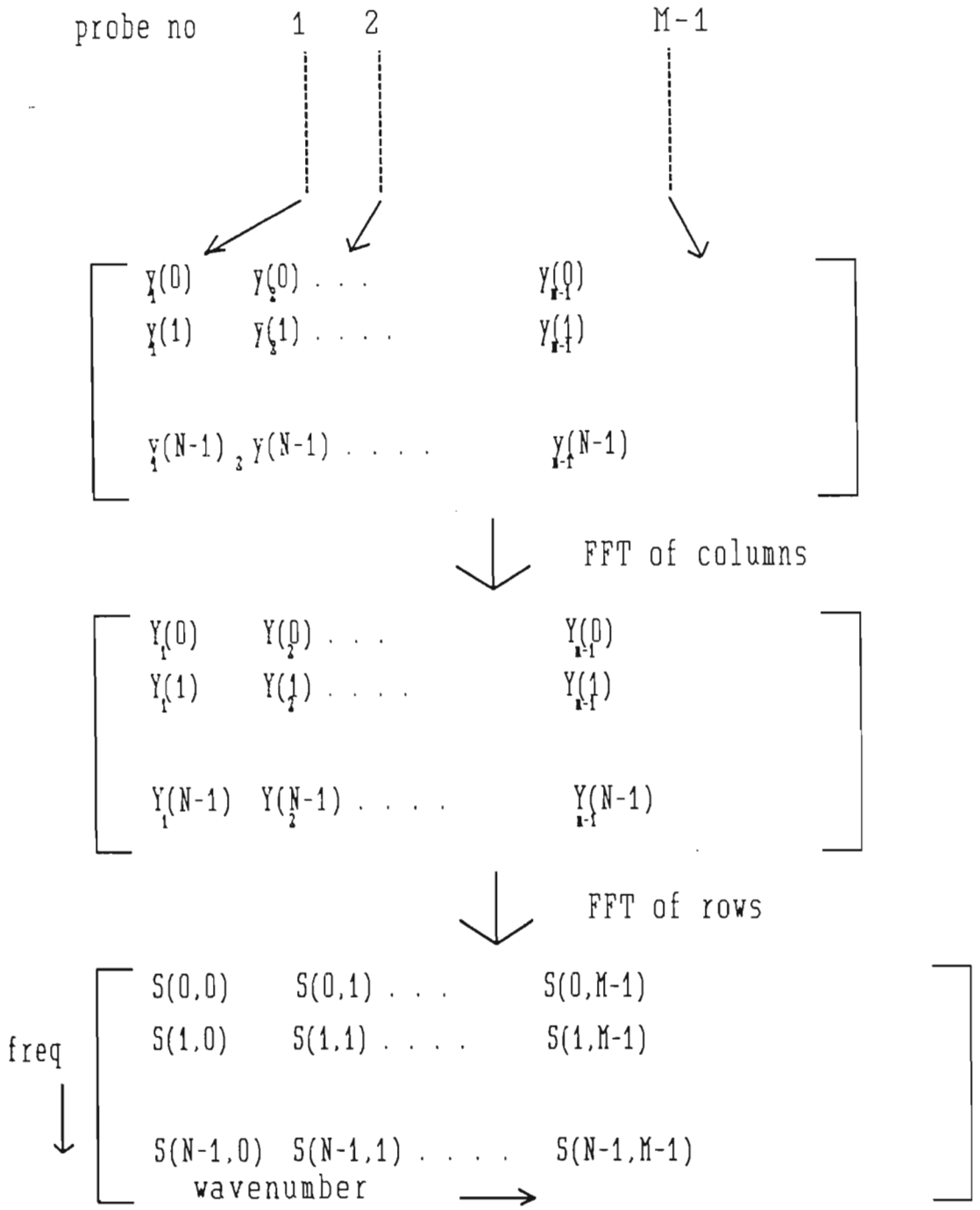

Figure 5.5: Frequency-wavenumber measurement using an array of probes. This type of measurement is necessary when there are many wave components of identical frequencies but differing wavenumbers present in the flume.

The setting up of a large number of probes is a costly and a tedious exercise, and a way around this is to employ an array of virtual probes. In order to construct the frequency-wavenumber spectrum, it is necessary to measure the amplitude and phase of oscillation at various point along the flume with respect to a fixed point, say the signal at the wave paddle. Thus, the time series of the water level are sequential extracted at regularly space intervals along the flume using a single probe, but the start of capture is triggered with a signal from the wave generator. These time series are then inserted into the appropriate columns in the first matrix in Figure 5.5. This arrangement, assuming paddle repeatability, is equivalent to having a number of simultaneously measuring probes. It is also important to note that this technique implies spatial and temporal homogeneity of ω and k. Thus, this technique has been applied in the flat-bed section of the flume.

Examination of reflected and free harmonic waves

In order to successfully make water level measurements in a flume it is necessary that there are no reflected waves from the beach and that the amplitude of the second free harmonic is minimised. Free harmonics tend to interfere with the position of the breakpoint, causing it to shift gradually. Reflections were attenuated by absorptive rubble material placed at the upper end of the beach.

Figures 5.6(a) and 5.7(a) shows the frequency-wavenumber spectrum for the spilling and plunging wave cases, respectively, obtained from a sequence of video images of the wave in the deep water section of the flume. The wavenumber spectrum, at the fundamental and 2nd harmonic frequencies, are shown in Figures 5.6(b) and 5.6(c) for the spilling case and Figures 5.7(b) and 5.7(c) for the plunging case, respectively. These figures clearly show a large peak at the fundamental and second harmonic frequencies, corresponding to the two bound wave components. All other peaks are very much smaller (by a factor of 4 or more) than the bound components and we conclude that the effects of free harmonics and reflected components are negligible.

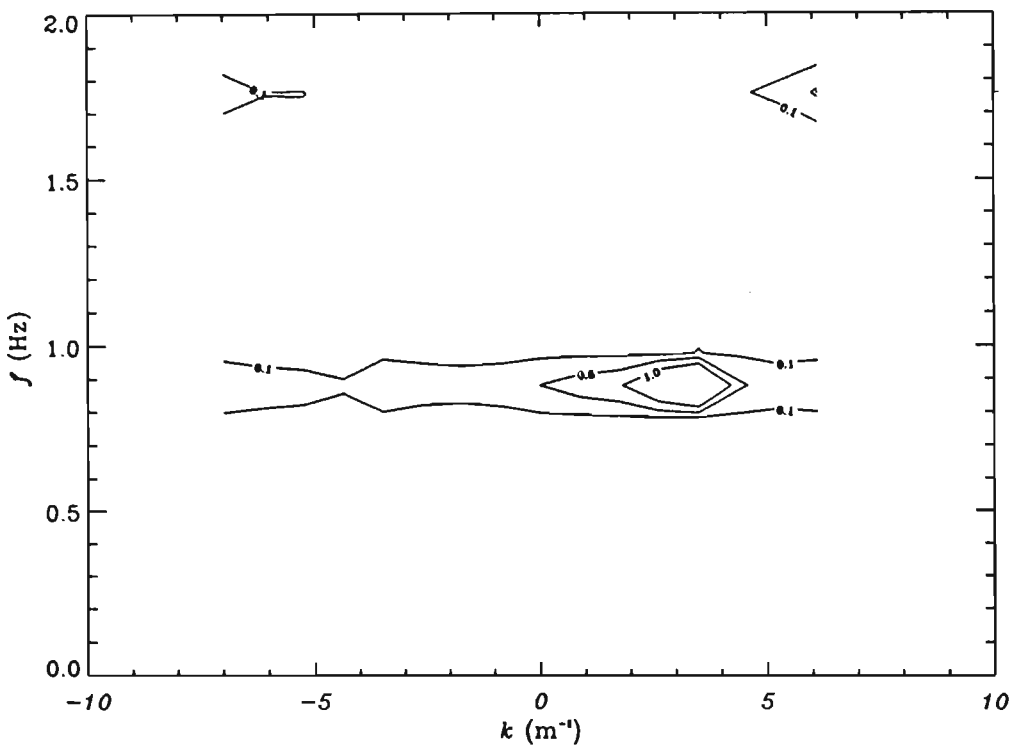

Figure 5.6: (a) Contour plot of the deep water frequency-wavenumber spectrum of a 0.9 hz wave having H_0=16 cm. Positive wavenumber corresponds to waves moving away from the generator.

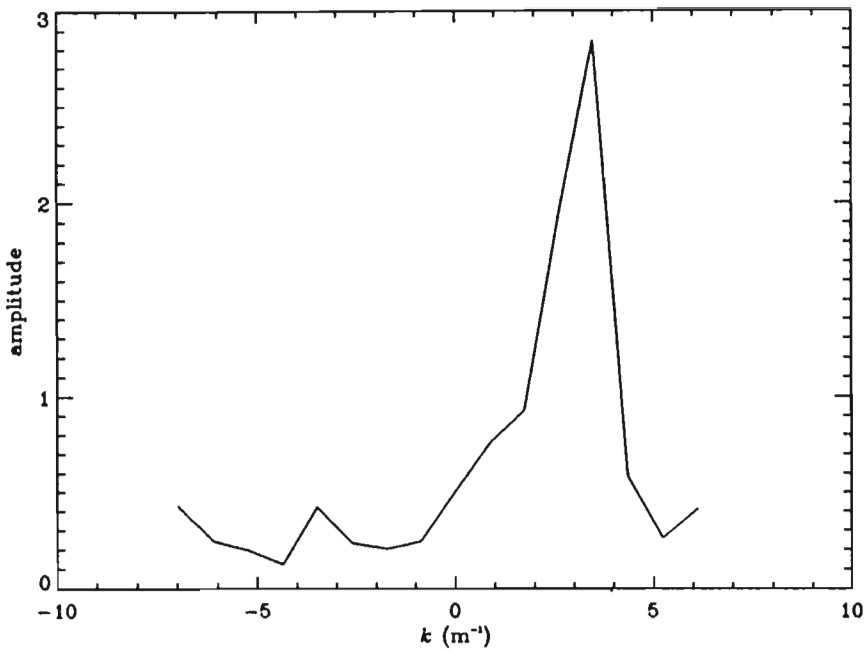

Figure 5.6 cont.:(b) Amplitude-wavenumber spectrum of the spilling wave at the fundamental frequency, corresponding to a horizontal slice of the contour plot at f=0.9 Hz in Figure 5.6(a).

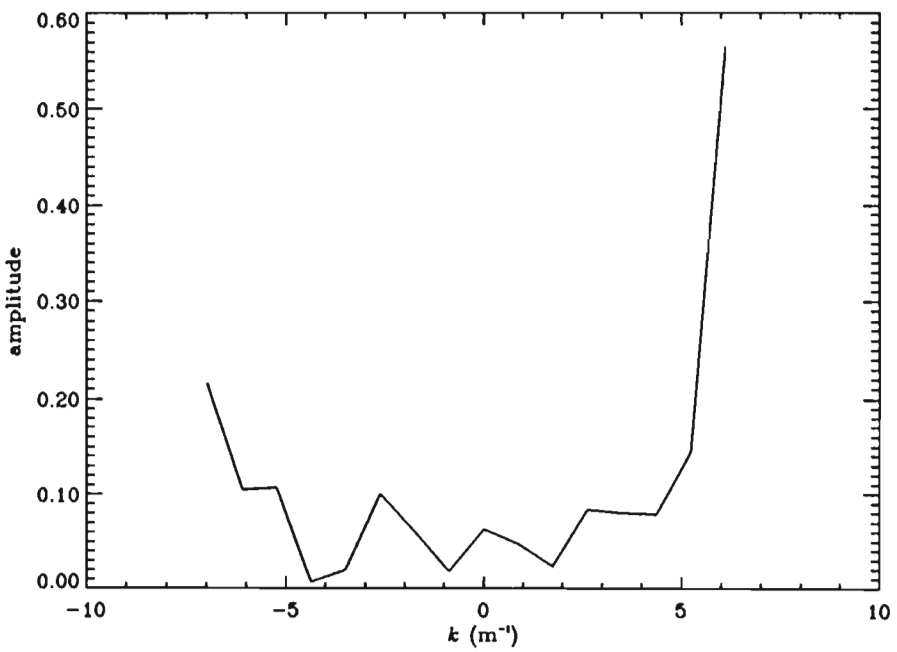

Figure 5.6 cont.:(c) Amplitude-wavenumber spectrum of the spilling wave at the 2nd harmonic frequency, corresponding to a horizontal slice of the contour plot at f=1.8 Hz in Figure 5.6(a).

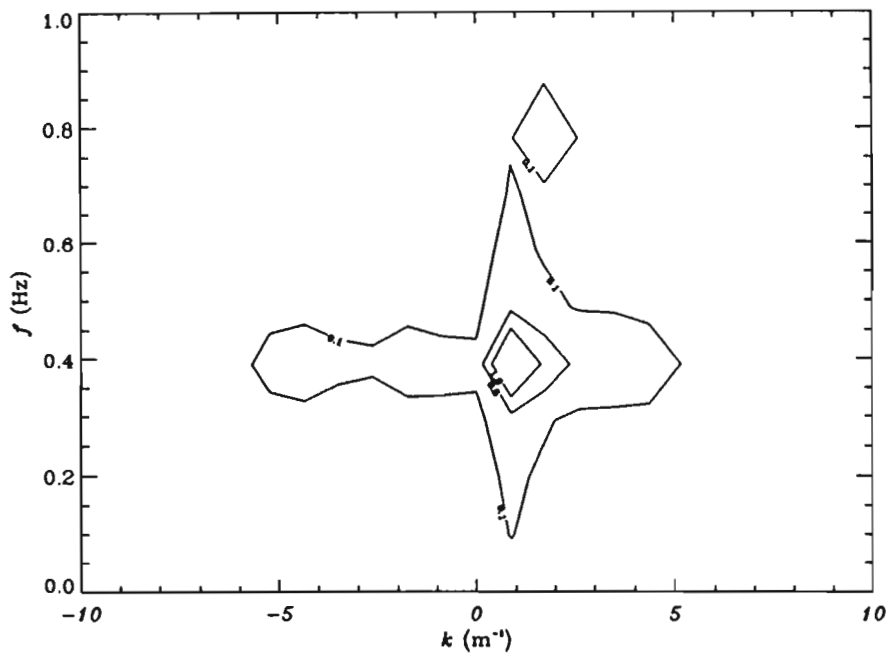

Figure 5.7: (a) Contour plot of the deep water frequency-wavenumber spectrum of a 0.4 Hz plunging wave having H_0=11 cm.

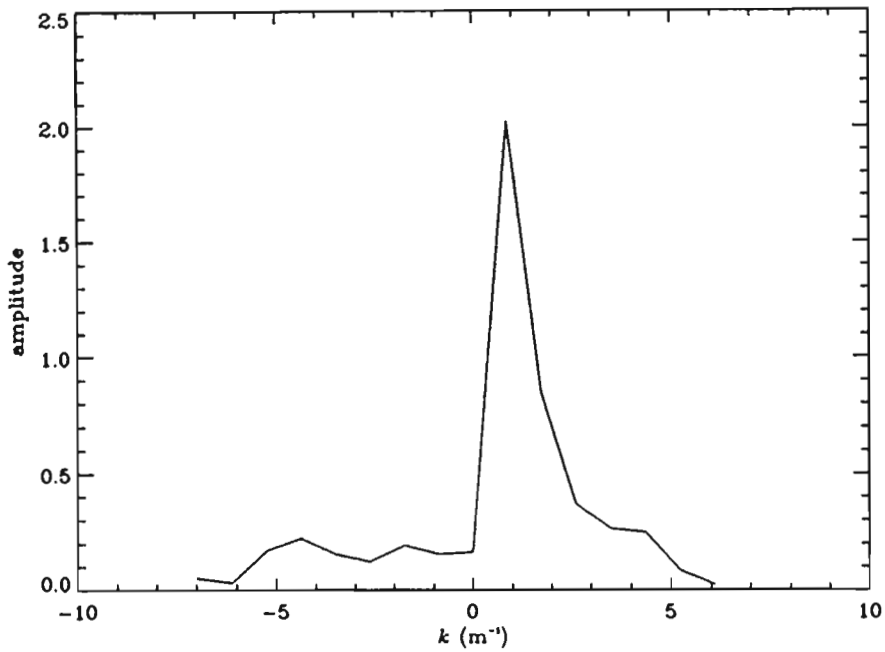

Figure 5.7 cont.: (b) Amplitude-wavenumber spectrum of the fundamental component for the plunging wave.

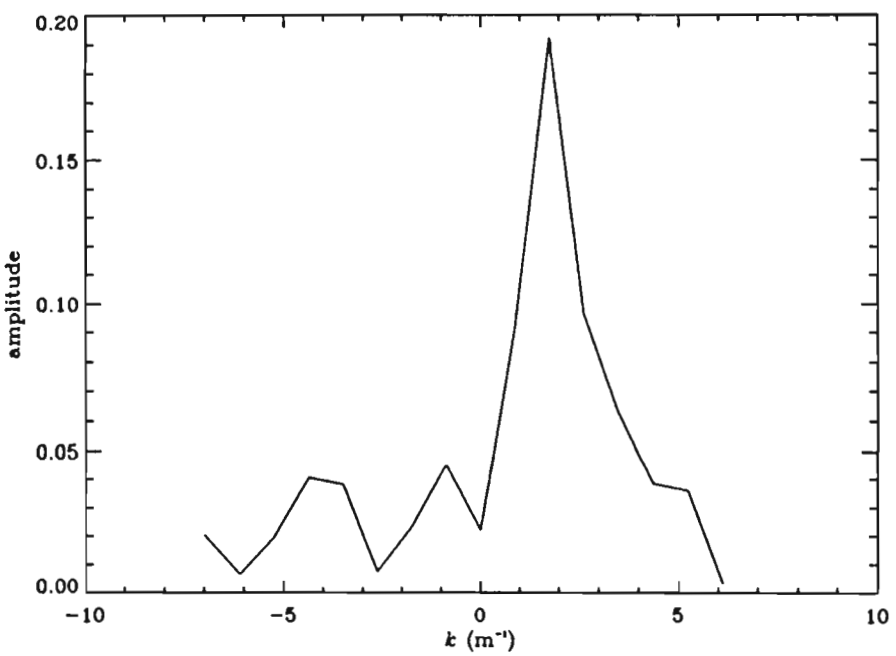

Figure 5.7 cont.: (c) Amplitude-wavenumber spectrum of the 2nd harmonic component for the plunging wave.

5.5 Water level measurements

The time series of water levels were measured at stations approximately 0.1 m apart over the experimental section of the flume. This spans the pre-breaking stages of the wave and the surf zone. Measurements were accomplished using the keogram method with a sampling time of 40 ms, corresponding to the video frame update rate. A selection of time series, showing the evolution of the wave profile as the wave approaches breaking and propagates into the surf zone, is presented below. The mean wave height and water level are derived from the time series of the water level. Figure 5.8 shows the time series of the spilling wave at 7.16 m, 5.83 m and 4.18 m from the still water mark on the beach. Wave breaking occurs at a position 4.50 m from the beach, while Figure 5.9 shows the time series of the plunging wave at 6.20 m, 3.99 m and 2.49 m from the still water mark on beach. Wave breaking in this case occurs at a position 3.25 m from the beach.

The variation of the wave height and mean water level as a function of position along the flume for a 0.9 Hz spilling and a 0.4 Hz plunging wave cases are shown in Figures 5.10 and 5.11, respectively. These figures show an increase in wave height up to the break point and then an almost linear decay in the surf zone. The mean water level was estimated by computing the average value of the time series of waterlevel at each position along the flume. This is represented by (*) in Figures 5.10(b) and 5.11(b). In the surf zone the mean water level, as computed above, has a lower contribution to the hydrostatic pressure due to aeration. The contribution of the aerated area to the mean water level should therefore be weighted accordingly. A possible correction involves subtracting from the mean water level $\overline{\eta}$, computed as above, a fraction that is proportional to the roller/aerated area, A_r, as follows:

$$\overline{\eta}'(x) = \overline{\eta}(x) - \alpha \frac{A_r(x)}{T}$$

A_r is measured, in cm-s, from the keograms of the waterlevels and T is the wave period. The procedure of estimating the roller/aerated area is discussed in the next section. α is an empirical constant chosen such that the corrected mean water level in the surf zone meets the mean water level at the breakpoint and in the upper end of the surf zone, where there is very little aeration, without a distinct discontinuity. A value of approximately 0.4 and 0.8 was

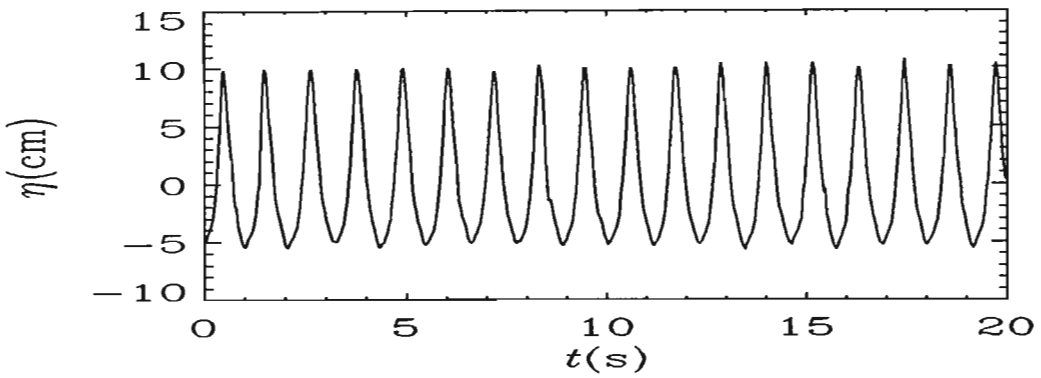

(a)

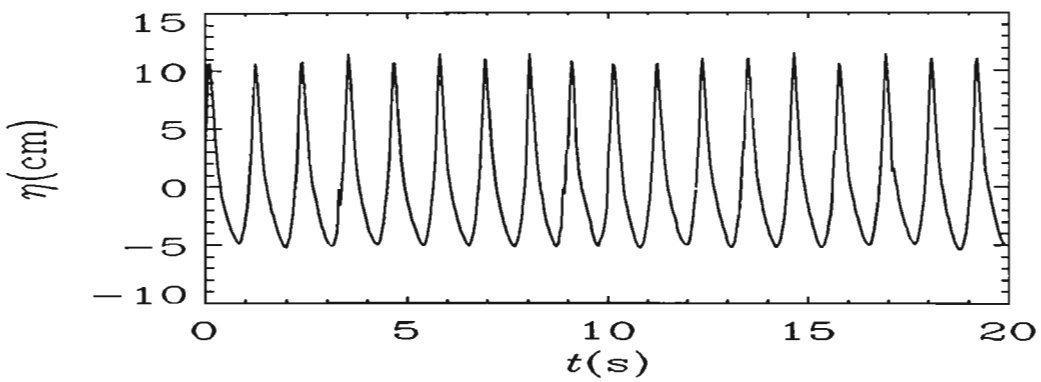

(b)

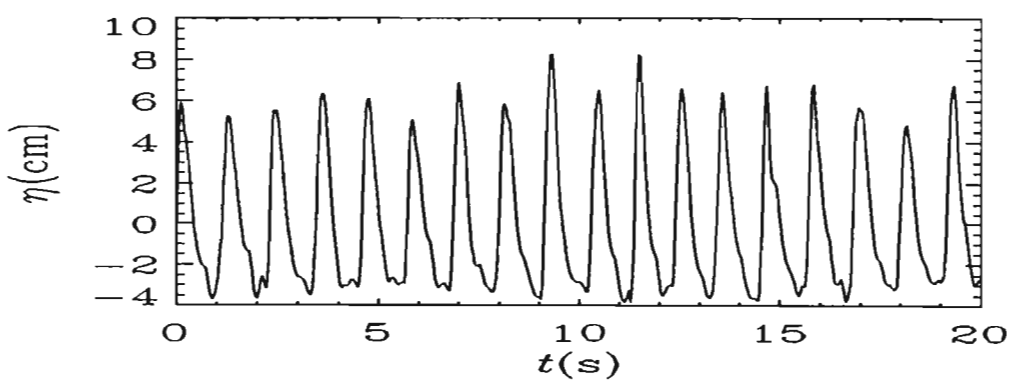

(c)

Figure 5.8: Time series of the surface position in the presence of a 0.9 Hz spilling wave at (a) 7.16 m, (b) 5.83 m and (c) 4.18 m from the beach.

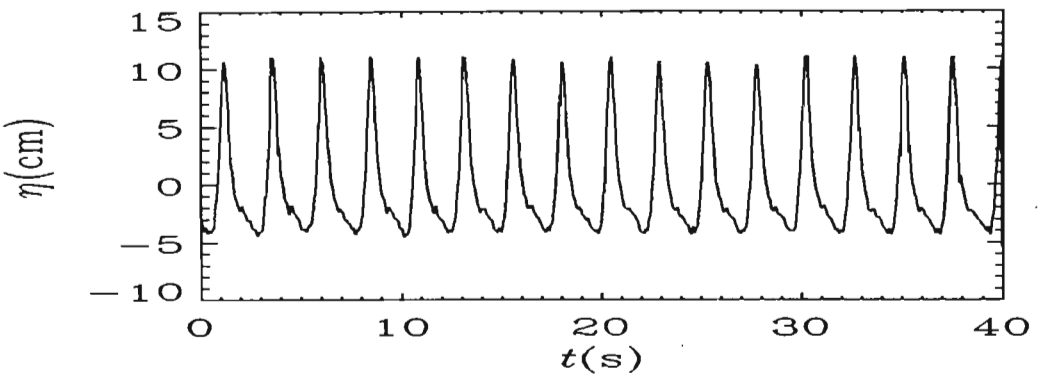

(a)

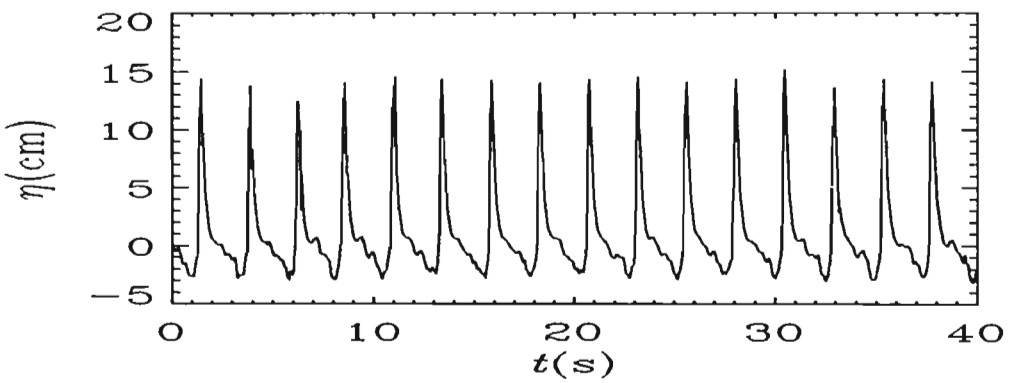

(b)

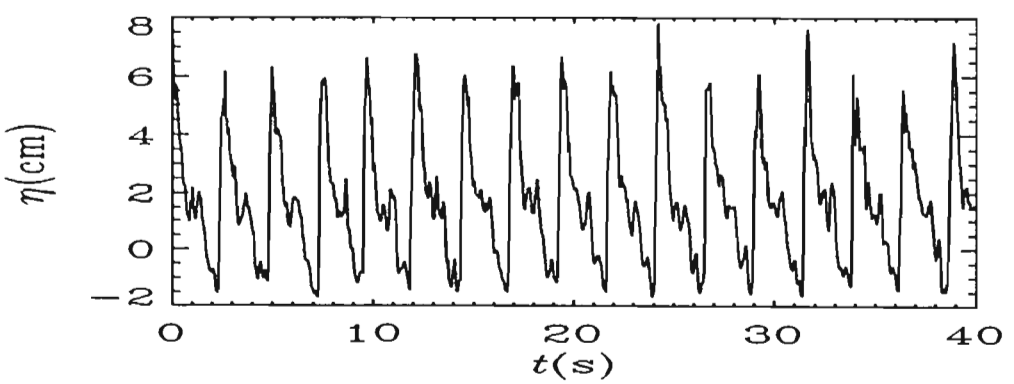

Figure 5.9: Time series of the surface position in the presence of a 0.4 Hz plunging wave at (a) 6.20 m, (b) 3.99 m and (c) 2.49 m from the beach.

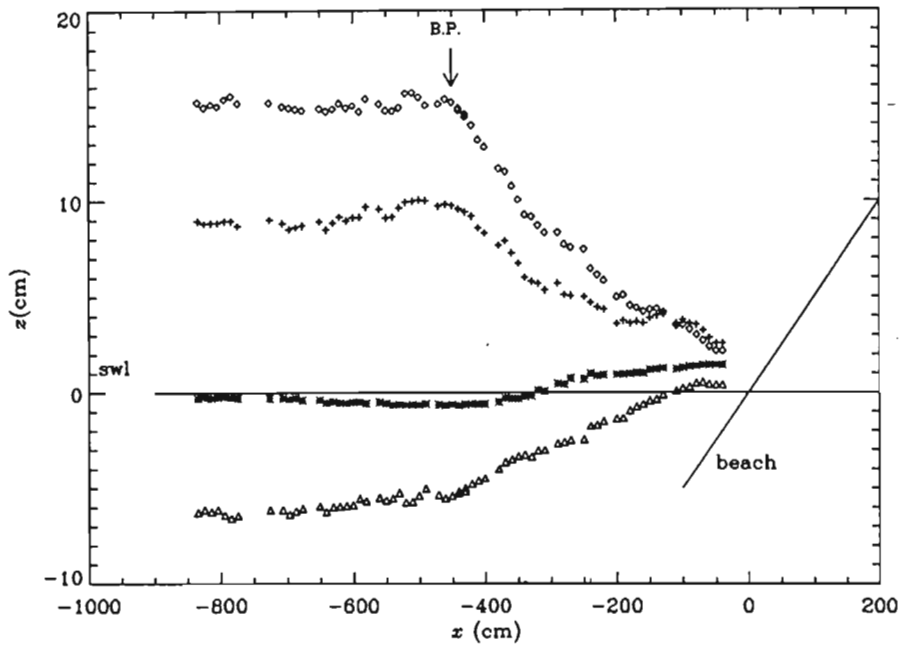

Figure 5.10: (a) Crest level(+), trough level(△), wave height(◇) and mean water level(*) as a function of distance from the beach, for a 0.9 Hz spilling wave. The position of the still water line and the beach is also shown.

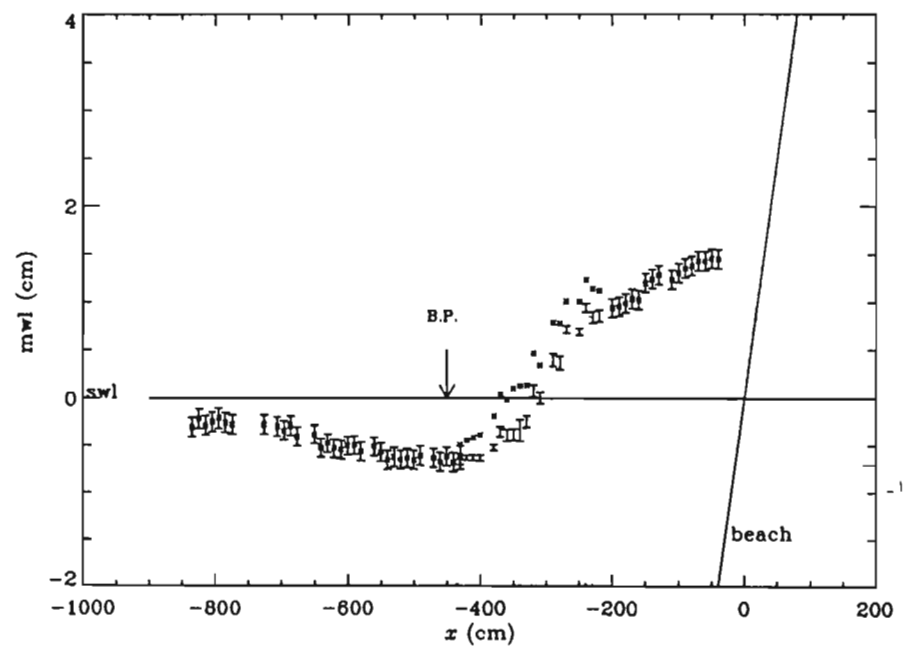

Figure 5.10: (b) Mean water level along the flume for the 0.9 Hz spilling wave. The mean level including any aeration is represented by * and the mean level, without the contribution by aeration, is shown using error bars.

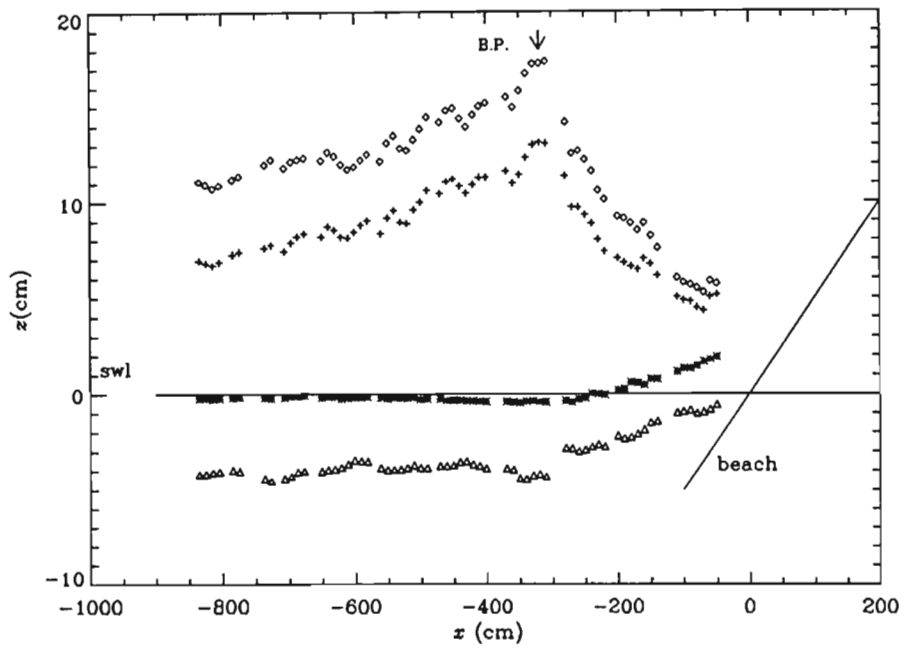

Figure 5.11: (a) Crest level(+), trough level(△), wave height(◇) and mean water level(*), as a function of distance from the beach, for a 0.4 Hz plunging wave. The position of the still water line and the beach is also shown.

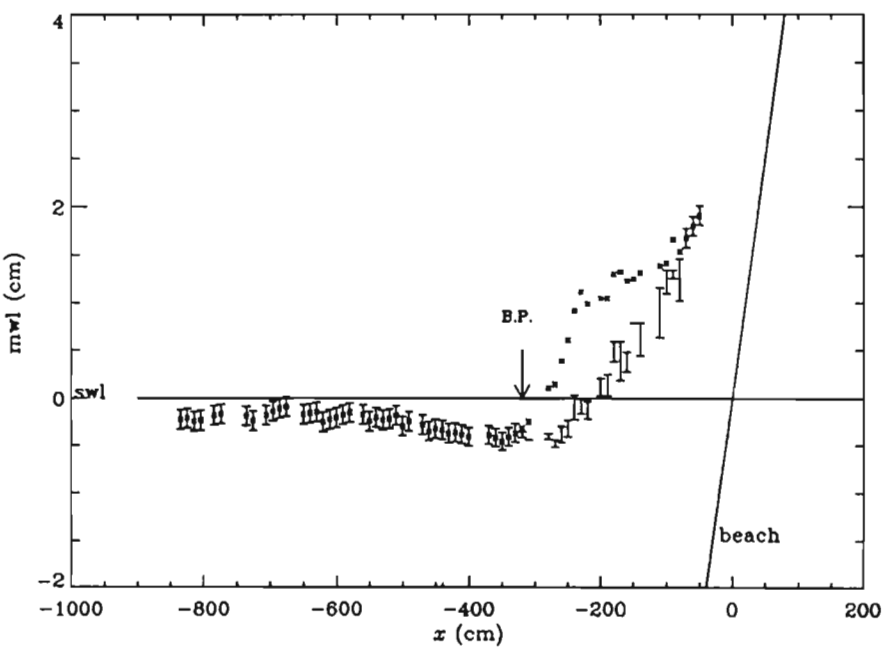

Figure 5.11: (b) Mean water level along the flume for the 0.4 Hz plunging wave. The mean level including any aeration is represented by * and the mean level, without the contribution of aeration is shown using error bars.

found suitable for the spilling and plunging case, respectively. These values are in fact closely linked to the mean density in the wave crests in both cases. The mean relative density in the crests of spilling waves is shown in Chapter 6 to be $\approx$ 0.7 throughout the surf zone. The corrected mean water levels are shown as error bars in Figures 5.10(b) and 5.11(b). The error bars indicate uncertainty in the measurement of the roller area and in the location of the still water line reference used in extracting the time series of the waterlevels from the keograms.

5.6 Aeration/roller area and slope measurements

The models of wave height decay(e.g. *Svendsen, 1984*), and the Boussinesq equations (e.g. *Schaffer et al, 1993*) for wave propagation in the surf zone, incorporate an energy dissipation term, $D_r=\beta\rho gA/T$, which is proportional to the area, A, of the highly aerated region in the crest of the wave. Most of the wave energy is transformed into turbulent kinetic energy in this region. Near the breakpoint, the dissipative region consists mostly of the roller formed as a result of wave breaking. It forms a body of fluid riding on the front face of the wave and moving with a speed equal to the wave celerity. Further into the surf zone, the dissipative region consists of the roller plus a portion of the wave adjacent to the front face of the wave. There is complete mixing of the roller and the portion of the wave adjacent to the front face of the wave and identification of these two regions is not possible. In the Boussinesq modelling, the roller area is estimated by *Schaffer et al.(1992)* to be that body of fluid above the 20° sloped line. The 20° sloped line is defined to be a line beginning at the toe of the wave-front and extending upwards to the crest at an angle of 20° with respect to the horizontal. *Svendsen(1984)* estimated the roller area, using the experimental measurements of wave breaking behind a towed hydrofoil by *Duncan(1981)*, to be $A=0.9H^2$. As stated by *Fredsoe & Deigaard(1992)*, no other formal measurements of the aeration area of waves in the surf zone have been published. An attempt, therefore, is made at measuring the aeration area and roller slope for the wave cases under study.

The aeration area and wave slope were estimated from the keograms used in the water level measurements. A phase-averaged keogram was generated from each keogram. A selection of these is shown in Figures 5.12 and 5.13 for the spilling and plunging case respectively. Near the breakpoint, the white aerated region of the wave is concentrated mainly at the front

face of the wave and is due mostly to the roller. Further away from the breakpoint the aeration tends to spread over a greater region below the crest.

Visual and numerical analysis of the grey-scale intensity of the keograms indicate that in the aerated area high grey-scale intensities occur and throughout this region the intensity is almost constant. Immediately outside the aerated area the intensity decreases rapidly to a small value. This transition is used to demarcate the inner boundary of the roller or aeration area and a grey scale threshold is used to form a contour identifying this boundary. The actual relationship between the percentage aeration and the grey scale intensity is not important since we are using a threshold to determine the roller area. Figures 5.14 and 5.15 show a number of such contours at grey scale values of 250, 245, 240, 235 and 225. The normalised aeration area has been calculated from these figures with the minimum and maximum values of the error bars being determined by the corresponding minimum and maximum values of the intensities contours.

The contour closest to the wave-front in Figures 5.14 and 5.15 corresponds to the minimum aeration and the contour furthest away from the wave-front correspond to the maximum estimate of aeration. The horizontal axis of the phase-averaged keograms at each position has been scaled to have units of length and the resulting aeration area is thereafter normalised with respect the square of the local wave height. The minimum and maximum aeration areas have been estimated for a number of positions in the surf zone for the spilling and plunging waves, and these are plotted in Figures 5.16 and 5.17, respectively. The normalised aeration area for the spilling case spans a range of 0.5 to 1.5. The measurement for the spilling wave is almost evenly distributed about the $A_r/H^2=0.9$ line. Close to the breakpoint the aeration is approximately 0.5, thereafter the aeration has a mean of approximately 1. The normalised aeration for the plunging case shows an increasing trend and is greater than 0.9 for the major part of the surf zone.

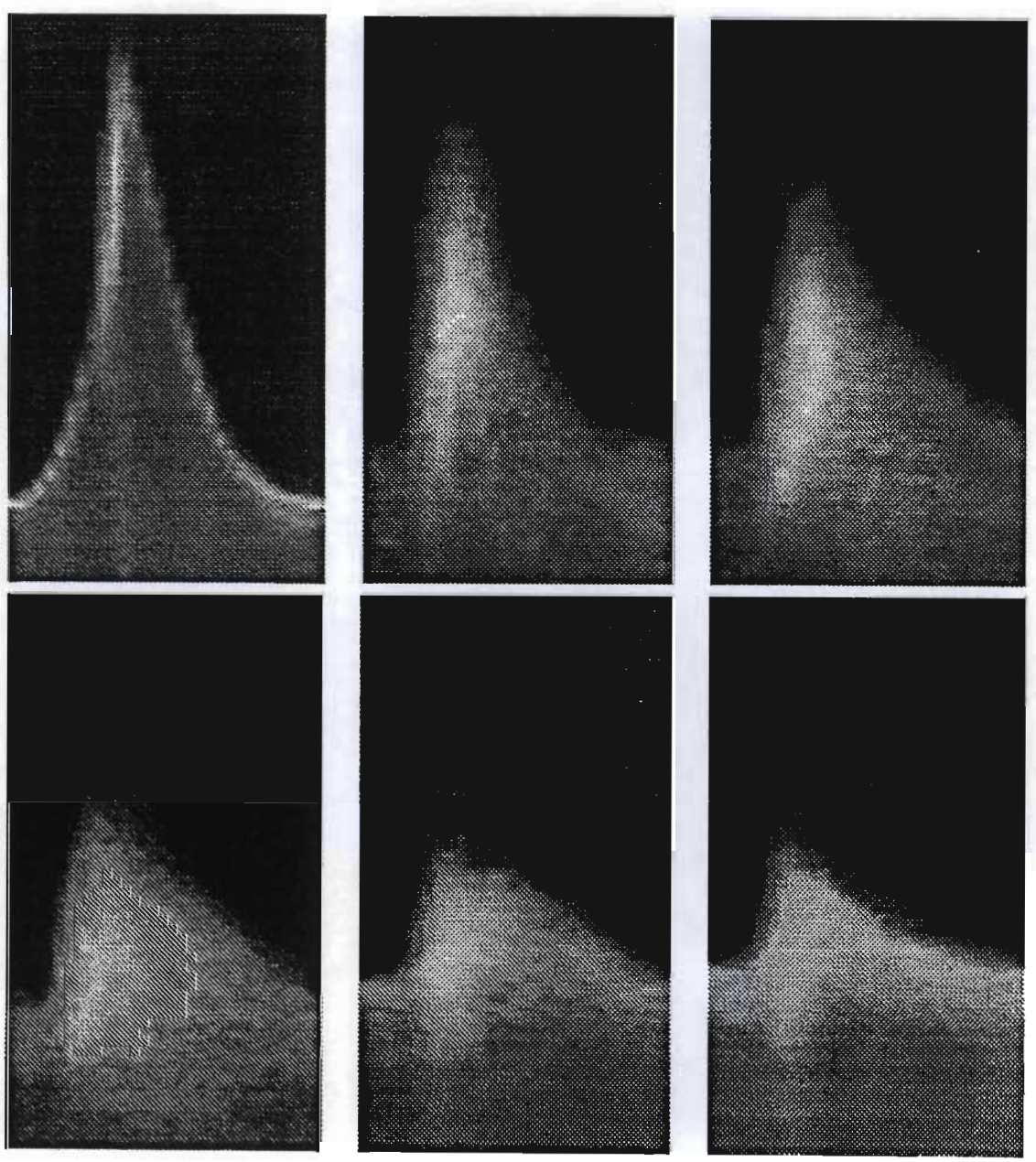

Figure 5.12: Phase ensemble-averaged keograms of the spilling wave (arranged in rows) at 0.39, 1.0, 1.5, 2.1, 2.7 and 3 m beyond the breakpoint. The aeration in these images correspond to pixels having a high(white) grey scale intensity.

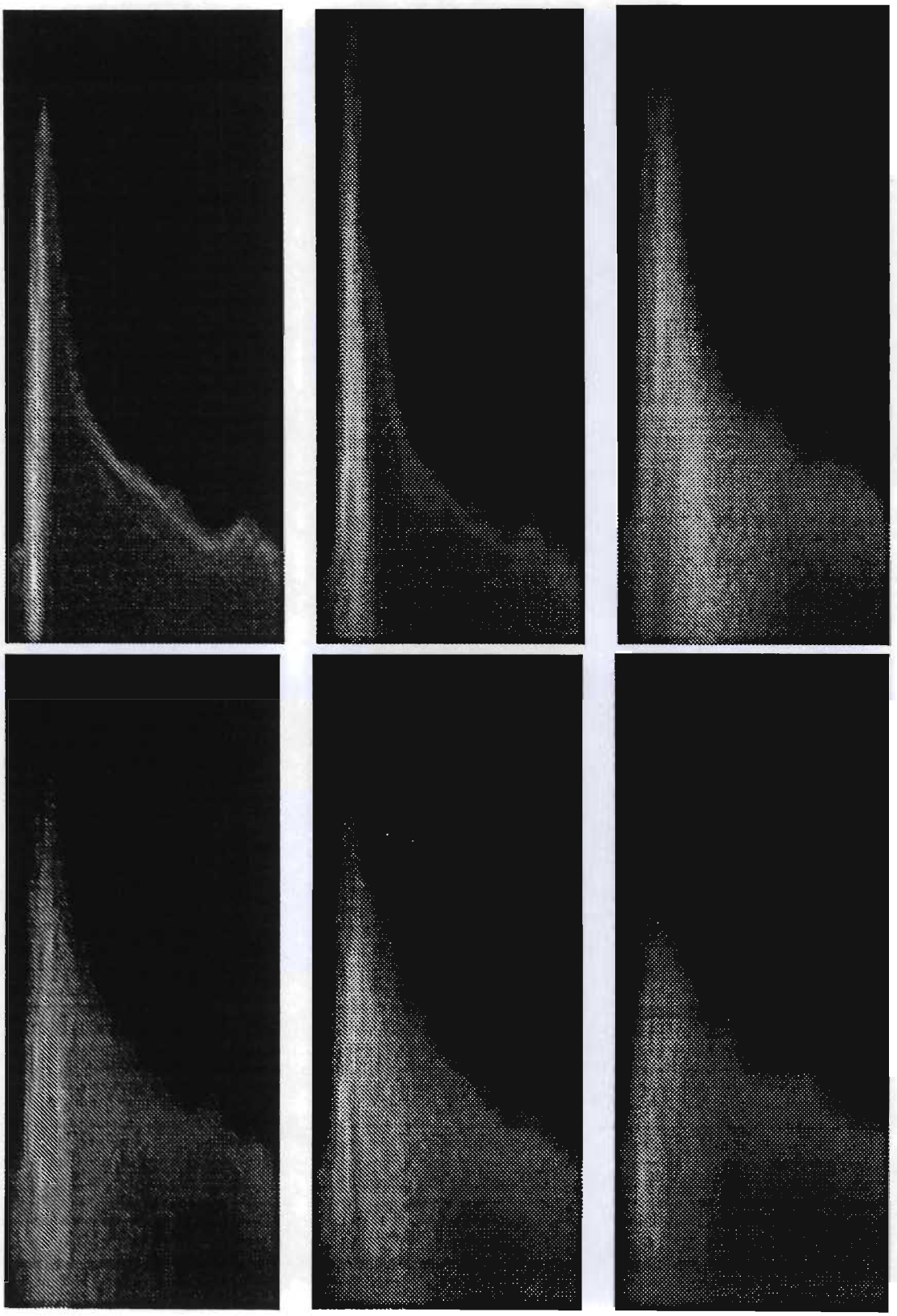

Figure 5.13: Phase ensemble-averaged keograms of the plunging wave (arranged in rows) at 0.4, 0.6, 0.9, 1.2, 1.5 and 2 m beyond the breakpoint. The aeration in these images correspond to pixels having a high(white) grey scale intensity.

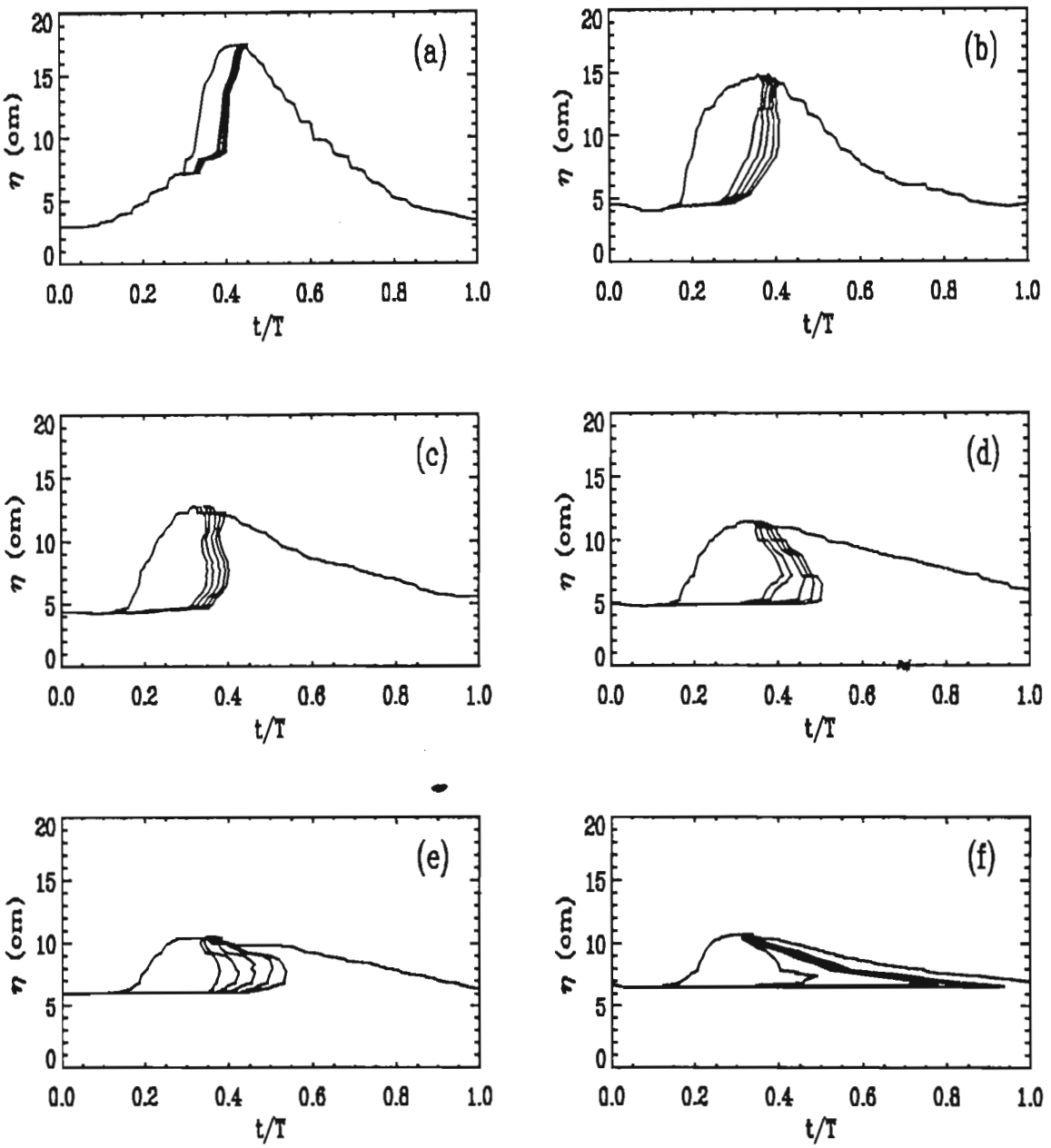

Figure 5.14: Aeration contours corresponding to different levels of grey scale intensity for the phase-averaged keograms of the spilling wave at (a) 0.39, (b) 1.00, (c) 1.50, (d) 2.10, (e) 2.70 and (f) 3.00 m beyond the breakpoint.

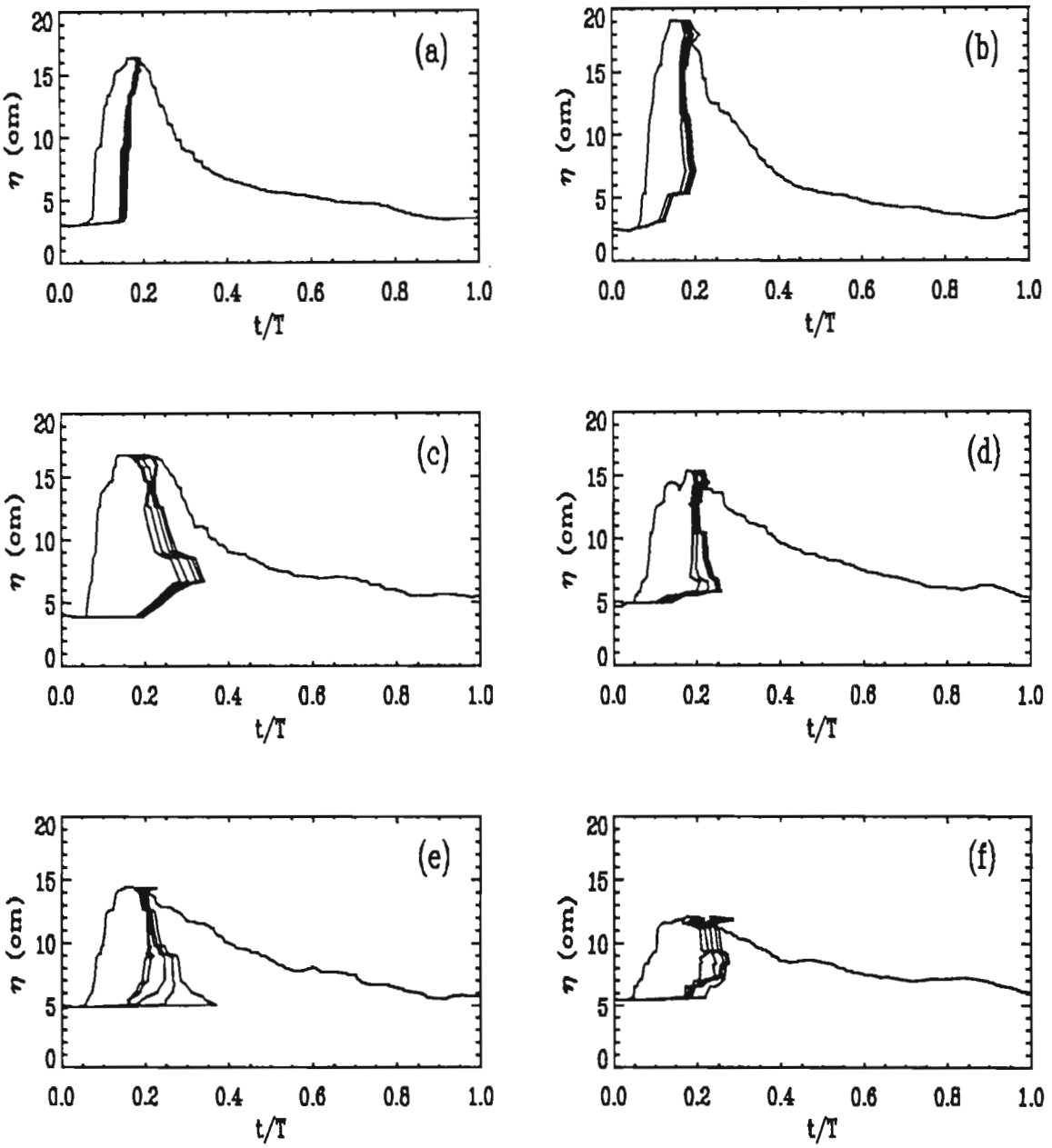

Figure 5.15: Aeration contours corresponding to different levels of grey scale intensity for the phase-averaged keograms of the plunging wave at (a) 0.40, (b) 0.60, (c) 0.90, (d) 1.20 (e) 1.50 and (f) 2.00 m beyond the breakpoint.

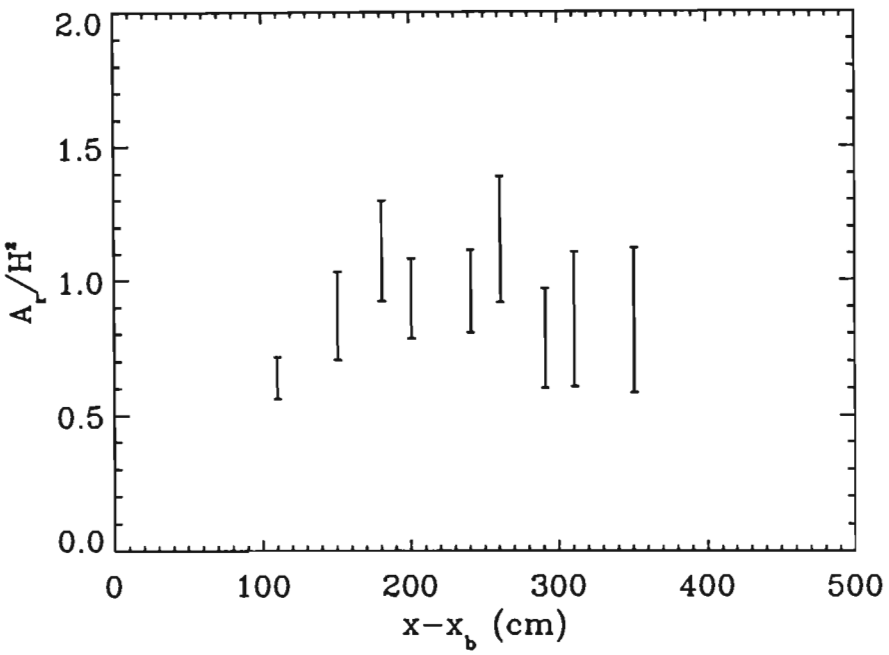

Figure 5.16: Normalised aeration area versus position along surf zone for the spilling wave. A_r is the aeration area, H is the local wave height and x_b is the break-point of the wave.

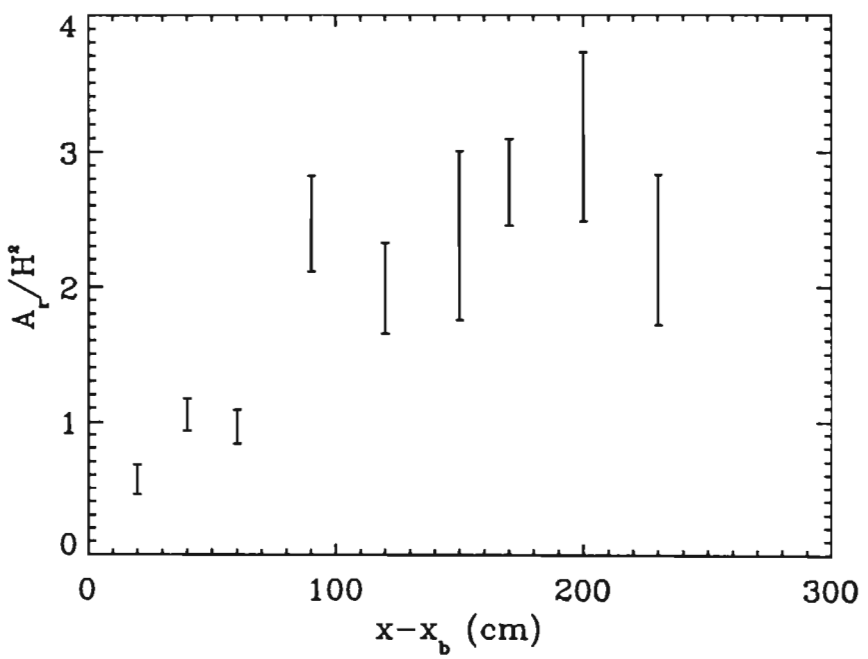

Figure 5.17: Normalised aeration area versus position along surf zone for the plunging wave. A_r is the aeration area, H is the local wave height and x_b is the plunge-point of the wave.

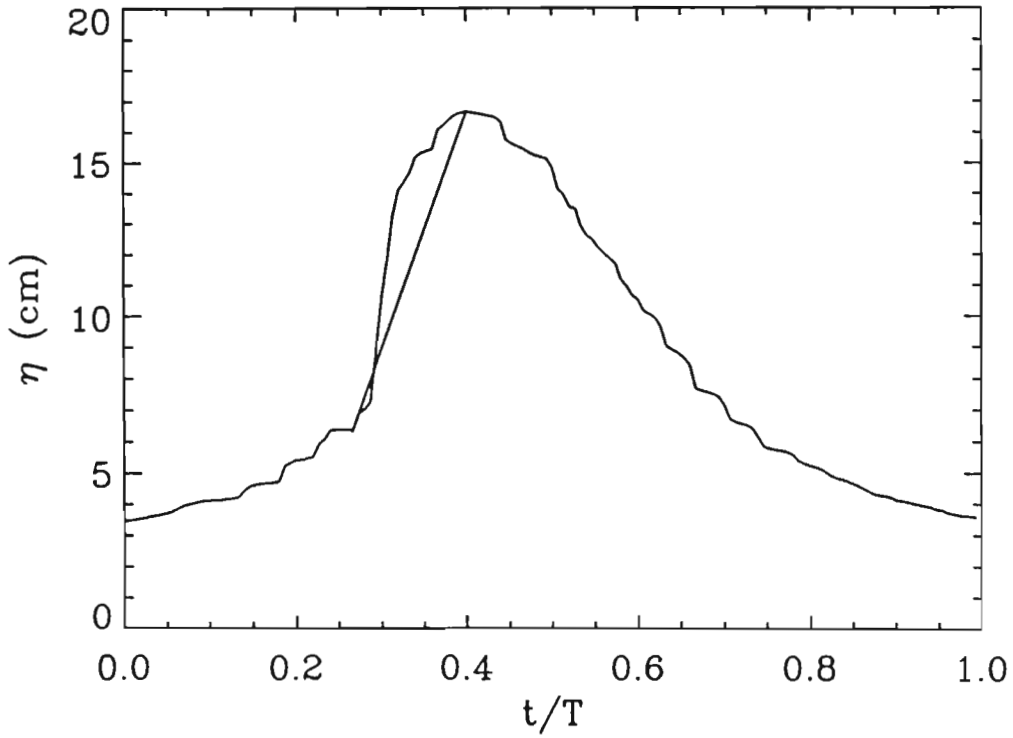

Figure 5.18: Plot indicating the measurement of wave slope.

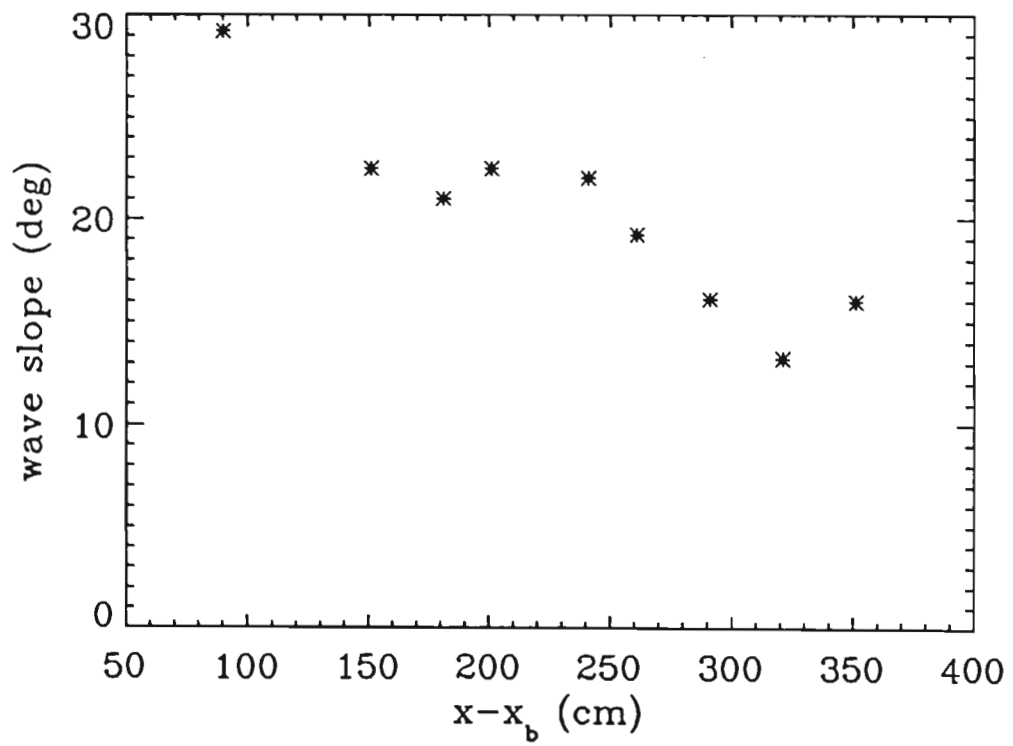

Figure 5.19: Wave slope versus position in surf zone for the 0.9 Hz spilling wave.

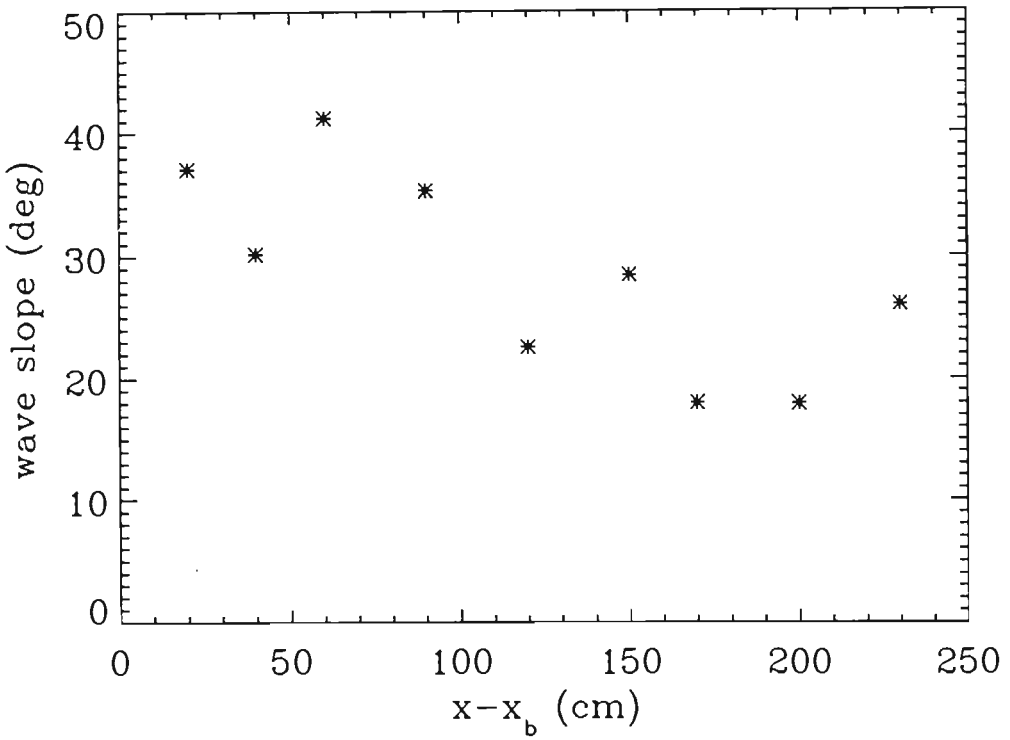

Figure 5.20: Wave slope versus position in surf zone for the 0.4 Hz plunging wave.

Figure 5.18 shows the measurement of the roller slope of the wave in the phase-averaged keogram shown in Figure 5.14(a). Figures 5.19 and 5.20 show the roller slopes for the spilling and plunging waves as a function of distance from the breakpoint. The wave slope for the spilling wave is approximately 30° near the breakpoint and decreases to around 15° further in the surf zone. The roller slope for the plunging wave is approximately 40° near the breakpoint and decreases to around 15° further in the surf zone.

5.7 Summary

The measurements of the wave height and mean water levels of spilling and plunging waves breaking in a laboratory surf zone have been accomplished via the measurement of the time series of the water level using the keogram concept. Comparison of the time series with those obtained using wave gauges showed similar results for wave in the non -breaking region of the flume. In the surf zone the video technique showed greater variation in the crest of the wave, while the wave gauges showed almost constant wave heights. The video technique has been shown to provide high spatial resolution measurements of water levels along the length of the flume with relative ease. Measurement of the water level are available at intervals of

approximately 0.100 m along the surf zone.

The frequency- wavenumber spectrum of waves in the deep water end of the flume was also measured, using an array of virtual probes. The frequency-wavenumber measurements were used to determine the fraction of free harmonics and reflected waves and it was shown that the free harmonics and reflected waves were less than than the bound forward propagating components by at least a factor of 4.

The wave roller area was measured, using the video technique, by identifying the aerated area, which appears white in the images. This may seem to be subjective, since the air bubbles are buoyant. This method, however, has the advantage that the estimated roller area can be checked by visual inspection. Also, since there is a constant supply of air bubbles into the roller, as a result of wave breaking, the shape of the roller area is maintained irrespective of the buoyancy of the air bubbles. The normalised roller area for the spilling wave is similar to that estimated by *Svendsen(1984)*, being approximately 0.9. The normalised roller area for the plunging wave, however shows an increasing trend in the surf zone.

CHAPTER 6

VELOCITY FLOW FIELD MEASUREMENTS AND ANALYSIS OF SPILLING AND PLUNGING WAVES IN A LABORATORY SURF ZONE

In this chapter we report on the measurements of the velocity flow fields at three positions in the surf zone for both a spilling and a plunging wave. The velocities were measured using digital correlation image velocimetry (DCIV). The mean and turbulent velocity components are extracted through a process of phase ensemble-averaging. A sensitivity analysis is performed on the velocity data to determine the influence of the number of samples and bin sizes on the convergence of the mean and turbulent components. The undertow velocity is also computed from the phase ensemble-averaged flow fields.

6.1 Introduction

Measurement of the velocity flow field of waves in the surf zone is an integral part of modelling the wave height decay and the energy dissipation in the surf zone. Knowledge of the fluid velocities in the surf zone is also crucial in the study of sediment dynamics. The velocity of a particle or an infinitesimal fluid element which is subject to the action of a breaking wave is composed of a time-averaged component, a component due to the orbital motion of the waves and a turbulent or fluctuating component. The turbulent component is responsible for the transport of energy from the wave to the sediment, resulting in sediment suspension, and the time-averaged component is responsible for the movement of sediment from one location to another.

Measurements of the velocity flow fields of spilling and plunging waves were conducted in the surf zone of a two dimensional wave flume, initially using digital particle image velocimetry (DPIV) and later using digital correlation image velocimetry (DCIV). The bulk of the measurements presented here have been obtained using DCIV. A cross comparison of PIV and DCIV measurements is provided for the spilling case at one position in the surf zone. The experimental conditions and procedure are described. The phase ensemble-averaged velocity fieid, at three positions in the surf zone, is provided for spilling and plunging waves. The time-average of the horizontal velocity as a function of height above the bed, derived from the phase-ensemble-averaged flow, is also provided.

A sensitivity analysis of velocity data is conducted to determine the influence of sample size and bin size on the convergence of the mean and turbulent velocities. It is shown that there is sufficient number of samples per bin and that the bin size is small enough to provide true turbulence measurements.

6.2 Experimental conditions and procedures

Figure 6.1 shows a schematic of the flume indicating dimensions and measurement positions. Measurements were restricted to the upper end of the beach, referred to as the experimental section in Figure 6.1. Velocity measurements were conducted for the spilling and plunging wave cases used in the waterlevel measurements which were presented in Chapter 5. The velocity flow field for the spilling wave was measured at stations 1, 2 and 3, and the flow field of the plunging wave was measured at stations 1, 3 and 4. Table 1 and 2 summarises the characteristics of the spilling and plunging waves used in the experiments at their respective measurement positions.

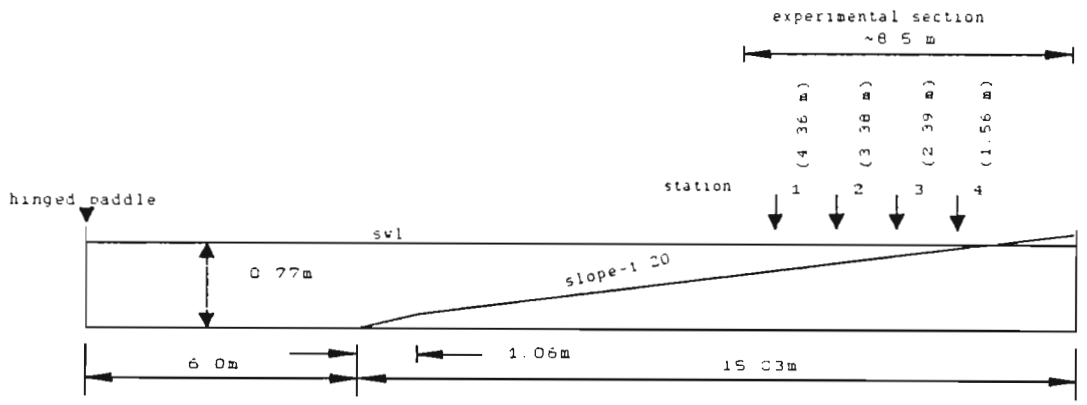

Figure 6.1: Dimensions of the flume and measurement positions. Flow field measurements were conducted at 4.36 m, 3.38 m, 2.39 m and 1.56 m from the still water mark on the beach, corresponding to stations 1-4, respectively.

Table 6.1: Spilling wave characteristics

$(x\text{-}x_b)$ (m)	H_0 (m)	T (s)	h_b (m)	H (m)	d (m)	h (m)	H/h
(station 1) 0.024	0.16	1.11	0.218	0.15	0.218	0.211	0.71
(station 2) 1.22				0.11	0.169	0.166	0.66
(station 3) 2.21				0.065	0.119	0.129	0.51

H_0 is the deep water wave height, T is the wave period, H and h are the local wave height and mean water depth, respectively, h_b is the mean water depth at the breakpoint and $(x\text{-}x_b)$ is the distance beyond the breakpoint.

Table 6.2: Plunging wave characteristics

$(x\text{-}x_b)$ (m)	H_0 (m)	T (s)	h_b (m)	H (m)	d (m)	h (m)	H/h
(station 1) -1.11	0.11	2.5	0.156	0.15	0.218	0.215	0.69
(station 3) 0.86				0.115	0.119	0.118	0.97
(station 4) 1.69				0.078	0.078	0.084	0.93

The velocity vector field of the wave was measured using two methods, viz, DPIV and DCIV. Initial measurements were accomplished using digital particle image velocitmetry and results for the spilling wave case will be presented here for comparison with DCIV measurements. More recently digital correlation image velocimetry was used as the predominant method of flow measurement. DCIV, as described in Chapter 4, offers the capability of measuring the flow field well into the aerated region of the wave, a feature that is not easily achieved using the standard DPIV. This is achieved by tracking the structure created by the air bubbles during wave-breaking. DCIV is also a more robust algorithm that allows greater automation.

Three different sampling times, of nominal values 1, 5 and 9 ms, were used to measure each flow field. The small sampling time is necessary to measure the very large velocities

occurring in the crests of the breaking waves, and the longer sampling times are used to measure the smaller particle velocities.

The procedure used to measure the velocity flow field in the wave is illustrated in Figure 6.2. The camera is capable of imaging only a 30 cm section of the wave. To construct the flow field over the entire wavelength, it is necessary to make a series of measurements at different wave phases and appropriately concatenate the measurements. It is necessary to make a number of measurements of the instantaneous velocity flow field at each section of the wave in order to estimate turbulence parameters. The mean, turbulent and Reynolds stress field is then computed by phase-ensemble averaging.

The spilling wave was imaged at 10 equally spaced wave phases and the plunging wave at 12 equally spaced wave phases. Fifty image pairs are captured at each wave phase using sampling intervals of 1, 5 and 10 ms. One image pair is obtained from a single wave cycle, and this results in a total of 150 image pairs per phase position.

The analysis of the images was performed off-line. Each image pair results in an instantaneous velocity flow field of the section of the wave, giving 150 instantaneous flow fields at each wave phase. These 150 images are then processed to yield the phase ensemble-averaged mean velocity, turbulence intensity or rms velocity and Reynolds stress fields. This analysis was repeated for the images at the other wave phases.

Finally the flow fields of the individual sections were combined to yield the flow field over the entire wave. The flow field of each section of the wave consists of velocity samples at intervals of approximately 0.25 cm and is thus a high spatial resolution measurement of the flow field. For presentation purposes, the velocity flow fields and contour plots are drawn using only two vertical slices of each high resolution section. Thus the flow fields of the spilling and plunging waves presented here, consists of measurements at 20 and 24 phase positions. However, the time averaged quantities such as velocity undertow, turbulent intensities and kinetic energy, and Reynolds stress are computed using the high resolution fields of each section.

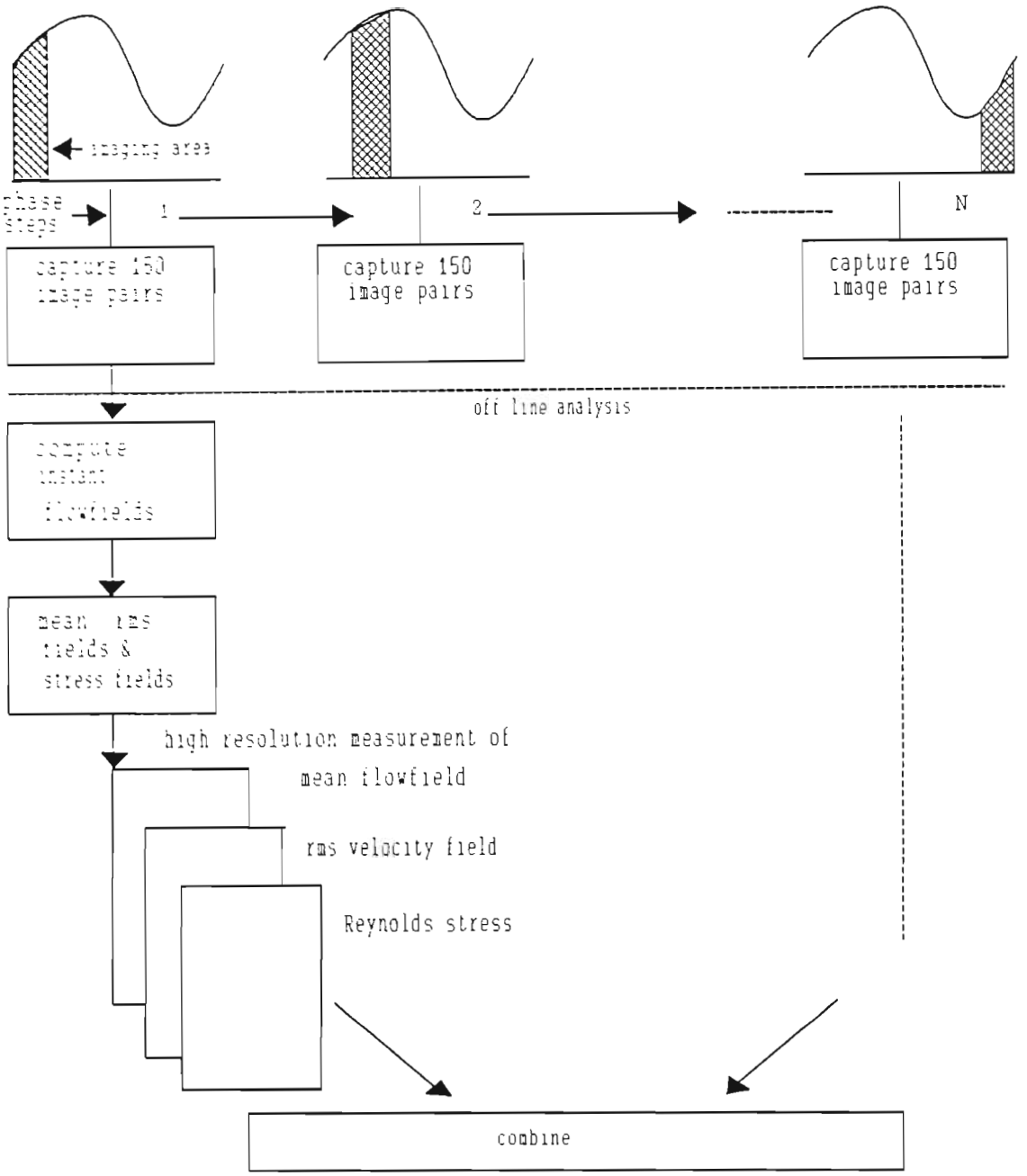

Figure 6.2: Instantaneous velocity fields are measured for a section of the wave (cross hatched area) using 150 image pairs, corresponding to 150 wave cycles. Phase ensemble averaged mean and turbulent velocities, and Reynolds stress are computed.

6.3 Calibration

It is necessary to quantify and calibrate certain parameters, viz, spatial distances and sampling times. Spatial distances in the video images were calibrated using a board, containing grid lines, that is placed in the object plane of the camera. Sampling times were measured indirectly by measuring the velocity vector field of marked positions on a rotating disk having a known angular velocity.

The velocities obtained using the video techniques are in units of pixel/second. These units are retained throughout all computations and are converted to cm/s at the very end. The conversion from pixel to real object distances was carried out using the following procedure: A calibration board, containing horizontal and vertical grid lines spaced 5 cm apart, was placed in line with the light sheet at each measurement position. A video image of this board was captured and stored. A conversion factor was then obtained by examining the pixel spacing of the grid lines in the calibration image. The calibration board was removed prior to any velocity measurements.

The quantification or verification of the sampling times was achieved by measuring the velocity of points on a rotating disk, containing randomly distributed white dots on a black background. The angular velocity of the disk was calculated by measuring the time for one revolution, using a slotted optical switch. The disk contained a slot on its circumference and each time it passed the optical switch, it allowed light from a source to impinge onto a detector, so generating a pulse that could be observed on an oscilloscope. The time to complete a revolution was thus the time between consecutive pulses.

Figure 6.3 shows the radial profile of the velocity vector field of the disk, computed using DCIV with a sampling interval of 1.08 ms. The expected radial profile of the velocity vector, computed using the measured angular velocity is also shown. It can be seen that the velocity profile measured using DCIV is consistent with expected velocities computed using the angular velocity, with an error between them of less than 2%.

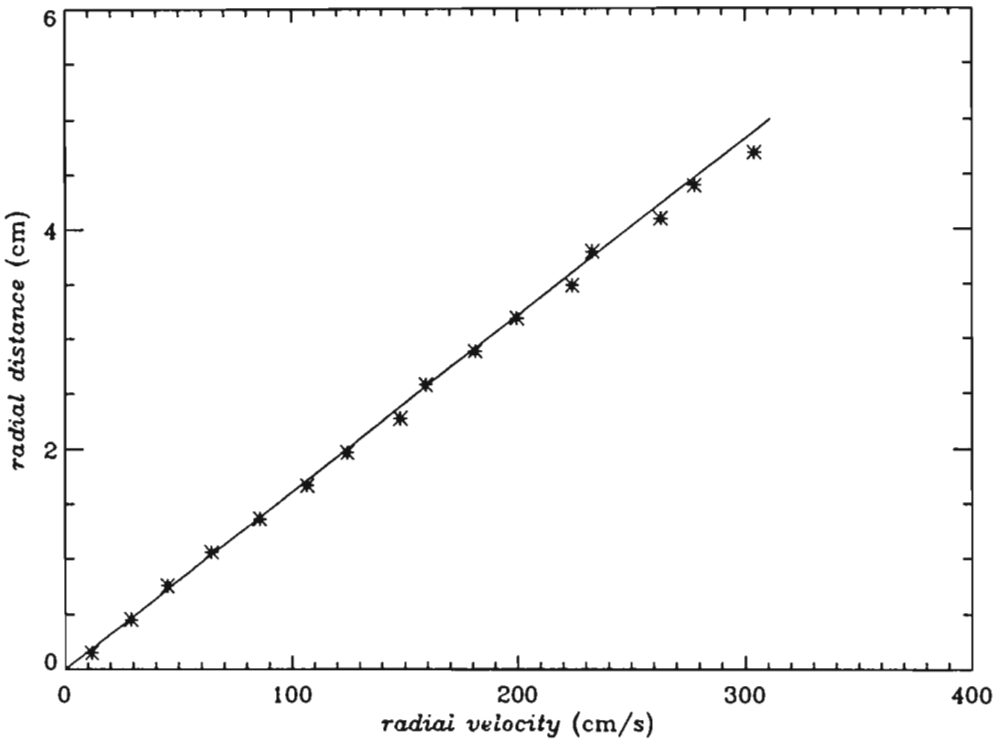

Figure 6.3: Radial profile of the velocity vector of points on a rotating disk, computed using the measured angular velocity(solid line), and DCIV(*) with a sampling interval of 1.08 ms.

6.4 Velocity measurements in the spilling wave

6.4.1 Phase ensemble-averaged velocity field in the spilling wave.

In the study of turbulent processes one is usually interested in ensemble averaged quantities. However, if the process is assumed to be ergodic then one can substitute time-averages for ensemble-averages. The processes in the surf zone cannot be considered ergodic due to the orbital wave motion of the particles. In this case the ensemble average velocities are approximated by computing the phase ensemble-averaged velocity $<(u, w)>$ defined as follows:

$$<(u, w)> = \frac{1}{N}\sum_{0}^{N-1} (u(\omega(t+iT),z),\ w(\omega(t+iT),z)) \qquad (6.1)$$

Where $<\ >$ signifies averaging operation, N is the sample size, z is the vertical position above the bed, t is the time, T is the wave period and, u and w are the horizontal and vertical velocity components, respectively.

Velocities of the neutrally buoyant particles were measured over a small section of the wave at a time and this was repeated for a number of wave phases. The velocity estimates were then placed in bins corresponding to their wave phase and the vertical position. The phase ensemble averaged velocity is then the average velocity in each bin.

Figures 6.4(A), 6.5(A) and 6.6(A) show the phase-averaged velocity vector field at stations 1, 2 and 3, respectively, for the spilling wave case. The vertical axis, z, represents the height above the bed at each station. The phase, -t/T, of the wave is plotted along the horizontal axis. These flow fields show certain characteristic features. The velocity streamlines at station 1 still retains most of the characteristics of a non breaking wave. The front face of the wave is however steeper. The magnitude of the velocities in the crest of the wave at station 1 is approximately 200 cm/s and this decreases gradually to the bottom of the wave. The magnitude of the velocities in the trough region are lower than those in the crest and are directed opposite to the direction of wave propagation. The velocities in the trough are almost constant over the depth, decreasing slightly in magnitude at the bottom due to boundary effects. The profile of the horizontal and vertical velocity components, at depths 4, 8, 12,

16, 21 and 25 cm above the bed, is plotted in Figure 6.4(B) as a function of the wave phase. The variation of u, as a function of depth, is plotted in figure 6.4(C) for wave phases 0.15, 0.3, 0.45, 0.6, 0.75 and 0.9. These are essentially horizontal and vertical sections of the flow field presented in figure 6.4(A). Figure 6.4(B) shows that the horizontal velocity near the bed is approximately sinusoidal with respect to the wave phase, while the vertical velocity has a asymmetrical shape. Further above the bed the horizontal velocity profile begin to show signs of asymmetry. Figure 6.4(C) shows that the horizontal velocity in the wave trough is almost constant throughout the depth.

Velocity measurement, by *Stive(1980)*, in a spilling wave near the breakpoint and having similar local wave characteristics, reveal velocities in the middle of crest to be ~ 60 cm/s and ~ 40 cm/s near the bed. These LDA measurements are similar to the peak horizontal velocities in Figure 6.4(B)(a) and (f).

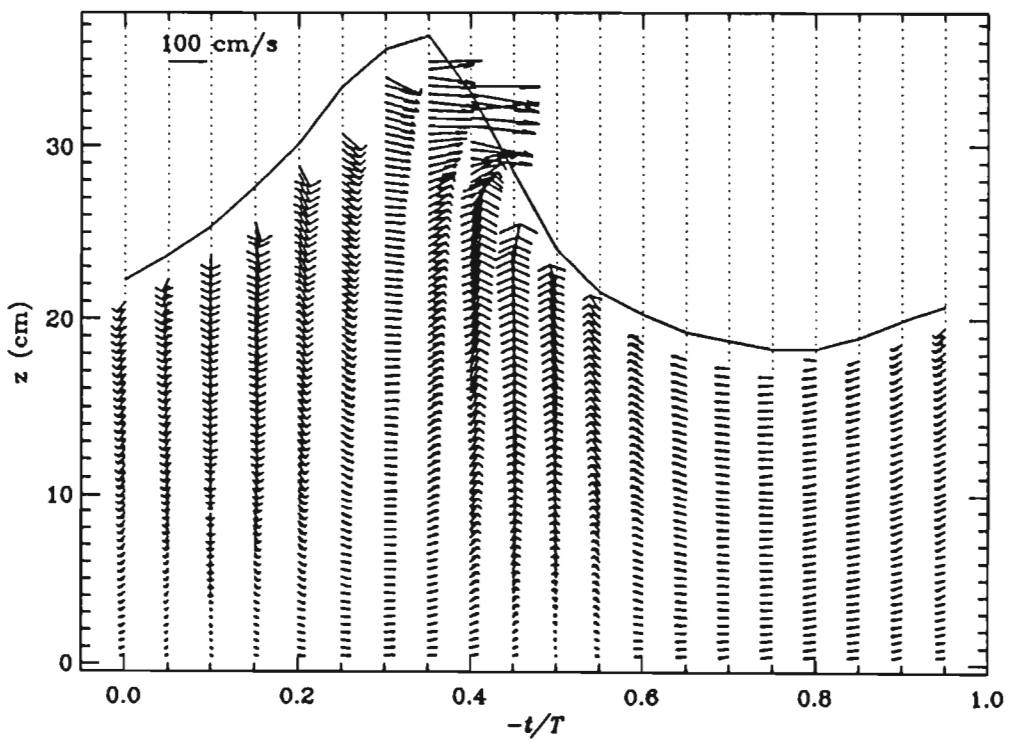

Figure 6.4: (A) Velocity flow field of a spilling wave at station 1 which is located ~ 0.24 m beyond the break-point.

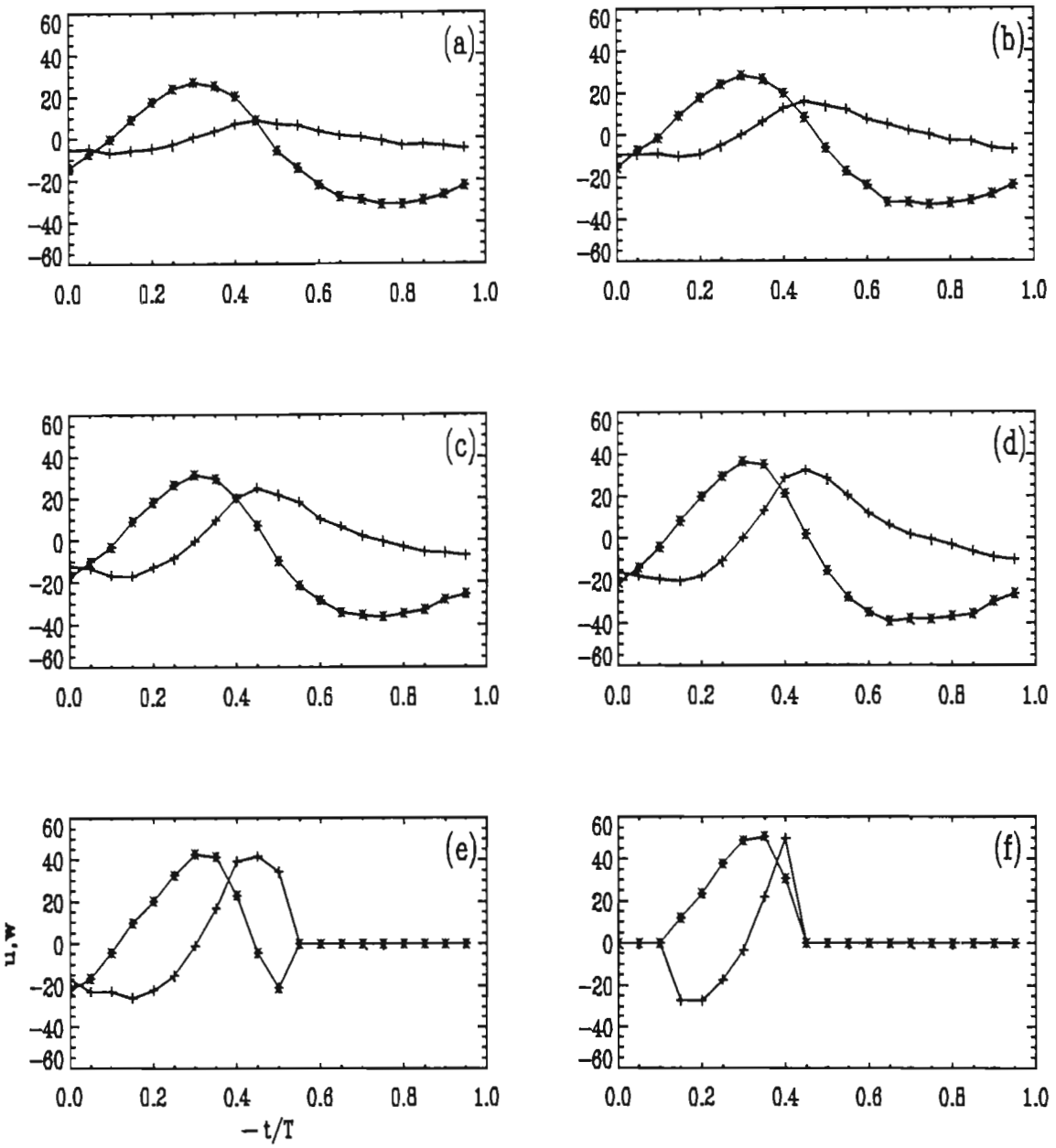

Figure 6.4 cont.: (B) Phase ensemble-averaged velocities, $<u>$ (*) and $<w>$ (+) in cm/s, as a function of wave phase at (a) 4, (b) 8, (c) 12, (d) 16, (e) 21 and (f) 25 cm above the bed, extracted from Figure 6.4 (A).

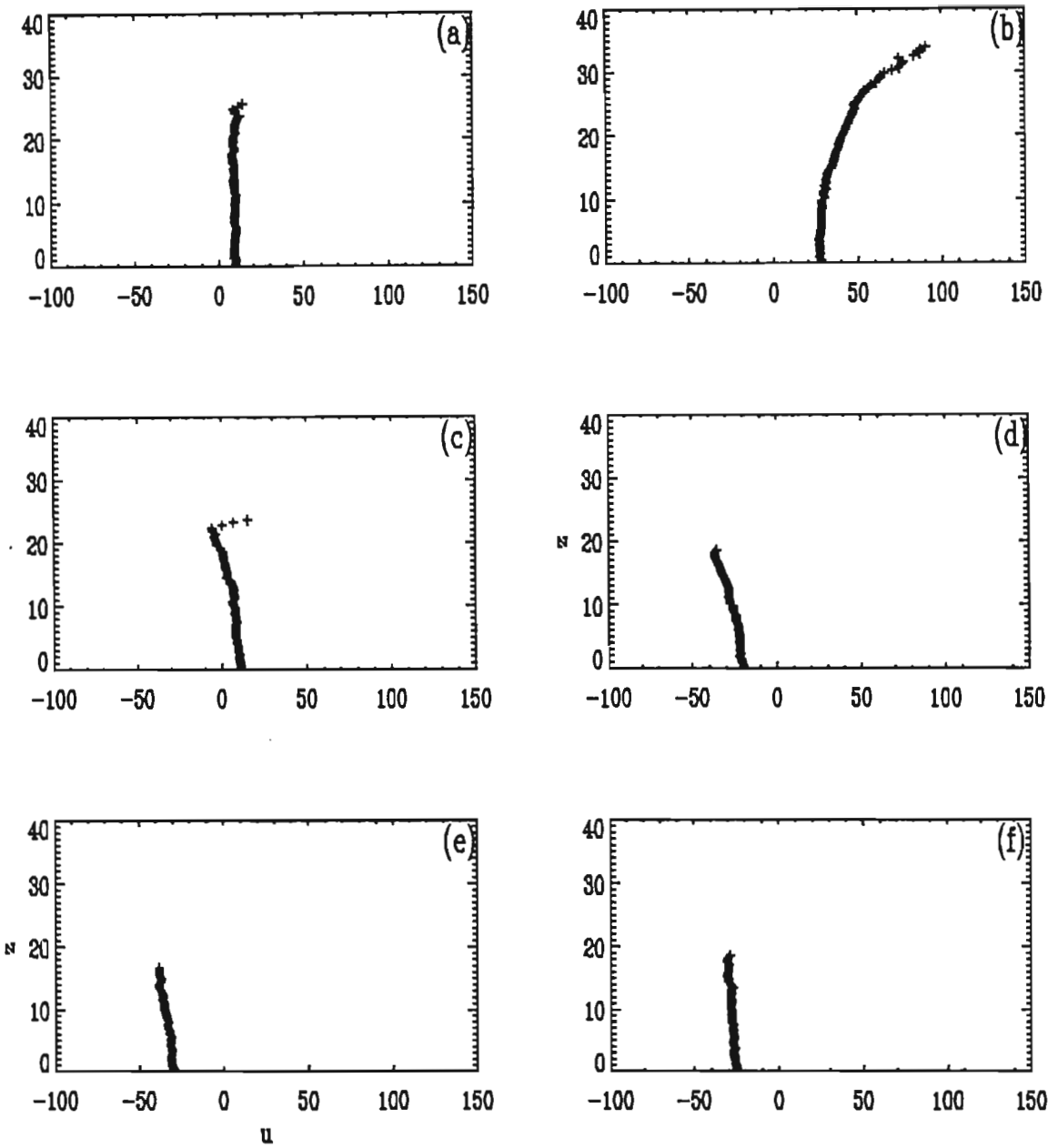

Figure 6.4(C): Ensemble-averaged horizontal velocity, $<u(z)>$, at wave phases, t/T, (a) 0.15 (b) 0.3, (c) .45, (d) 0.6, (e) 0.75 and (f) 0.9, extracted from Figure 6.4(A). u(cm/s) and z(cm) are plotted on the x and y axes, respectively.

The phase ensemble averaged flow field for the spilling wave at station 2, shown below, shows further development as the wave moves up the beach. The wave profile is tending towards a saw-tooth shape. There is also a large shear being created at the base of the wave front, which is responsible for the formation of a horizontal vortex or eddy in that region (see Figure 4.9). Velocities in the crest of the wave are ~ 100 cm/s and ~ 40 cm/s in the trough region. The variation of u and w as a function of phase is shown in figure 6.5(B), and the variation of u as a function of position above the bed is shown in figure 6.5(C). These figures show that the horizontal velocity profile as a function of wave phase is asymmetrical at all positions in the wave. The particle velocity near the surface at the rear of the crest has a strong downward component. This is due to the fact that this point along the wave corresponds to the point of inflection of the velocity streamlines between those in the trough and those in the crest and also due to the fact that the vertical velocity component increases in magnitude with distance above the bed. At positions below the trough level, the horizontal velocity is almost constant through the depth.

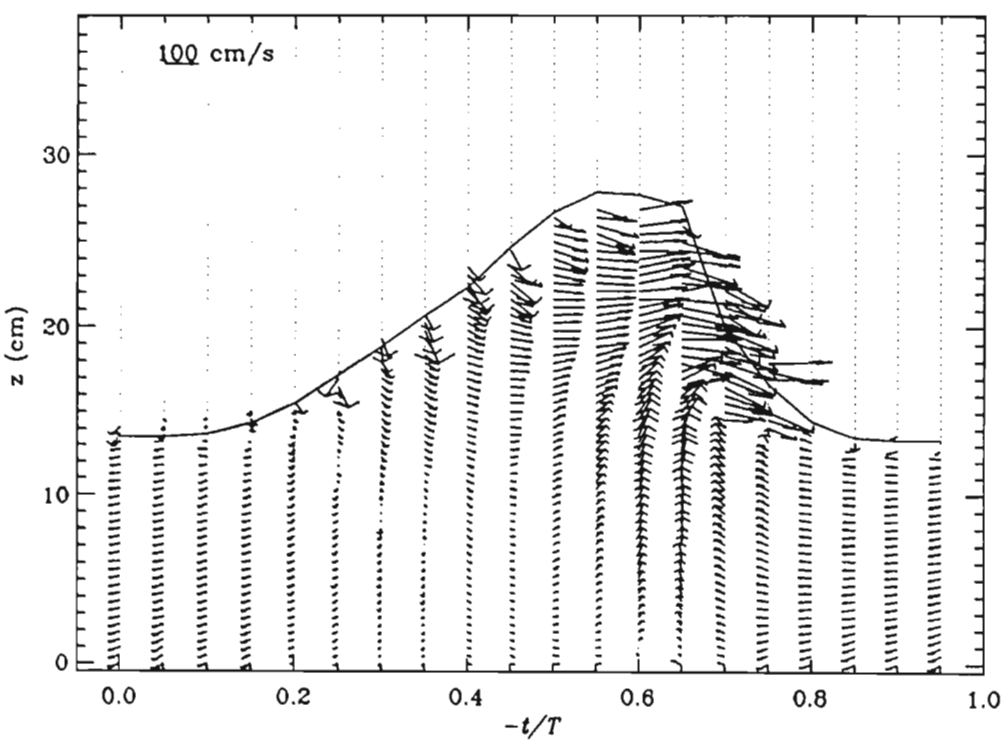

Figure 6.5: (A) Velocity flow field of a 0.9 Hz spilling wave at station 2 which is located ~ 1.22 m beyond the break-point.

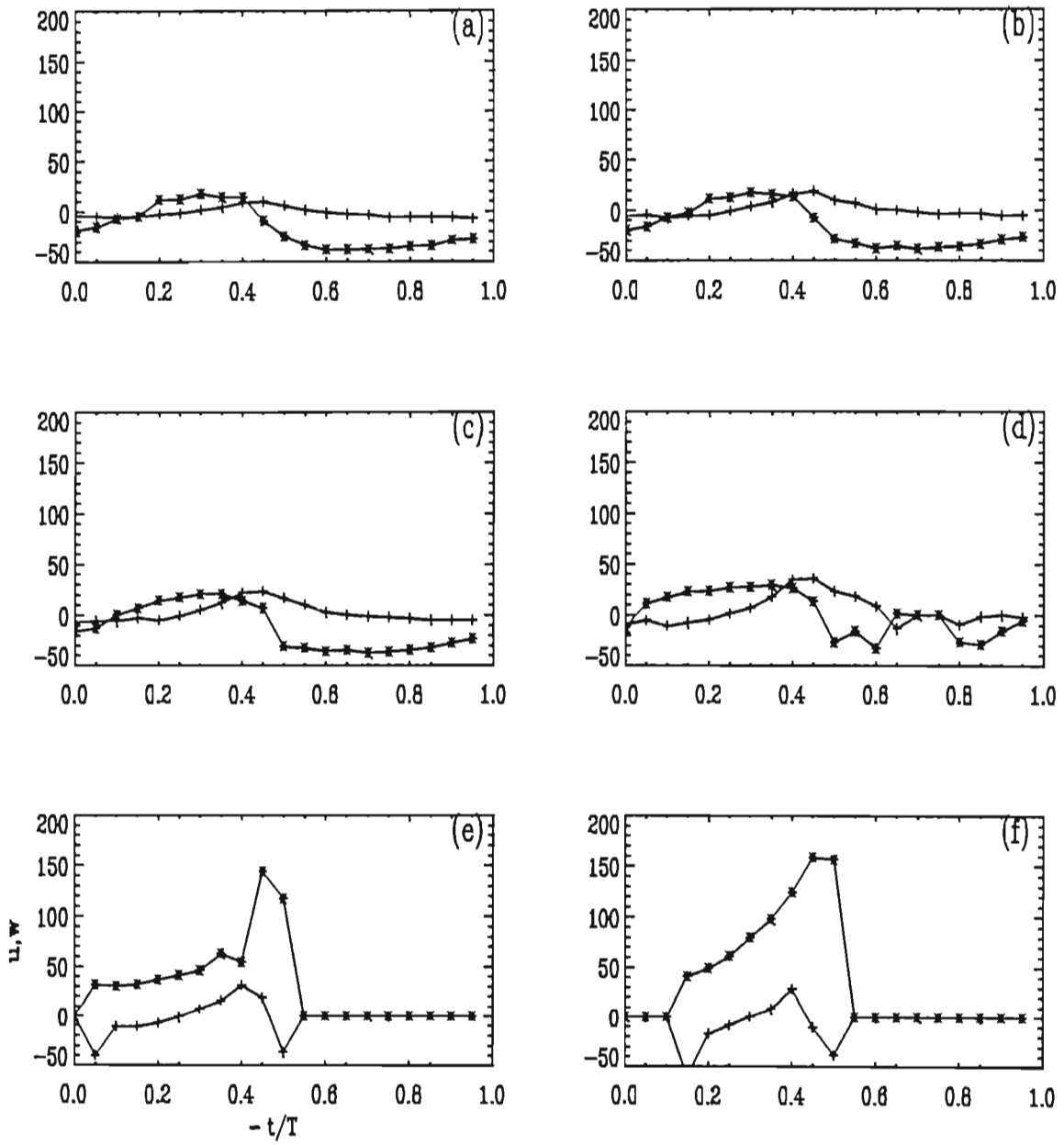

Figure 6.5 cont.: (B) Phase ensemble averaged velocities, $<u>$ (*) and $<w>$ (+) in cm/s, as a function of wave phase at (a) 3, (b) 7, (c) 10, (d) 13, (e) 16 and (f) 20 cm above the bed, extracted from Figure 6.5(A).

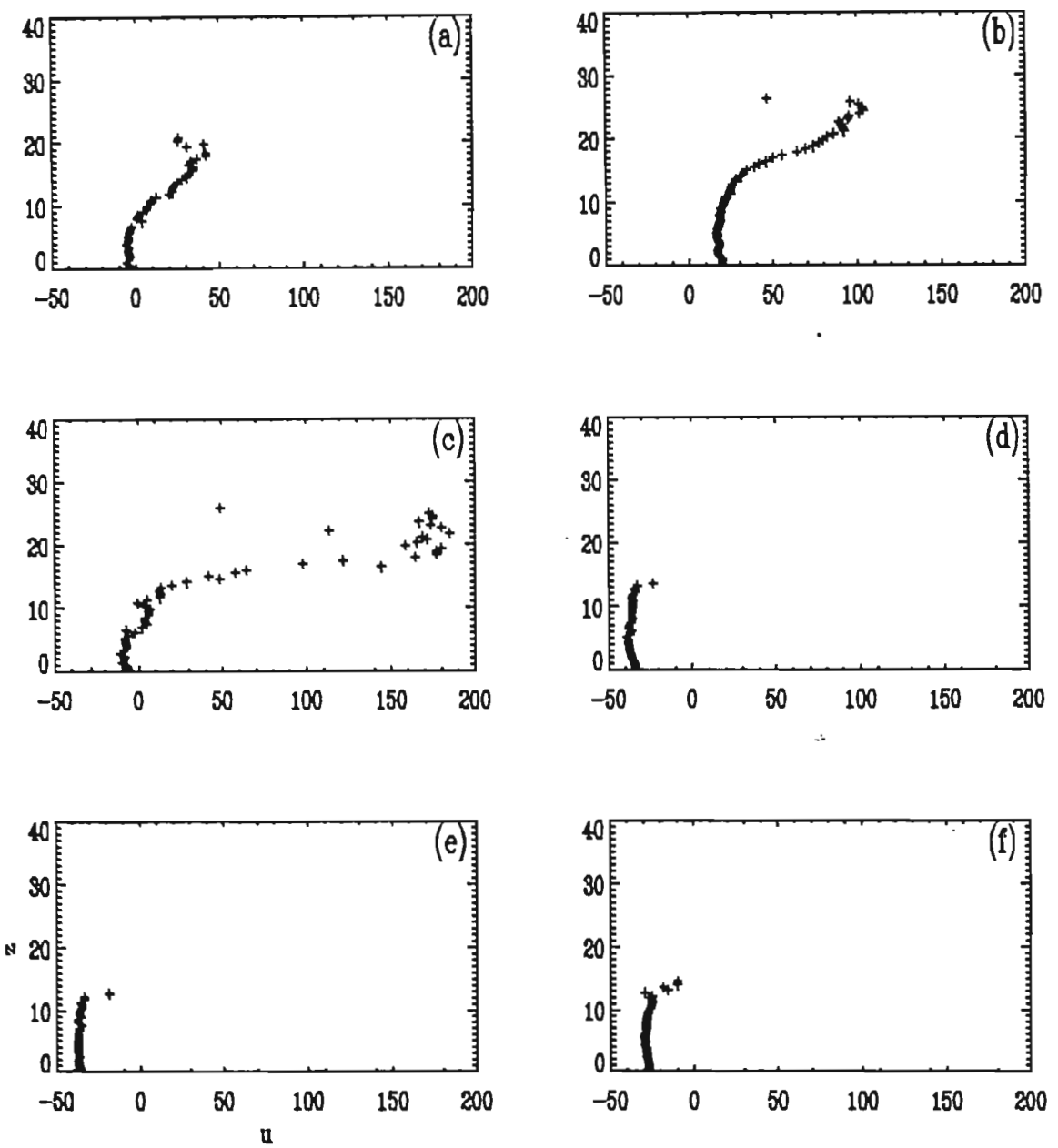

Figure 6.5(C): Ensemble-averaged horizontal velocity, $<u(z)>$, at t/T of (a) 0.15, (b) 0.3, (c) 0.45, (d) 0.6, (e) 0.75 and (f) 0.9, extracted from Figure 6.5(A). u(cm/s) and z(cm) are plotted on the x and y axes, respectively.

The form of the spilling wave at station 3, shown in Figure 6.6(A), is very asymmetric, with the surface profile having a saw-tooth shape. This asymmetry also shows up in the flow field. The magnitude of the velocities in the crest are once again higher than those in the trough. The velocities in the crest have magnitudes in the order of 100 cm/s and 20 cm/s in the trough. The point of inflection of the velocity vectors at the front face of the wave occurs almost at the peak of the wave. The point of inflection at the rear of the wave is now almost non existent. The particle velocities at the expected point of inflection, just behind the crest, have a varying phase with respect to their orbital motion. Shown in Figure 6.6(B) is the flow field of the spilling wave at station 3 measured using DPIV. Comparison of Figure 6.6(A) and (B) reveal similar features. The velocities have similar magnitudes. The DCIV measurement however provides greater spatial resolution of the flow field and also provides velocity estimates higher up in the crest region. The variation of u and w as a function of wave phase and depth is shown in figures 6.6(C) and (D), respectively. Below the trough level($z \sim 10$ cm) there is little variation in u as a function of z.

LDA measurements by *Stive(1980)* in a spilling wave at a similar position and with similar local wave characteristics, reveal horizontal velocities $\sim$ 25 cm/s below the crest at the trough level. This correspond well with the peak positive horizontal velocity in Figure 6.6(C)(e). Near the bed *Stive* reports velocity $\sim$ 10 cm/s which is similar to the peak positive horizontal velocity in Figure 6.6(C)(a). Measurements by *Nadaoka et al.(1989)* also give velocities $\sim$ 60 cm/s in the middle of the crest and maximum velocities $\sim$ 25 cm/s in the wave trough.

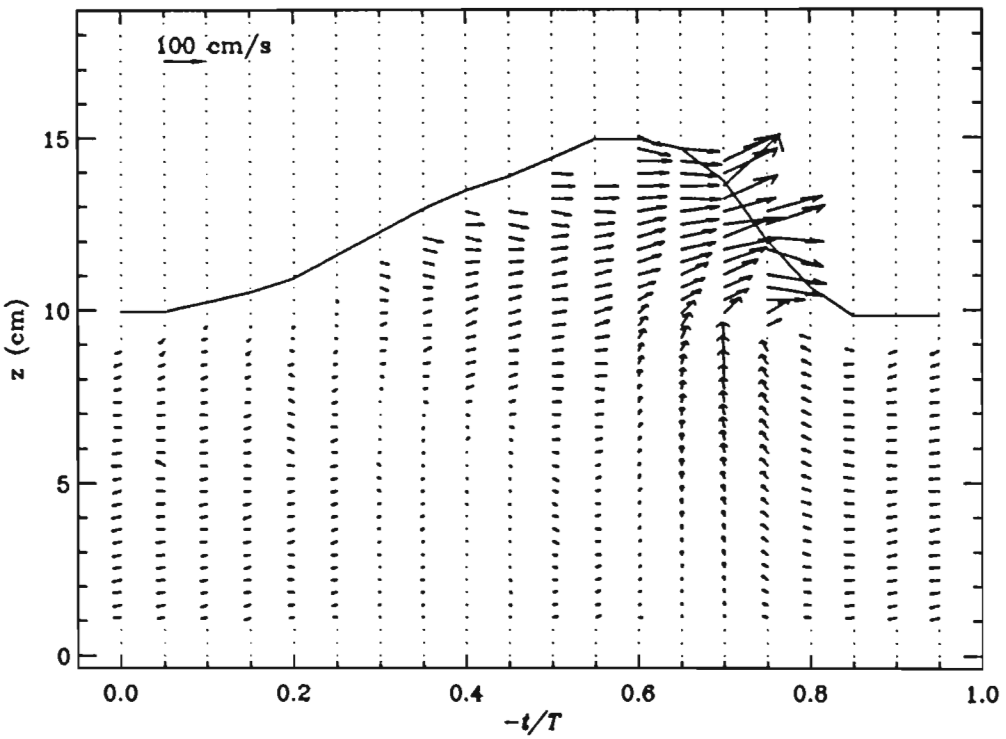

Figure 6.6: (A) Velocity flow field of a spilling wave at station 3 which is located ~2.21 m beyond the break-point.

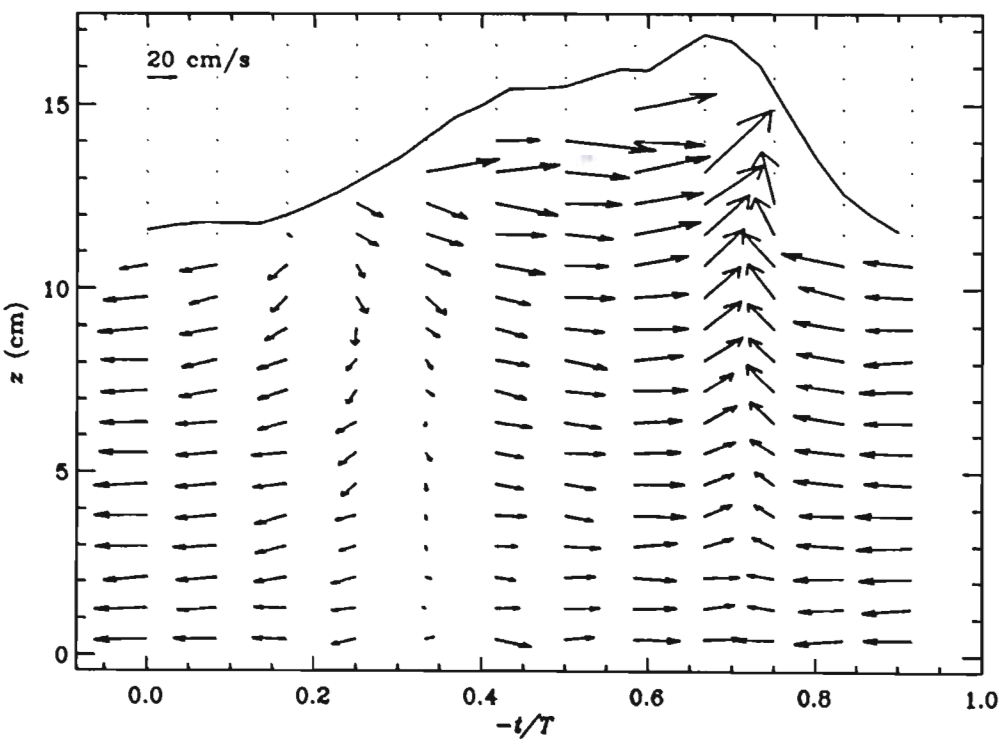

Figure 6.6:(B) Velocity flow field of a spilling wave at station 3 measured using DPIV.

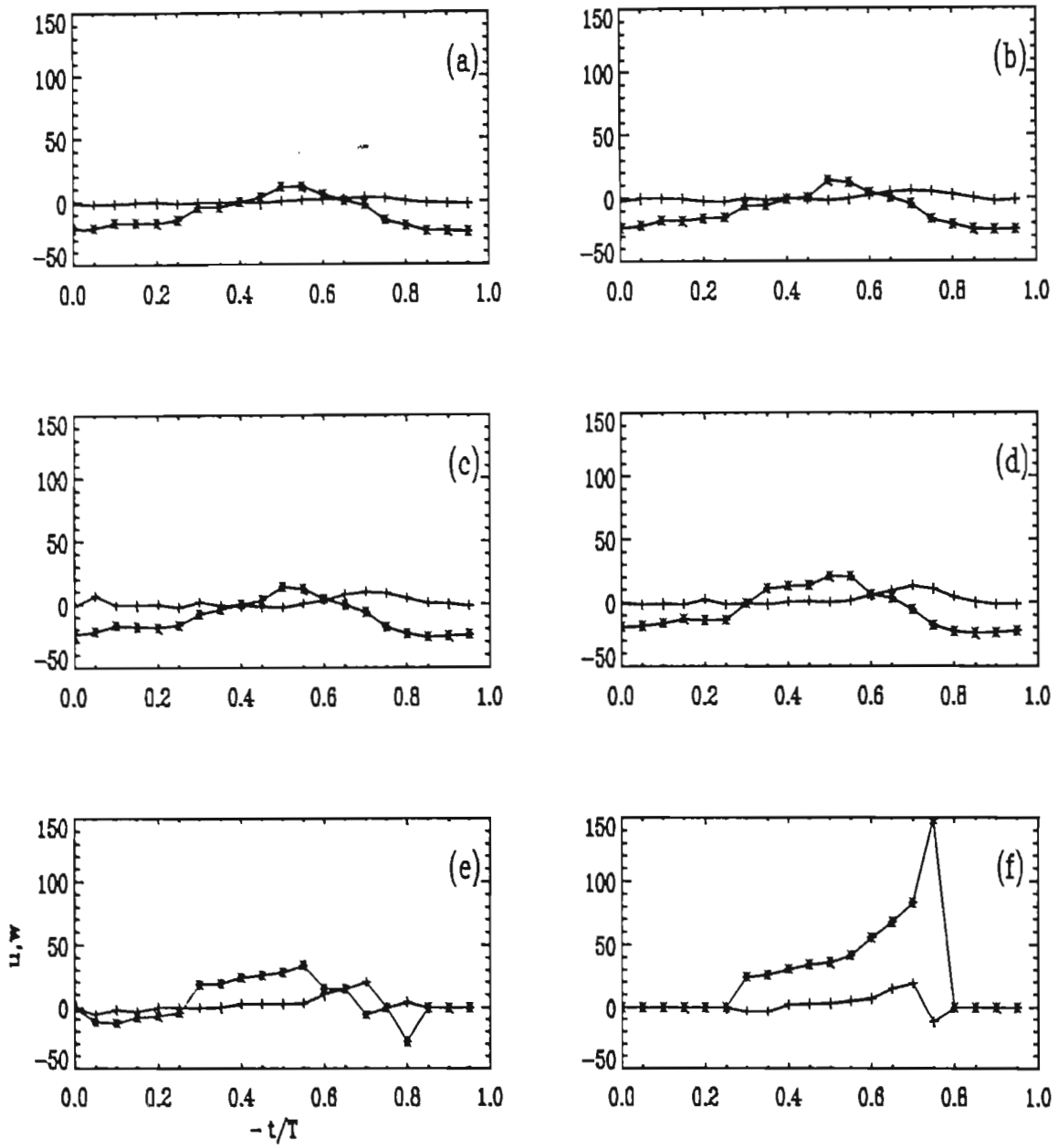

Figure 6.6 cont.: (C) Phase ensemble averaged velocities, $<u>$ (*) and $<w>$ (+) in cm/s, as a function of wave phase at (a) 2, (b) 4, (c) 5, (d) 7, (e) 9 and (f) 11 cm above the bed, extracted from Figure 6.6(A).

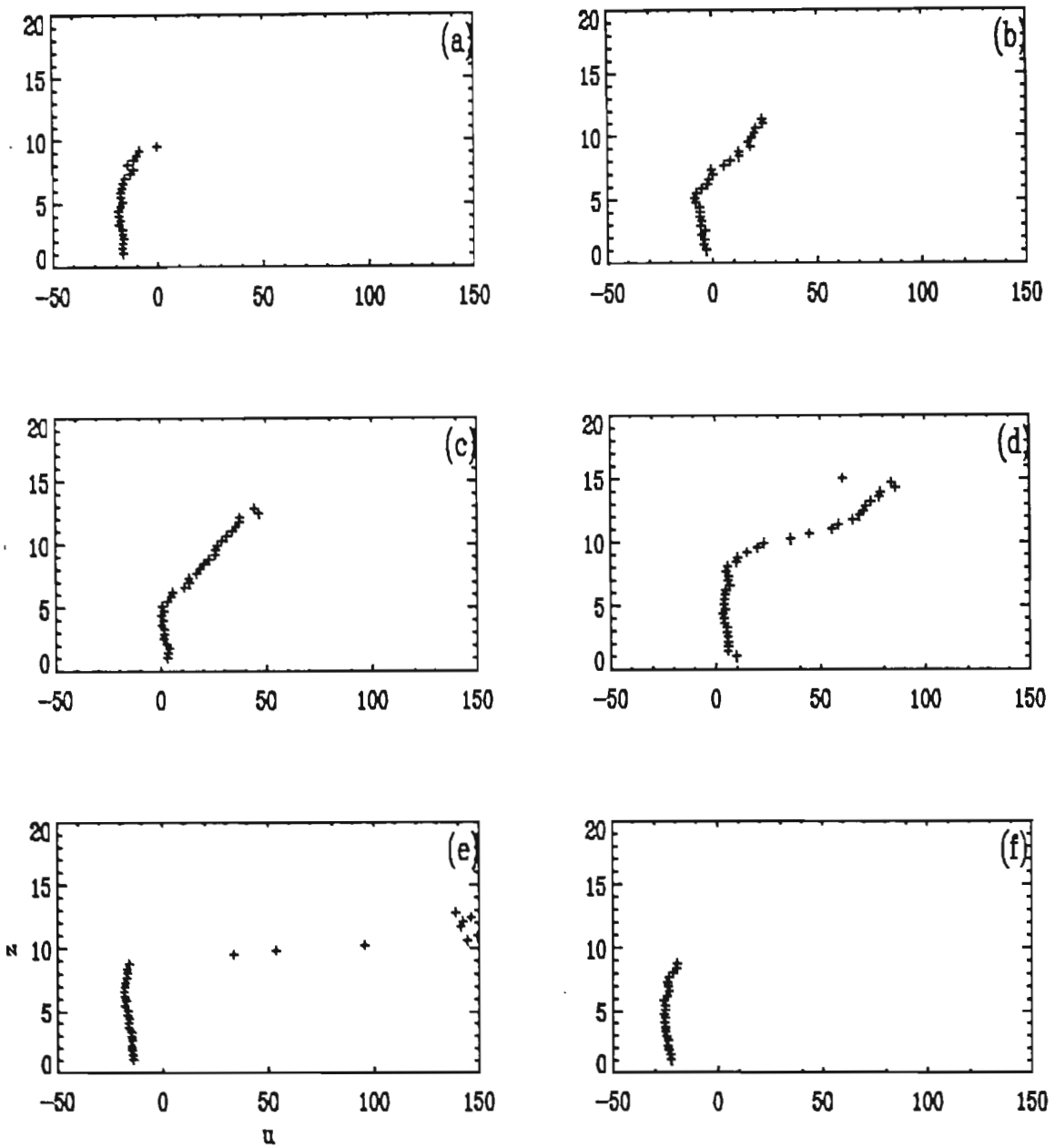

Figure 6.6(D): Ensemble-averaged horizontal velocity, $<u(z)>$, at wave phases, t/T, (a) 0.15, (b) 0.3, (c) 0.45, (d) 0.6, (e) 0.75 and (f) 0.9, extracted from Figure 6.6(A). u(cm/s) and z(cm) are plotted on the x and y axes, respectively.

6.4.2 Time-averaged horizontal flow in the spilling wave

The undertow is the wave or time-averaged horizontal flow below the trough level. The time-averaged horizontal velocity $<u(z)>$ as function of height above the bed, z, is defined as:

$$<u(z)> = \frac{1}{T}\int_0^T u(\omega t, z)dt \tag{6.2}$$

In the case where the flow field is composed of samples spaced at regular intervals, such as the phase-averaged flow fields presented here, the time-averaged flow is estimated using a discretised version of the above equation, that is:

$$\begin{aligned} <u(z)> &= \frac{1}{2\pi}\sum_{i=0}^{N-1} u(\theta_i, z)\delta\theta \\ &= \frac{1}{N}\sum_{i=0}^{N-1} u(\theta_i, z) \end{aligned} \tag{6.3}$$

where $\delta\theta$ is the spacing of the bins along the x-axis and N is the total number of phase bins.

Figures 6.7, 6.8 and 6.9 show the time-average of the horizontal velocity component, $<u(z)>$, at stations 1, 2 and 3 respectively. At station 1 there is a peak reverse flow of approximately 11 cm/s, occurring close to the trough level. The velocity then decreases almost linearly to about 5 cm/s near the bottom. Above the trough level there is transition from a reverse current to a forward current. This reaches a peak value of approximately 17 cm/s. The velocity above the trough level is due to the forward mass flux in the crest of the wave and the reverse mass flux is due to the undertow current. Measurements by *Ting and Kirby(1994)*, using LDA at a similar position but using smaller wave heights, show very similar linear increase in velocity from the bed upwards. Near the bed *Ting and Kirby* obtained a velocity of -3.4 cm/s and a peak reverse flow near the trough level of $\sim$ 6.8 cm/s. Station 1 is very close to the break-point and the flow below the trough level, neglecting boundary layer effects, can be considered to be non-turbulent.

At station 2 the undertow is almost constant near the bottom. There is also an increase in the forward mass flux. At station 3 there is once again a reverse current below the trough level and a forward current above. The undertow, which is maximum near the bottom decreases gradually with height in a parabolic fashion. The peak reverse current near the bottom at station 3 is approximately 12 cm/s. The forward current reaches a peak velocity of approximately 26 cm/s at a height of approximately 11 cm above the bottom. There is, thus, an overall decrease in the peak undertow velocity and an increase in the forward mass flux at station 3. For a similar position in the surf zone *Ting and Kirby(1994)* and *Hansen and Svendsen(1984)* measured a reverse flow near the bed of ~ 10 cm/s which is similar to that measured using DCIV. Table 6.3 summarises the peak forward and reverse flow in the spilling wave at stations 1,2 and 3.

In the past, time-averaged horizontal velocity components were derived from LDA measurements, and only measurement below the trough level were available. It has been clearly demonstrated here that by using video image techniques it is possible to obtain similar measurement to those obtained using conventional techniques and also to quantify the mass flux occurring in the aerated region of the crest.

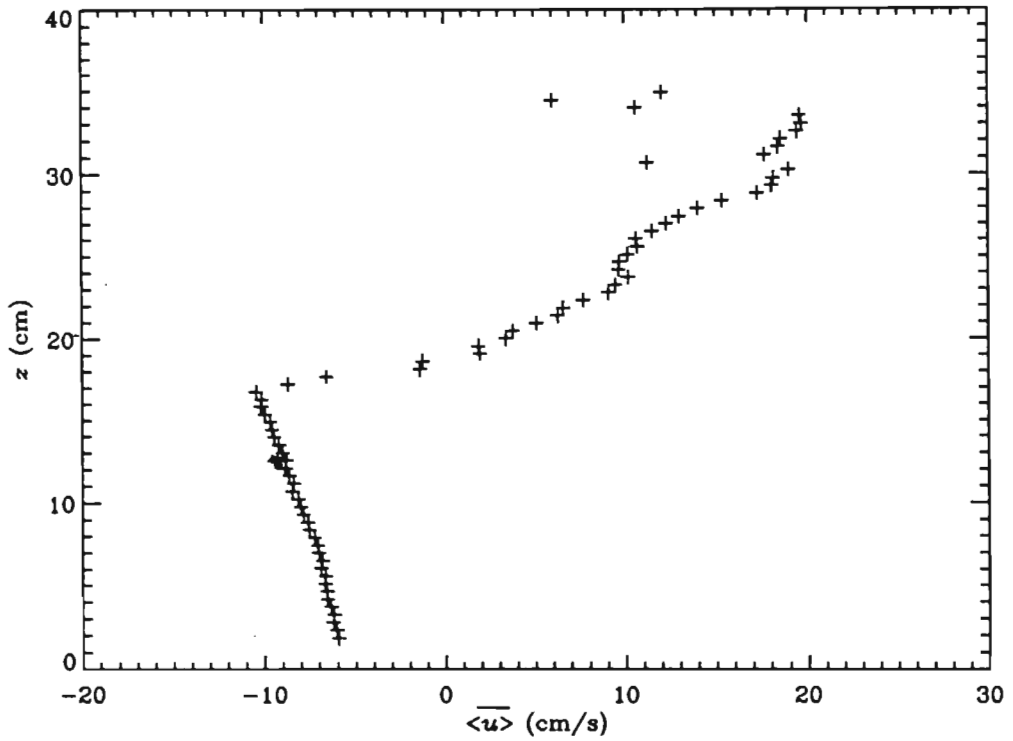

Figure 6.7: Time-averaged horizontal velocity, $\overline{<u(z)>}$, of a spilling wave at station 1 which is located ~ 0.24 m beyond the break-point.

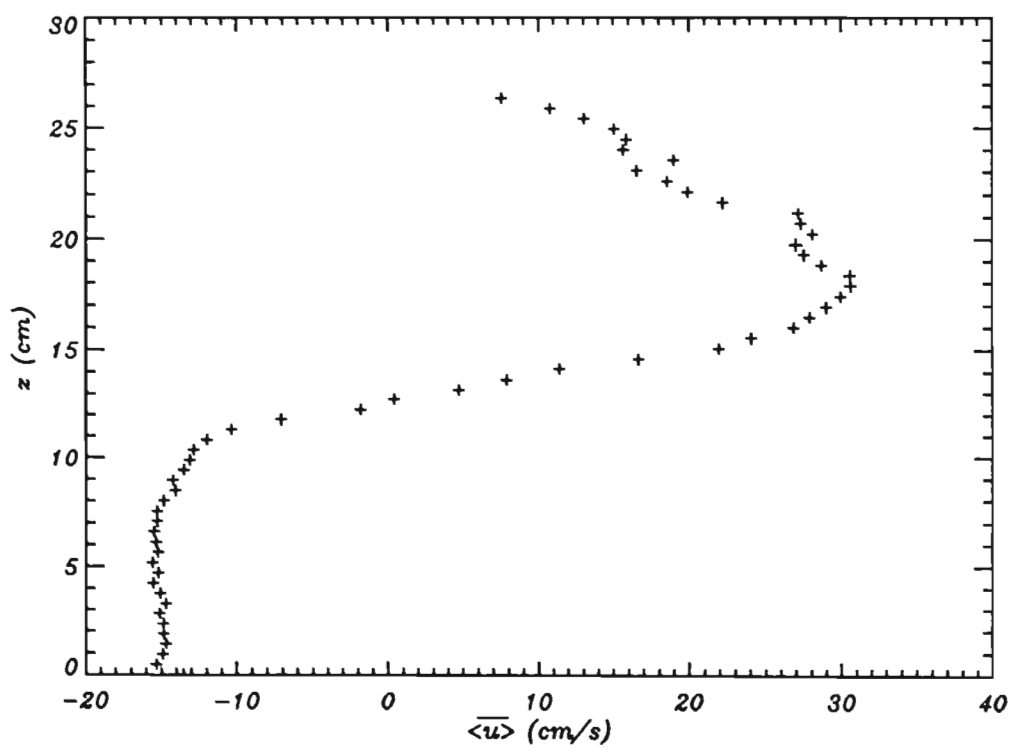

Figure 6.8: Time-averaged horizontal velocity, $\overline{<u(z)>}$, of a spilling wave at station 2 which is located ~ 1.22 m beyond the break-point.

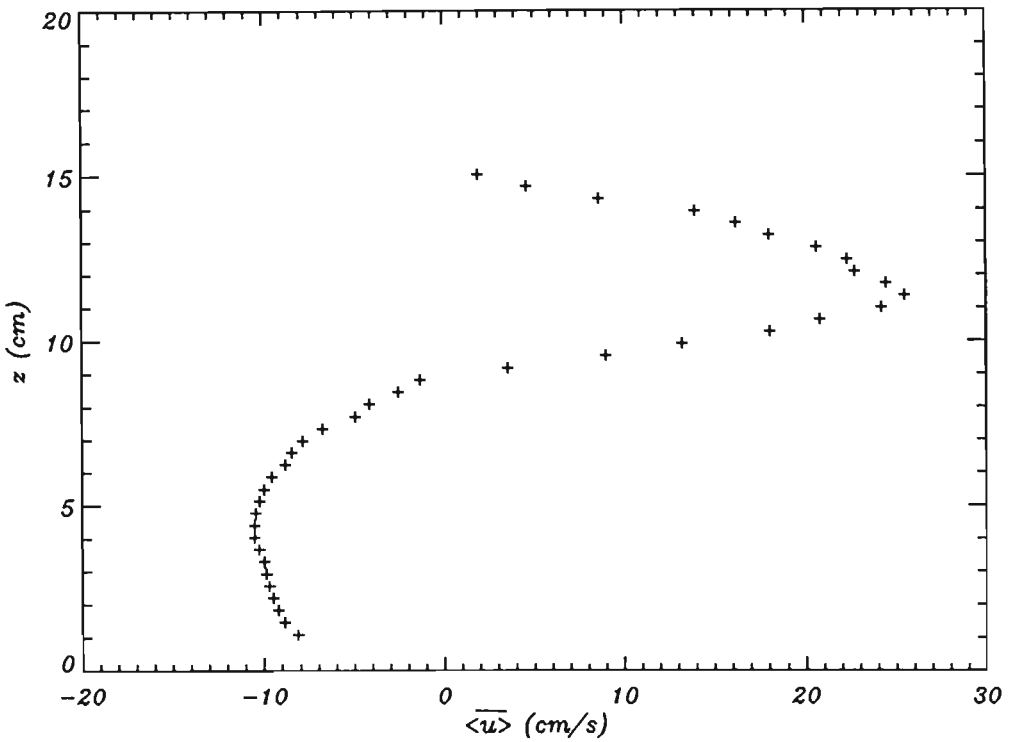

Figure 6.9: Time-averaged horizontal velocity, $<\overline{u(z)}>$ in cm/s, of a spilling wave at station 3 which is located ~2.21 m beyond the break-point.

Table 6.3: Peak time-averaged forward and reverse flow in the spilling wave.

$x-x_b$	(station 1) 0.24	(station 2) 1.22	(station 3) 2.22
Peak forward velocity (cm/s)	17	31	26
Peak reverse velocity (cm/s)	-11	-15	-12
Peak reverse velocity (cm/s)*	_	_	-10

*measured by *Ting and Kirby(1994)* and *Hansen and Svendsen(1984)*.

The forward and reverse mass flux at stations 1,2 and 3 for the spilling wave have been computed using the time averaged horizontal velocities. These are presented in Table 6.4 below. The fractional density of the fluid in the crest of the wave can be estimated using the ratio of the reverse and forward mass fluxes assuming that the net flux through a vertical cross section should be zero. This is tabulated below.

Table 6.4: Forward and reverse mass flux in spilling waves

$x-x_b$ (m)	(station 1) 0.3	(station 2) 1	(station 3) 1.9
Forward mass flux ($x10^{-4}$ kg/ms)	ρ_r186.8	ρ_r282.6	ρ_r97
Reverse mass flux ($x10^{-4}$ kg/ms)	-ρ138.3	-ρ167.8	-ρ63.6
Fraction density of crest	~0.7	~0.6	~0.65

where ρ is the density of water.

The fractional density of the fluid in the crests of the spilling waves is nearly constant at stations 1,2 and 3. This also corresponds to the aeration measurements presented in Chapter 5 where it was shown that the normalised aeration for the spilling wave is approximately constant for the major part of the surf zone.

6.5 Velocity measurements in the plunging wave

6.5.1 Phase ensemble-averaged velocity field in the plunging wave.

The velocity vector flow field of a 0.4 Hz plunging wave having a deep water wave height of 11 cm, was measured at approximately 1.4 m before the breakpoint and 0.5 m and 1.3 m beyond the break point, corresponding to stations 1, 3 and 4, respectively. These measurement were accomplished using DCIV.

Figure 6.10(A) depicts the pre-breaking flow field of the plunging wave. The crests has become very narrow and peaked, while the troughs are very flat. The velocities in these regions show distinct features as well, below the trough the velocities are mostly horizontal. Peak velocities are ~ 100 cm/s in the crest. The variation of u and w with respect to the wave phase is shown in Figure 6.10(B), and the variation of u with respect to depth is shown in Figure 6.10(C). It can be seen from these figures that the vertical velocity is very small in the trough of the wave and varying in magnitude and sign below the crest of the wave.The profile of the horizontal velocity has a similar shape to the surface wave profile.

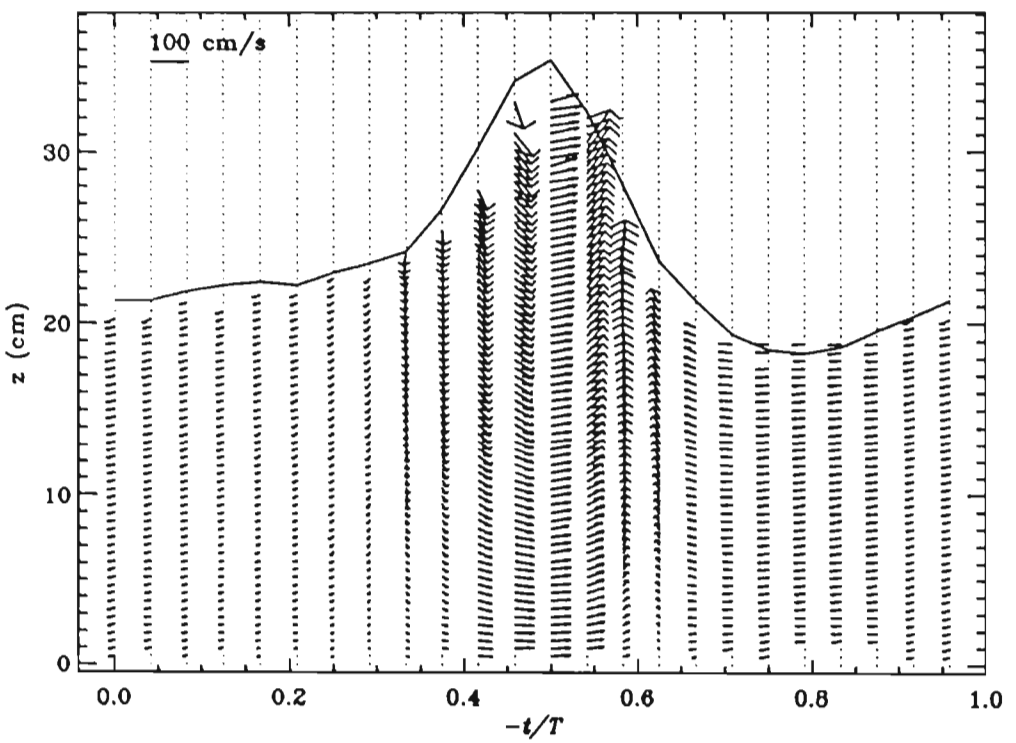

Figure 6.10: (A) Velocity flow field of a plunging wave at station 1 which is located ~ 1.11 m before the break-point.

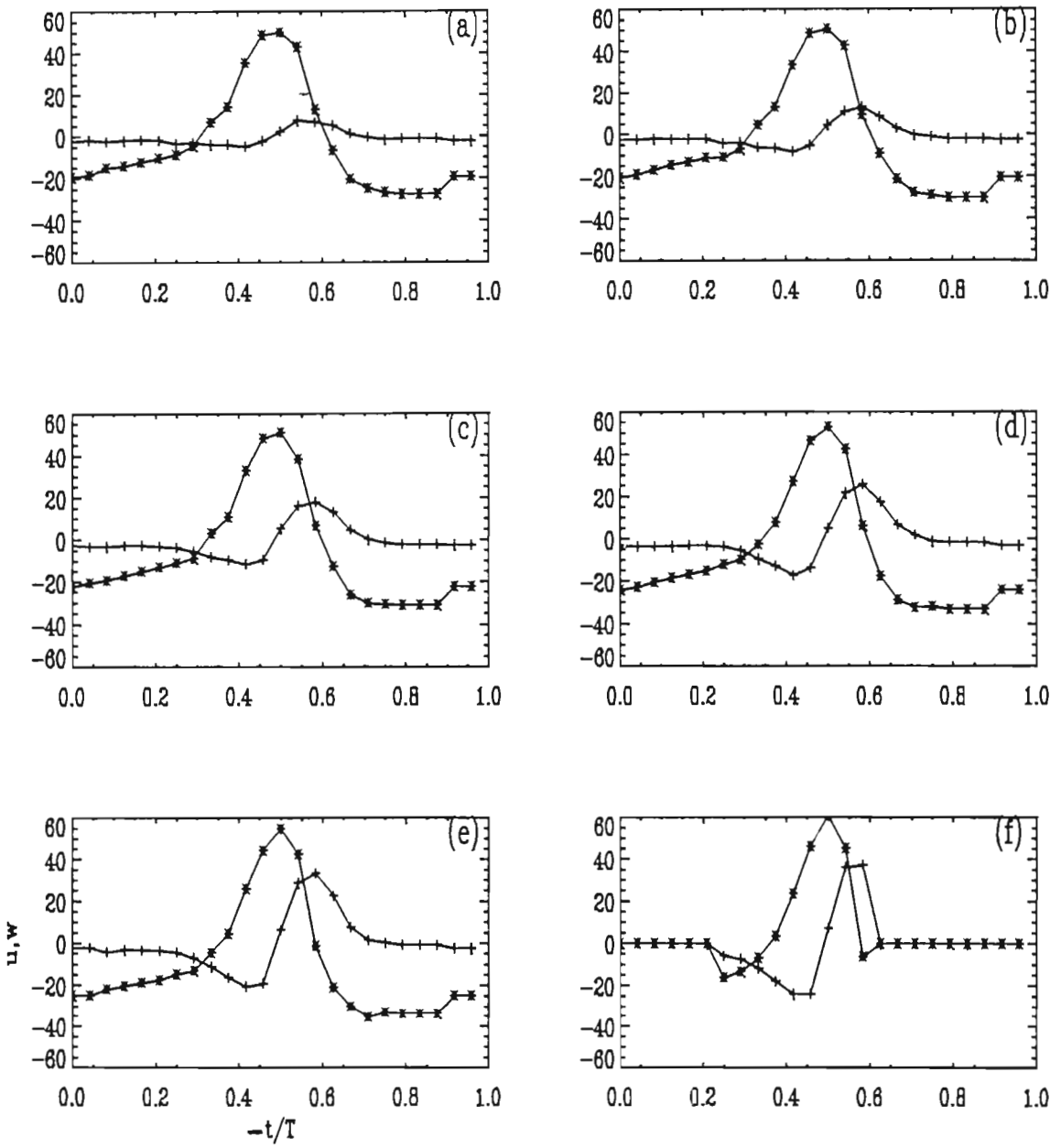

Figure 6.10 cont.: (B) Phase ensemble averaged velocities, $<u>$ (*) and $<w>$ (+) in cm/s, as a function of wave phase at depths (a) 4, (b) 7, (c) 11, (d) 15, (e) 19 and (f) 23 cm above the bed, extracted from Figure 6.10(A)

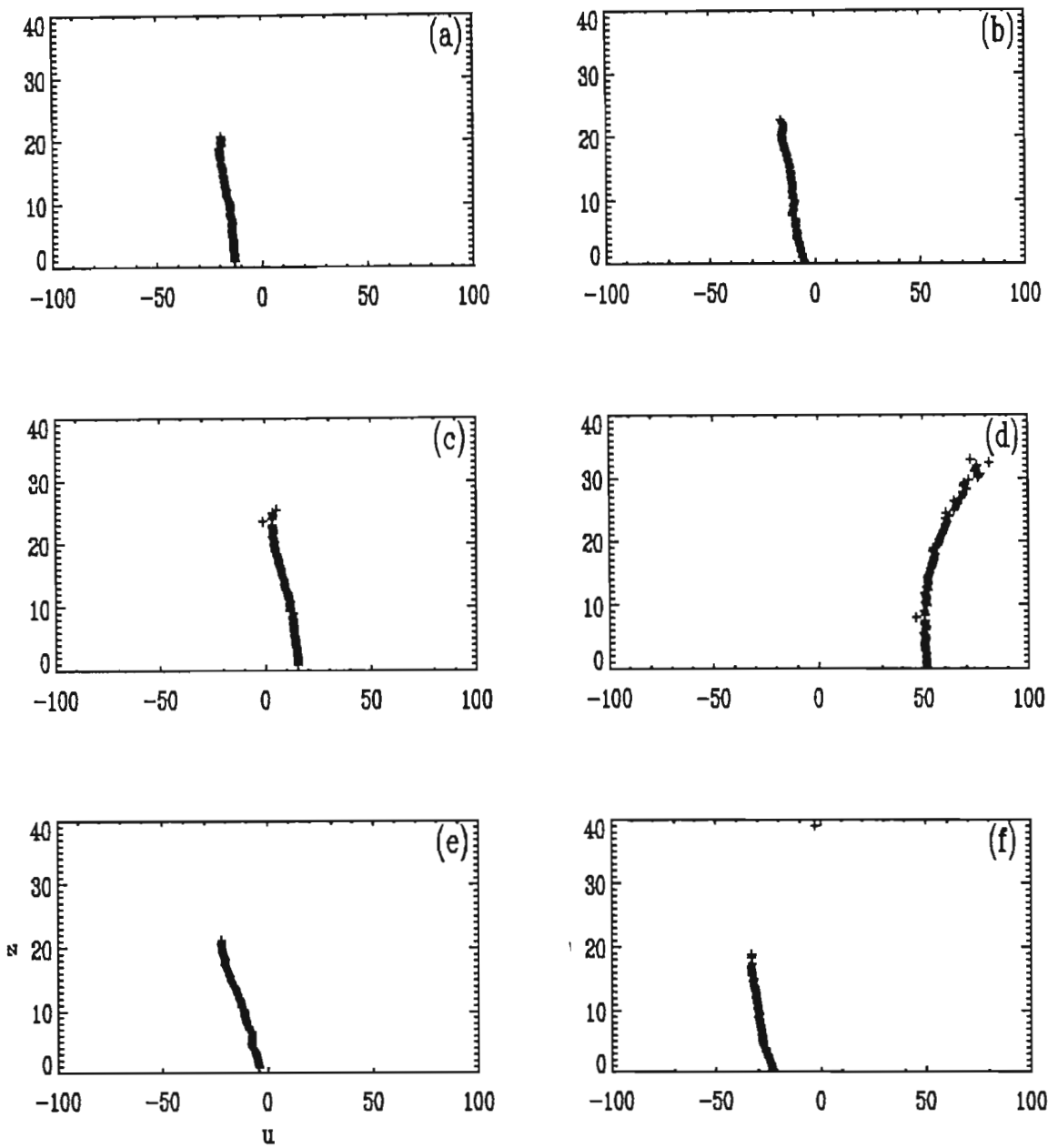

Figure 6.10(C): Ensemble-averaged horizontal velocity, $<u(z)>$, at wave phases, t/T, (a) 0.125 (b) 0.25 (c) 0.375, (d) 0.5, (e) 0.625 and (f) 0.75, extracted from Figure 6.10(A). u(cm/s) and z(cm) are plotted on the x and y axes, respectively.

Figures 6.11(A) and 6.12(A) illustrate the phase averaged velocity vector field at 0.5 m and 2.0 beyond the break-point, respectively. These flow fields show similar characteristics, with high velocities in the crest and directed almost horizontally everywhere. The magnitude of the velocities in the crest is ~ 200 cm/s and ~ 25 cm/s in the trough. There is a steepening of the wave-front as the wave propagates through the surf zone. The curling of the velocity vectors at the bottom of the wave-front is visible in figures 6.11(A) and 6.12(A), resulting in the formation of a large vortex similar to the instantaneous vector field in figure 4.13 in Chapter 4. This vortex is due to the large shear created by forward flow in the crest and the reverse flow in the previous trough.

LDA measurements by *Stive(1980)* in a plunging wave at similar positions show peak forward velocities in the order of 25 cm/s below the trough level.

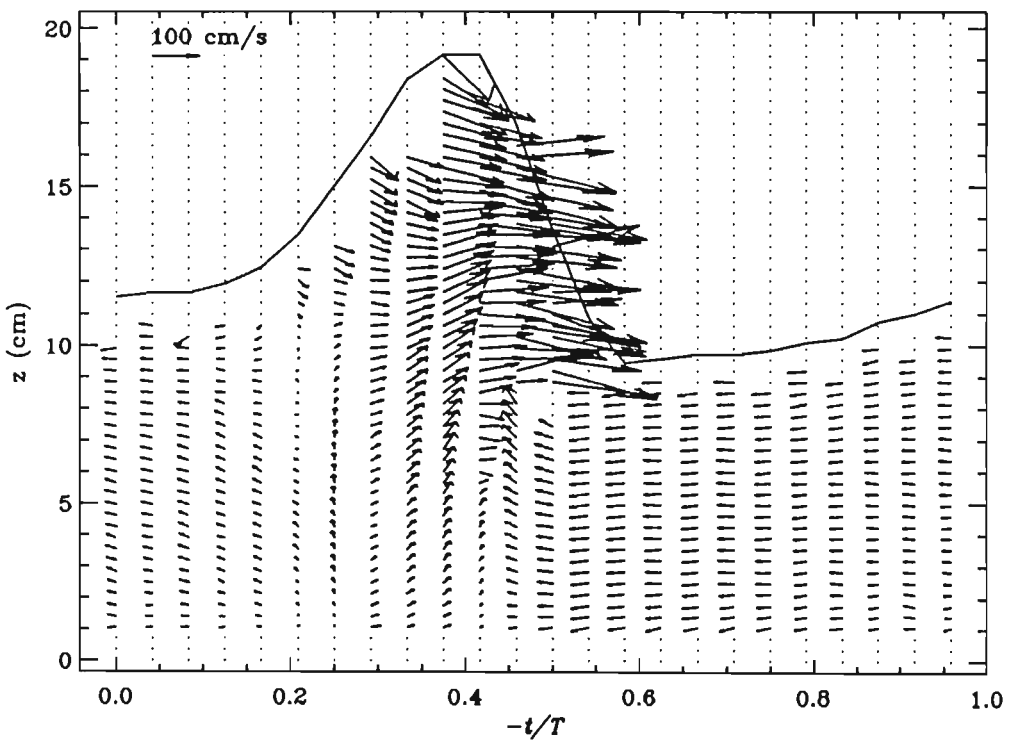

Figure 6.11: (A) Phase averaged velocity of a plunging wave at station 3 which is located ~ 0.86 m beyond the break-point.

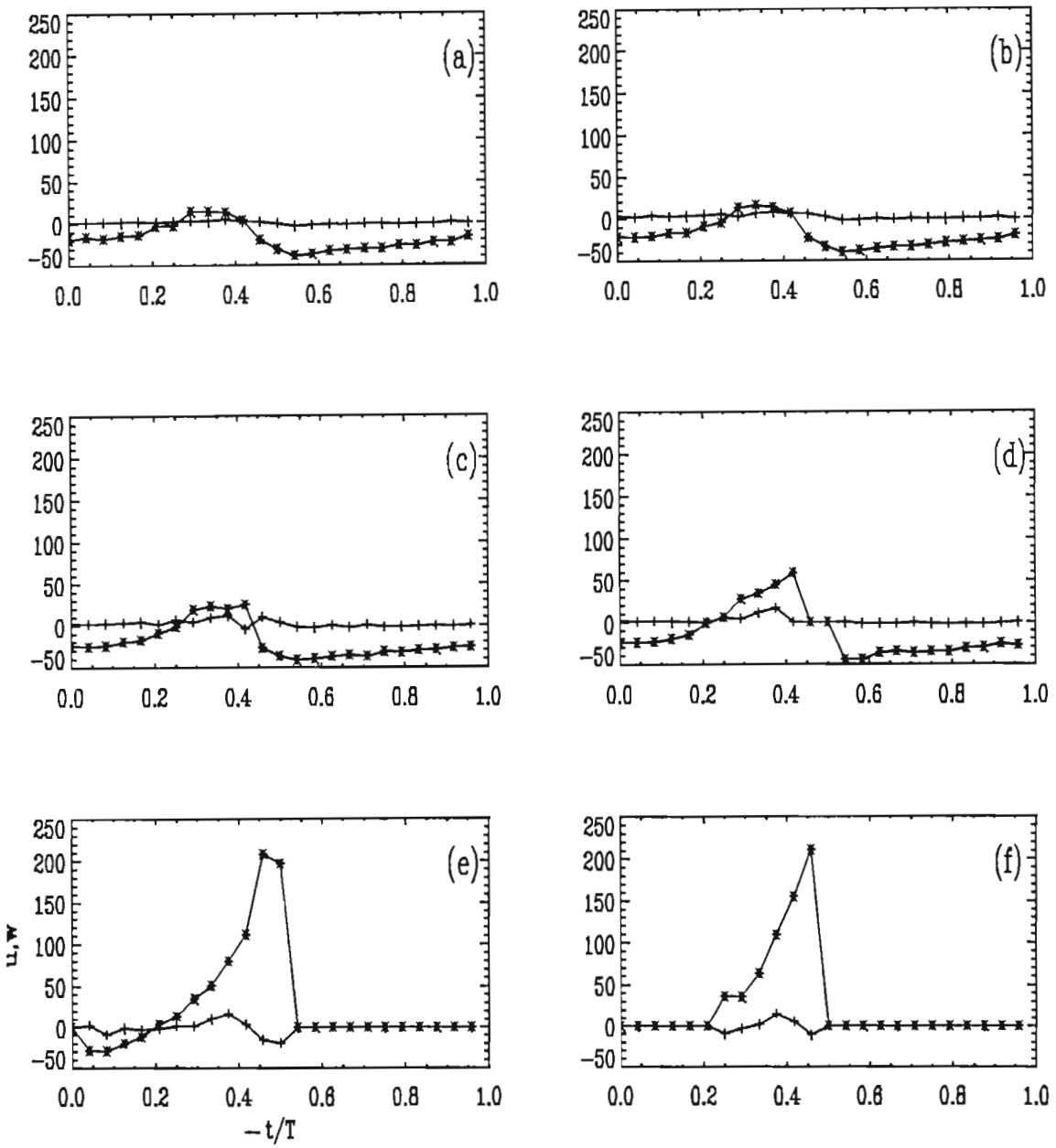

Figure 6.11 cont.: (B) Phase ensemble averaged velocities, $<u>$ (*) and $<w>$ (+) in cm/s, as a function of wave phase at (a) 1.5, (b) 3 (c) 4, (d) 6, (e) 7 and (e) 9 cm above the bed, extracted from Figure 6.11(A).

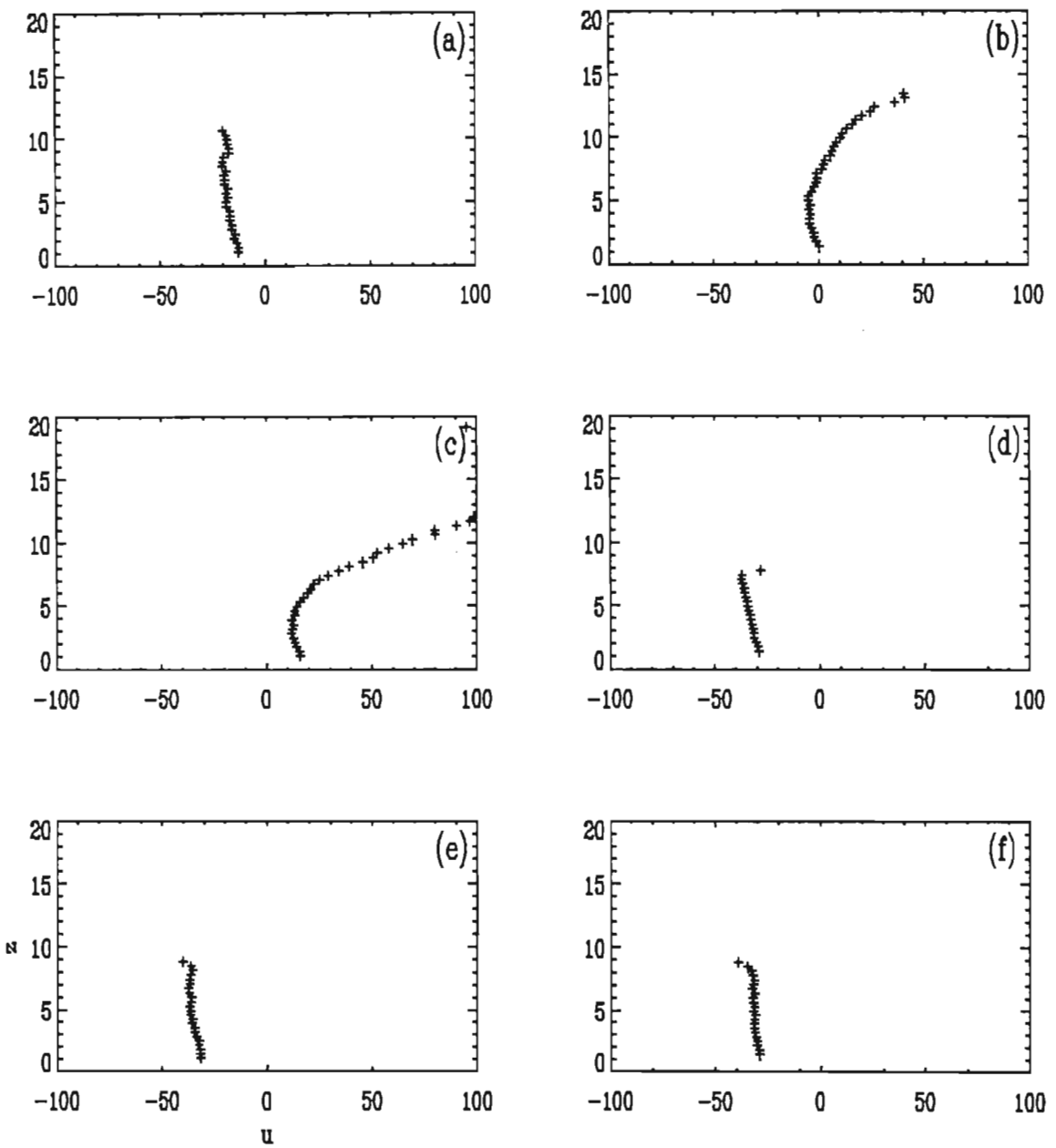

Figure 6.11(C): Ensemble-averaged horizontal velocity, $<u(z)>$, at wave phases, t/T, (a) 0.125, (b) 0.25, (c) 0.325, (d) 0.5, (e) 0.625 and (f) 0.75, extracted from Figure 6.11(A). u(cm/s) and z(cm) are plotted on the x and y axes, respectively

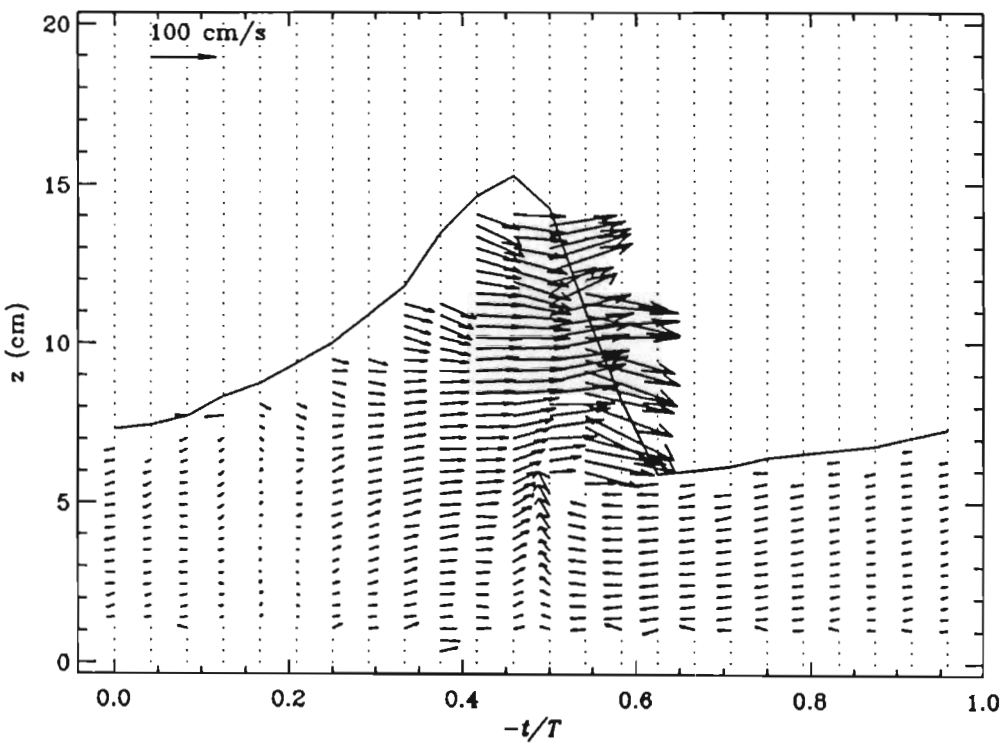

Figure 6.12: (A) Phase averaged velocity of a plunging wave at station 4 which is located ~ 1.69 m beyond the break-point.

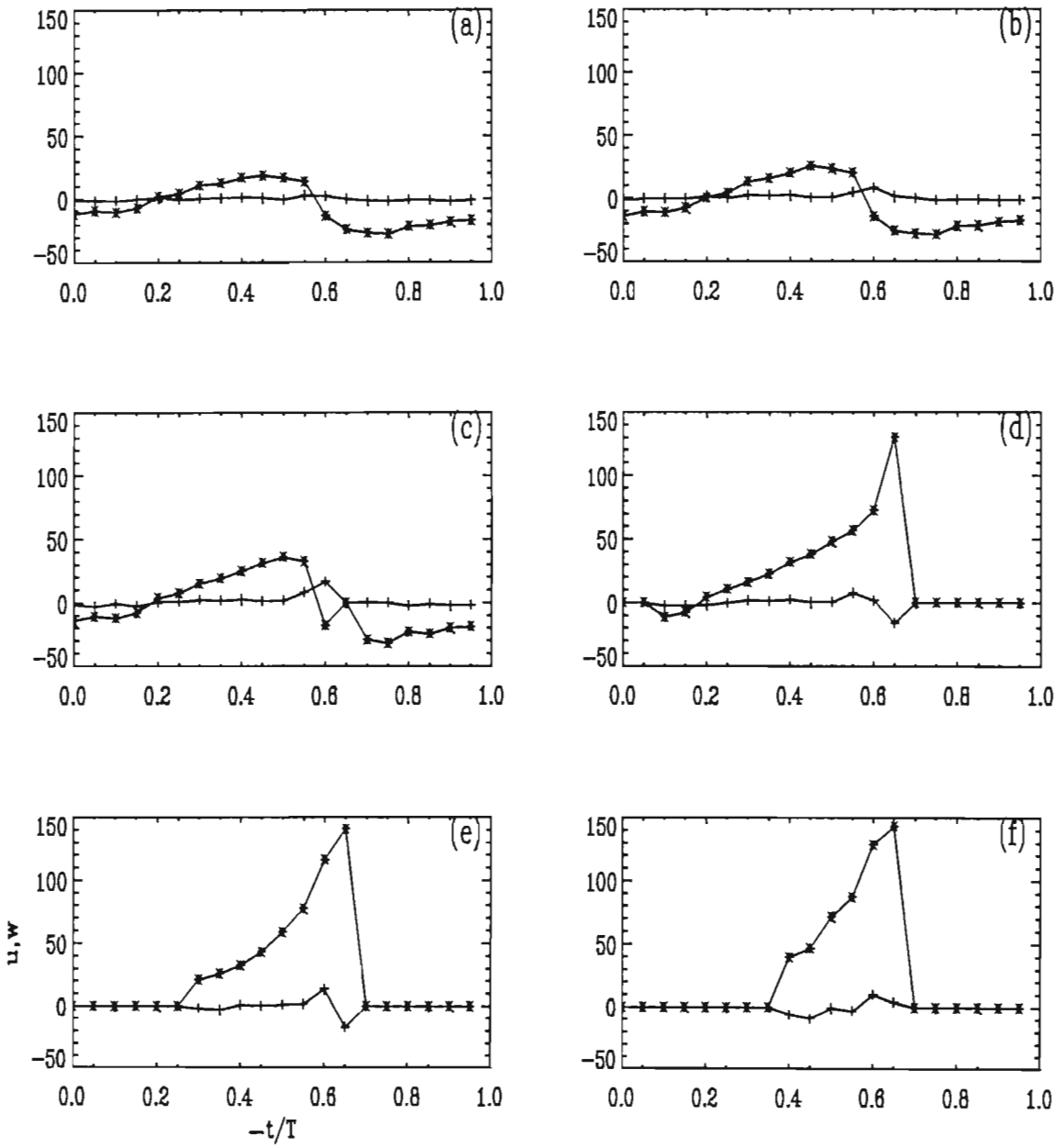

Figure 6.12: (B) Phase ensemble averaged velocities, $<u>$ (*) and $<w>$ (+) in cm/s, as a function of wave phase at depths (a) 2, (b) 4, (c) 5, (d) 7, (e) 9 and (f) 10 cm above the bed, extracted from Figure 6.12(A).

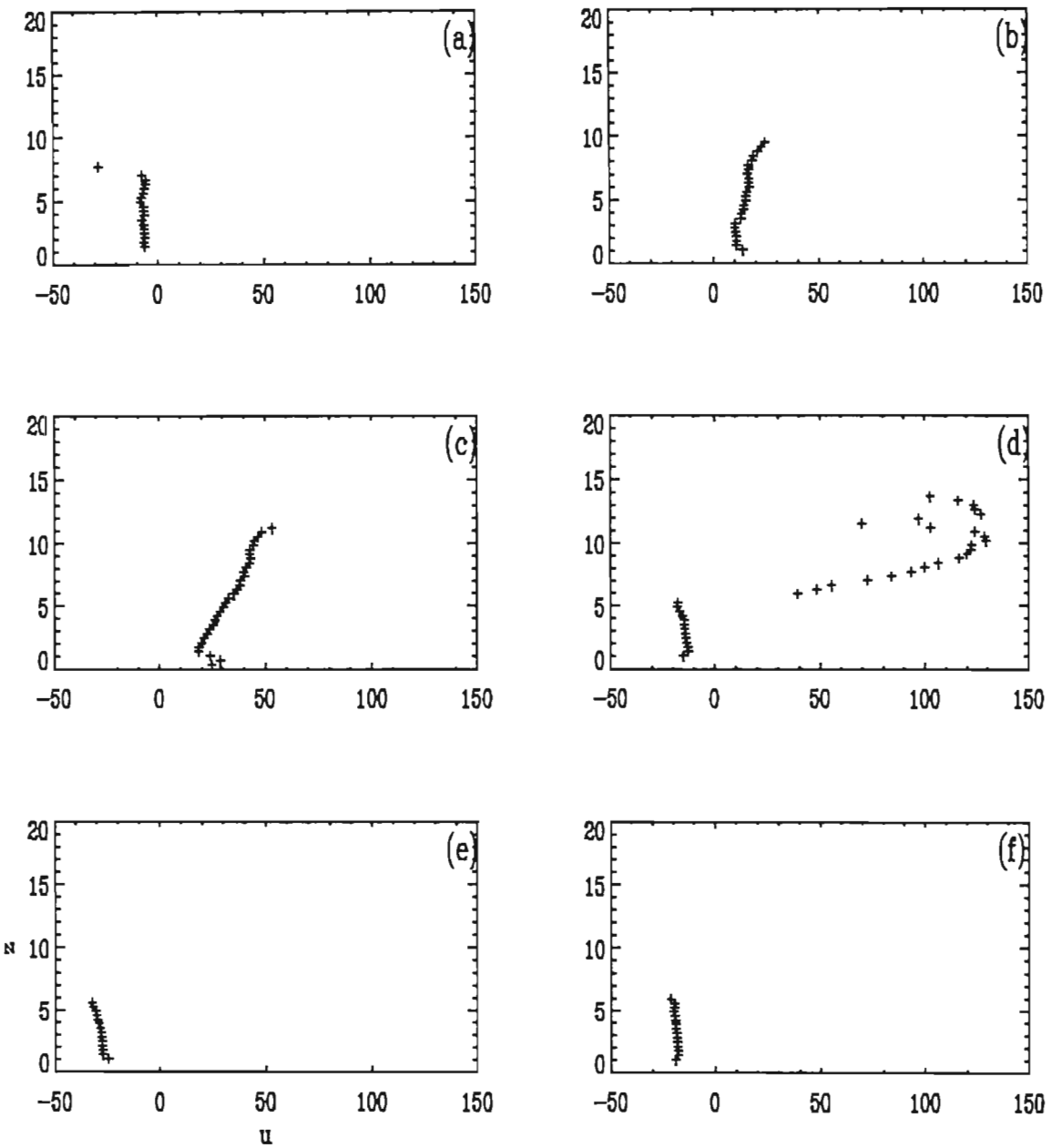

Figure 6.12(C): Ensemble-averaged horizontal velocity, $<u(z)>$, at wave phases, t/T, (a) 0.125, (b) 0.25, (c) 0.375, (d) 0.5, (e) 0.625 and (f) 0.75, extracted from Figure 6.12(A). u(cm/s) and z(cm) are plotted on the x and y axes, respectively

6.5.2 Time-averaged horizontal flow in the plunging wave

The time-average of the horizontal velocity component, $<u(z)>$, at stations 1, 3 and 4 are shown in Figures 6.13, 6.14 and 6.15, respectively. These time-averaged velocities were derived from the phase ensemble-averaged velocity using Equation 6.3. There is a forward mass flux in the region above the trough level and a reverse flow below the trough level. Station 1 corresponds to a pre-breaking position for the plunging case and the flow here, neglecting boundary layer effects, can be considered to be non-turbulent. The undertow at station 1 are very similar to pre-breaking measurements by *Putrevu and Svendsen(1993)*. Since there is no fluid leaving or entering the flume, there should be a conservation of mass across a vertical cross section of the flume. The time-averaged flow at station 1 shows the conservation of mass, that is, the total forward mass flux is approximately equal to the total reverse mass flux. Table 6.5 summarises the peak forward and reverse flow in the plunging wave at stations 1, 3 and 4.

Once again there is a discrepancy between the total forward and reverse mass fluxes further in the surf zone, due to the fact that there is greater aeration present at station 3 and 4, reducing the effective density of the fluid in the crest region.

Table 6.5: Peak time-averaged forward and reverse flow in the plunging wave.

$x-x_b$ (cm)	(station 1)1.11	(station 3) 0.86	(station 4) 1.69
Peak forward velocity (cm/s)	10	30	18
Peak reverse velocity (cm/s)	-10	-20	-7

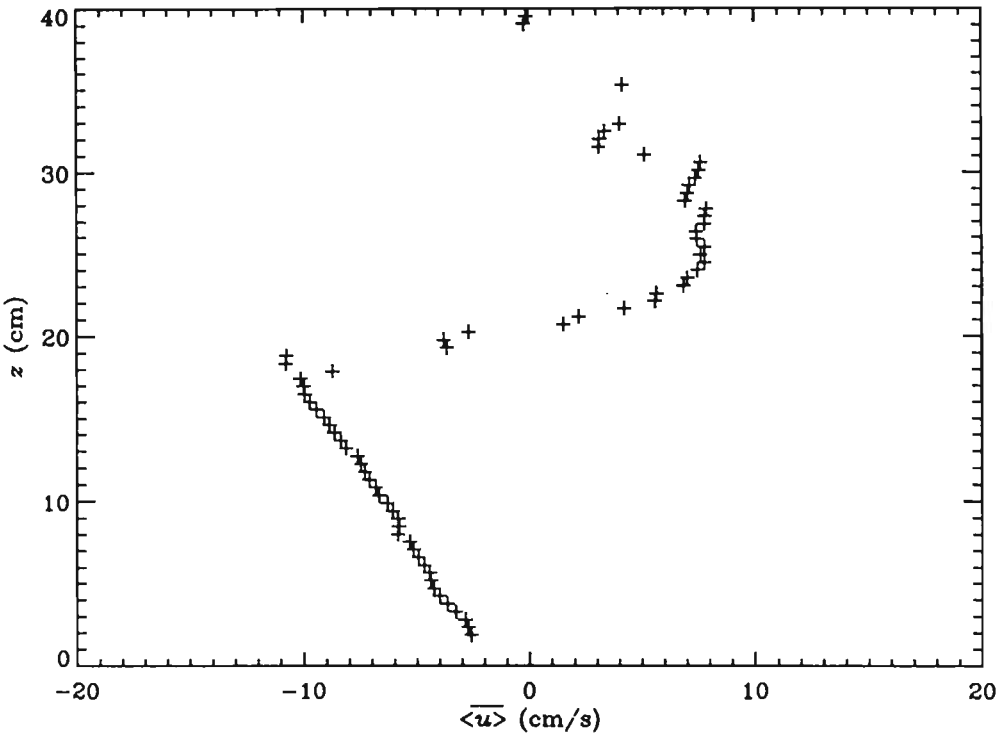

Figure 6.13: Time-averaged horizontal velocity component, $<\overline{u(z)}>$, of a plunging wave at station 1 which is located ~ 1.11 m before the plunge-point.

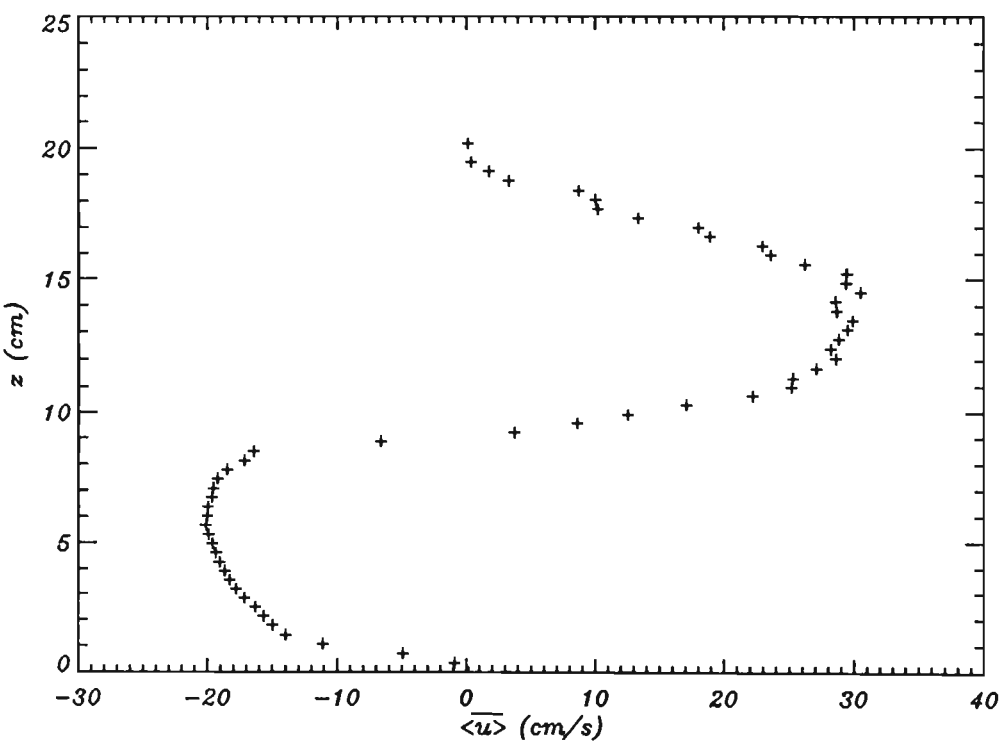

Figure 6.14: Time-averaged horizontal velocity component, $<\overline{u(z)}>$ in cm/s, of a plunging wave at station 3 which is located ~ 0.86 m beyond the break-point.

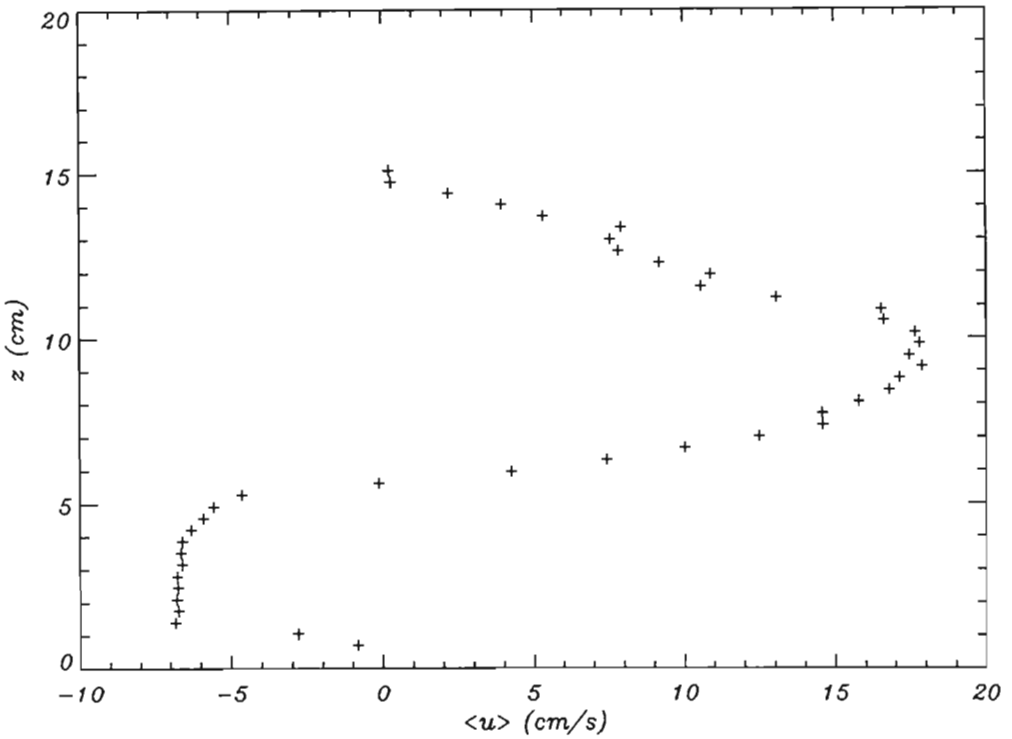

Figure 6.15: Time-averaged horizontal velocity, $<u(z)>$, of a plunging wave at station 4 which is located ~ 1.69 m beyond the break-point.

The forward and reverse mass flux at each measurement station as been computed using the time-averaged horizontal velocity. These are presented in Table 6.6 below. The fractional density of the fluid in the crest of the wave is computed using the ratio of the reverse and forward mass fluxes. These are also shown below.

Table 6.6: Forward and reverse mass flux in plunging waves

$x-x_b$ (m)	-1.4	0.5	1.5
Forward mass flux ($x10^{-4}$ kg/ms)	$\rho_r 131.4$	$\rho_r 209.1$	$\rho_r 102.4$
Reverse mass flux ($x10^{-4}$ kg/ms)	$-\rho 144.9$	$-\rho 143.1$	$-\rho 27.7$
Fraction density of crest	~ 1	~ 0.7	~ 0.3

The computed fractional density of the fluid in the crest of the wave shows that there is increasing aeration as the wave moves across the surf zone, which also corresponds to the

aeration measurements presented in Chapter 5.

6.6 Measured and predicted orbital velocities

The phase ensemble-averaged flow fields in the spilling and plunging waves showed a high degree of asymmetry in the velocity profile across the phase. The peak horizontal velocities, in the crest of the waves, also showed a rapid increase above the trough level. A comparison of the peak orbital velocities across the depth with those predicted by linear theory is useful, since linear theory is often used to obtain a first estimate of the peak velocities. A comparison with Stokes 2nd order theory is also provided. In shallow water the Stokes 2nd horizontal velocity is given by:

$$u = u^{(1)} + u^{(2)}$$

where $u^{(1)}$ is given by Equation 2.10 in Chapter 2 and $u^{(2)}$ is given by (*Fredsoe & Deigaard, 1992*):

$$u^{(2)} = \frac{3}{4}\left(\frac{H}{2}\right)^2 \omega k \frac{\cosh(2k(d+z))}{\sinh^4(kd)} \cos(2(\omega t - kx)) - \frac{H^2}{8cg}$$

Figures 6.16 shows the measured and predicted peak horizontal velocities in the spilling and plunging waves at stations 1 and 3. In the plunging wave at station 1 (which corresponds to a prebreaking position for this case) there is a close correspondence between the measured and linear predicted values below the approximate trough level. Above the trough level there is an increasing error between the measured and predicted values. In the spilling wave at station 1 and 3 and in the plunging wave at station 3, linear theory over predicts by more than 50% near the bed and under-predicts in the wave crest.

Comparison with Stokes 2nd order theory shows that the predicted and measured profile are very similar for both spilling and plunging waves. In each case, however, there is an over-prediction by a constant amount over the entire water column. Near the bed at station 1, there is an over-prediction of $\sim 100\%$ in the spilling wave and $> 100\%$ in the plunging wave. Near the bed at station 3, the over-prediction in the spilling wave is $> 200\%$.

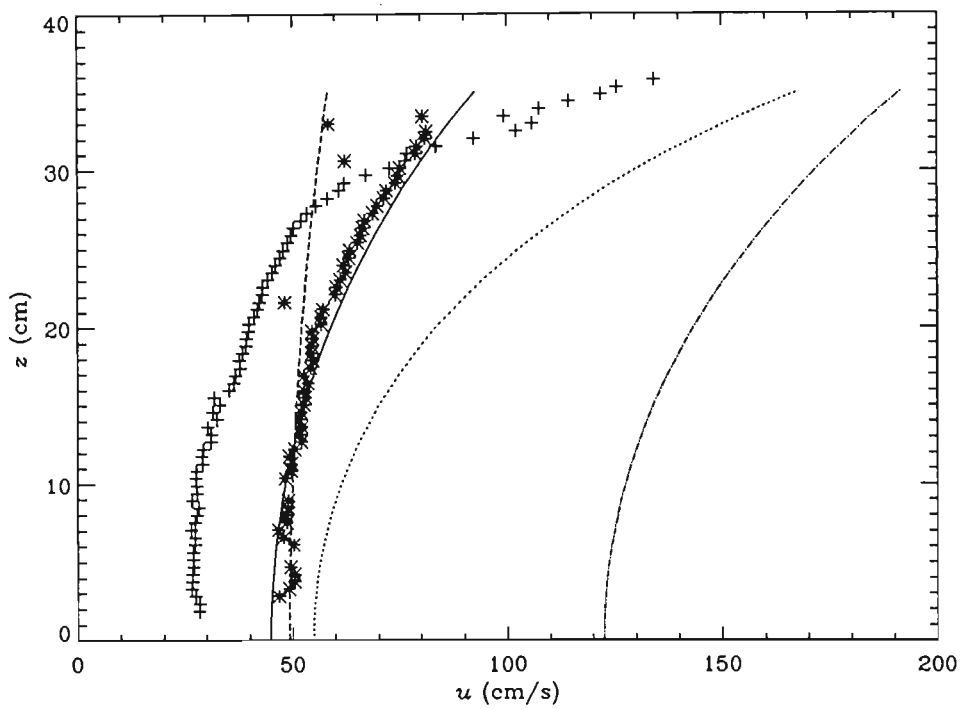

Figure 6.16:(A) Peak horizontal velocity, from measurements(+), linear(__) and 2nd order stokes(...) theories, in the spilling wave, and from measurements(*), linear (--) and 2nd order stokes(_._) theories, in the plunging waves, both at station 1.

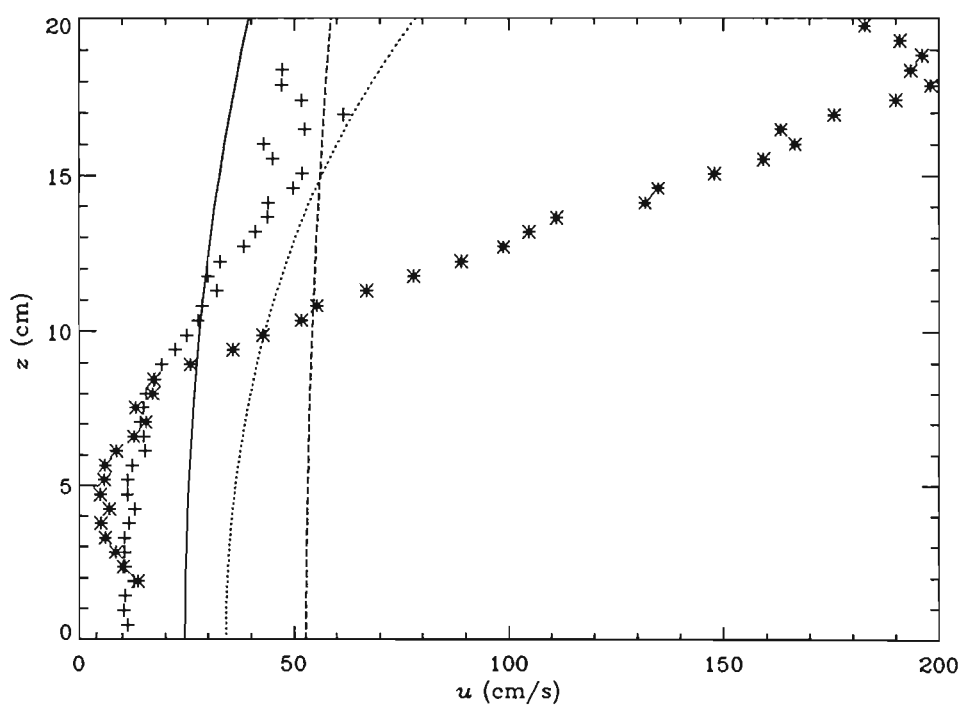

Figure 6.16:(B) Peak horizontal velocity, from measurements(+), linear(___) and 2nd order stokes(...) theories, in the spilling wave, and from measurements(*)and linear theory(--), in the plunging waves, both at station 3.

6.5 Sensitivity Analyses

The statistical averages, mean and standard deviation (some of which were computed in the previous sections) can be significantly influenced by the size of each bin and the number of samples within each bin if these experimental parameters are not chosen carefully. Ideally, the sample size should be as large as possible. However, for most cases there is a sample size for which the deviation from the true averages is small and it is important to determine this minimum sample size. The bin size on the other hand should be small enough so that the processes occurring within each bin is correlated, that is, the bin size should be smaller than the correlation radius of process. The choice of a particular bin size will result in turbulence features having a scale size smaller than the bin size to be smoothed out.

Bin size sensitivity

The computation of velocities, using DCIV, involves estimating the displacement of a small region of the fluid over a known time interval using cross correlation techniques. The estimated velocity is then an average velocity of the region in question and all variation within the region is lost. In order to effectively measure turbulent intensities and turbulent kinetic energies it is necessary that the pattern box be sufficiently small so that there is very little velocity variation with the pattern box. Using a pattern box that is too large results in lower estimates of turbulent intensities and kinetic energies. The velocities presented in this thesis were estimated using a 24 $\times$ 24 pixel pattern box. This pattern size corresponds to a $\sim$1 cm $\times$ 1 cm region in the actual flow. This box size was chosen on the basis of seed densities that were available in the images and also to obtain as many velocity estimates at a given point within the wave phase from a set of 150 image pairs. *Willert and Gharib(1991)* show results of error associated with varying seed densities and conclude that a seed density of 5 seeds per pattern box results in an error, in estimating the peak position in the correllogram, of 0.03 pixels. In order to show that the chosen pattern size is sufficiently small, the mean and turbulent velocity components were computed for the spilling and plunging waves at station 3 using pattern sizes of 16 $\times$ 16, 20 $\times$ 20, 24 $\times$ 24, 28 $\times$ 28 and 32 $\times$ 32 pixels. The results of the mean and turbulent velocities at selected positions, as a function of bin sizes, are presented.

Figures 6.17 shows the wave profile and the maximum number of available sample/bin for pattern sizes 16 × 16, 20 × 20, 24 × 24, 28 × 28 and 32 × 32 pixels, at wave phases 0, 1/5, 2/5, 3/5 and 4/5 for the spilling wave at station 3. Figures 6.18 shows the wave profile and the maximum number of available sample/bin for pattern sizes 16 × 16, 20 × 20, 24 × 24, 28 × 28 and 32 × 32 pixels, at wave phases 0, 1/6, 2/6, 3/6, 4/6 and 5/6 for the plunging wave at station 3. At each position in figures 6.17 and 6.18, that is wave phase and height above the bed, there are 5 numbers listed corresponding to pattern sizes 16 × 16, 20 × 20, 24 × 24, 28 × 28 and 32 × 32 pixels, respectively. Examination of the numbers in these figures reveals that for the 24 × 24 pattern size there are in the region of 40 to over 100 samples per position, which is typical of the number of samples that were used in computing the mean and turbulent velocity for all the other positions and wave cases presented in this thesis. There are at some positions a low number of samples (in the order of 28) which occur mostly near the wave surface. *Stive(1980)* used 20 samples in computing the mean and turbulent intensities. *Ting and Kirby(1994)* used measurements from 102 wave cycles in their computation, however, due to signal drop-out not all of the 102 measurements were actually used. *Craig and Thieke(1996)* employed approximately 60 wave samples per bin in their computation. Thus the number of samples used in calculating each data point in this work is comparable to or exceed the number employed by other researchers. At each position in figures 6.16 and 6.17, the mean and turbulent velocities were computed for each of the pattern size. The results for a subset of positions identified by a * in Figures 6.17 and 6.18 are presented below.

Figures 6.19-6.22 shows the effects of bin size on the mean and turbulent velocities for the spilling wave and Figures 6.23-6.26 show the result for the plunging case. Each figure contains six plots labelled a-e, corresponding to measurements at wave phase, t/T, of 0, 1/6, 2/6, 3/6, 4/6 and 5/6 respectively. Each plot contains the measured quantity at vertical positions identified by a * in figures 6.16 and 6.17. The symbols +, *, ◇, ◇ and the dotted and dashed line represent measurements at 2, 4, 6, 8, 10.3 and 12 cm above the bed, respectively.

These plots show that the mean, $<u>$, is almost insensitive to the bin size, showing only minor variation at only some places. Turbulent velocities, u'_{rms} and w'_{rms}, as a function of

pattern or bin size show that, for bin sizes of 20 × 20, 24 × 24,and 28 × 28, the estimates are very much the same, with variation being of the order of 10%. There is a decrease in the estimated values at the largest bin size, 32 × 32, which is expected for the reason explained at the beginning of this section. There is also an increase in the estimate using the smallest bin size, 16 × 16, this due mostly to the fact that there considerably less samples available for the computation, the sample size is now influencing the result. It will be shown in Chapter 7 that the smallest turbulent length scale are of the order of 1 cm or greater. Thus using a pattern size of 1 cm × 1 cm is deemed to be more than adequate.

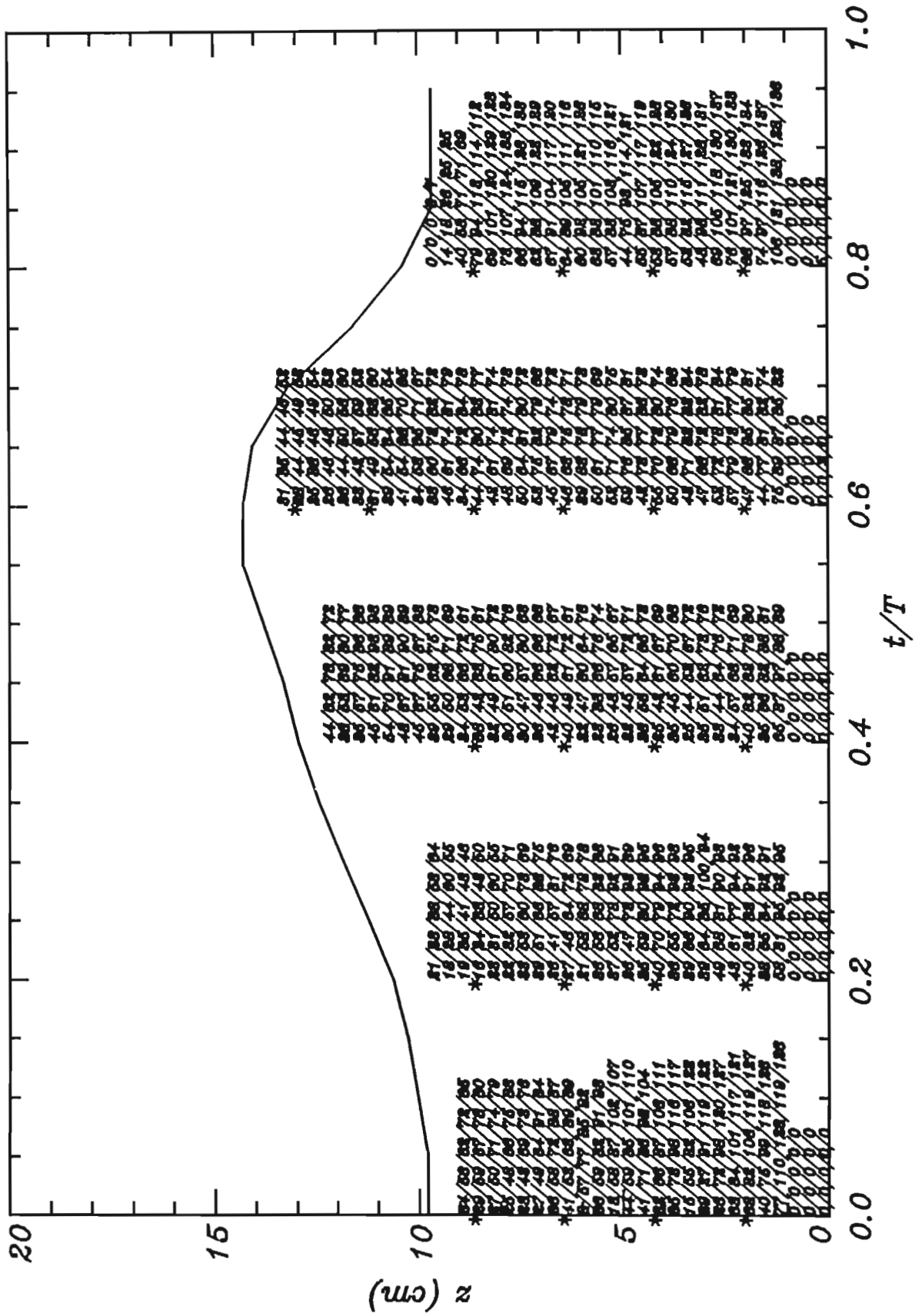

Figure 6.17: Maximum number of samples/bin for the spilling wave at station 3 for bin sizes, 16 × 16, 20 × 20, 24 × 24, 28 × 28 and 32 × 32 pixels. Results for -t/T of 0, 1/5, 2/5, 3/5 and 4/5 are given.

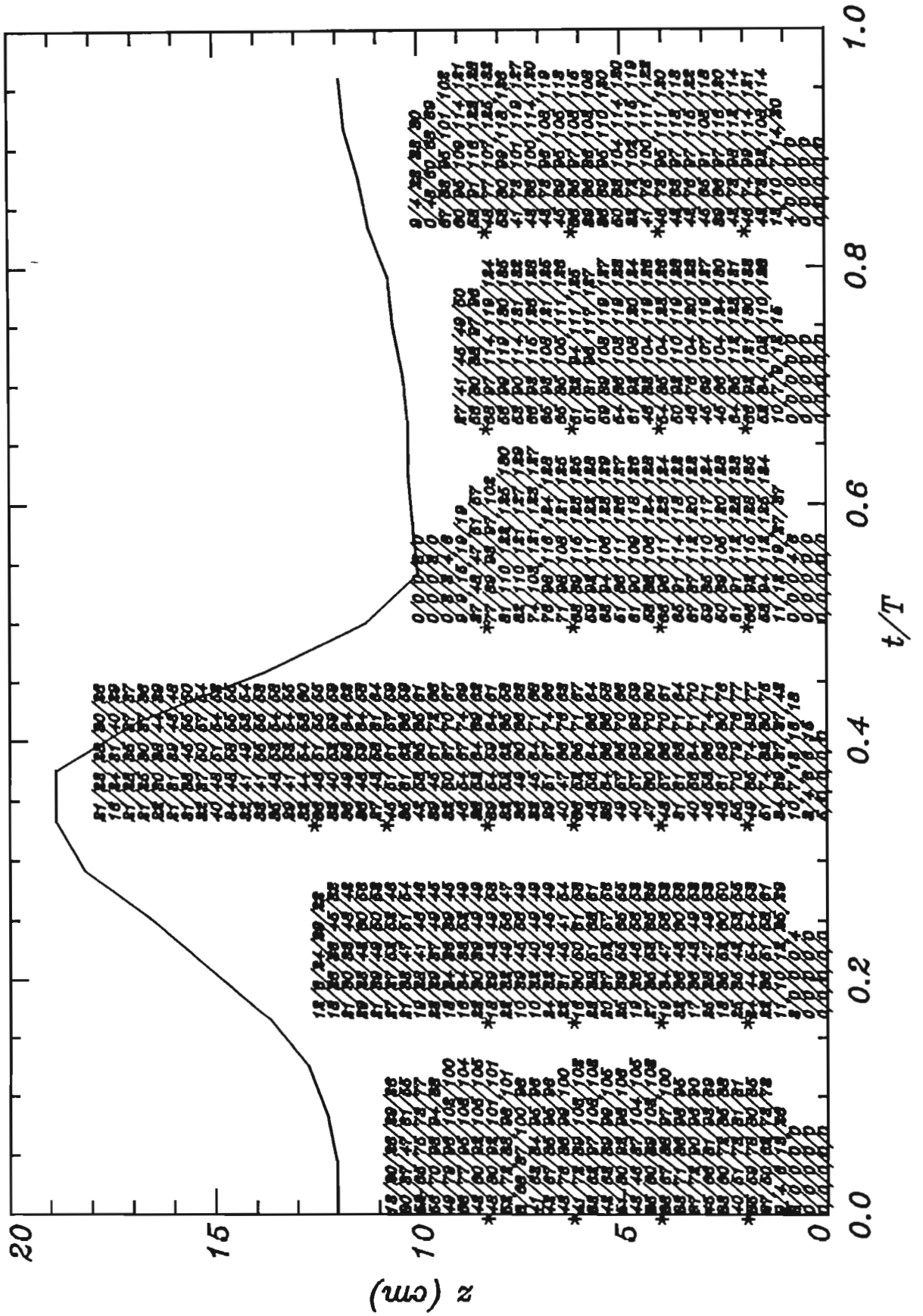

Figure 6.18: Number of samples/bin for the plunging wave at station 3 for bin sizes, 16 × 16, 20 × 20, 24 × 24, 28 × 28 and 32 × 32 pixels, respectively. Results for -t/T of 0, 1/6, 2/6, 3/6, 4/6 and 5/6 are given.

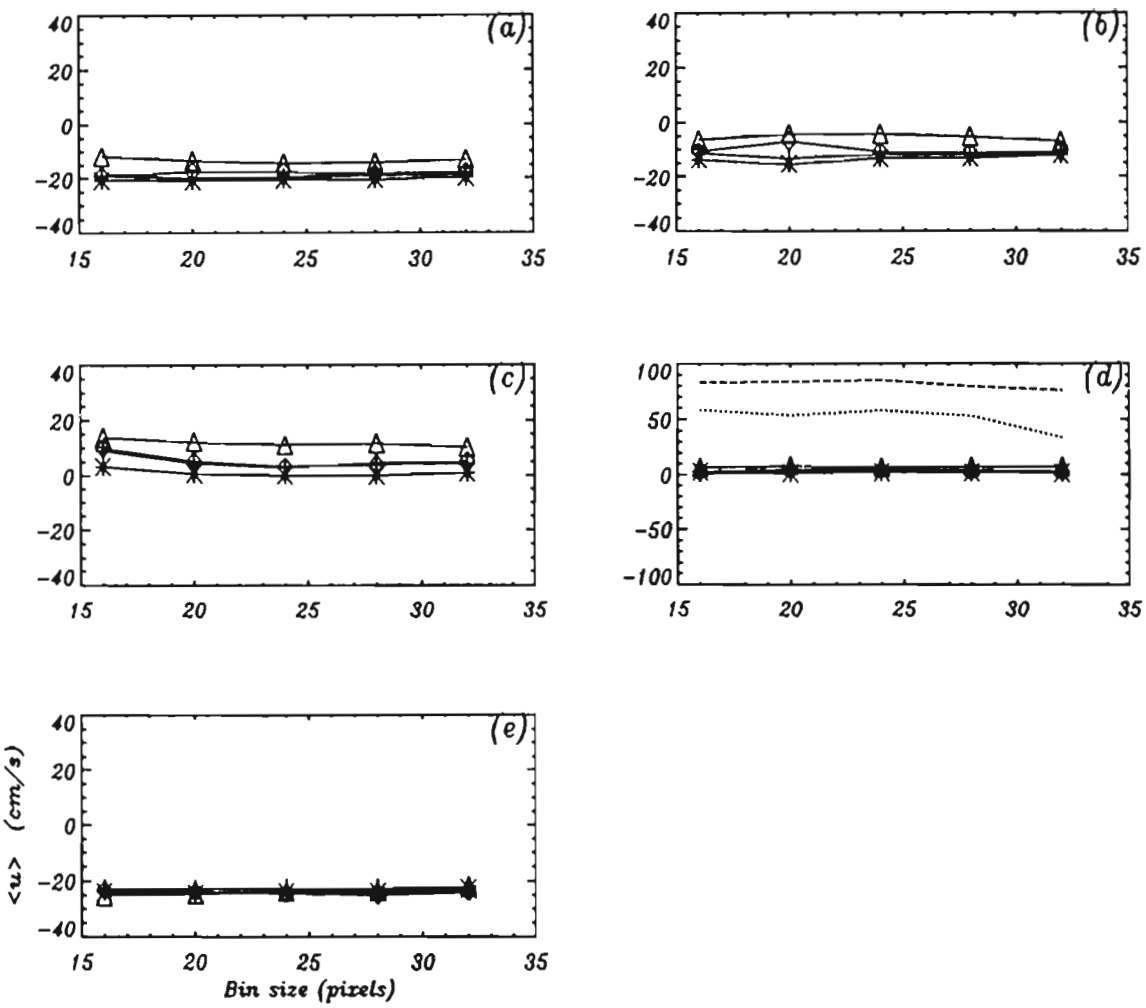

Figure 6.19: Dependence of $<u>$ on bin size for the spilling wave at station 3. Results are shown for t/T of (a)0, (b) 1/5, (c) 2/5, (d) 3/5 and (e)4/5 and depths 2(+), 4(*), 6(◇), 8(△), 10.3(....) and 12(- - -) cm above the bed.

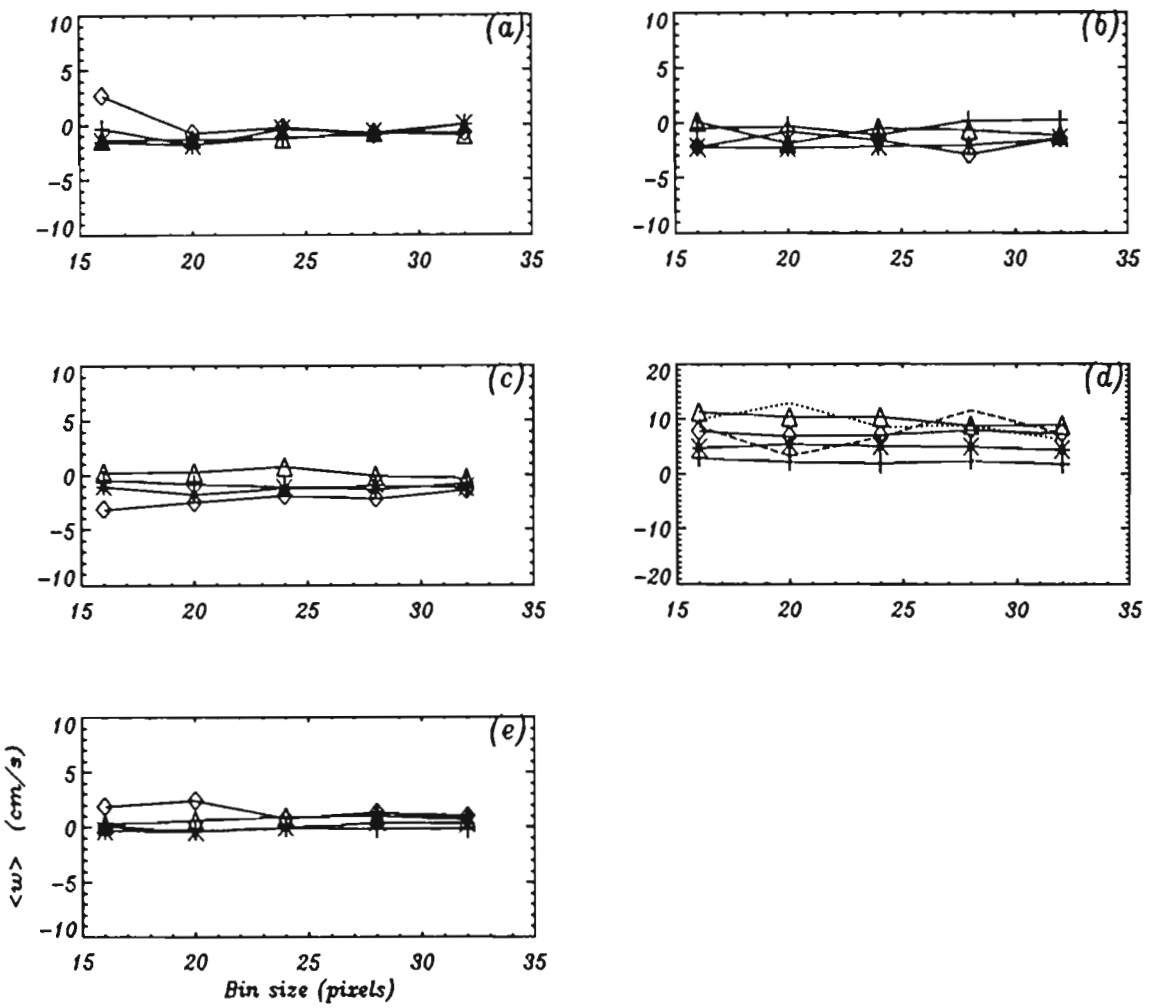

Figure 6.20:Dependence of <w> on bin size for the spilling wave at station 3. Results are shown for t/T of (a)0, (b) 1/5, (c) 2/5, (d) 3/5 and (e)4/5 and depths 2(+), 4(*), 6(◇), 8(△), 10.3(....) and 12(- - -) cm above the bed.

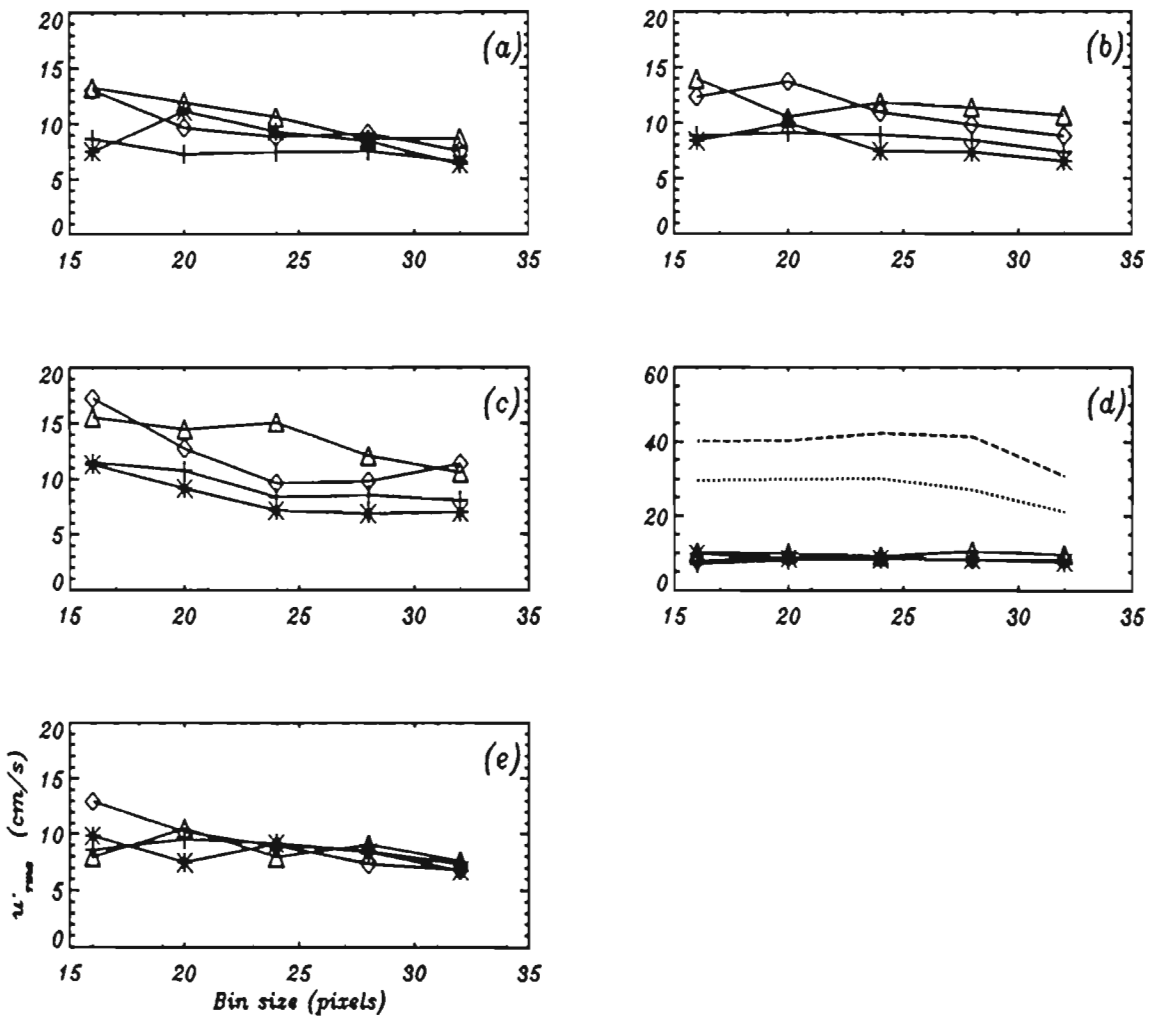

Figure 6.21:Dependence of u'_{rms} on bin size for the spilling wave at station 3. Results are shown for t/T of (a)0, (b) 1/5, (c) 2/5, (d) 3/5 and (e)4/5 and depths 2(+), 4(*), 6(◇), 8(△), 10.3(....) and 12(- - -) cm above the bed.

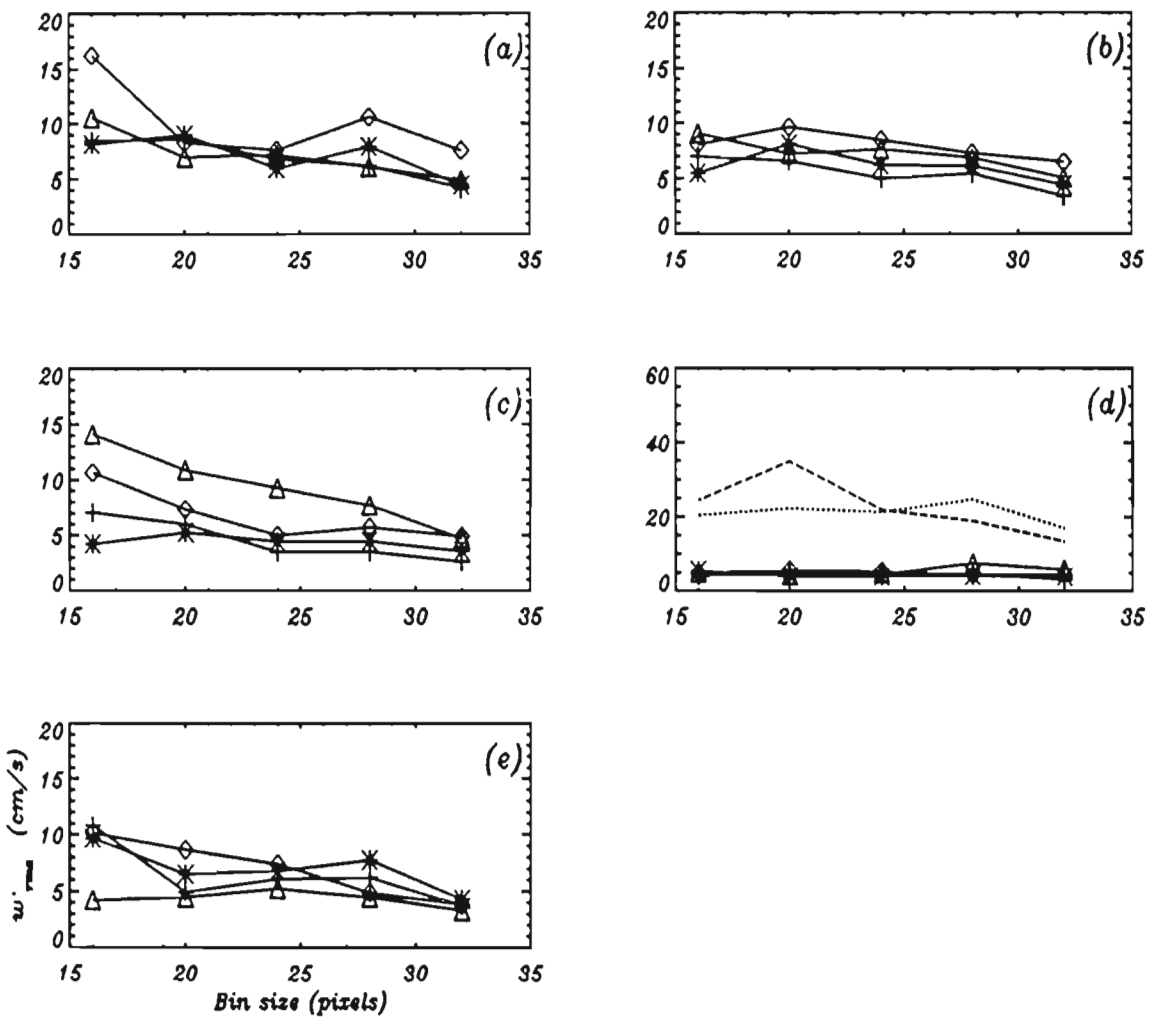

Figure 6.22:Dependence of w'_{rms} on bin size for the spilling wave at station 3. Results are shown for t/T of (a)0, (b) 1/5, (c) 2/5, (d) 3/5 and (e)4/5 and depths 2(+), 4(*), 6(◇), 8(△), 10.3(....) and 12(- - -) cm above the bed.

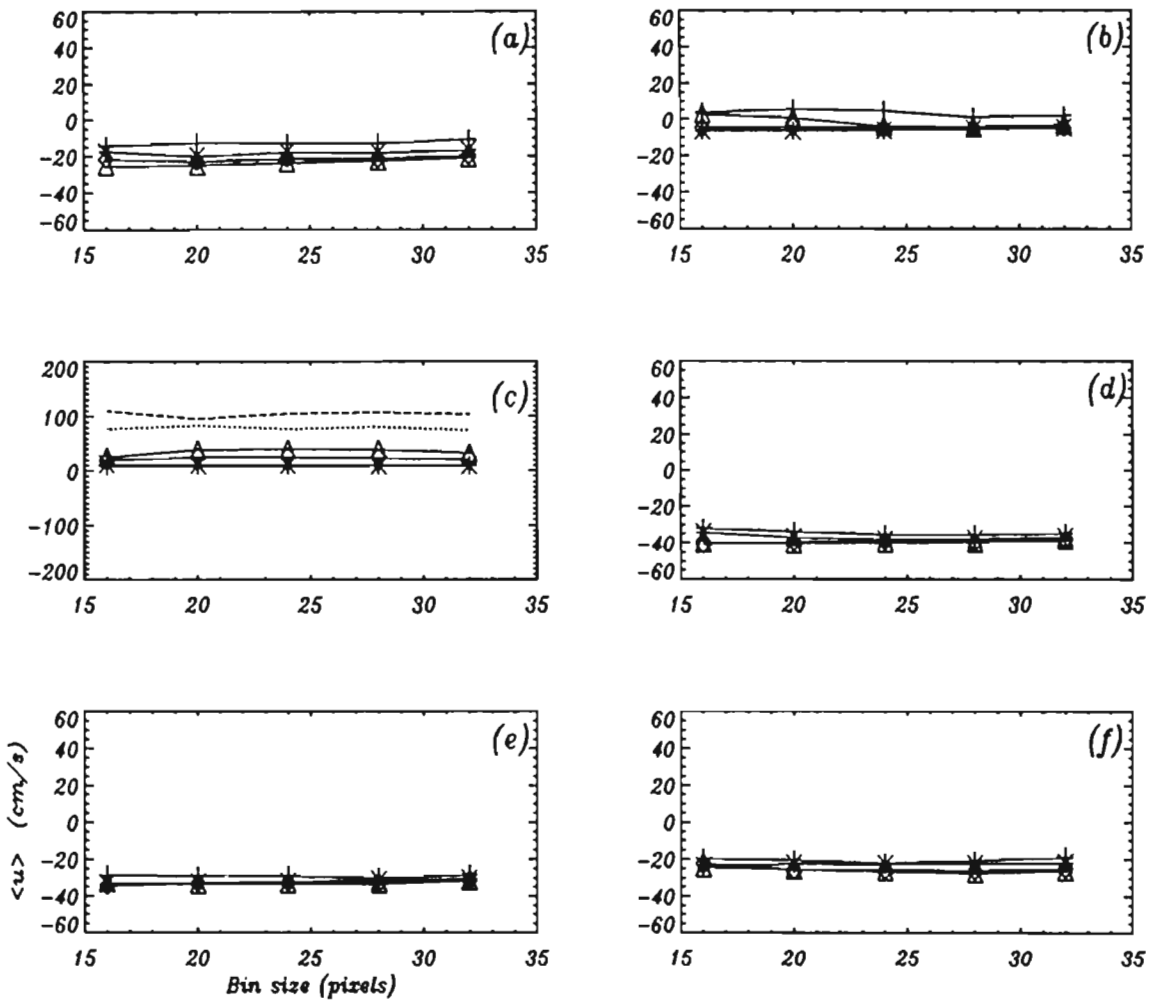

Figure 6.23: Dependence of <u> on bin size for the plunging wave at station 3. Results are shown for t/T of (a)0, (b) 1/6, (c) 2/6, (d) 3/6, (e) 4/6 and (f) 5/6 and depths 2(+), 4(*), 6(◇), 8(△), 10.3(....) and 12(- - -) cm above the bed.

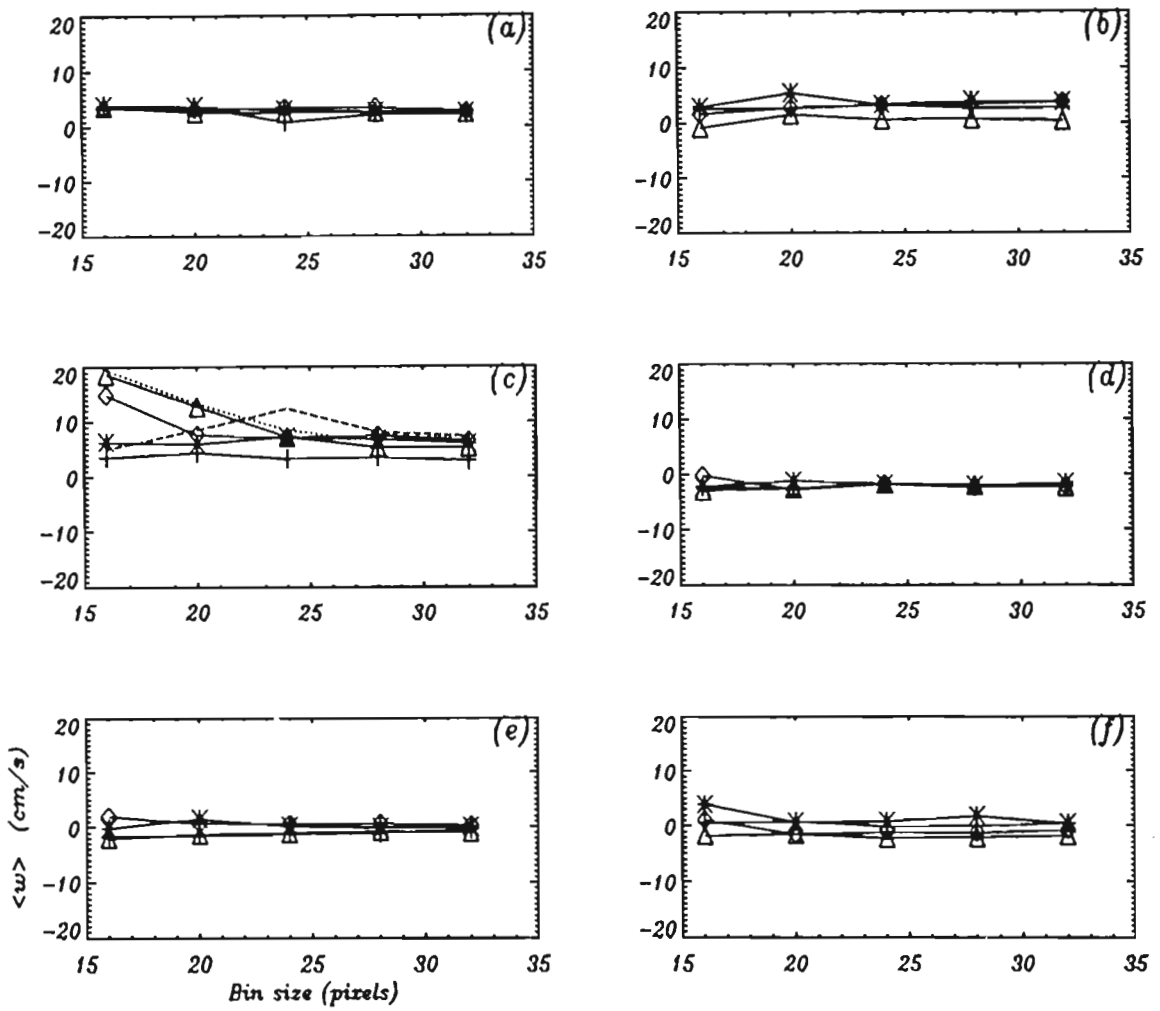

Figure 6.24:Dependence of $<w>$ on bin size for the plunging wave at station 3. Results are shown for t/T of (a)0, (b) 1/6, (c) 2/6, (d) 3/6, (e) 4/6 and (f) 5/6 and depths 2(+), 4(*), 6(◇), 8(△), 10.3(....) and 12(- - -) cm above the bed.

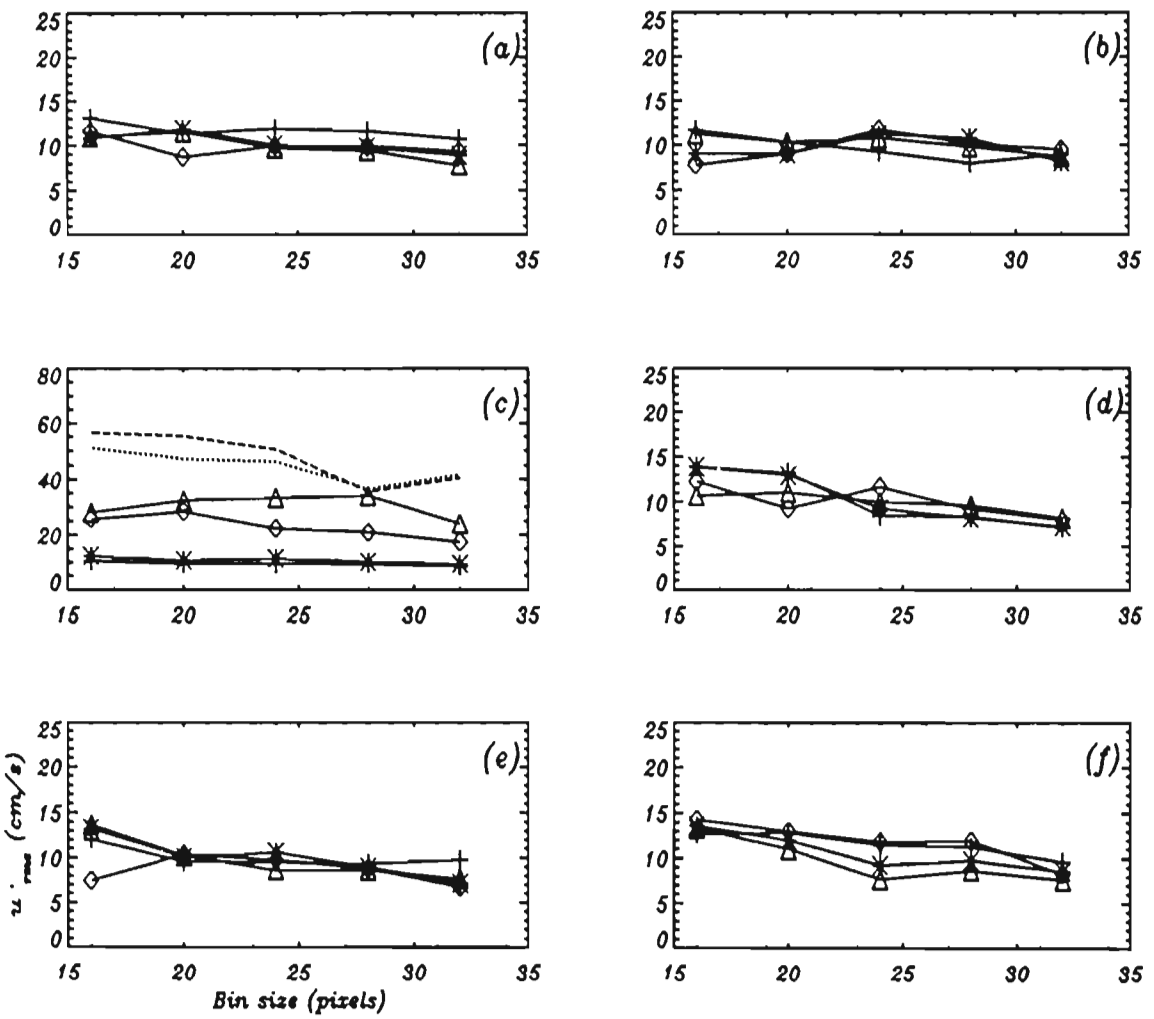

Figure 6.25: Dependence of u'_{rms} on bin size for the plunging wave at station 3. Results are shown for t/T of (a) 0, (b) 1/6, (c) 2/6, (d) 3/6, (e) 4/6 and (f) 5/6 and at 2(+), 4(*), 6(◇), 8(△), 10.3(..) and 12(- -) cm above the bed.

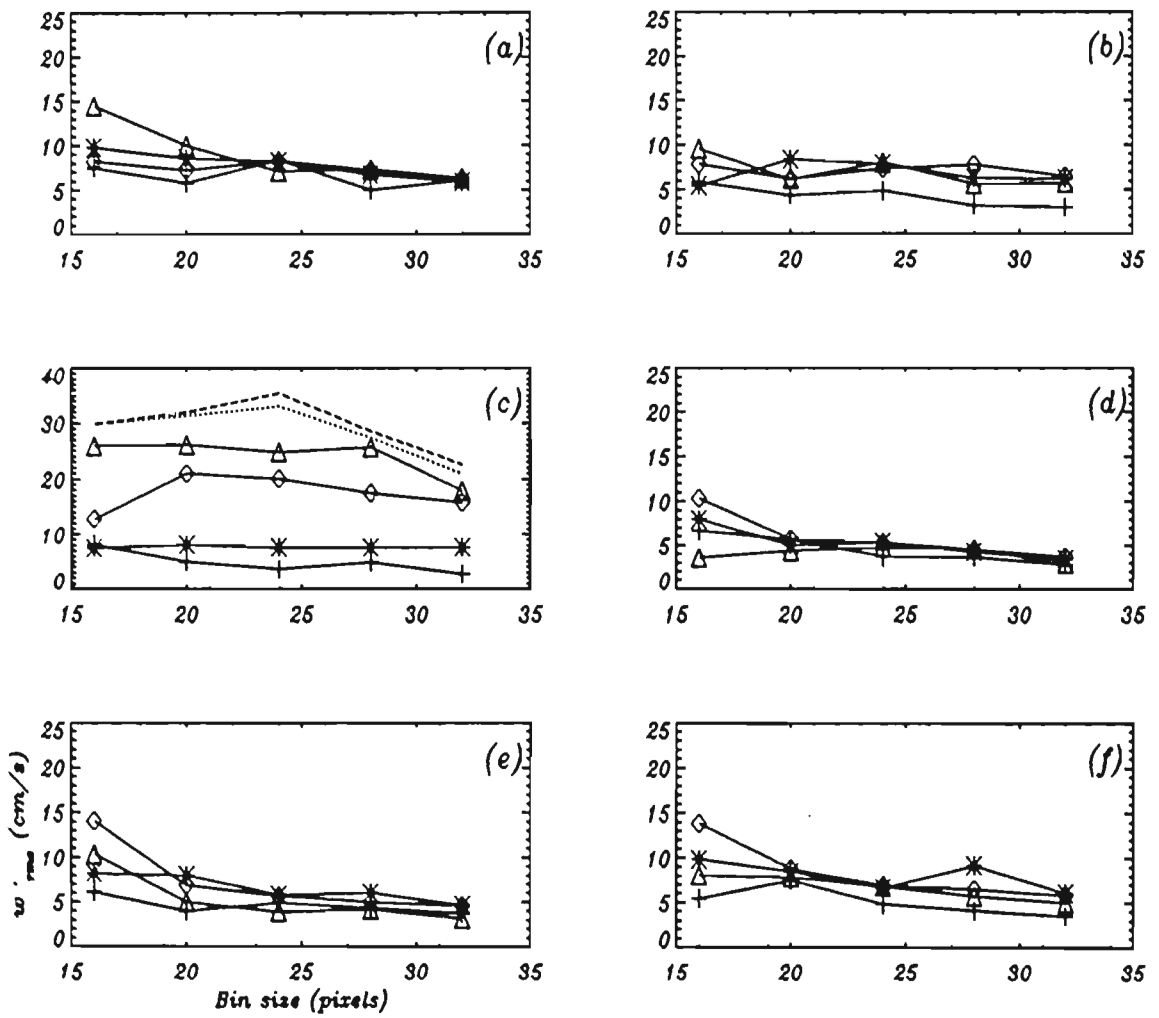

Figure 6.26:Dependence of w'_{rms} on bin size for the plunging wave at station 3. Results are shown for t/T of (a) 0, (b) 1/6, (c) 2/6, (d) 3/6, (e) 4/6 and (f) 5/6 and at 2(+), 4(*), 6(◇), 8(△), 10.3(..) and 12(- -) cm above the bed.

Sample size sensitivity

The effects of the sample size on the mean and turbulent components will be investigated here with a view to estimating errors associated with the measurements. For these purposes the velocity data obtained using the 24 × 24 bin size in Figures 6.17 and 6.18 will be used.

The effects of the sample size on the convergence of the mean and standard deviation are investigated by computing these quantities using various sample sizes and examining the manner in which they converge. Figures 6.27-6.34 shows the dependence of $<u>$, $<w>$, $\sqrt{<u'^2>}$ and $\sqrt{<w'^2>}$ on the sample size per bin for the spilling and plunging wave flow fields measured at station 3.

Each figure contains six plots labelled a-e, corresponding to measurement at wave phase, *t/T*, of 0, 1/6, 2/6, 3/6, 4/6 and 5/6 respectively. Each plot contains the measured quantity at vertical positions identified by a * in Figures 6.16 and 6.17. The symbols +, *, ◇, ▵ and □ represent measurements at 2, 4, 6, 8 and 12 cm above the bed, respectively. The unmarked curve represent measurement at 10.3 cm above the bed. The curves in each plot are drawn by joining individual data points and only a few symbols are used to identify each curve.

The mean converges rather quickly, that is, within 20 samples. There is also a mild deviation from the asymptotic value as sample size is decreased. The standard deviation is, however, much more sensitive to the sample size. The $\sqrt{<u'^2>}$ component appears to converge only after 20 to 30 samples. Even here, there is an error of approximately 10% from the asymptotic value. The behaviour of $\sqrt{<w'^2>}$ is very similar to the mean components, that is, it also converges after about 10 samples. A similar test performed by *Ting and Kirby(1994)* showed that $\sqrt{<u'^2>}$ converges after approximately 40 samples. Thus, in summary it maybe conservatively concluded that ~25 samples/bin is adequate to ensure statistical convergence throughout the wave .

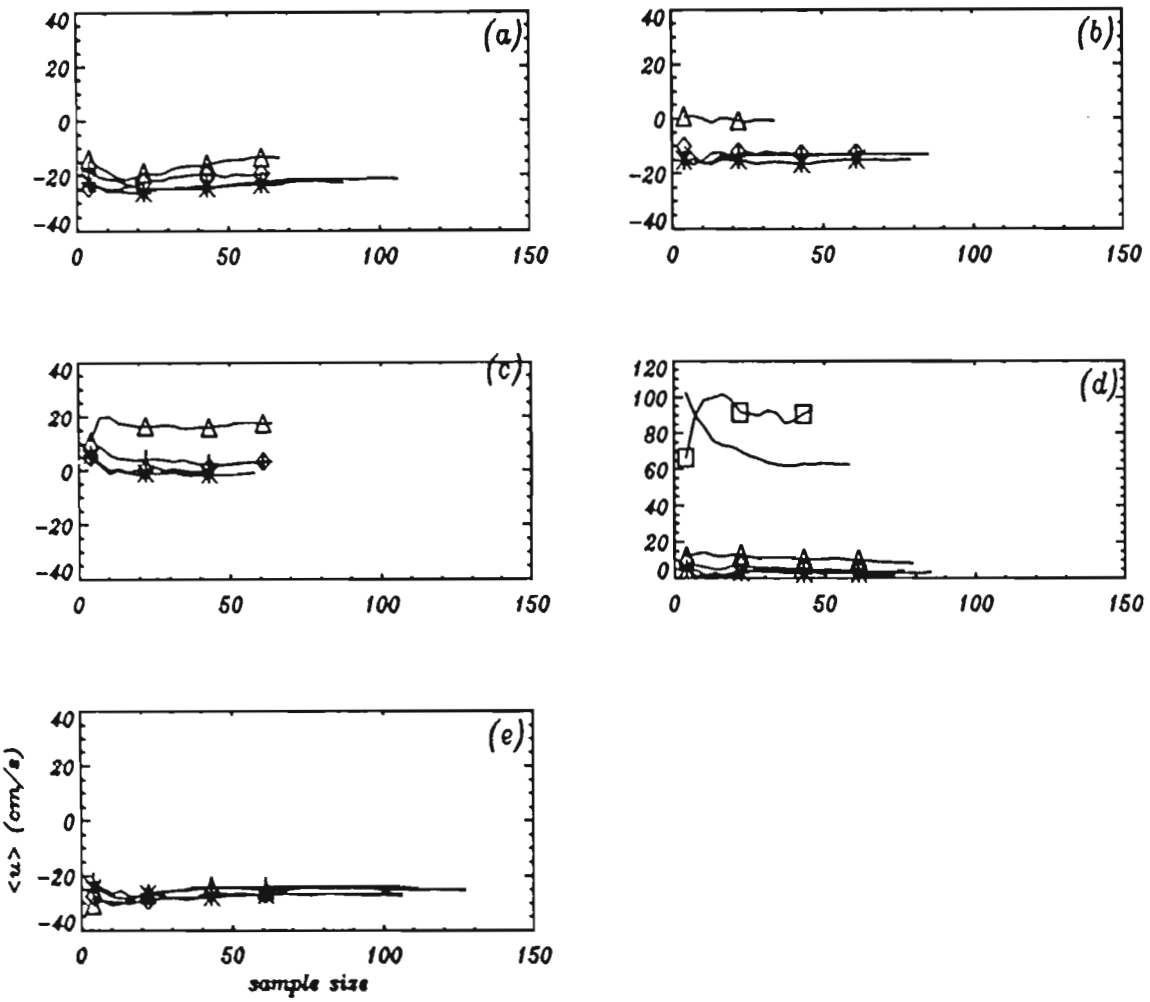

Figure 6.27: Dependence of $<u>$ on sample size for the spilling wave at station 3. Results are shown for t/T of (a) 0, (b) 1/5, (c) 2/5, (d) 3/5 and (e) 4/5 and at 2(+), 4(*), 6(◇), 8(▲), 10.3(no symbol) and 12(□) cm above the bed.

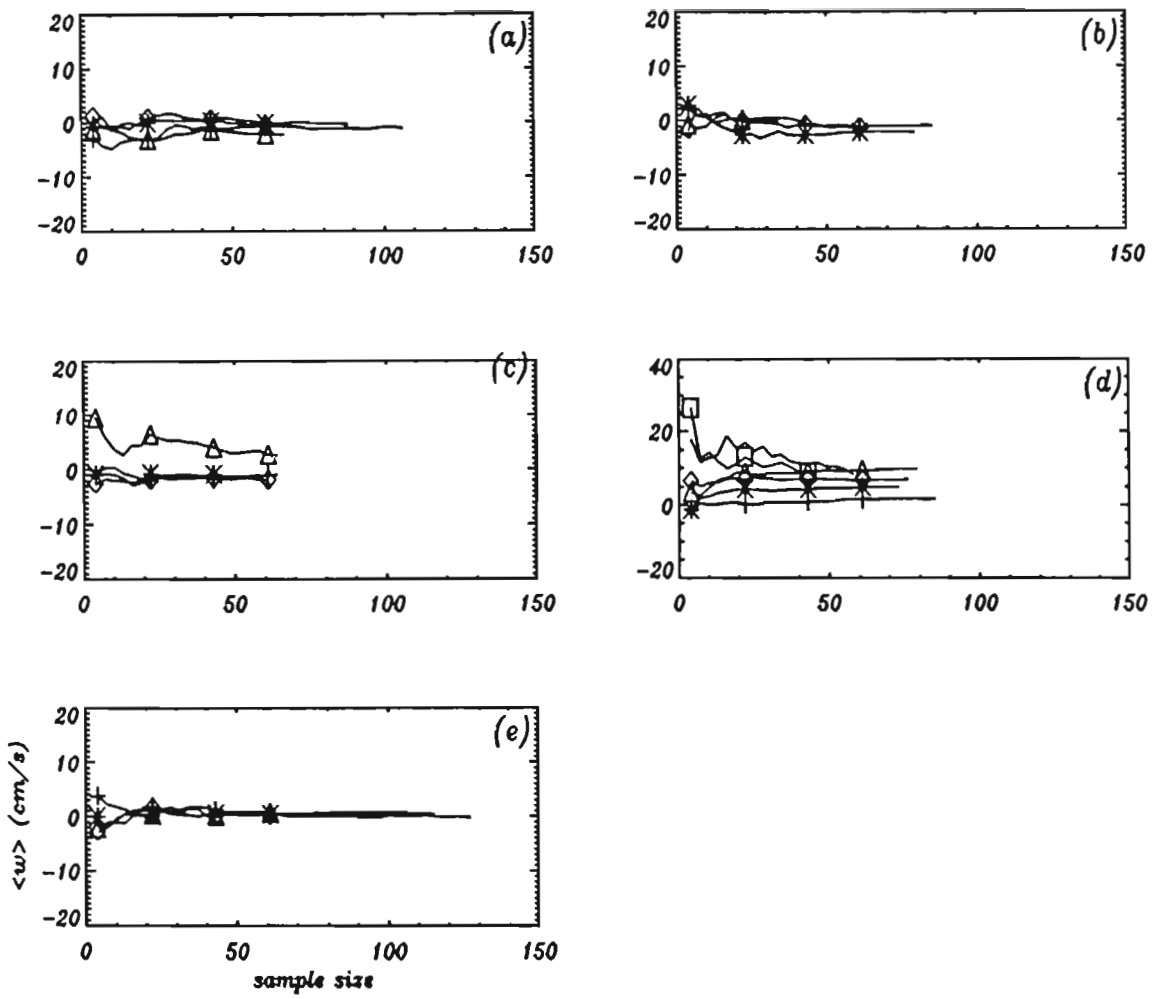

Figure 6.28:Dependence of <w> on sample size for the spilling wave at station 3. Results are shown for -t/T of (a) 0, (b) 1/5, (c) 2/5, (d) 3/5 and (e) 4/5 and at 2(+), 4(*), 6(◇), 8(▲), 10.3(no symbol) and 12(□) cm above the bed.

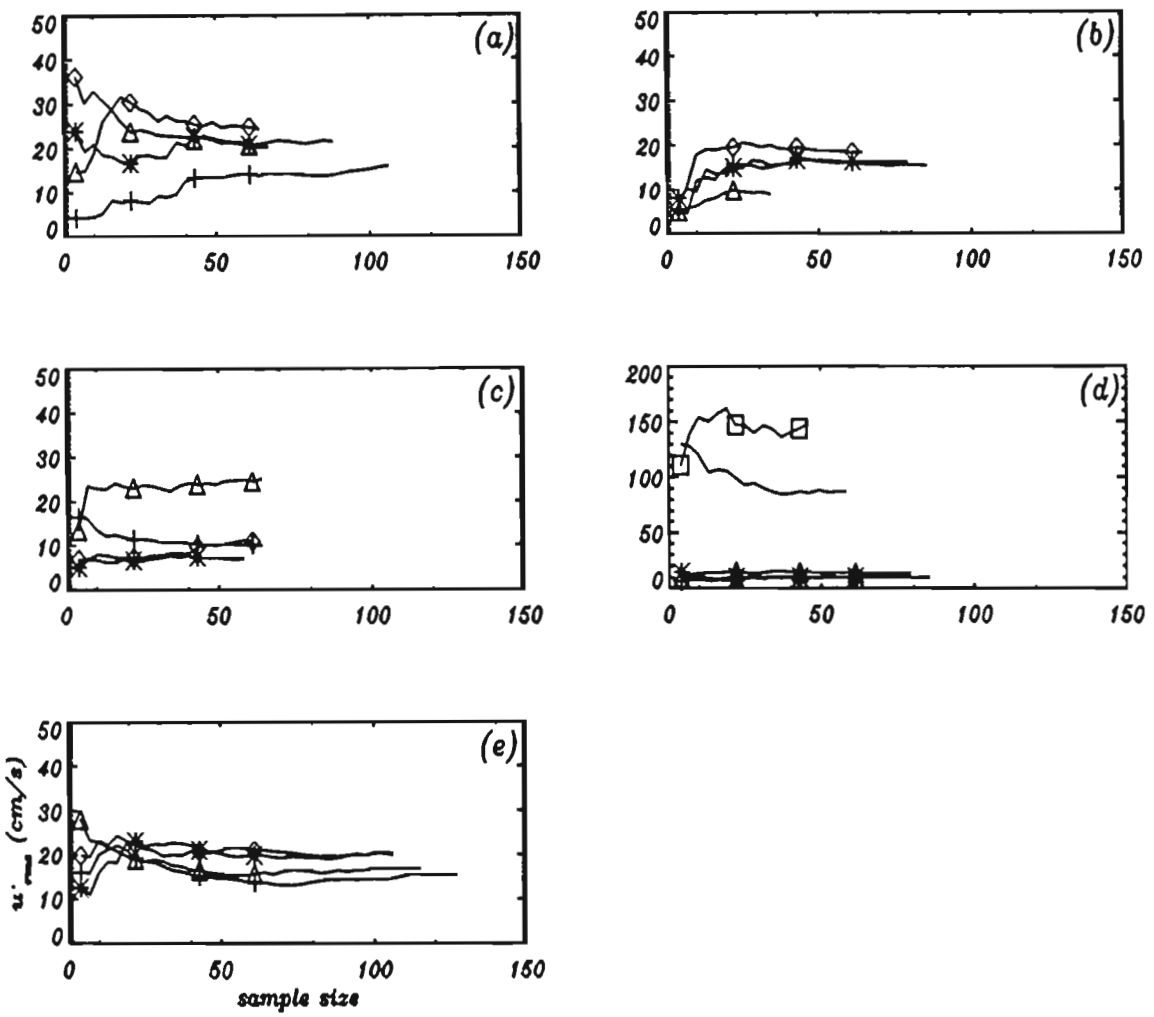

Figure 6.29:Dependence of u'_{rms} on sample size for the spilling wave at station 3. Results are shown for -t/T of (a) 0, (b) 1/5, (c) 2/5, (d) 3/5 and (e) 4/5 and at 2(+), 4(*), 6(◇), 8(▲), 10.3(no symbol) and 12(□) cm above the bed.

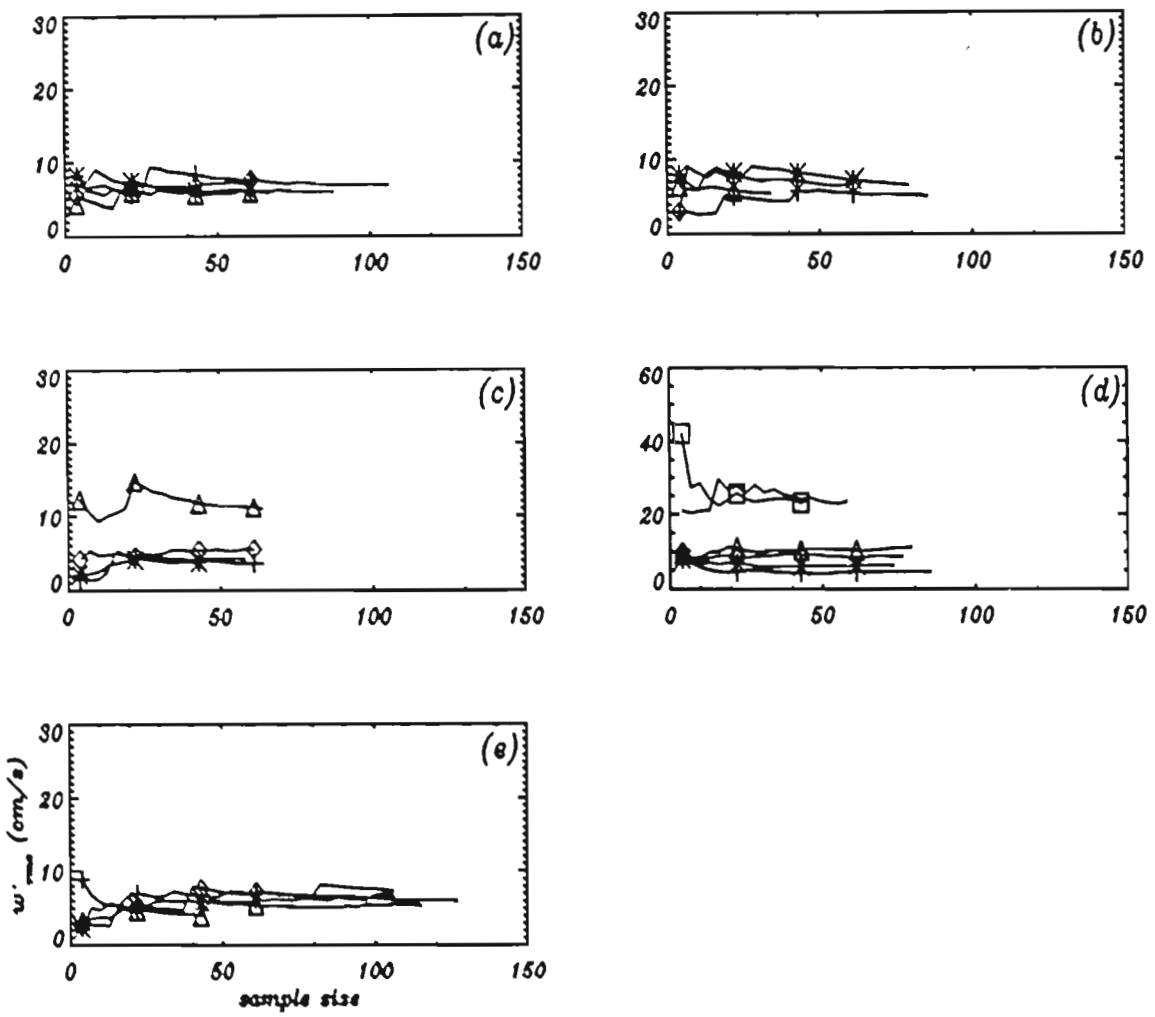

Figure 6.30: Dependence of w'_{rms} on sample size for spilling wave at station 3. Results are shown for -t/T of (a) 0, (b) 1/5, (c) 2/5, (d) 3/5 and (e) 4/5 and at 2(+), 4(*), 6(◇), 8(▵), 10.3(no symbol) and 12(□) cm above the bed.

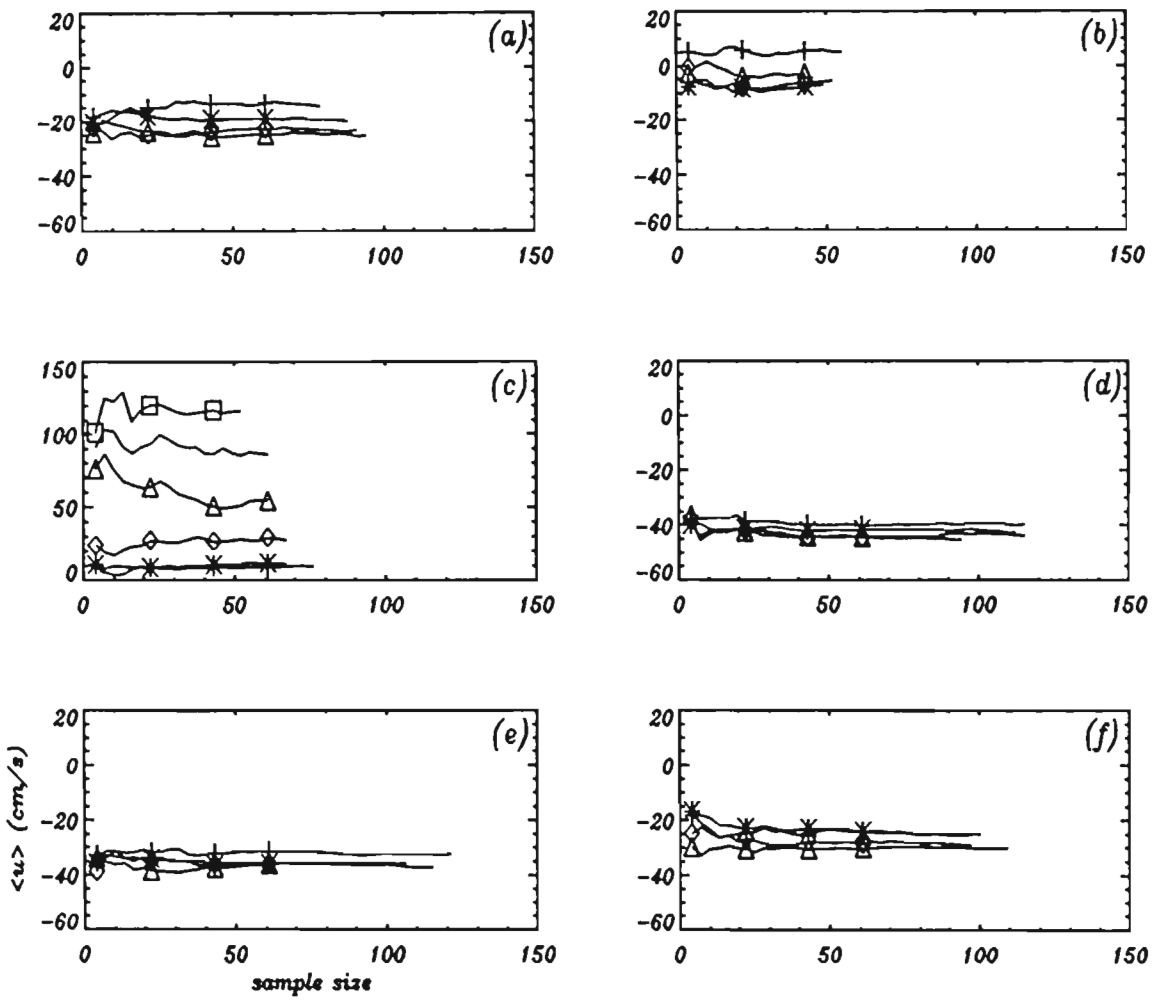

Figure 6.31: Dependence of <u> on sample size for the plunging wave. Results are shown for -t/T of (a) 0, (b) 1/6, (c) 2/6, (d) 3/6, (e) 4/6 and 5/6, and at 2(+), 4(*), 6(◇), 8(▵), 10.3(no symbol) and 12(□) cm above the bed.

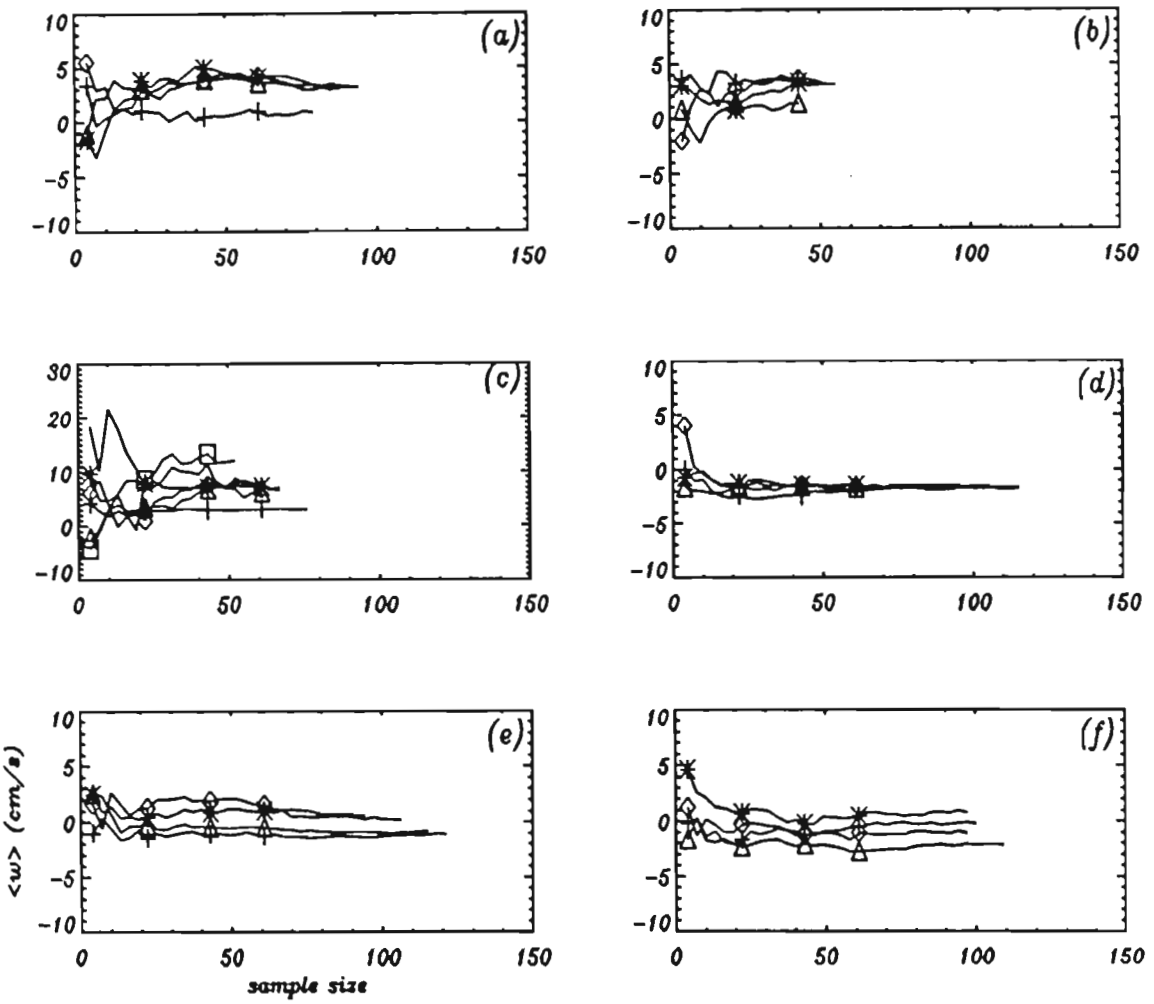

Figure 6.32: Dependence of $<w>$ on sample size for the plunging wave. Results are shown for -t/T of (a) 0, (b) 1/6, (c) 2/6, (d) 3/6, (e) 4/6 and 5/6, and at 2(+), 4(*), 6(◇), 8(▵), 10.3(no symbol) and 12(□) cm above the bed.

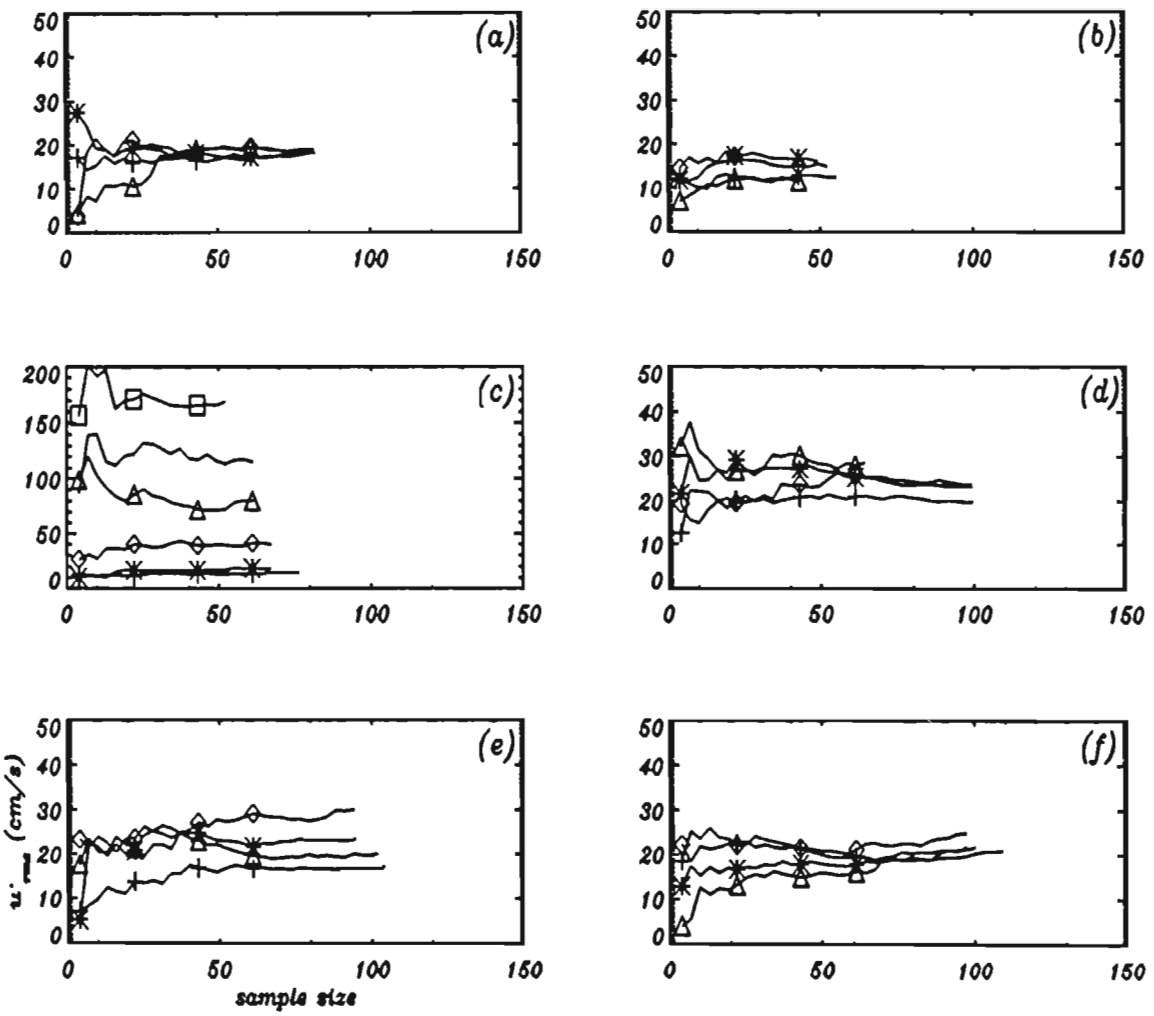

Figure 6.33: Dependence of u'_{rms} on sample size for the plunging wave at -t/T of (a) 0, (b) 1/6, (c) 2/6, (d) 3/6, (e) 4/6 and 5/6, and at 2(+), 4(*), 6(◇), 8(▲), 10.3(no symbol) and 12(□) cm above the bed.

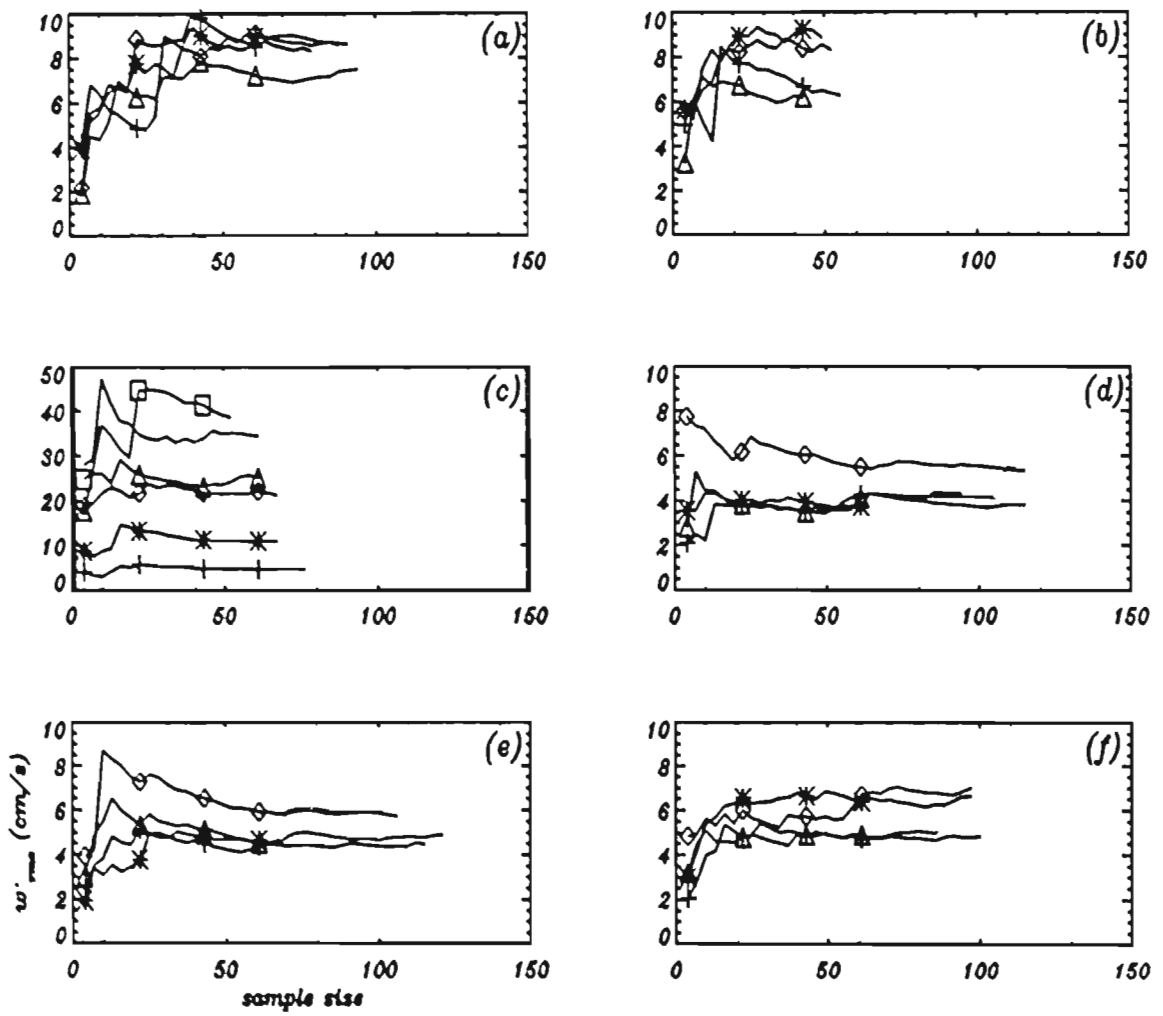

Figure 6.34: Dependence of w'_{rms} on sample size for the plunging wave at -t/T of (a) 0, (b) 1/6, (c) 2/6, (d) 3/6, (e) 4/6 and 5/6, and at 2(+), 4(*), 6(◇), 8(▵), 10.3(no symbol) and 12(□) cm above the bed.

6.8 Summary

The velocity flow fields of spilling and plunging waves, breaking on a 1:20 slope beach, was measured using digital correlation image velocimetry (DCIV). Measurements of the phase ensemble-averaged flow field in the spilling wave at 24 (station 1), 122 (station 2) and 221 (station 3) cm from the break point and in the plunging wave at -111 (station 1), 86 (station 3) and 169 (station 4) cm from the break point were presented. A comparison of the flow field in the spilling wave at station 3, measured using digital particle image velocimetry (DPIV) and DCIV, was also presented. It was shown that both techniques provide comparable measurements, however, DCIV was shown to be more superior, providing velocity estimates in the extremely aerated region of the wave with a high spatial resolution. The measurements below the trough level have been compared with existing LDA measurements presented in the literature.

Velocities in the crest of the spilling wave at stations 1, 2 and 3 were $\sim$200, 100 and 100 cm/s, respectively. Typical velocities of $\sim$100, 200 and 150 cm/s was found to occur in the crest of the plunging waves at stations 1, 3 and 4, respectively.

The time-averaged flow in the spilling and plunging waves were also presented. The forward flux in the crest of the waves in the surf zone was found to be greater than the reverse flux below the approximate trough level. This is due to the lower fluid density in the crest of the waves as a result of wave-breaker related aeration. The fractional density of the fluid in the crest of the spilling waves was shown be approximately 0.7 throughout surf zone and the fractional density of the fluid in the crest of the plunging waves was shown be $\sim$1, 0.7 and 0.3 at stations 1, 3 and 4, respectively.

A comparison of the peak orbital velocities with those predicted by linear theory showed an over-prediction at positions below the trough level and an under-prediction above. Linear theory is shown to over predict velocities by $\sim$100% in the spilling wave and greater than 100% in the plunging wave.

A sensitivity analysis was also performed on the velocity data measured in the spilling and plunging waves at station 3, in order to determine the influence of the sample and bin size on the mean and standard deviation. It was shown that the mean converges after 10 to 20 samples and the standard deviation converges after 20 to 30 samples.

CHAPTER 7

TURBULENCE, VORTICITY AND SPECTRAL ANALYSIS OF SPILLING AND PLUNGING WAVES

The instantaneous velocity flow fields of spilling and plunging waves, measured using DCIV, are analysed with the aim of estimating turbulence velocities, turbulent kinetic energies, Reynolds stress and rate of energy dissipation. The instantaneous flow fields at each position along the flume is analysed by decomposing each velocity vector into its mean and fluctuating components. The time-averaged vertical distribution of turbulence intensities, turbulent kinetic energy and Reynolds stress are computed from the turbulence flow fields. The eddy viscosity is then computed using the Reynolds stress and the time-averaged horizontal velocity. The vorticity of the phase ensemble-averaged flow is also examined. The rate of energy dissipation is estimated from the wavenumber spectrum of turbulence in the equilibrium range, and the scale lengths are then estimated using the rate of dissipation.

7.1 Introduction

Turbulence is a state of the fluid flow that is characterised by high levels of velocity fluctuations. These fluctuations are usually driven by velocity shear that exists in the flow, such as over a stationary boundary. Vortices are also a prominent feature in shear flows. The velocity shear is responsible for extracting energy from the mean flow creating large eddies. In the surf zone turbulence is also generated by the breaking of waves. The net result in both cases is the transfer of energy to the large scale eddies. The large scale eddies, in turn, transfer their energy to eddies of smaller size. Thus there is a cascade of energy from the large scales to the small scales. Dissipation of energy to heat occurs at the small scale. The net result of turbulence in the surf zone is the dissipation of wave energy and the resulting sediment suspension and transport, which is of crucial importance to the coastal engineering community. Hence, the experimental measurements and analysis of turbulence in the spilling and plunging waves (*Govender et al, 1999*) are presented here.

Theoretical analysis of turbulence is performed via Reynolds decomposition of the variables in the Navier-Stokes equation into their mean and fluctuating parts, and computing the time averaged equation for the mean flow, kinetic energy of the mean and turbulent parts of the flow, etc. The equations describing the turbulent processes have been presented in Chapter 2. The turbulent kinetic energy, k, is described, in tensor notation by $k=1/2<u_i'u_i'>=1/2<u'_1{}^2+u'_2{}^2+u'_3{}^2>$ and the total rate of change of k is given by:

$$\frac{dk}{dt}=\frac{\partial k}{\partial t}+\frac{\partial}{\partial x_j}<u_i>k=\frac{\partial}{\partial x_j}\left(\frac{1}{\rho}<u_j'p'>+<u_j'k'>-2\nu u_i's_{ij}'\right) \qquad (7.1)$$
$$-<u_i'u_j'><s_{ij}>-2\nu<s_{ij}'s_{ij}'>$$

where u_i are the velocity components, p is the pressure, ν is the kinematic viscosity, and, $<s_{ij}>$ and s'_{ij} are the mean and fluctuating strain rate, respectively. The terms in brackets on the right hand side represent the transport of kinetic energy due to the action of pressure, turbulence diffusion and viscous stresses. The second last term on the right, $-<u'_iu'_j>s_{ij}$, represents the production of turbulence by the action of the Reynolds stresses, $-<u'_iu'_j>$, and the last term represents the dissipation by viscous stresses. The viscous dissipation is always a drain in energy and therefore appears as a negative quantity in Equation 7.1. The quantities, $-<u_iu_j>$, form the Reynolds stress tensor, which contains nine components, of

which six are independent. The Reynolds decomposition, thus results in additional unknowns in the form of cross products of the horizontal and vertical fluctuating velocities, $<u_i u_j>$. Thus we now have more unknowns than equations and this is referred to as the closure problem. Methods of effecting closure involves finding expressions to model the Reynolds stress terms and also the energy dissipation term. Typical models of turbulence are Prandtl's mixing length and, the *k-l* and *k-ε* (*Jones and Launder, 1972; Launder and Spalding, 1972*) models. Mixing length models represent the Reynolds stress and the energy dissipation rate as a function of the mixing or scale length of the turbulent process. Thus the measurement of scale lengths are also of significance.

The measurement of the turbulence intensities, kinetic energies, Reynolds stress and vorticity in spilling and plunging waves breaking on a 1:20 slope beach are presented here. Measurements are provided only for positions above the bottom boundary layer. Tables 7.1 and 7.2 summarises the wave characteristics and the measurement positions for the spilling and plunging wave case, respectively. It will be shown that there are high levels of turbulence and vorticity in the crests of the wave. The Reynolds stress near the bed increases almost linearly with distance above the bed. The turbulence viscosity was computed using the Reynolds stresses and the time-averaged horizontal velocity, which was presented in the previous chapter. The energy dissipation rates were estimated from the wavenumber spectrum in the so-called equilibrium range. Scale lengths, as a function of depth, were computed using the energy dissipation rate.

Table 7.1: Spilling wave characteristics

$(x-x_b)$ (cm)	H_0 (cm)	T (s)	h_b (cm)	H (cm)	h (cm)	H/h	h/h_b
(station 1) 24	16	1.11	21.8	15	21.1	0.71	0.968
(station 2) 122				11	16.6	0.66	0.762
(station 3) 221				6.5	12.9	0.51	0.59

Table 7.2: Plunging wave Characteristics

$(x-x_b)$ (cm)	H_0 (cm)	T (s)	h_b (cm)	H (cm)	h (cm)	H/h	h/h_b
(station 1) -111	11	2.5	15.6	15	21.5	0.69	1.38
(station 3) 86				11.5	11.82	0.97	0.76
(station 4) 169				7.8	8.38	0.93	0.54

This chapter includes four major sections, viz., turbulence intensities, Reynolds stress and eddy viscosity, vorticity analysis and spectral analysis. Each section present results for the spilling wave followed by those for the plunging wave.

7.2 Turbulence intensities

The turbulence intensities in the spilling and plunging waves were computed using a decomposition similar to the Reynolds decomposition. Since there is a surface wave present it is necessary to perform decomposition using an ensemble of data at each wave phase. The phase ensemble-averaged velocities presented in the previous chapter were computed by collecting all velocities vector in spatial bins approximately 1 cm x 1 cm in size, and estimating the average in each bin.

The turbulence velocities in each of the bins were determined by separating the vertical and horizontal velocity components into their orbital, averaged and turbulent components. The instantaneous particle velocity can thus be written as:

$$\begin{aligned} u(t,z) &= \tilde{u}(t,z) + \bar{u}(z) + u'(t,z) \\ w(t,z) &= \tilde{w}(t,z) + \bar{w}(z) + w'(t,z) \end{aligned} \tag{7.2}$$

where $\tilde{u}(t,z)$ and $\tilde{w}(t,z)$ are velocities due to the orbital motion of the wave, $\bar{u}(z)$ and $\bar{w}(z)$ are the time-averaged velocities, and $u'(t,z)$ and $w'(t,z)$ are the instantaneous turbulent velocities. The phase ensemble-averaged velocities presented previously are the sum of the orbital velocity and the time-averaged velocity. The rms turbulence velocities or turbulence intensities, $u'_{rms}(\theta,z)$ and $w'_{rms}(\theta,z)$, at each point in the wave were estimated by computing the standard deviation of the velocity components in each bin.

$$u'_{rms}(\theta,z)=\sqrt{\langle u'^{2}(\theta,z)\rangle}=\sqrt{\frac{\sum_{0}^{N-1}(u(\theta/\omega+iT)-\langle u(\theta,z)\rangle)^{2}}{N-1}}$$

$$w'_{rms}(\theta,z)=\sqrt{\langle w'^{2}(\theta,z)\rangle}=\sqrt{\frac{\sum_{0}^{N-1}(w(\theta/\omega+iT)-\langle w(\theta,z)\rangle)^{2}}{N-1}} \qquad (7.3)$$

where $\theta=\omega t$ is the wave phase, T is the wave period, N is the number of samples in each bin, which is also the number of wave cycle, $\langle u(\theta,z)\rangle$ and $\langle w(\theta,z)\rangle$ are the phase ensemble-averaged components, or simply the average velocity components in each bin. In keeping with the notation used in published literature, turbulence intensities will be denoted by u' and w' in the remainder of this chapter, unless stated otherwise.

7.2.1 Spilling wave

7.2.1.1 Phase ensemble-averaged intensities

The contours of horizontal and vertical turbulence intensities, u' and w', in the spilling wave at stations 1, 2 and 3 are shown in Figures 7.1, 7.2, and 7.3. The turbulence intensities are also shown as a function of wave phase at various depths. Pseudo-colour plots of the turbulence intensities at station 3 are also shown.

Most of the high turbulence levels at station 1 (Figure 7.1) are confined to a small region near the top of the crest, due to spilling of the wave at that point. Peak turbulence intensities here are $\sim$20 cm/s. In the rest of the wave, the turbulence intensities are lower, 5 - 10 cm/s, and due mostly to the velocity shear that is present in the wave. The magnitude of u' and w' are approximately of the same order throughout the wave.

The peak intensities at station 2 (Figure 7.2) are in the order of 70 cm/s, occurring in the crest of the wave. The horizontal component of the turbulence in the crest of the wave, u', is greater than and the vertical component, w', indicating that the turbulence in the crest is non-isotropic. There are also high levels of turbulence throughout the crest. In the trough, the intensities are similar to those occurring at station 1. The peak turbulence intensities at station 2 are higher than those occurring at station 1 and there is greater spreading of the

velocity fluctuation throughout the wave. This is due to the fact that at station 2, the wave breaking is more intense with almost full formation of the roller.

At station 3 (Figure 7.3), there is still a greater spreading of turbulence towards the lower and rear of the wave. The peak intensities of ~60 cm/s occur in the crest, and are lower than those occurring at station 2. Once again the turbulence intensities in the trough of the wave are very similar to those occurring at stations 1 and 2, that is 5-10 cm/s. LDA measurements by *Stive(1980)* in a plunging wave breaking on a 1:40 slope beach (see Section 2.5 in Chapter 2), show similar results at similar positions below the trough level. Typically, LDA measurement reveal peak intensities of ~12 cm/s below the trough level. These measurements are very similar to those measured using DCIV at station 3.

Table 7.3 summarises the peak intensities occurring in the spilling wave. The following conclusions can be drawn, based on the observation of turbulence in the spilling wave; The wave breaking results in high levels of turbulence in the crest of the waves compared to the turbulence values in the rest of the wave, which is generated mostly by the velocity shear and advection of turbulence from the crest. In the lower part of the wave and in the troughs the turbulence is tending towards isotropy and is thus indicative of dissipation, that is, there is complete mixing in all direction resulting the conversion of ordered motion into randomised motion. In the wave crest the turbulence is greatest in the horizontal direction. In the spilling wave the turbulence level reaches a peak some distance beyond the spilling point and decreases thereafter.

Table 7.3: Peak turbulence intensities in the spilling wave

x-x_b (cm)	(station 1) 24	(station 2) 122	(station 3) 221
z_t (cm)	16	14	10
u' (cm/s)	20	70	60
w' (cm/s)	20	50	60
$u'/(gh)^{1/2}$	0.14	0.54	0.53
$w'/(gh)^{1/2}$	0.14	0.39	0.53

where z_t is the elevation of the trough level above the bed.

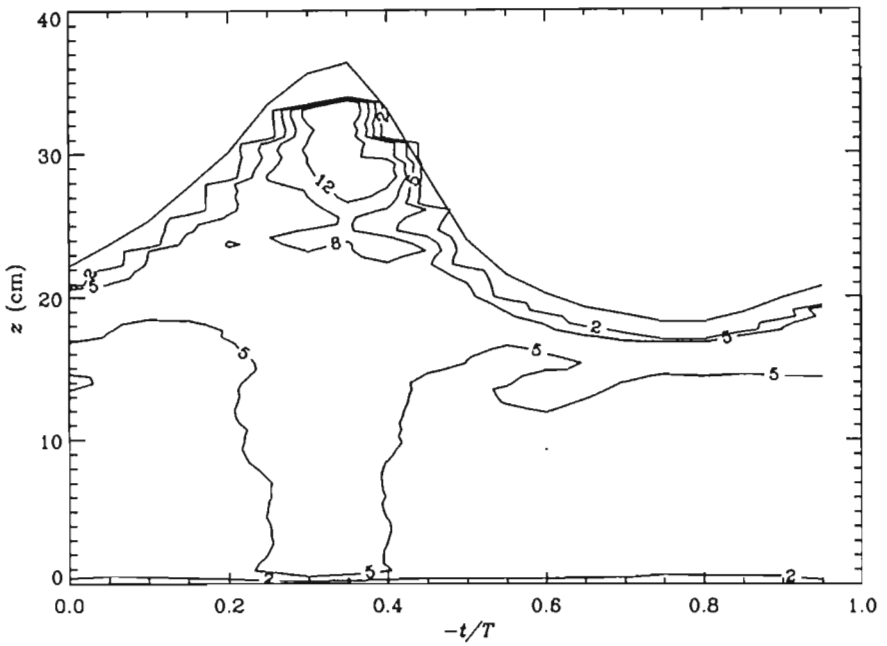

Figure 7.1:(A) Contours of the phase ensemble-averaged horizontal turbulence intensities, u' (cm/s), in the spilling wave at station 1($x-x_b = 24$ cm, $H \sim 15$ cm, $h \sim 21.1$ cm, $h_b \sim 21.8$ cm).

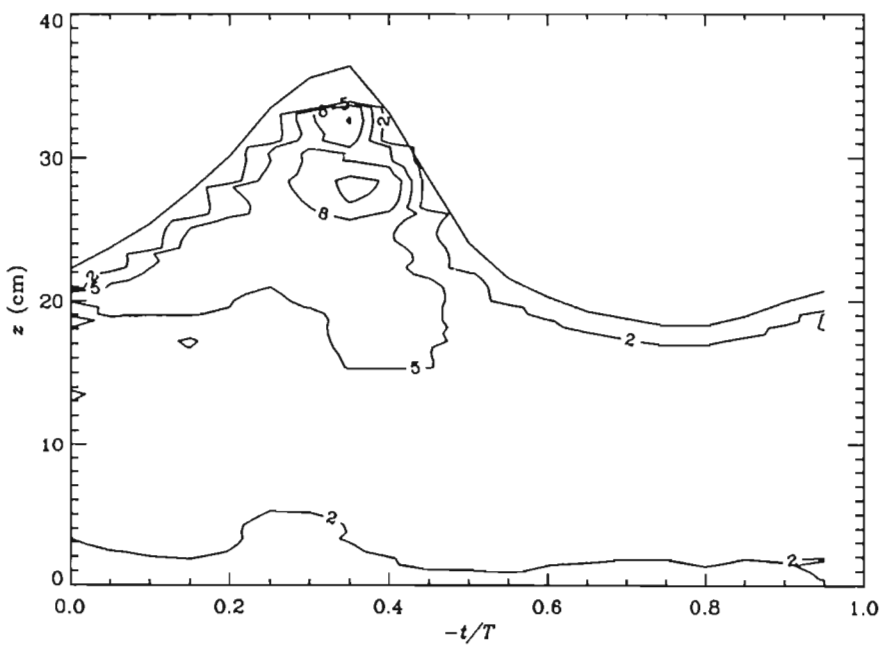

Figure 7.1:(B) Contours of the phase ensemble-averaged vertical turbulence intensities, w' (cm/s), in the spilling wave at station 1($x-x_b = 24$ cm, $H \sim 15$ cm, $h \sim 21.1$ cm, $h_b \sim 21.8$ cm).

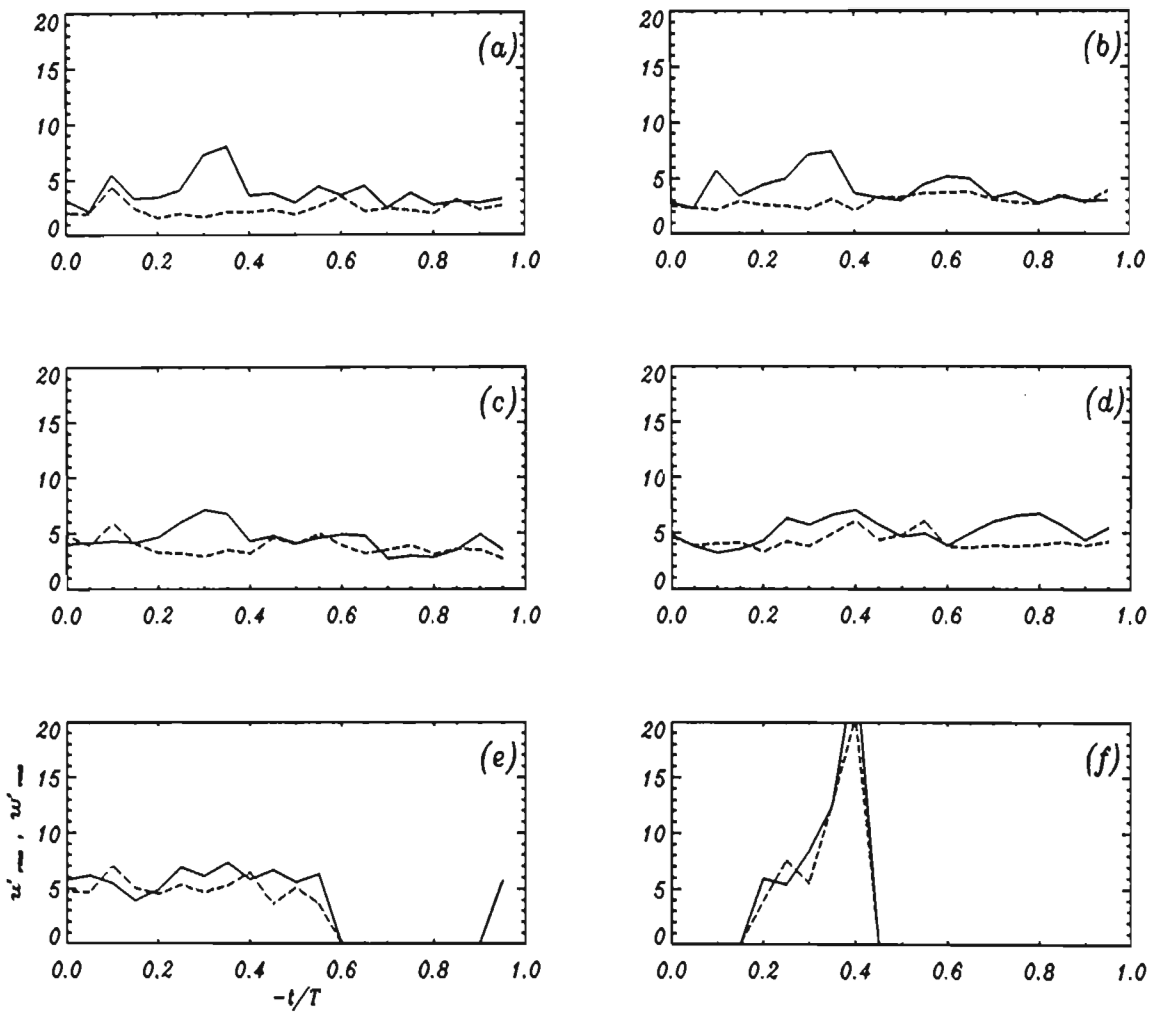

Figure 7.1:(C) Turbulence intensities, u'(-) and w'(- -) in cm/s, in the spilling wave at station 1, as a function of wave phase at (a) 4, (b) 8, (c) 12, (d) 16, (e) 20 and (f) 28 cm above the bed.

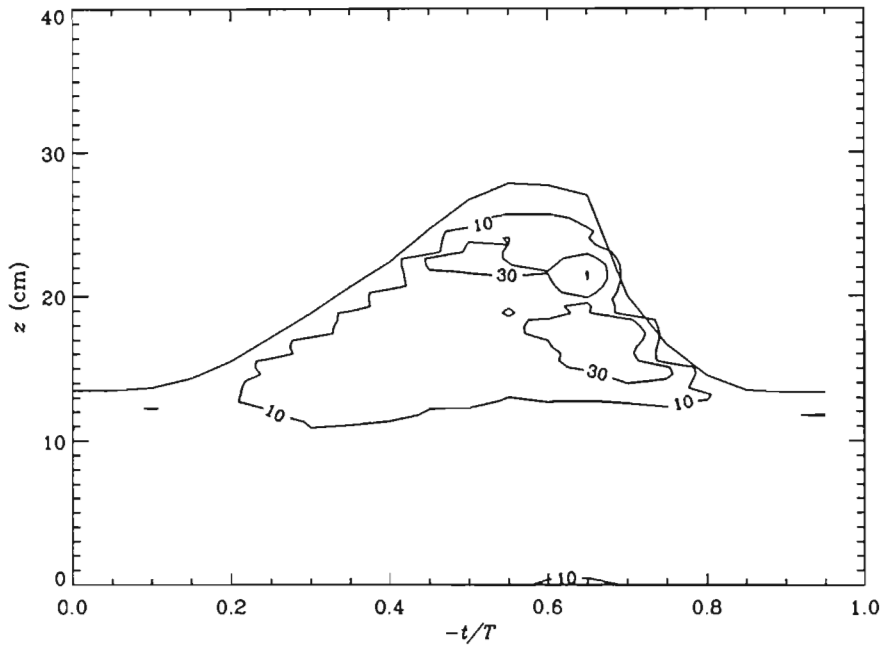

Figure 7.2:(A) Contours of the phase ensemble-averaged horizontal turbulence intensities, u' (cm/s), in the spilling wave at station 2($x-x_b = 122$ cm, $H \sim 11$ cm, $h \sim 16.1$ cm, $h_b \sim 21.8$ cm).

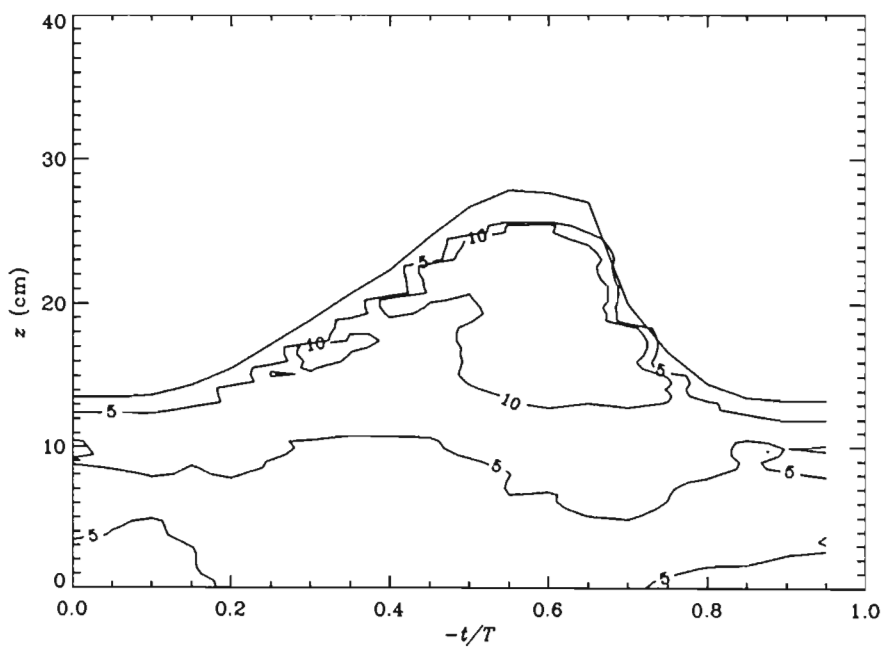

Figure 7.2:(B) Contours of the phase ensemble-averaged vertical turbulence intensities, w' (cm/s), in the spilling wave at station 2($x-x_b = 122$ cm, $H \sim 11$ cm, $h \sim 16.6$ cm, $h_b \sim 21.8$ cm).

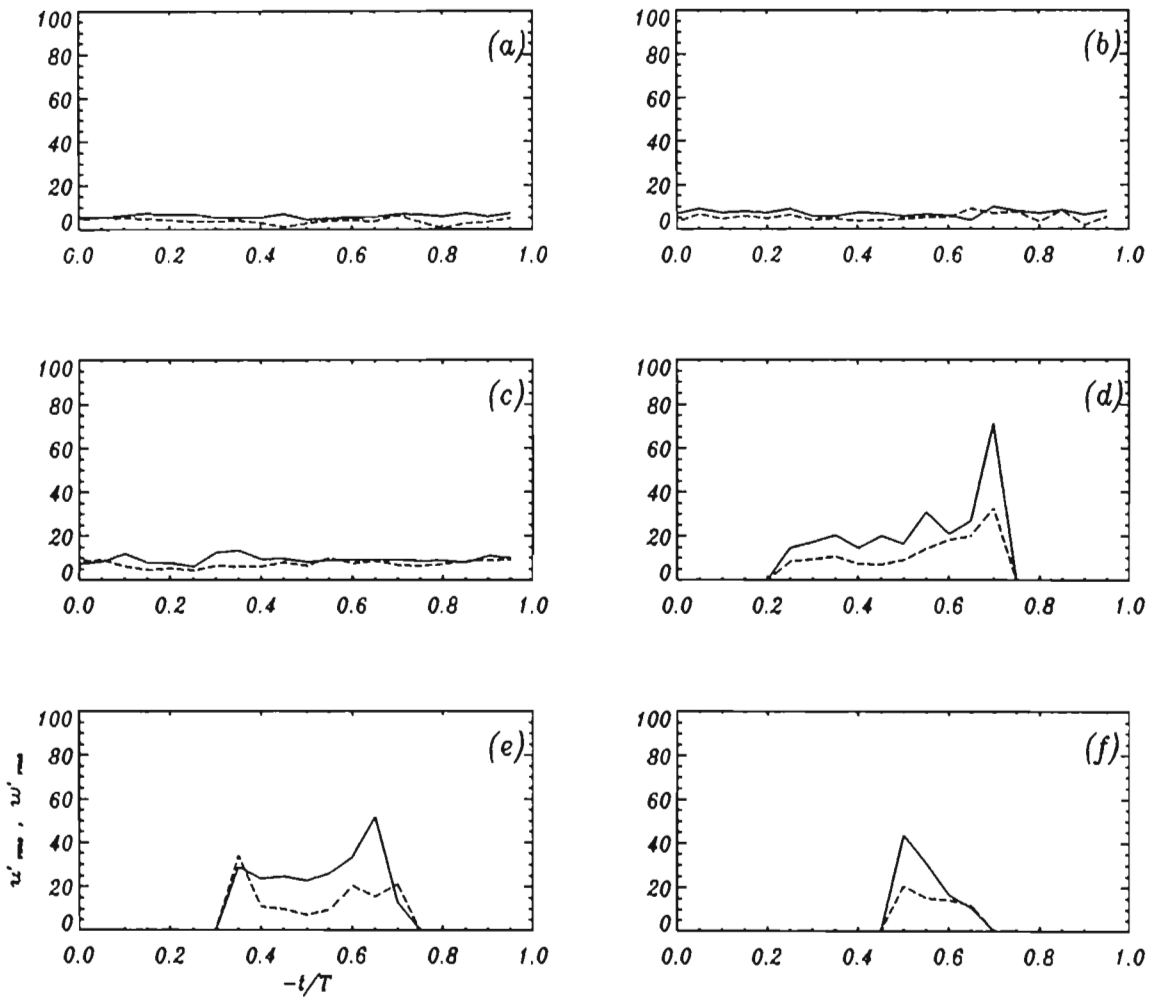

Figure 7.2:(C) Turbulence intensities, u'(-) and w'(- -) in cm/s, in the spilling wave at station 2, as a function of phase at (a) 4, (b) 8, (c) 12, (d) 16, (e) 20 and (f) 24 cm above the bed.

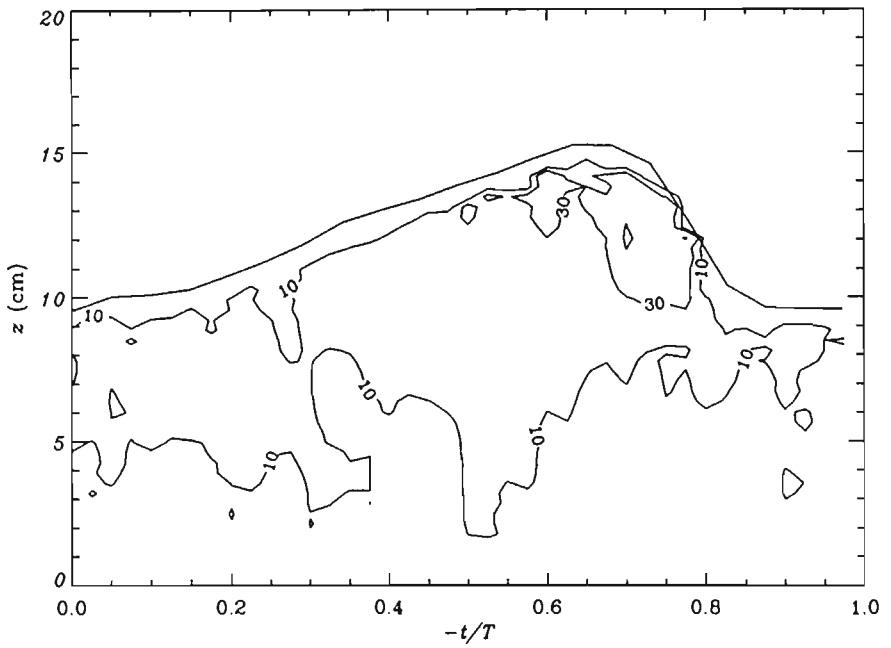

Figure 7.3:(A) Contours of the phase ensemble-averaged horizontal turbulence intensities, u' (cm/s), in the spilling wave at station 3($x-x_b$=221 cm, H ~ 6.5 cm, h ~ 12.9 cm, h_b ~ 21.8 cm).

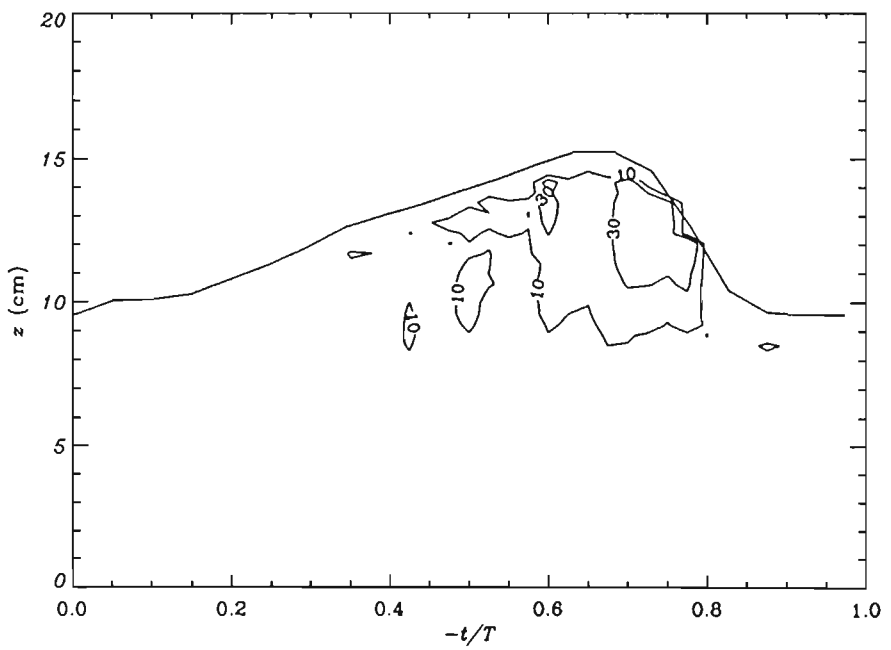

Figure 7.3:(B) Contours of the phase ensemble-averaged vertical turbulence intensities, w' (cm/s), in the spilling wave at station 3($x-x_b$=221 cm, H ~ 6.5 cm, h ~ 12.9 cm, h_b ~ 21.8 cm).

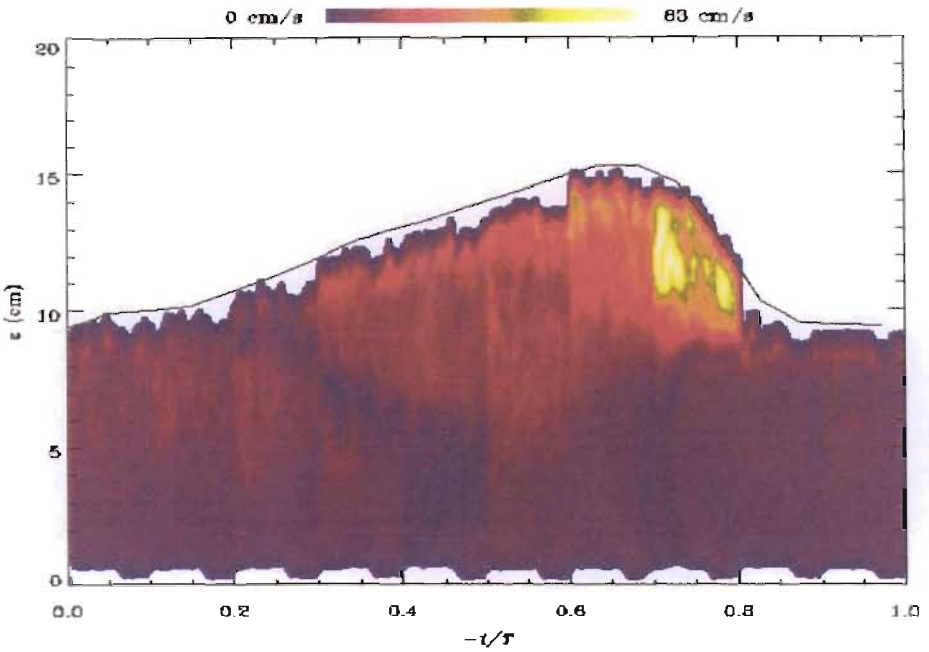

Figure 7.3 :(C) Pseudo-colour plot of the phase ensemble-averaged horizontal turbulent intensities (cm/s) in the spilling wave at station 3.

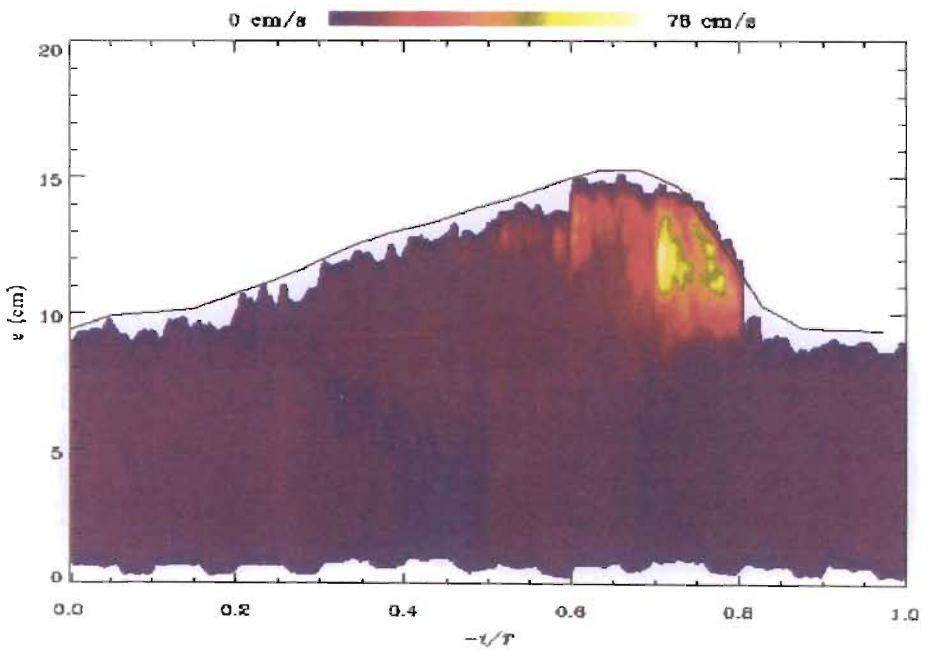

Figure 7.3 :(D) Pseudo-colour plot of the phase ensemble-averaged vertical turbulent intensities (cm/s) in the spilling wave at station 3.

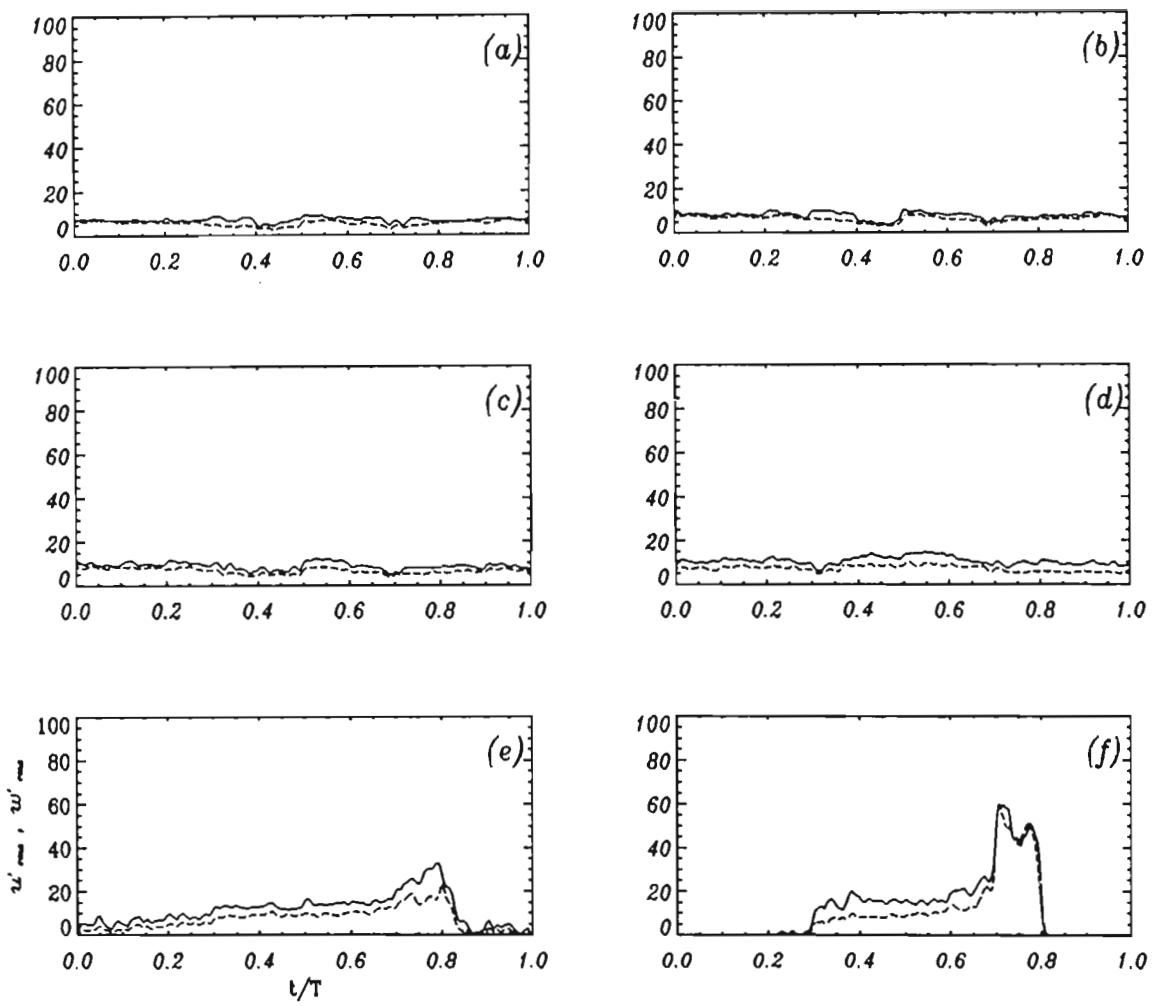

Figure 7.3:(E) Turbulence intensities, u'(-) and w'(- -) in cm/s, in the spilling wave at station 3, as a function of phase at (a) 2, (b) 4, (c) 6, (d) 8, (e) 10 and (f) 12 cm above the bed.

7.2.1.2 Time-averaged turbulence intensities and kinetic energy: spilling wave

The time-averaged turbulence intensities and kinetic energy, as a function of depth, in the spilling wave at stations 1, 2 and 3 are shown in Figures 7.4, 7.5 and 7.6, respectively. The time averaged turbulence intensities were computed, using the high resolution flow fields measured at each phase position, by averaging along a horizontal line over the entire wave phase.

The plots of time-averaged intensities show that the time-averaged horizontal turbulence intensity, u', and vertical turbulence intensity, w', increases from the bed upwards, reaching a maximum at approximately the trough level and decreasing thereafter. This is particularly apparent for station 1, where the trough is at the approximate level z_t= 16 cm.
The time-averaged intensities at positions below the trough level (z_t= 14 cm) at station 2, however, is nearly constant, i.e. ~5 cm/s. Above the trough level, the turbulence intensities increase rapidly to a peak value of ~15 cm/s. The increase is due to the dynamic wave breaking at this position. The turbulence intensity below the trough level (z_t= 10 cm)at station 3 are higher than those occurring at station 2, with peak intensities of the order 10 cm/s.

The turbulent kinetic energy (TKE) is define by the following relation:

$$k=\frac{1}{2}(u'^2+v'^2+w'^2) \tag{7.4}$$

However, DCIV measurement provide only two components of the turbulence intensities and therefore the TKE is estimated using the following approximation (*Svendsen, 1978*) assuming plane wake flow:

$$k=1.33\frac{1}{2}(u'^2+w'^2) \tag{7.5}$$

The TKE have been computed using the phase ensemble-averaged turbulence intensities. Below the trough level, the TKE have similar trend to the turbulence intensities at their respective positions. Above the trough level the time-averaged kinetic energy increases

rapidly and remains almost constant for a distance corresponding to the wave height and decreasing thereafter. This is further evidence that turbulence production occurs in the crest of the wave were breaking is dominant. At station 1 the TKE is smallest with a peak value of 80 cm^2/s^2 while the peak TKE at stations 2 and 3 are ~ 750 cm^2/s^2 and 150 cm^2/s^2, respectively.

A common plot showing the time-averaged TKE presented here together with existing LDA measurements is shown in Figure 7.7. The measured profiles, as extracted from *Mocke(1998)*, correspond to surf zone positions where h/h_b is of the order 0.7. The TKE are plotted using normalised coordinates. The elevation is normalised with respect to the water depth, h, and the TKE is normalised with respect to (gh). It can be seen that below the trough level, the TKE measurements presented here are consistent with those of *Stive(1980)* and *Ting and Kirby(1994)*. Unlike previous LDA measurements, Figure 7.7 clearly shows that DCIV provides measurements that extend well above the trough level and with a high spatial resolution.

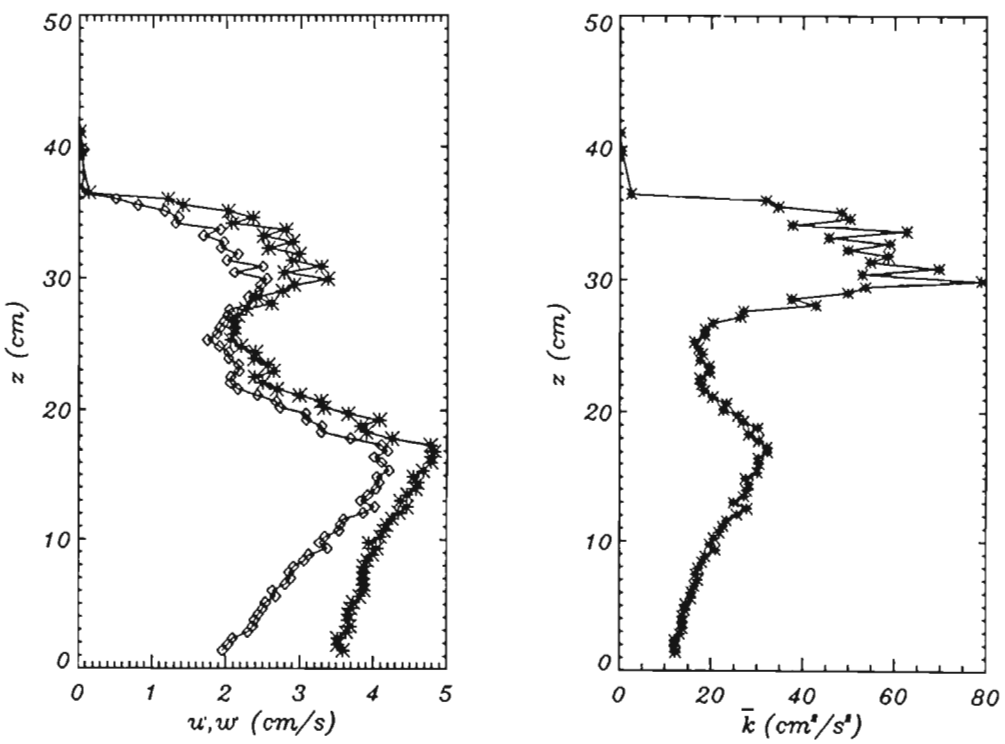

Figure 7.4:Time-averaged (left) horizontal(*) and vertical(◇) turbulence intensities, and (right) turbulent kinetic energy in the spilling wave at station 1($x-x_b$=24 cm, H ~ 15 cm, h ~ 21.1 cm, h_b ~ 21.8 cm).

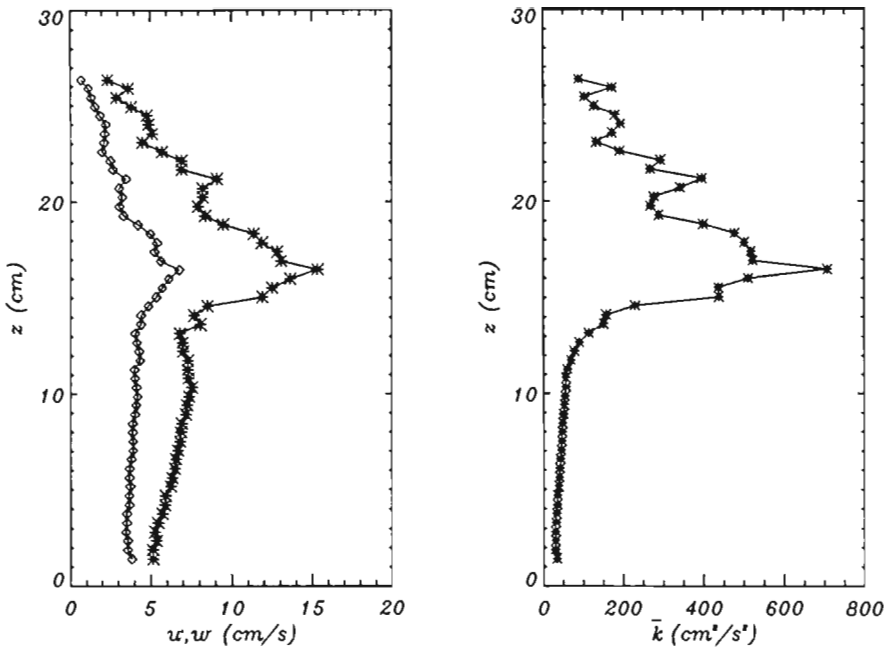

Figure 7.5:(a) Time-averaged (left) horizontal(*) & vertical(◇) turbulence intensities and (right) TKE in the spilling wave at station 2($x-x_b = 122$ cm, $H = 11$ cm, $h \sim 16.6$ cm, $h_b \sim 21.8$ cm).

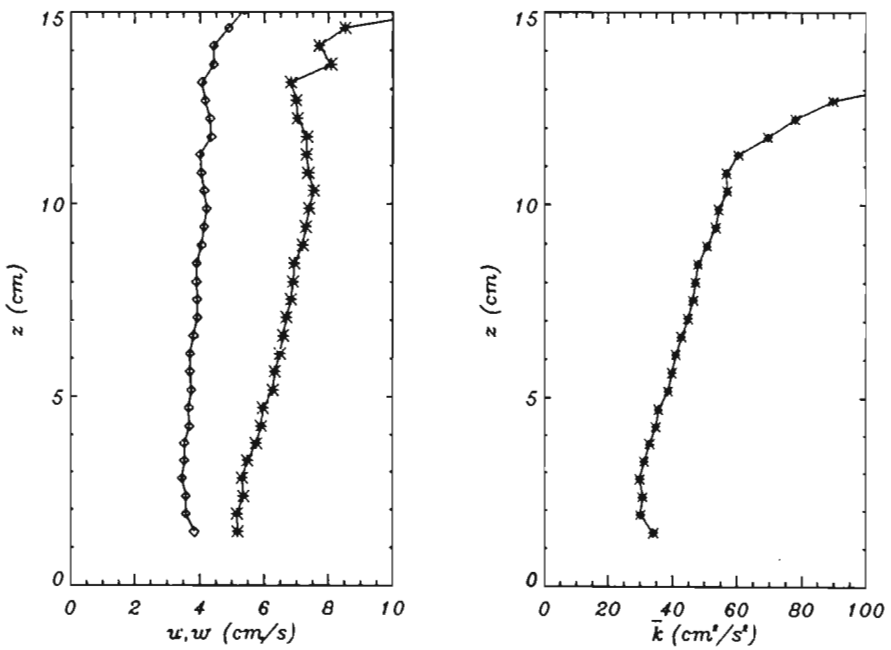

Figure 7.5:(b) Time-averaged (left) horizontal(*) and vertical(◇) turbulence intensities and (right) TKE below the approximate trough level in the spilling wave at station 2, corresponding to $z < 15$ cm in Figure 7.5(a).

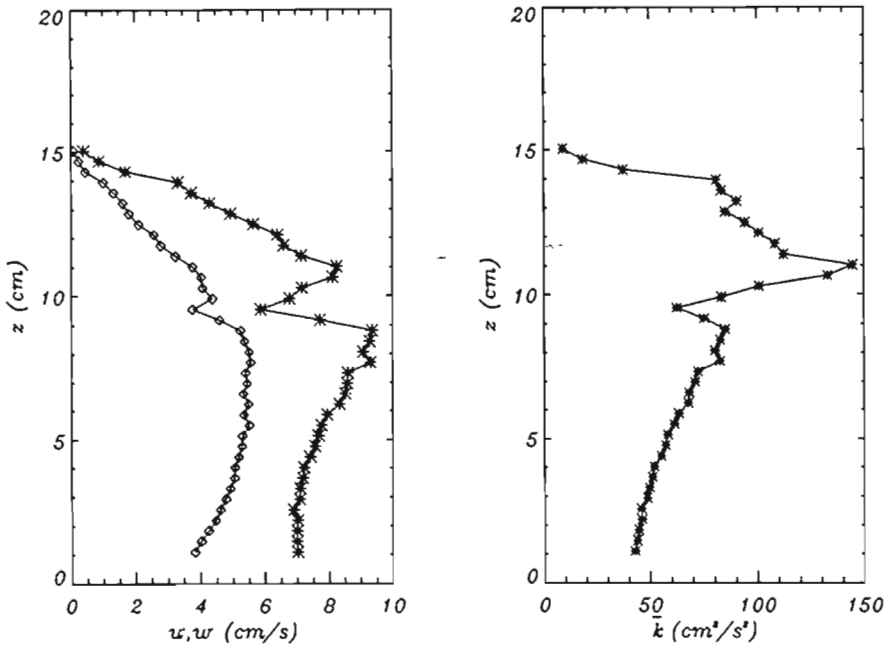

Figure 7.6: Time-averaged (left) horizontal(*) and vertical(◇) turbulence intensities and (right) TKE in the spilling wave at station 3($x-x_b=221$ cm, $H\sim 6.5$ cm, $h\sim 12.9$ cm, $h_b\sim 21.8$ cm).

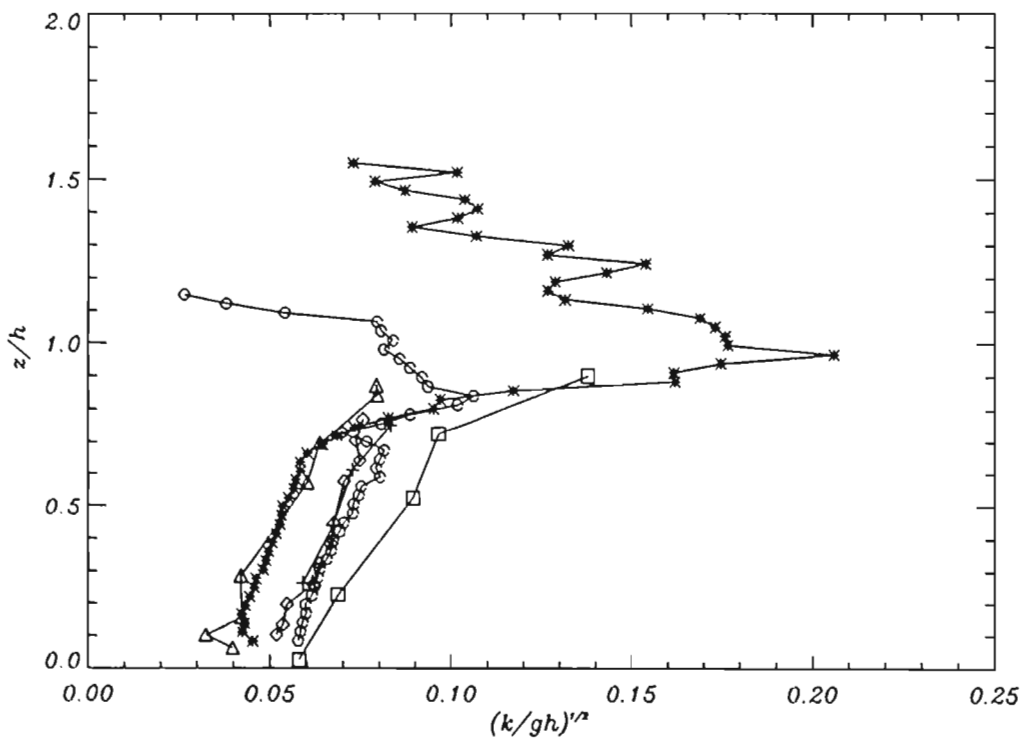

Figure 7.7: Comparison of time-averaged TKE of *Stive(1980)*(+), *Ting & Kirby(1994)*(◇), *Cox et al.(1994)*(△), *Okayasu(1989)*(□) and DCIV measurements at stations 2(*) and 3(o).

7.2.2 Turbulence measurements in plunging waves

7.2.2.1 Phase ensemble averaged intensities

The contours of horizontal and vertical turbulence intensities, u' and w', in the plunging wave at stations 1, 3 and 4 are shown in Figures 7.8, 7.9, and 7.10, respectively. The turbulence intensities are also shown as a function of wave phase at various depths. Pseudo-colour plot of the turbulence intensities at station 3 are also shown.

Station 1 corresponds to a pre-breaking position for the plunging wave and the turbulence here is due solely to the presence of velocity shear and advection of turbulence from the breaking region. Turbulence intensities in the crest are ~ 10 cm/s. In the rest of the wave the turbulence intensities are lower, ~ 2 cm/s. u' and w' are similar in magnitude through out the wave.

The peak intensities at station 3 (Figure 7.9) are ~ 120 cm/s, occurring near the toe of the wave front. The horizontal component of the turbulence (u') is greater than and the vertical component (w') throughout the wave, indicating non-isotropic behaviour. There are also high levels of turbulence throughout the crest area. In the trough area, the horizontal turbulence intensities are ~ 10 cm/s, while the vertical turbulence intensities are ~ 6 cm/s. The peak turbulence intensities at station 3 are very much higher than those occurring at station 1 and there is a spreading of the velocity fluctuation throughout the wave.

At station 4 (Figure 7.10), there is greater spreading of turbulence towards the lower and rear part of the wave. The peak intensities are similar to those occurring at station 3. The turbulence intensities in the trough area of the wave are ~ 7 cm/s. Also, the magnitudes of the horizontal and vertical intensities are relatively similar. Peak intensities in the crest are ~ 120 cm/s.

LDA measurement by *Stive(1980)*(see Figure 2.5 in Chapter 2) in plunging wave (test 2), indicate peak intensities at the approximate trough level of 12 cm/s below the crest and 5 cm/s below trough. These measurements are similar to those measured using DCIV at stations 3 and 4.

Table 7.4 summarises the peak turbulence intensities present in the plunging wave.

The following conclusion can be drawn, based on the observation of turbulence in the plunging wave; The wave breaking results in higher levels of turbulence in the crest of the waves compared to turbulence in the rest of the wave, which is generated mostly by the velocity shear. In the lower part of the wave and in the troughs the turbulence is more isotropic. In the wave crest the turbulence is greatest in the horizontal direction. In the plunging wave the turbulence intensity is greatest at station 3. The turbulence intensities in the plunging wave are greater than those occurring in the spilling wave.

Table 7.4: Peak turbulence intensities in the plunging wave

$x-x_s$ (cm)	(station 1) -111	(station 3) 86	(station 4) 169
z_t (cm)	19	10	7.5
u' (cm s)	10	120	120
w' (cm s)	6	100	100
$u'/(gh)^{1/2}$	0.07	1.07	1.27
$w'/(gh)^{1/2}$	0.045	0.89	1.06

where z_t is the elevation of the trough level above the bed.

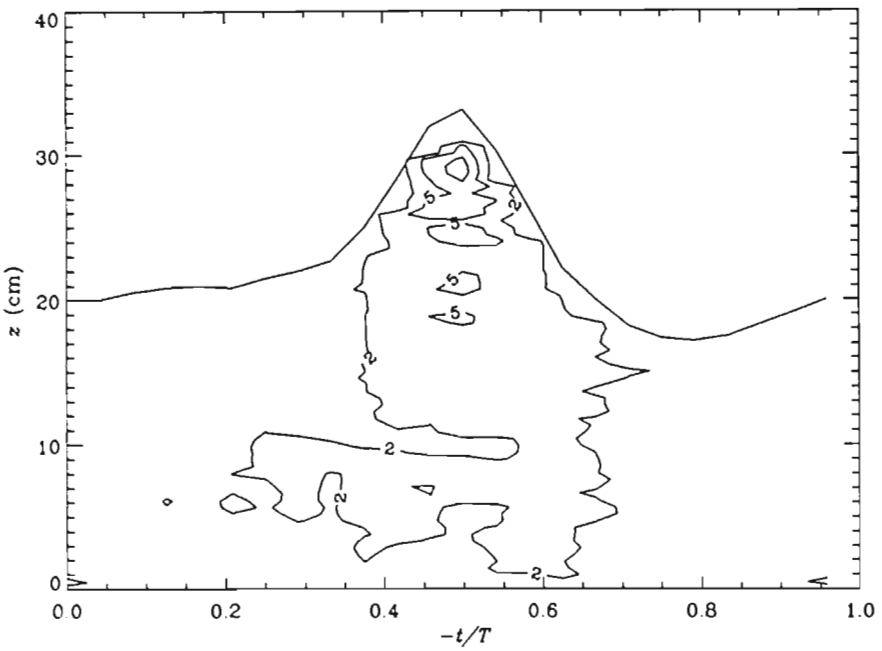

Figure 7.8:(A) Contours of the phase ensemble-averaged horizontal turbulence intensities, u' (cm/s), in the plunging wave at station 1($x-x_b$=-111 cm, H ~ 15 cm, h ~ 21.5 cm, h_b ~ 15.6 cm).

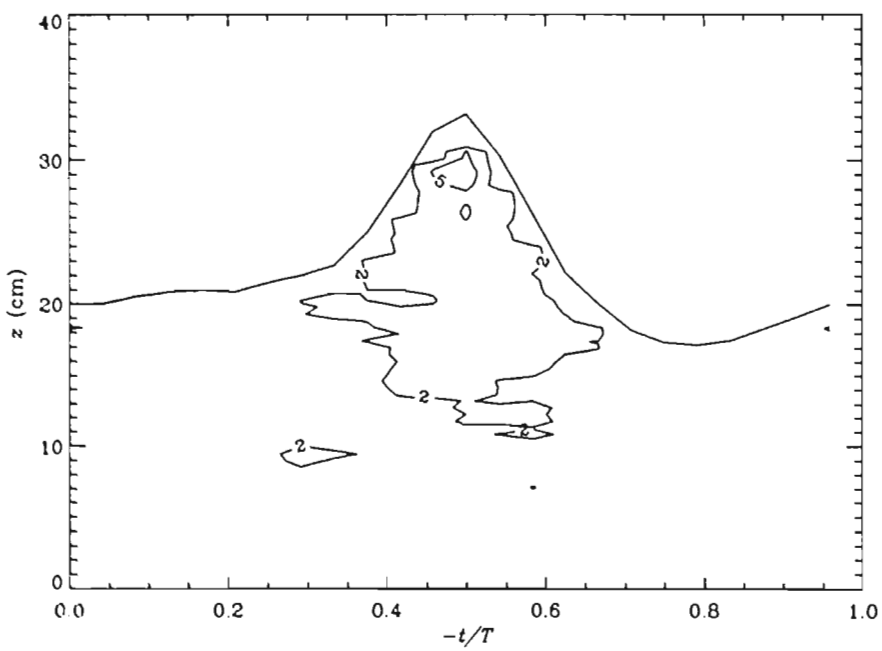

Figure 7.8:(B) Contours of the phase ensemble-averaged vertical turbulence intensities, w' in cms/s, in the plunging wave at station 1($x-x_b$=-111 cm, H ~ 15 cm, h ~ 21.5 cm, h_b ~ 15.6 cm).

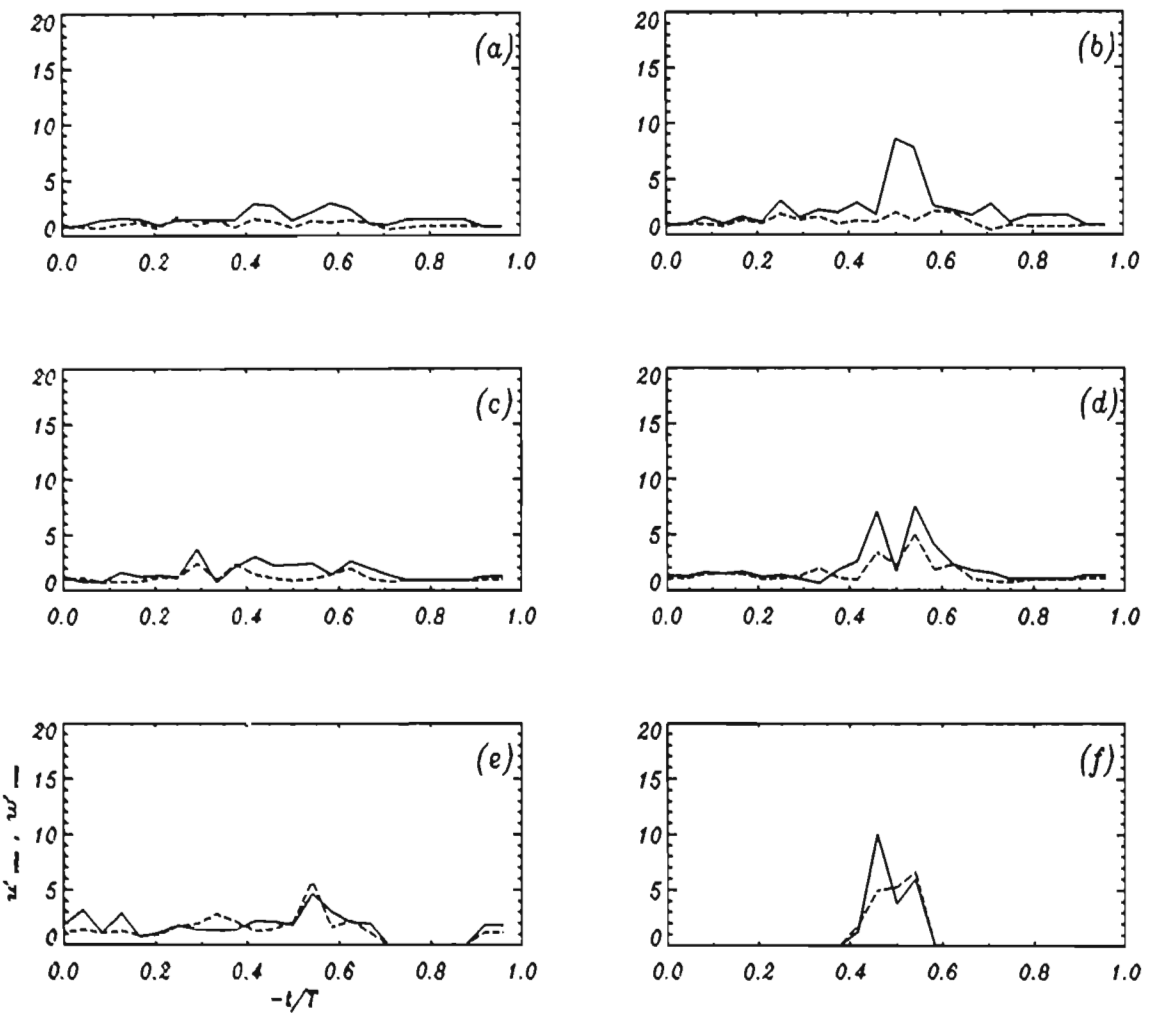

Figure 7.8: (C) Turbulence intensities, u'(*) and w'(+) in cm/s, in the plunging wave at station 1, as a function of wave phase at (a) 4, (b) 8, (c) 12, (d) 16, (e) 20 and (f) 28 cm above the bed.

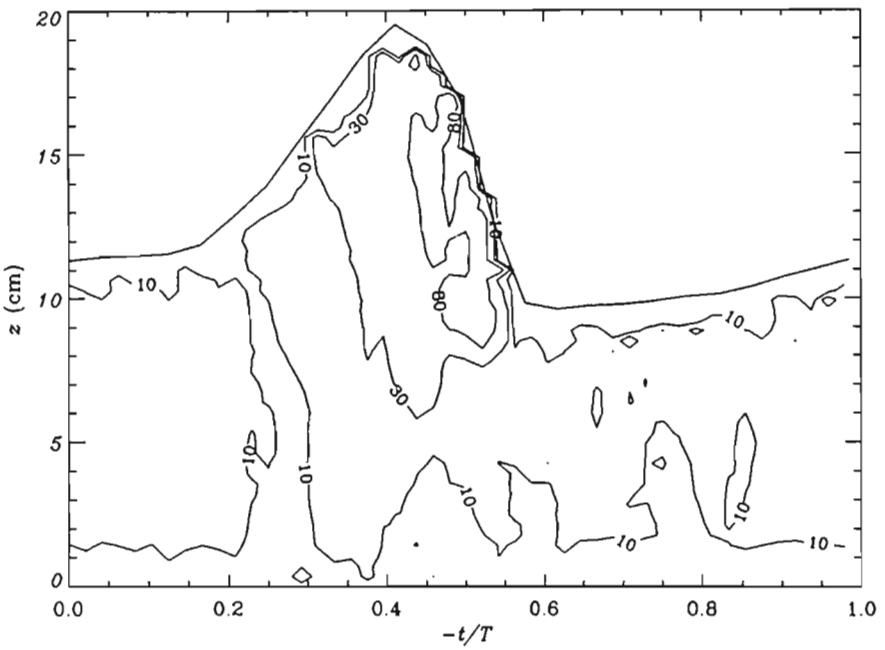

Figure 7.9:(A) Contours of the phase ensemble-averaged horizontal turbulence intensities, u' (cm/s), in the plunging wave at station 3($x-x_b$=86 cm, H ~ 11.5 cm, h ~ 11.8 cm, h_b ~ 15.6 cm).

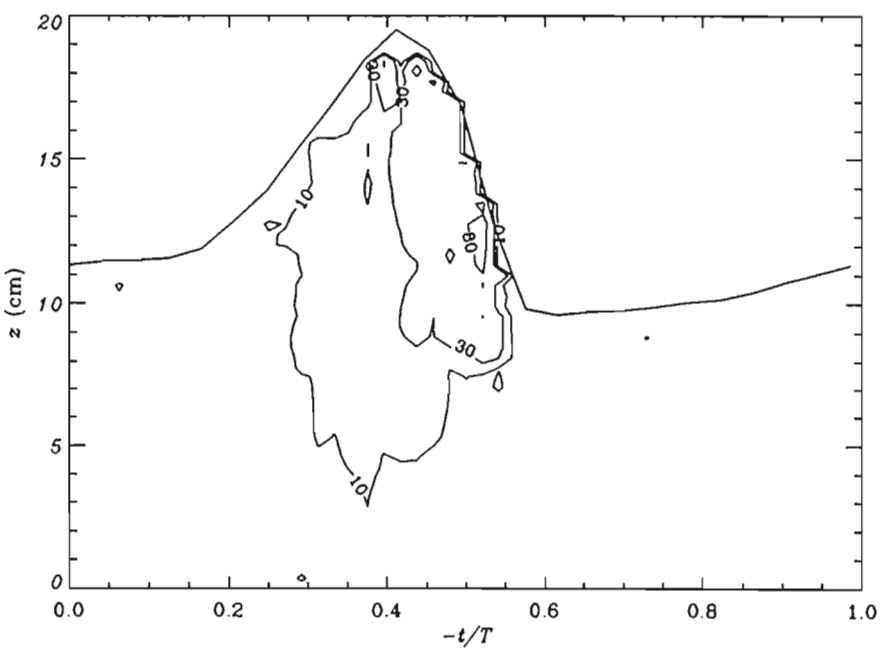

Figure 7.9:(B) Contours of the phase ensemble-averaged vertical turbulence intensities, w' in cm/s, in the plunging wave at station 3($x-x_b$=86 cm, H ~ 11.5 cm, h ~ 11.8 cm, h_b ~ 15.6 cm).

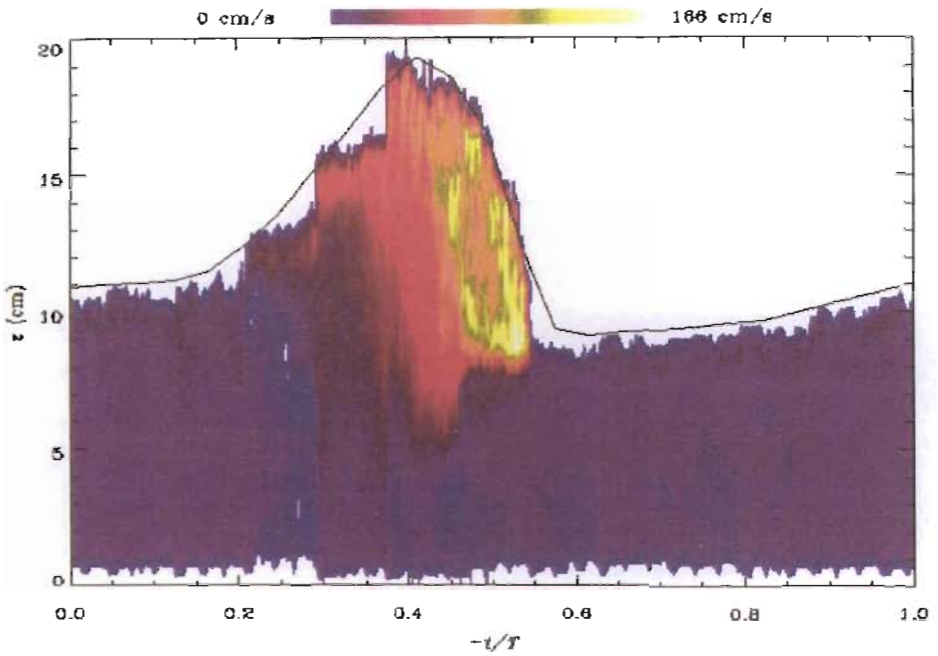

Figure 7.9:(C) Pseudo-colour plot of the phase ensemble-averaged horizontal turbulent intensities in the plunging wave at station 3.

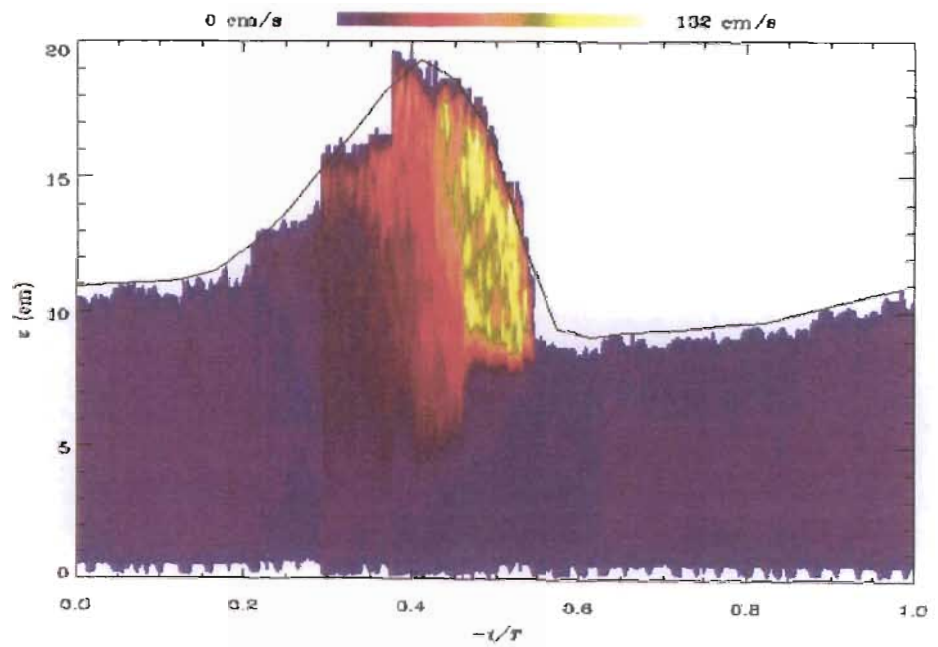

Figure 7.9:(D) Pseudo-colour plot of the phase ensemble-averaged vertical turbulent intensities in the plunging wave at station 3.

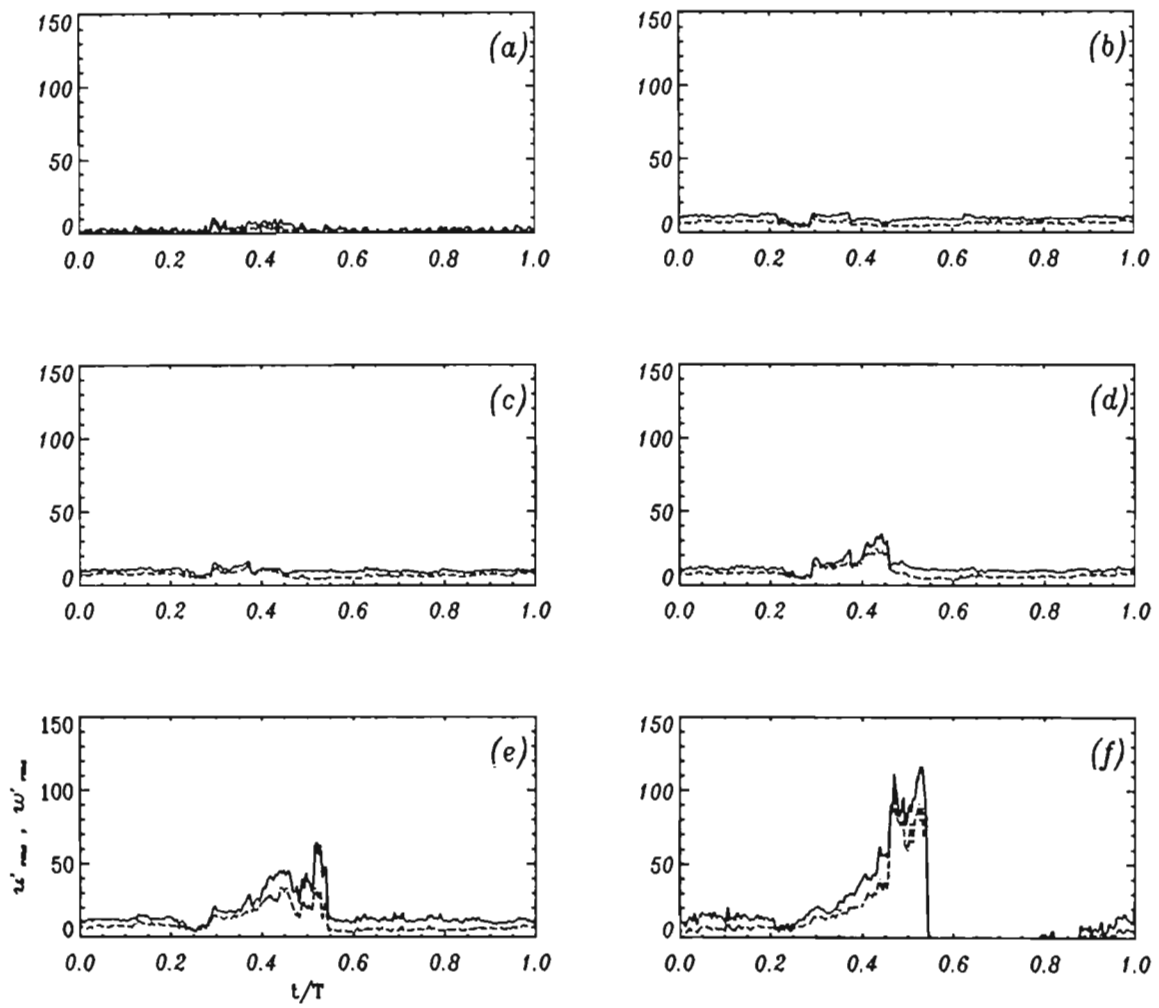

Figure 7.9:(E) Turbulence intensities, u'(-) and w'(- -) in cm/s, in the plunging wave at station 3, as a function of phase at (a) 2, (b) 4, (c) 6, (d) 8, (e) 10 and (f) 12 cm above the bed.

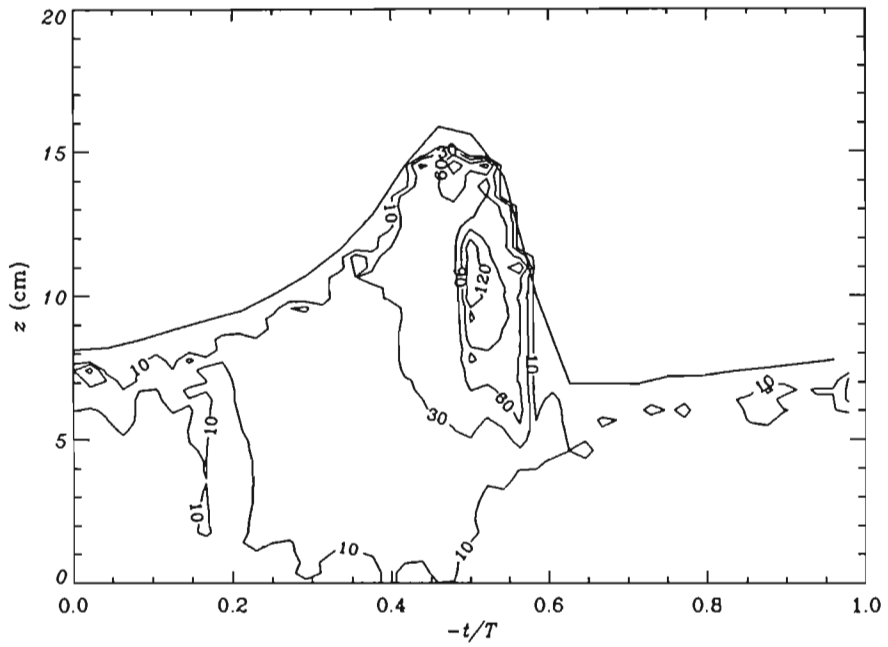

Figure 7.10:(A) Contours of the phase ensemble-averaged horizontal turbulence intensities, u' in cm/s, in the plunging wave at station 4($x-x_b=169$ cm, $H\sim7.8$ cm, $h\sim8.38$ cm, $h_b\sim15.6$ cm).

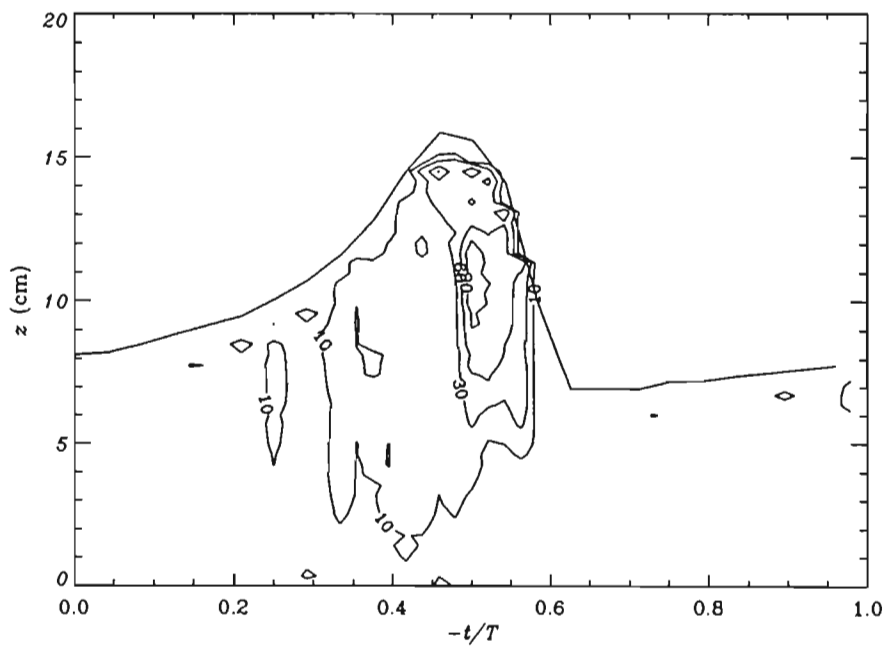

Figure 7.10:(B) Contours of the phase ensemble-averaged vertical turbulence intensities, w' in cm/s, in the plunging wave at station 4($x-x_b=169$ cm, $H\sim7.8$ cm, $h\sim8.38$ cm, $h_b\sim15.6$ cm).

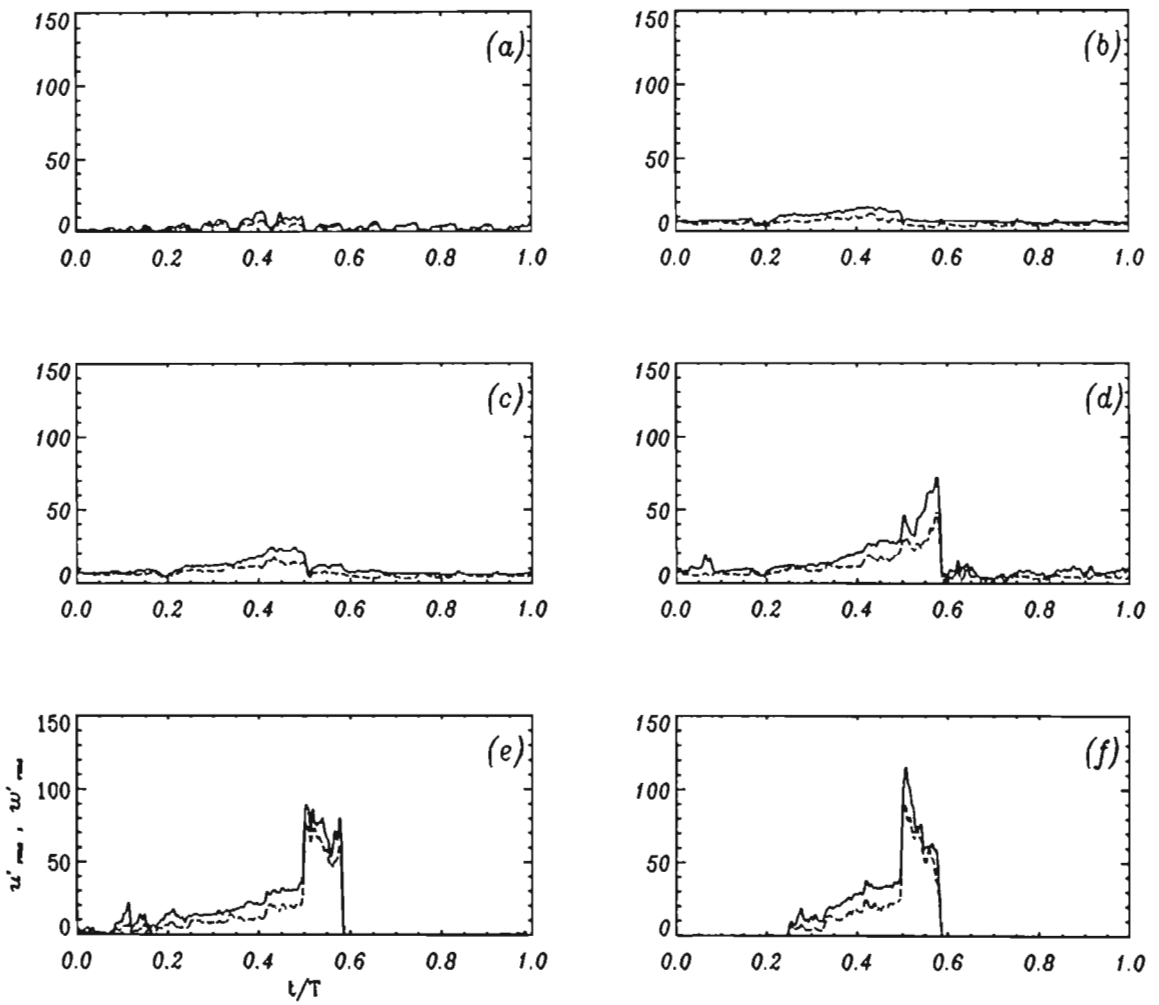

Figure 7.10:(C) Turbulence intensities, u'(-) and w'(- -) in cm/s, in the plunging wave at station 4, as a function of phase at (a) 4, (b) 6, (c) 8, (d) 10, (e) 12 and (f) 14 cm above the bed.

7.2.2.2 Time averaged turbulence intensities and kinetic energy: plunging wave

The time-averaged turbulence intensities and kinetic energy, as a function of distance above the bed, in the plunging wave at stations 1, 3 and 4 are shown in Figures 7.11, 7.12 and 7.13, respectively. These were computed, using the high resolution flow fields measured at each phase position, by averaging along a horizontal line over the entire wave phase. The plots of time-averaged intensities show that the time-averaged horizontal turbulence intensity, u', and vertical turbulence intensity, w', increase from the bed upwards, reaching a maximum near the approximate trough level and decreasing thereafter. The peak turbulence intensity at station 1 is ~ 1.5 cm/s. At stations 3 and 4, the turbulence intensity is approximately constant throughout the depth below the trough level. The horizontal and vertical turbulence intensities below the trough level at stations 3 and 4 are ~ 9 cm/s and 5 cm/s, and ~ 6 cm/s and 5 cm/s, respectively.

The time-averaged turbulent kinetic energies were computed using the phase ensemble-averaged turbulence intensities as discussed in Section 7.2.1.2. Below the trough level, both the TKE and turbulence intensities have similar trends at their respective positions. The time averaged kinetic energy above the trough level increases rapidly and remains almost constant for a distance corresponding to the wave height before decreasing thereafter. At station 1, the TKE is smallest with a peak value of 30 cm^2/s^2, while at stations 3 and 4, the peak values are ~ 200 cm^2/s^2 and 120 cm^2/s^2. The TKE also increases with distance above the bed at stations 3 and 4.

A composite plot showing the time-averaged TKE presented here together with other LDA measurements (refer *Mocke, 1998*), in plunging waves at positions where $h/h_b \sim 0.7$, is shown in Figure 7.14. The TKE are plotted using normalised coordinates. The height is normalised with respect to the mean water level, h, and the TKE is normalised with respect to (gh). It can be seen that below the trough level, the measurements presented here are higher than those of *Stive(1980)* but lower than those measured by *Ting and Kirby(1994)*. Figure 7.14 also show that the DCIV measurements extend well above the trough level. The DCIV measurements of TKE also show a steeper gradient with depth.

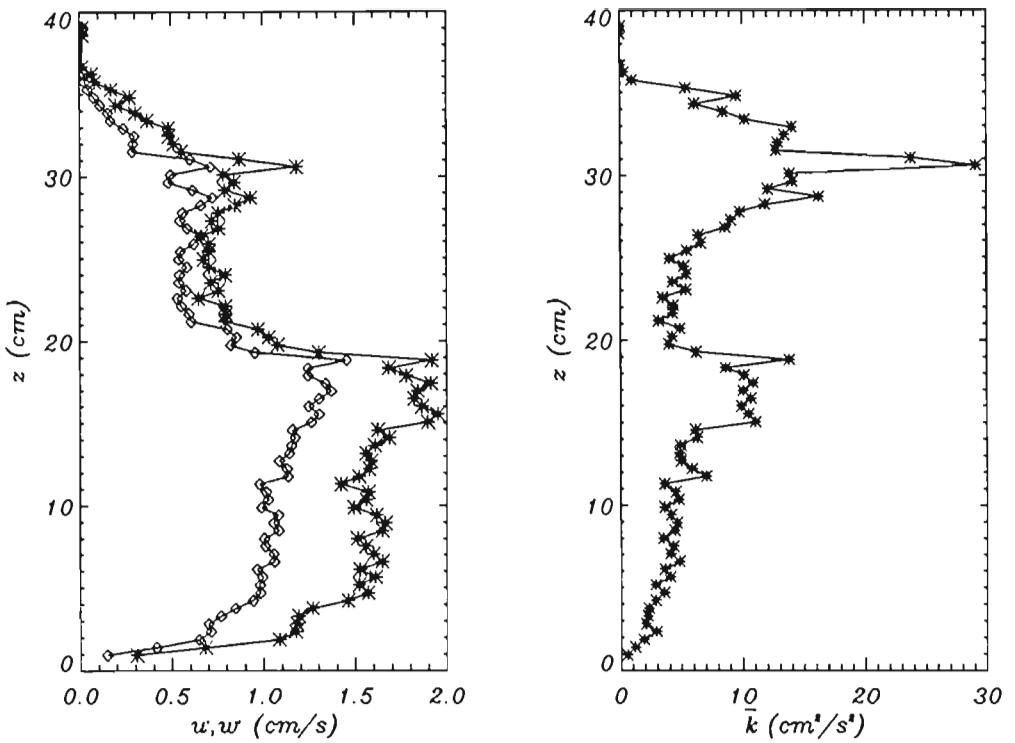

Figure 7.11: Time-averaged (left) horizontal(*) and vertical(◇) turbulence intensities and (right) TKE in the plunging wave at station 1($x-x_b$=-111 cm, H ~ 15 cm, h ~ 21.5 cm, h_b ~ 15.6 cm).

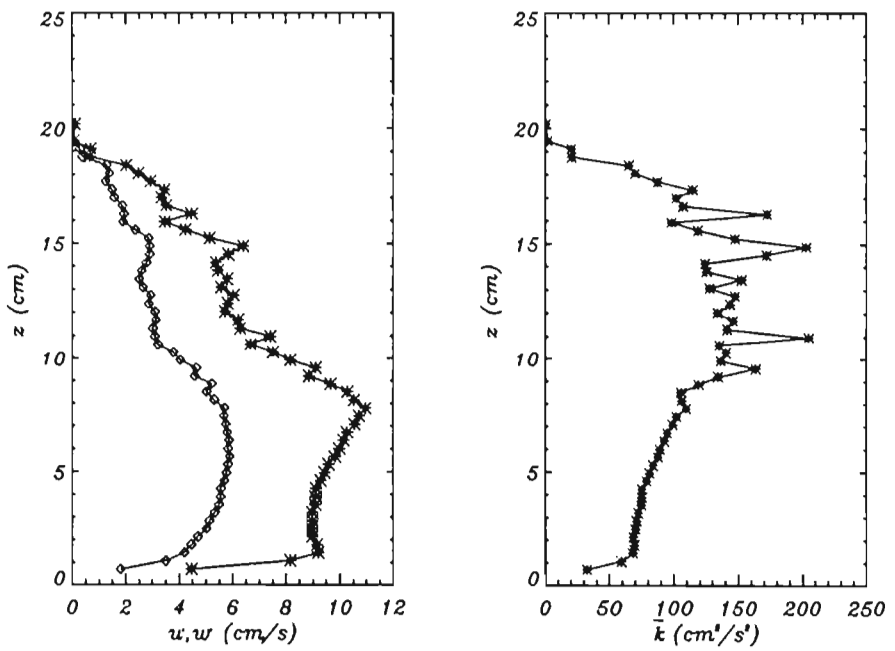

Figure 7.12: Time-averaged (left) horizontal(*) and vertical(+) turbulence intensities and (right) turbulent kinetic energy in the plunging wave at station 3($x-x_b$=86 cm, H ~ 11.5 cm, h ~ 11.8 cm, h_b ~ 15.6 cm).

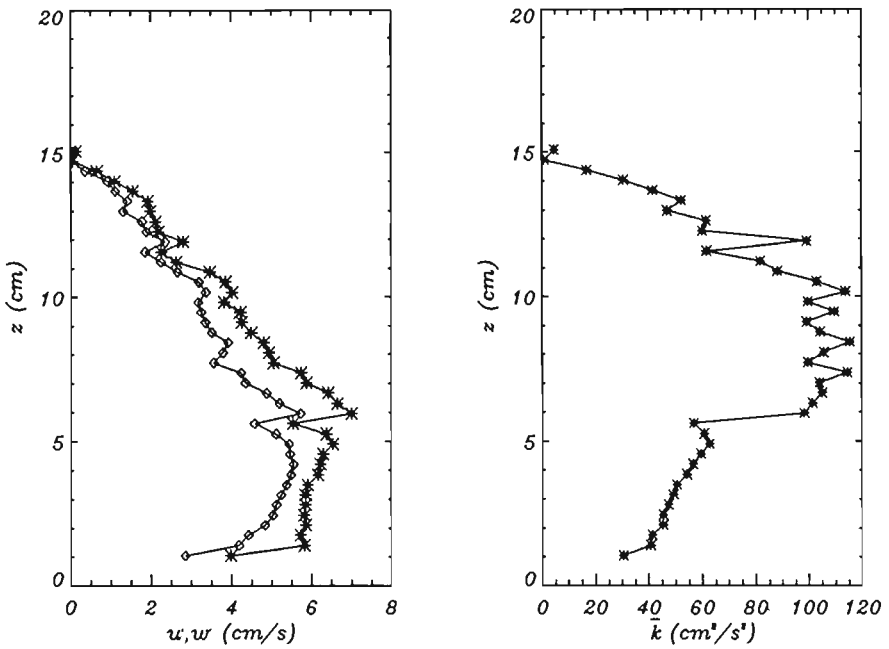

Figure 7.13: Time-averaged (left) horizontal(*) and vertical(+) turbulence intensities and (right) turbulent kinetic energy in the plunging wave at station 4($x-x_b = 169$ cm, $H \sim 7.8$ cm, $h \sim 8.38$ cm, $h_b \sim 15.6$ cm).

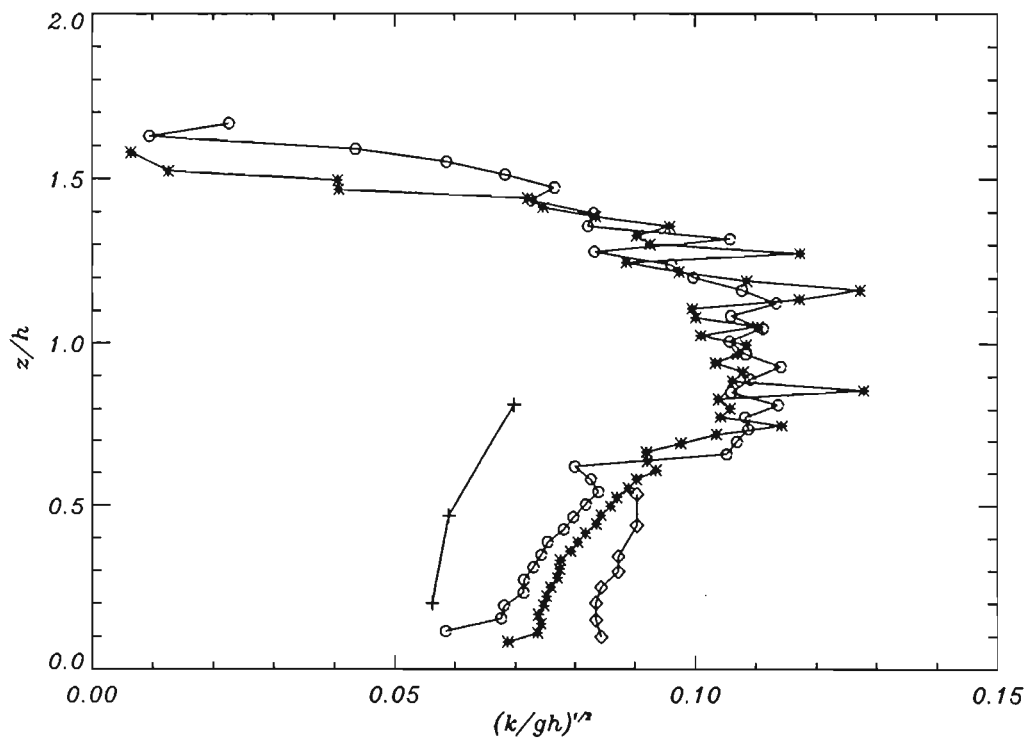

Figure 7.14: Comparison of time-averaged TKE of *Stive(1980)*(+), *Ting & Kirby(1994)*(◇) and DCIV measurements in the plunging wave at stations 3(*) and 4(o).

7.3 Reynolds stress and eddy viscosity

The Reynolds stresses were computed together with the turbulence intensities at each phase position using the snap shot of the instantaneous velocity fields. Thus the Reynolds stress measurements are available at intervals of ~ 0.25 cm in the vertical and horizontal directions over the entire wave phase. The time-averaged Reynolds stress, $-\langle u'w' \rangle$, was then computed by averaging over the wave phase, at each vertical position.

The Reynolds stress, τ, can be modelled using the Boussinesq approximation (*Boussinesq, 1877*), that is

$$\tau = -\rho \langle u'w' \rangle = \rho \nu_T \frac{\partial \bar{u}}{\partial z} \tag{7.6}$$

with the eddy viscosity given by:

$$\nu_T = \frac{-\langle u'w' \rangle}{\partial \bar{u}/\partial z} \tag{7.7}$$

where the overbar denotes time-averaged quantities.

7.3.1 Reynolds stress and eddy viscosity in spilling waves

The time-averaged Reynolds stress and the eddy viscosity in the spilling wave at stations 1, 2 and 3 are shown in Figures 7.15, 7.16 and 7.17, respectively. At stations 1 and 2, the Reynolds stress below the trough level is almost constant, showing a slight increase with distance above the bed, while above the trough level, the Reynolds stress show a rapid increase over a short distance and decreasing thereafter. The Reynolds stress at station 3 increases almost linearly with distance above the bed.

The eddy viscosity below the trough level at station 2 is almost zero, while above the trough level there is a rapid increase (corresponding to the point of maximum Reynolds stress) followed by a decrease thereafter. The eddy viscosity at station 3 shows an increasing trend towards the bed, reaching a maximum of ~ 5 cm^2/s at z ~ 4 cm, thereafter the eddy viscosity decreases almost linearly to zero near the bed.

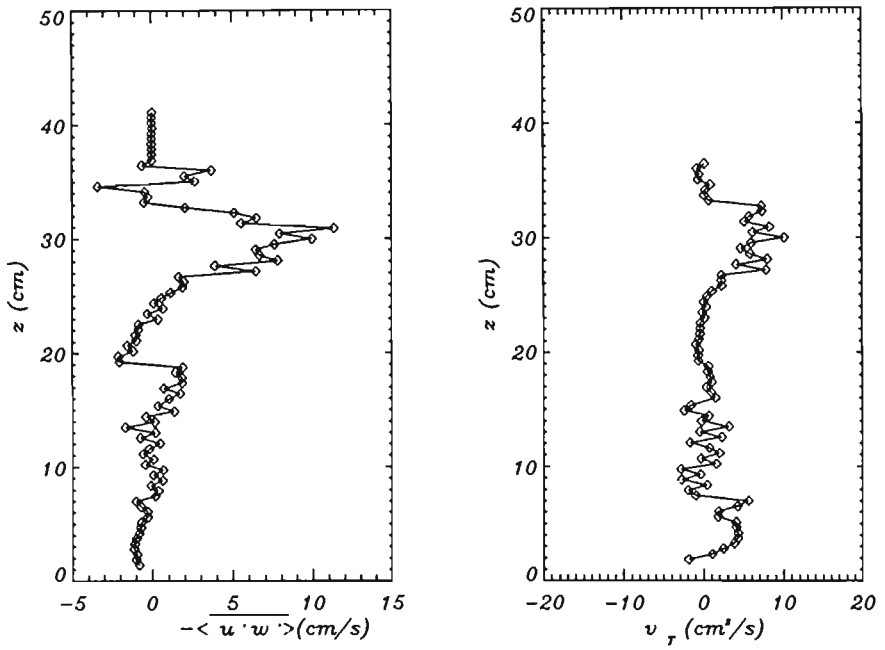

Figure 7.15: Time-averaged (left) Reynolds stress and (right) eddy viscosity in the spilling wave at station 1($x-x_b$=24 cm, H ~ 15 cm, h ~ 21.1 cm, h_b ~ 21.8 cm).

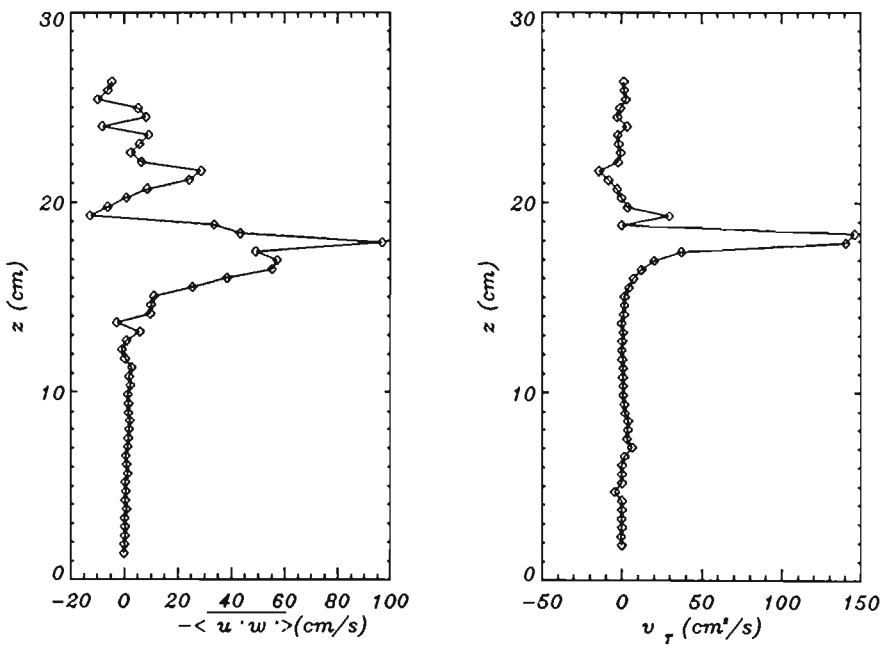

Figure 7.16:(a) Time-averaged (left) Reynolds stress and (right) eddy viscosity in the spilling wave at station 2($x-x_b$=122 cm, H ~ 11 cm, h ~ 16.6 cm, h_b ~ 21.8 cm).

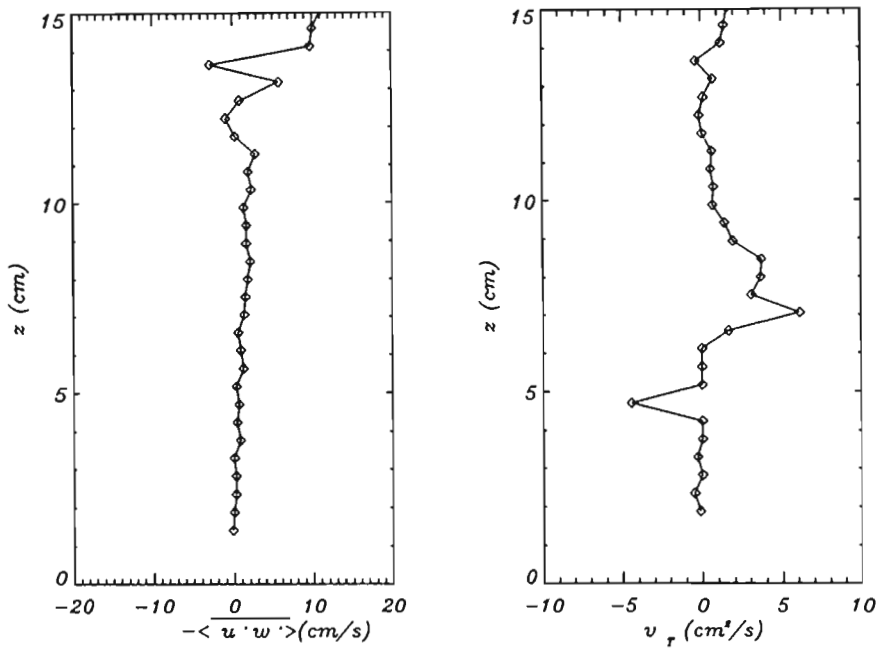

Figure 7.16:(b) Time-averaged (left) Reynolds stress and (right) eddy viscosity below the approximate trough level in the spilling wave at station 2, corresponding to the z < 15 cm in Figure 7.16(a).

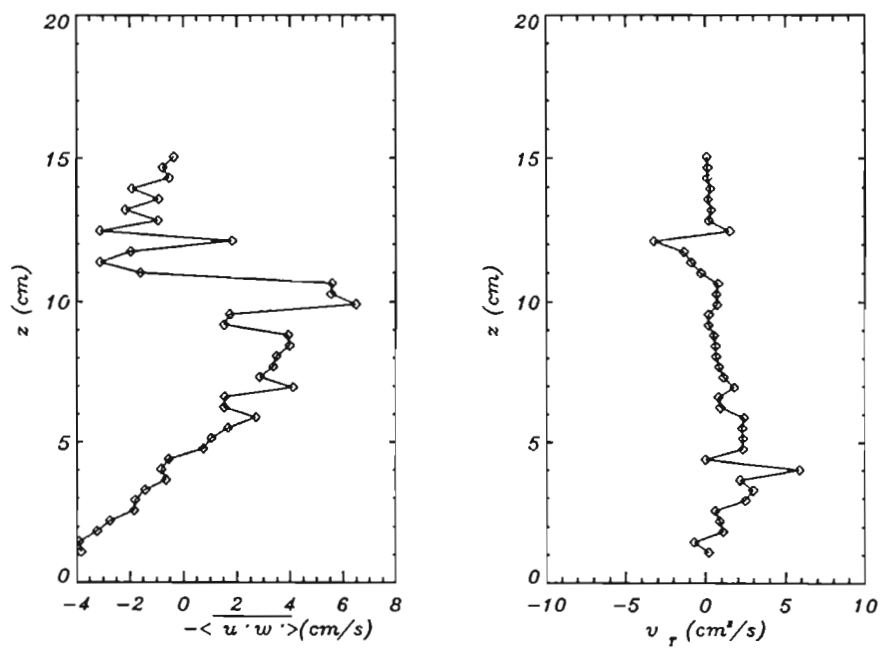

Figure 7.17: Time-averaged (left) Reynolds stress and (right) eddy viscosity for the spilling wave at station 3($x-x_b$=221 cm, H ~ 6.5 cm, h ~ 12.9 cm, h_b ~ 21.8 cm).

7.3.2 Reynolds stress and eddy viscosity in plunging waves

The time-averaged Reynolds stress in the plunging wave at stations 1, 3 and 4 are shown in Figures 7.18, 7.19 and 7.20, respectively. The Reynolds stress at station 1 is almost zero in the vicinity of the bed and increases very slightly near the trough level, while above the trough level the Reynolds stress fluctuates about zero, with a peak fluctuation of ~ 6 cm^2/s^2. The Reynolds stress near the bed at station 3 is negative, (-5 cm^2/s^2), and increases almost linearly with distance above the bed, reaching a maximum, ~ 20 cm^2/s^2, near the trough level and decreasing thereafter. At station 4, the Reynolds stress near the bottom is zero increasing very gently at first, followed by a rapid increase near the trough level.

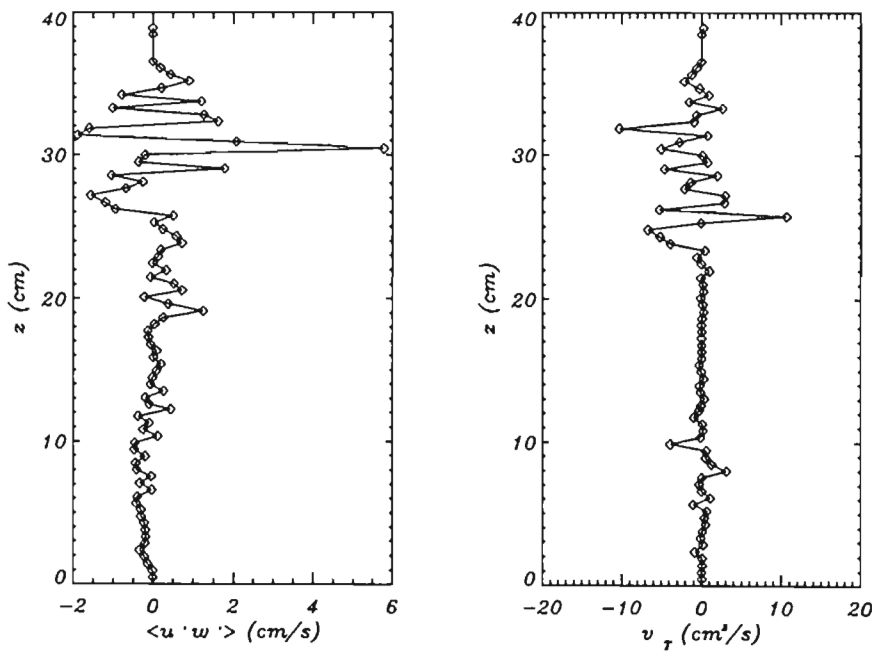

Figure 7.18: Time-averaged (left) Reynolds stress and (right) eddy viscosity in the plunging wave at station 1($x-x_b$=-111 cm, H ~ 15 cm, h ~ 21.5 cm, h_b ~ 15.6 cm).

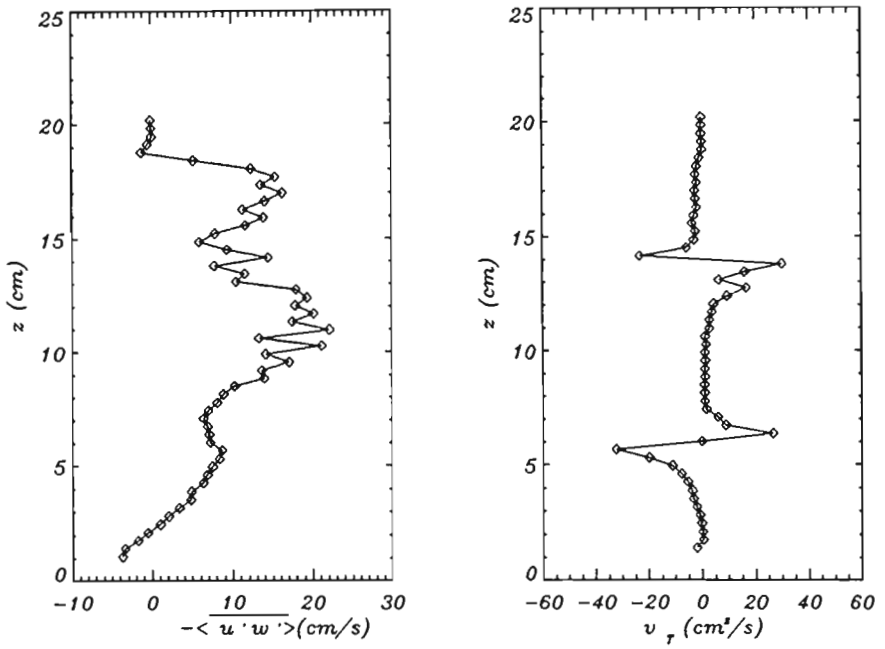

Figure 7.19: Time-averaged (left) Reynolds stress and (right) eddy viscosity in the plunging wave at station 3($x-x_b$=86 cm, H ~ 11.5 cm, h ~ 11.8 cm, h_b ~ 15.6 cm).

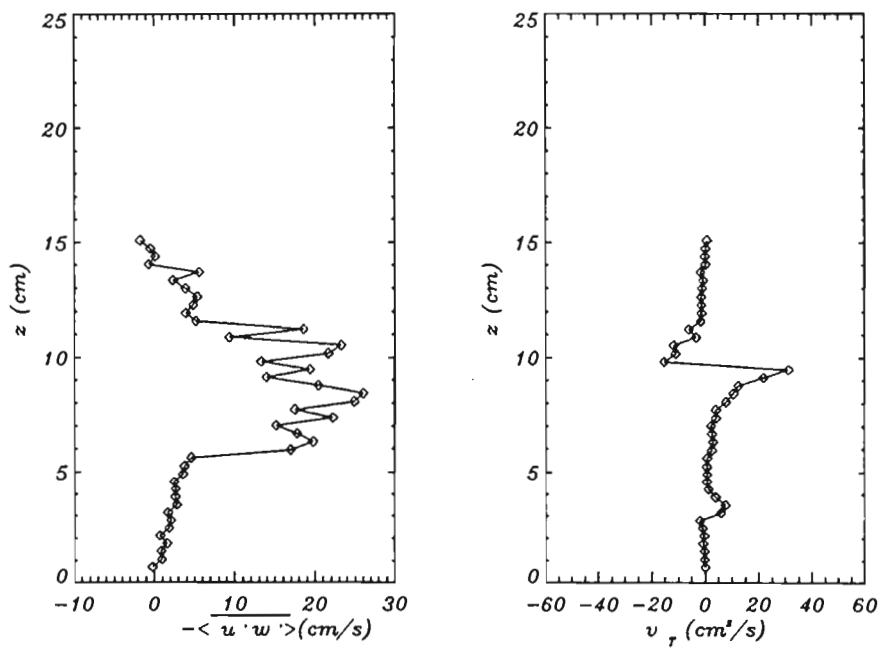

Figure 7.20: Time-averaged (left) Reynolds stress and (right) eddy viscosity in the plunging wave at station 4($x-x_b$=169 cm, H ~ 7.8 cm, h ~ 8.38 cm, h_b ~ 15.6 cm).

7.3.3 Comparison with LDA measurements

The Reynolds stress and eddy viscosity measurement by *Okayasu(1988)*, using LDA, are presented in Figure 7.21 below. Comparison of Reynolds stress measurements with DCIV measurement at station 3 for both spilling and plunging waves show consistent features for measurements below the trough level. At the bottom the Reynolds stress is in the order of 5 g/cm s^2 and increasing linearly to a peak of around 15 g/cm s^2 near the trough level, $z/h=1$.

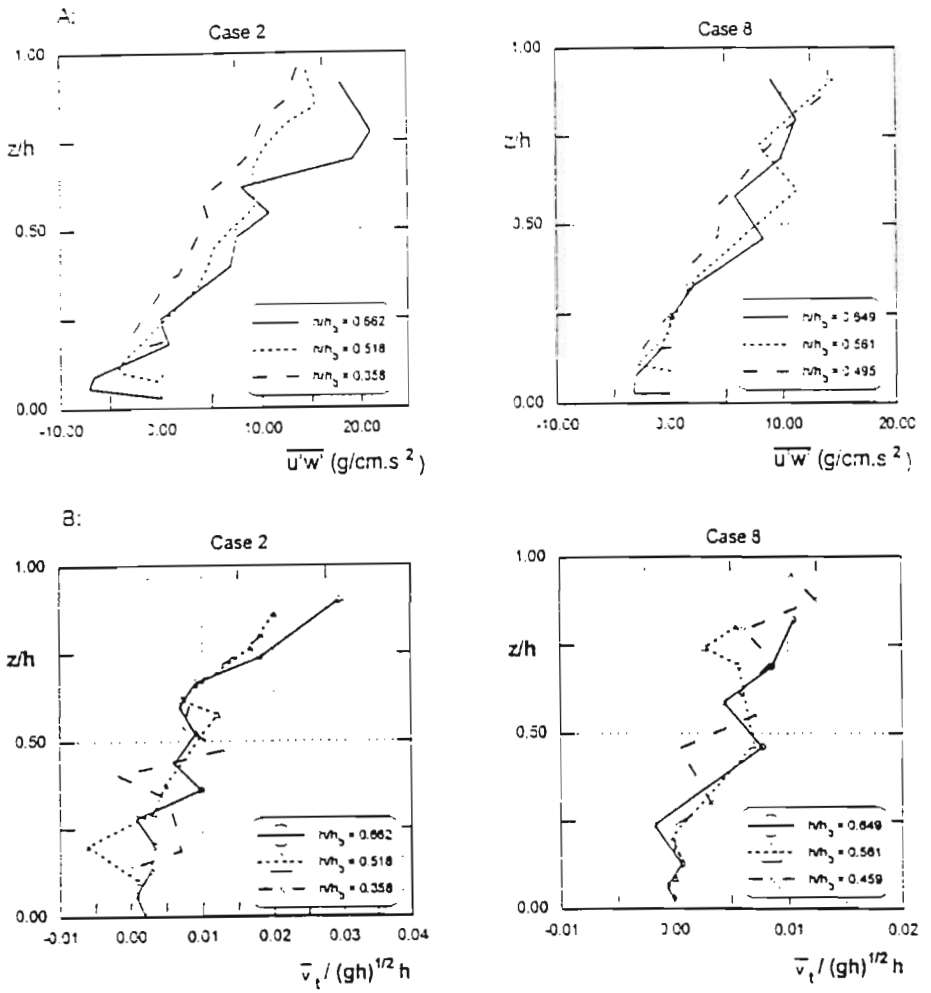

Figure 7.21: Vertical distribution of A) mean Reynolds stress and B) mean eddy viscosity for case 2 and 8 of *Okayasu et al.(1988)*, extracted from a compilation by *Mocke(1998)*.

The eddy viscosity measurement by *Okayasu(1988)* also show linear increasing trend with distance above the bed, these, however, are dissimilar to the DCIV measurements of eddy viscosity, possibly due to the sensitivity to the numerical computation of the gradient in Equation 7.7.

7.4 Vorticity analysis of the phase ensemble-averaged flow

Turbulent flow exhibits high levels of vorticity and fluctuations of vorticity. The presence of regions of non-zero vorticity in turn implies the presence of vortices. There are close links between the strain rate and vorticity as discussed in Chapter 2. The vortices that are aligned with the mean strain rate are stretched, while those that are perpendicular to the mean strain rate are compressed. The rate of strain and vorticity play a crucial role in transferring energy from the mean flow to large scale eddies, and from the large scale eddies down the hierarchy to the smaller scale eddies. The vorticity of the phase ensemble-averaged flow also influences the mass and momentum transport in the surf zone as shown by *Nadaoka(1989)*.

The phase-averaged vorticity is obtained by computing the curl of the phase-averaged velocity vector field as follows:

$$\omega_k = \nabla \times \langle \boldsymbol{u} \rangle = \frac{\partial \langle u \rangle}{\partial y} - \frac{\partial \langle w \rangle}{\partial x} \tag{7.8}$$

where $\langle u \rangle$ and $\langle w \rangle$ are the phase ensemble-averaged horizontal and vertical velocities, respectively. The derivatives have been evaluated using finite differences. The computation of derivatives using finite differences is sensitive to noise in the velocity measurements and should be implement with care. Since we are computing the vorticity of the phase ensemble-averaged flow field where most of the measurement noise has been removed as a result of the averaging operation, the finite difference scheme therefore does not pose a serious problem in this instance. However, the computation of the vorticity of the *instantaneous* velocity fields using finite differences should be done with caution. In these cases it is best to fit a 2D spline function to the velocity field and compute the vorticity analytically using the coefficients of the spline fit (e.g. *Fincham, 1997*).

7.4.1 Vorticity in Spilling waves

Figures 7.22, 7.23 and 7.24 shows the contour plot of the vorticity in the spilling wave at stations 1, 2 and 3, respectively. The peak values of vorticity occur at the base of the crest where a large velocity shear is created by the forward flow above the trough level and the reverse flow below.

At station 1 (Figure 7.22) the peak vorticity, $\sim +30\ s^{-1}$, occurs near the top of the wave, where spilling of the wave is taking place. In the major part of the wave below the trough level the there is a small negative vorticity, $\sim -1\ s^{-1}$.

At station 3 (Figure 7.23) peak vorticity, in the range $+30$ to $+100\ s^{-1}$, occurs at the toe of the wave. In the rear of the crest, the vorticity is $\sim 5\ s^{-1}$. In the region $3 < z < 6$, the vorticity is almost zero and near the bed it is negative ($\sim -2\ s^{-1}$). Measurements by *Nadaoka(1989)*(see Chapter 2) in spilling waves, breaking at the edge of a 1:20 slope beach, indicate similar values near the bed and in the major part of the wave. Peak vorticity measured in the crest by Nadaoka is lower, $\sim 14\ s^{-1}$. The lower vorticity is due to the measurement being conducted in the flat section of the beach where wave breaking is reduced. The large vorticity at the base of the crest is responsible for the large vortex created there. This vortex has a dimension comparable to the wave height.

The peak vorticity along the surf zone occurs in the vicinity of wave breaking and has a value that is almost constant throughout the surf zone. There is, however, spreading of vorticity into the rear of the wave as it propagates across the surf zone.

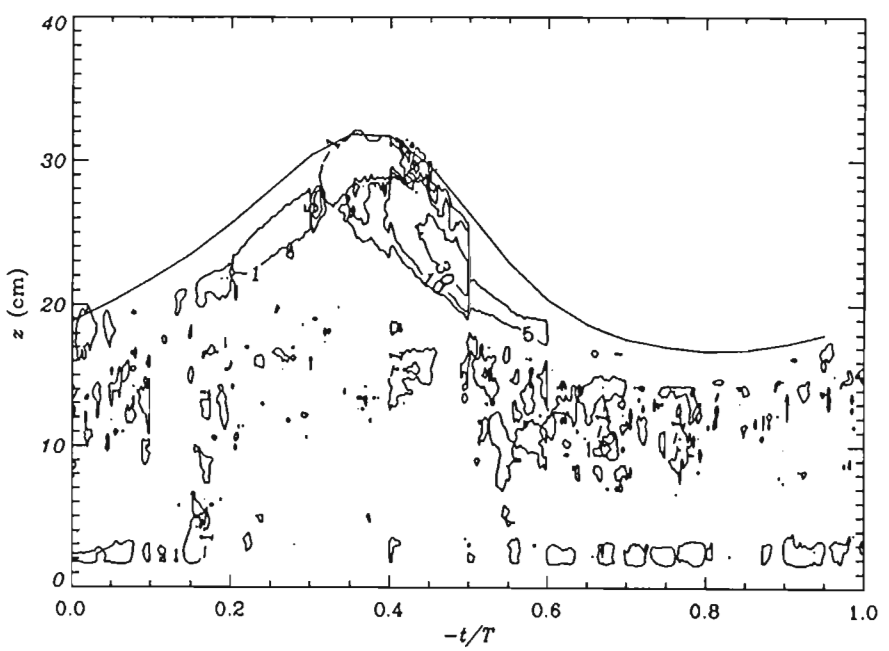

Figure 7.22: Vorticity, in s^{-1}, of the phase ensemble averaged velocity field in the spilling wave at station 1 which is located approximately 24 cm beyond the breakpoint.

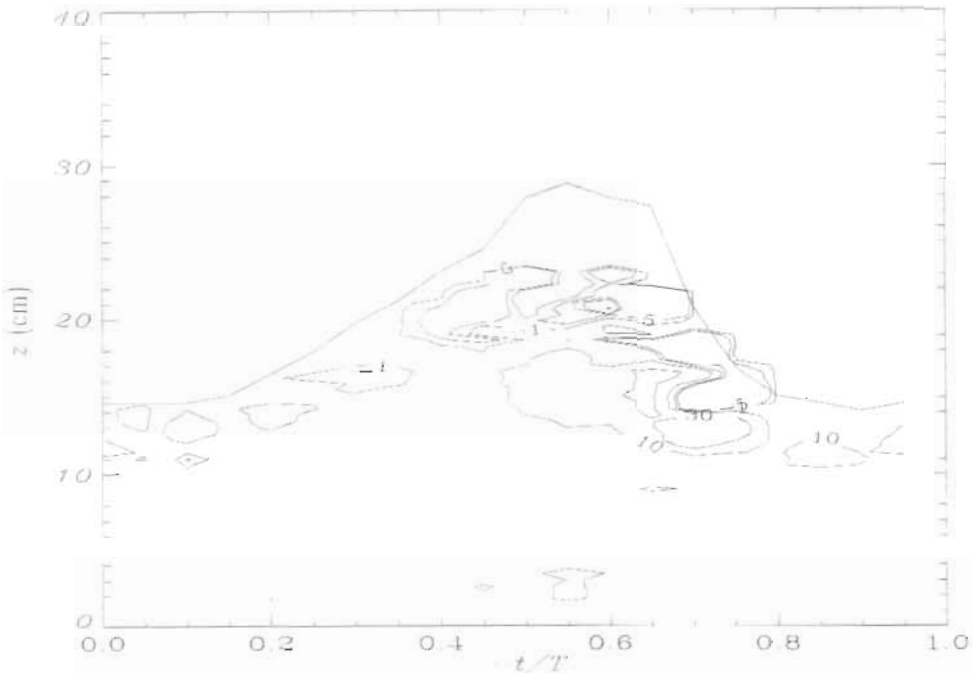

Figure 7.23: Contours of the phase ensemble-averaged vorticity, in s^{-1}, in the spilling wave at station 2 which is located approximately 122 cm beyond the breakpoint.

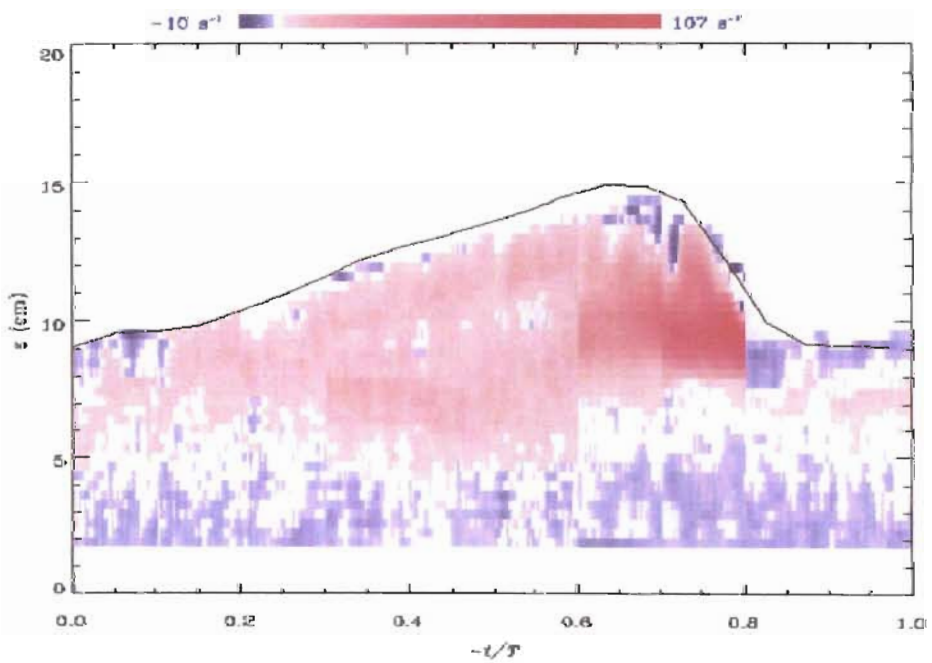

Figure 7.24: Pseudo-colour plot of the phase ensemble-averaged vorticity, in s^{-1}, in the spilling wave at station 3 which is located approximately 221 cm beyond the breakpoint.

7.4.2 Vorticity in plunging waves

Figures 7.25, 7.26 and 7.27 show the contour plots of the vorticity in the plunging wave at stations 1, 3 and 4, respectively. The peak values of vorticity occur at the base of the crest where a large velocity shear is created by the forward flow above the trough level and the reverse flow below.

The peak vorticity at station 1 (Figure 7.25), which corresponds to a pre-breaking position for the plunging wave case, is $\sim 2\ s^{-1}$ and occurs near the top of the wave. In the major part of the wave, below the trough level, there is a small negative vorticity, $\sim -1\ s^{-1}$.

At station 3 (Figure 7.26) and 4 (Figure 7.27) peak vorticity,in the range $+30$ to $+140\ s^{-1}$, occurs at the toe of the wave. In the rear of the crest and lower part of the wave the vorticity is $\sim 1\ s^{-1}$. Near the bed there is negative vorticity $\sim -2\ s^{-1}$.

The peak vorticity in the plunging waves are similar to those occurring in the spilling wave. In the plunging waves there is little spreading of vorticity. The vorticity in the surf zone is very much higher compared with that occurring at the pre-breaking position, implying that wave breaking is the primary mechanism of vorticity generation.

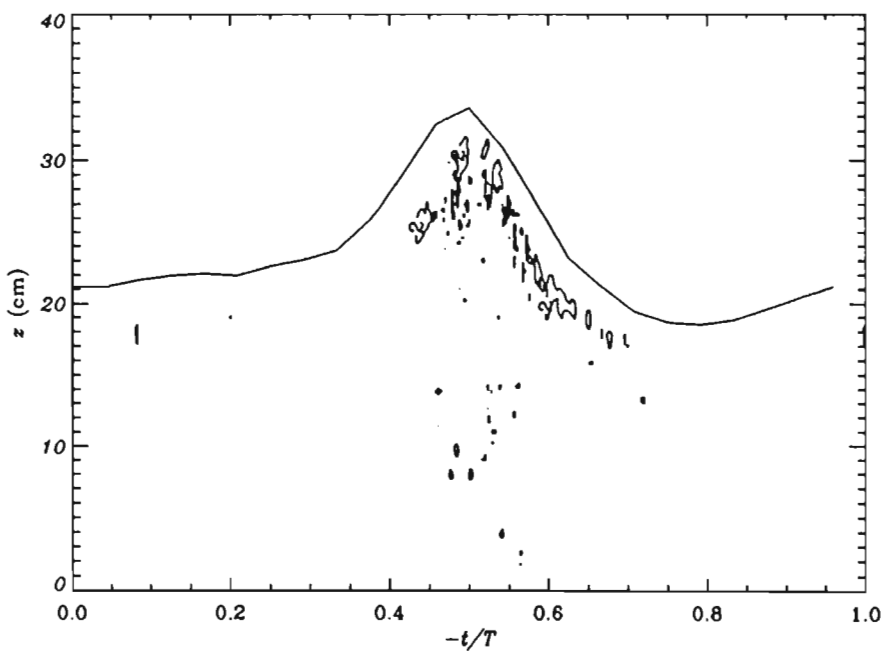

Figure 7.25: Vorticity, in s^{-1}, of the phase ensemble-averaged velocity field in the plunging wave at station 1 which is located approximately 111 cm before the breakpoint.

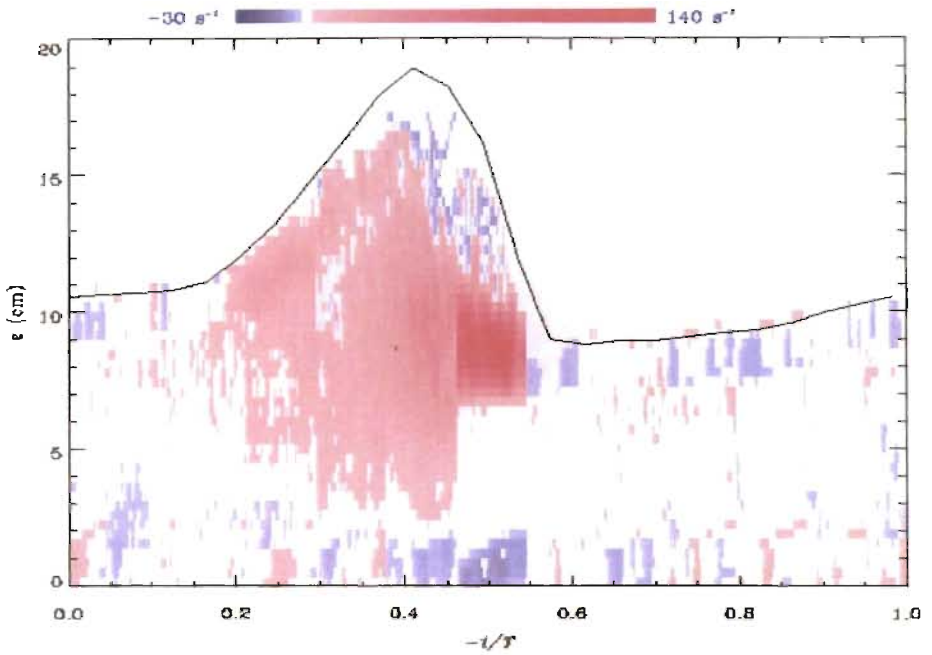

Figure 7.26: Pseudo-colour plot of the phase ensemble-averaged vorticity, in s^{-1}, in the plunging wave at station 3 which is located approximately 86 cm beyond the breakpoint.

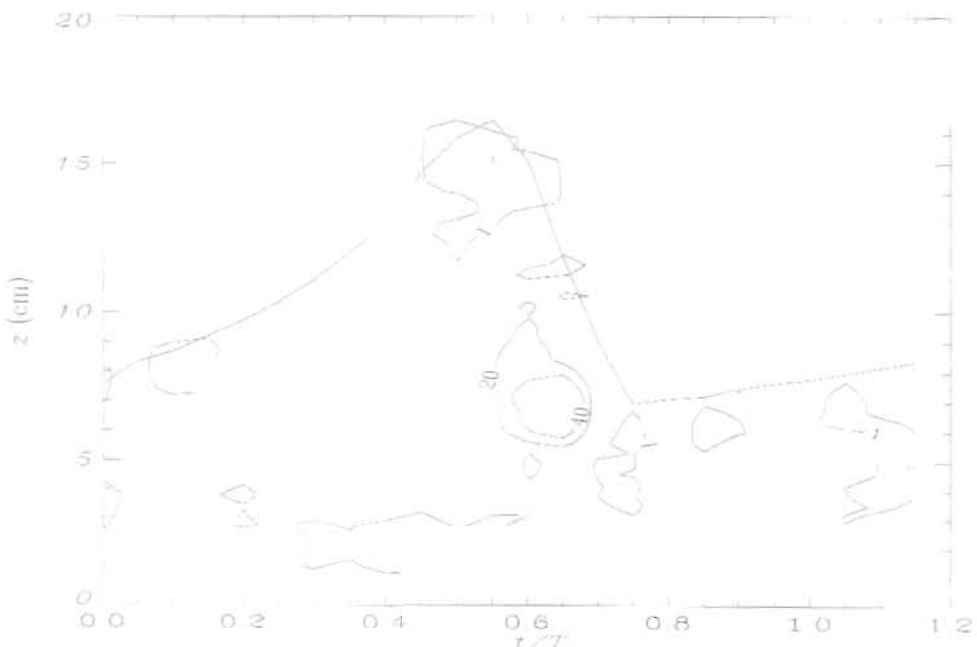

Figure 7.27: Contours of the Phase ensemble-averaged vorticity, in s^{-1}, in the plunging wave at station 4 which is located approximately 169 cm beyond the breakpoint.

7.5 Spectral analysis

The correlation and spectral density functions are used in the spectral analysis of turbulence. The spatial correlation tensor, R_{ij}, of the turbulence velocity component, $u_i(x)$, is used and is defined as follows:

$$R_{ij}(x') = \overline{u_i(x)u_j(x+x')} \tag{7.9}$$

where u_i and u_j are the velocity components along a particular coordinate axis. The spectral tensor, ϕ_{ij}, is then the Fourier transform of the correlation tensor. The sum of the diagonal elements of the spectrum tensor is of particular significance, since it represents the kinetic energy at a given wavenumber. The energy spectrum is usually represented as a function of a scalar wavenumber, k, and is obtained by integrating the sum of the diagonal components over a spherical shell of radius k (*Frost and Moulden, 1977; Tennekes and Lumely, 1972*).

$$E(k) = \frac{1}{2}\int\int \Phi_{ii}(k)d\sigma \tag{7.10}$$

The characteristic behaviour of the scalar wavenumber spectrum $E(k)$ can be inferred through a process of dimensional analysis and physical reasoning. A typical form of $E(k)$ is shown in Figure 7.28.

The largest eddies are those with a permanent character and occur at very low wavenumbers. The energy containing eddies occur at the peak of the spectrum, and the upper end of the spectrum, which is referred to as the equilibrium range, corresponds to the small eddies responsible for the dissipation of the turbulence energy. The turbulence in the equilibrium range is isotropic and the energy spectrum has the following form:

$$E(k) = \alpha \varepsilon^{2/3} k^{-5/3} \tag{7.11}$$

where ε is the rate of energy dissipation and $\alpha \approx 1.5$ is an empirical constant.

Equation 7.10 provides a full spectral description of the turbulence. However, most previous measurements of the wavenumber spectrum were obtained by measuring one dimensional spectra using point measuring techniques. The 1D auto and cross correlation function of the

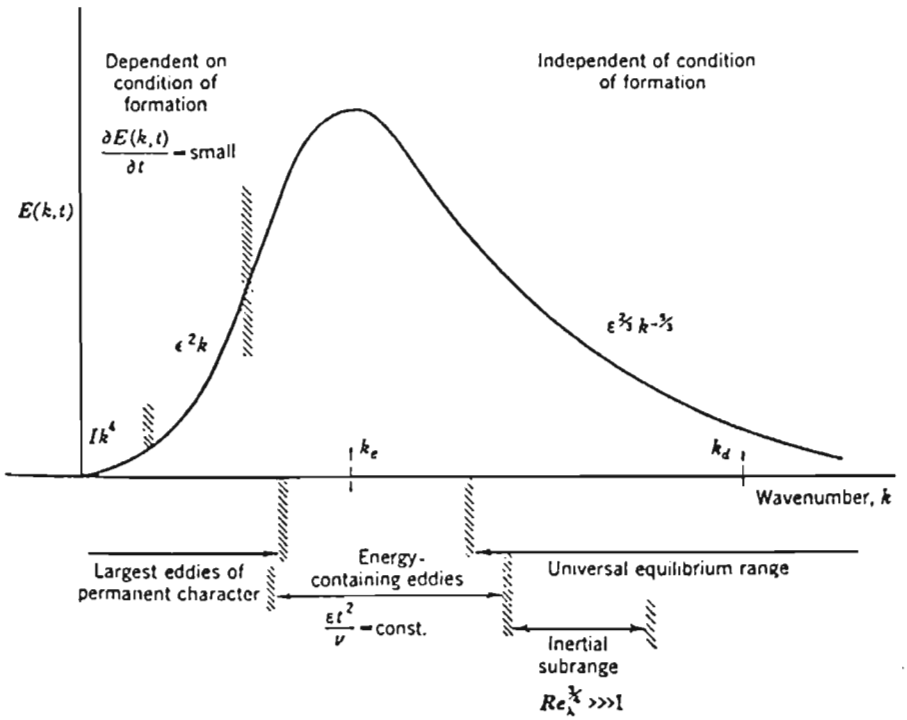

Figure 7.28: Typical energy spectrum, *E(k)*, of 3D turbulence (*Frost and Moulden, 1977*).

velocities were measured using point measuring techniques such as LDA, hot wire anemometry etc.. This type of spectral analysis is subjected to alaising of the wavenumber spectrum (*Frost and Moulden, 1977; Tennekes and Lumely, 1972*). There is however a large body of mathematical analysis based on this type of measurement and this form of measurement will be adopted here.

Essentially it is necessary to compute the 1D wavenumber spectrum of the horizontal and vertical velocity component over the entire wave phase at the desired depth using a number of wave cycles to form an average spectrum. Since the flow field of the entire wave is not available, the spectrum of the turbulent velocities, u' and w', are computed for each section of the wave using 50 instantaneous velocity vector fields. This is illustrated in Figure 7.29. Each instantaneous flow field is interpolated, the average along each row is subtracted from each vector along the row and a 1D FFT is computed for each row in each instantaneous flow field. This results in 50 instantaneous wavenumber spectrums. An average spectrum of each row is then computed for the wave phase in question. This procedure is repeated for the other sections of the wave. Finally, an average spectrum for the entire wave is computed. The procedure provides the wavenumber spectrum for $k > 10k_w$, where k_w is the

wavenumber of the surface wave. The spectrum of the horizontal velocity is referred to as lateral spectrum and that of the vertical velocity is referred to as the transverse spectrum. The spectrum computed as above still obeys the $k^{-5/3}$ law in the equilibrium range.

The relationship between $E(k)$ and the 1D spectrum of the horizontal velocity, F, is given by (*Hinze, 1959*):

$$E(k)=k^3\frac{d}{dk}\left(\frac{1}{k}\frac{dF}{dk}\right) \tag{7.12}$$

This relation is used to estimate $E(k)$ from measurements of F.

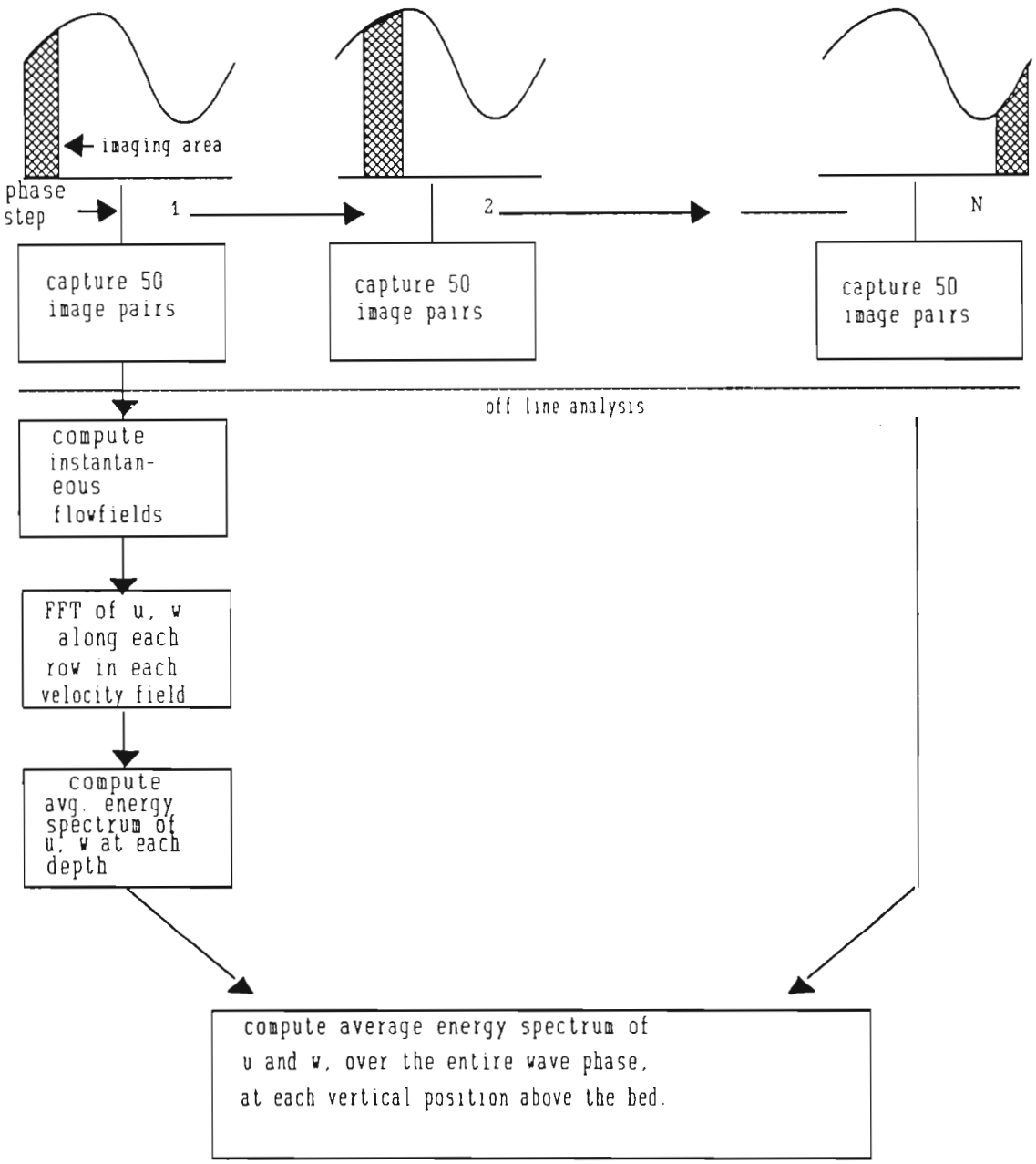

Figure 7.29: Computation of the lateral and transverse spectrum, using 50 instantaneous vector fields at each section of the wave.

7.5.1 Energy dissipation and length scales in spilling waves

The wavenumber spectrum in the spilling wave at stations 1 and 3 are shown in Figure 7.30. The spectrum is plotted on a log-log scale together with a -5/3 sloped line for comparison with the predicted characteristics in the equilibrium range. These plots show that for a wavenumber greater than that of the surface wave, the measured spectra at the various depths possess a slope $\sim$-5/3, but shifted vertically. The rate of dissipation,ε , was estimated by fitting a -5/3 sloped line and estimating the y-intercept of the measured spectra plotted on a log-log scale. The Taylor micro scale length, l, was then estimated using (*Hinge, 1959*)

$$\varepsilon(z)=15\nu\frac{\overline{u'_{rms}(z)}^2}{l^2(z)} \tag{7.13}$$

where $\nu=1.1\text{x}10^{-2}$ cm^2/s is the kinematic viscosity of water. The above expression is derived by expanding the dissipation term in Equation 7.1 and using Taylor's definition of the micro-scale length, which is inversely proportional to the slope of the auto correlation function at the peak. The use of Equation 7.11 to estimate the dissipation rate is justified, since it is applied at high wavenumbers where the behaviour of the flow at these wavenumbers are assumed to be isotropic. However, the use of Equation 7.13 should treated with caution, since it utilises the turbulence intensity of the overall flow, which is considered to anisotropic over some parts of the wave.

The estimated dissipation and length scale in the spilling wave at stations 1, 2 and 3 are shown in Figure 7.31, 7.32 and 7.33, respectively. Peak dissipation at stations 1, 2 and 3 are 7, 300 and 36 cm^2/s^3, respectively and occur above the trough level. Below the trough level, the dissipation decreases exponentially. At station 2 the dissipation shows an increase near the bottom due to boundary layer effects. Thus it can be seen that most of the wave energy is dissipated above the trough level.

The length scale shows a varying characteristic at each position in the surf zone. At station 1 (Figure 7.31), the length scale increases from the crest downwards. The length scale at the top of the crest is $\sim$0.9 cm and increases to $\sim$2 cm near the bottom in a near linear fashion.

The scale length at station 2 (Figure 7.31) is almost constant, $\sim$0.5 cm throughout the water

column.

The scale length at station 3 (Figure 7.32) decreases almost linearly from the bed upwards. The scale length near the bed is ~ 2 cm and 0.2 cm at the top of the crest.

Table 7.6 summaries the mean non-dimensional length scale in the crest of the spilling waves. It can be seen that the non-dimensional length scale in the crest of the waves is ~ 0.04h.

Table 7.5: Peak dissipation, ε, in the spilling wave

x-x_b (cm)	(station 1) 24	(station 2) 122	(station 3) 221
ε (cm^2/s^3)	7	300	36

Table 7.6: Non-dimensional length scale, l/h, in the spilling wave crests

x-x_b (cm)	(station 1) 24	(station 2) 122	(station 3) 221
l/h	0.04	0.03	0.06

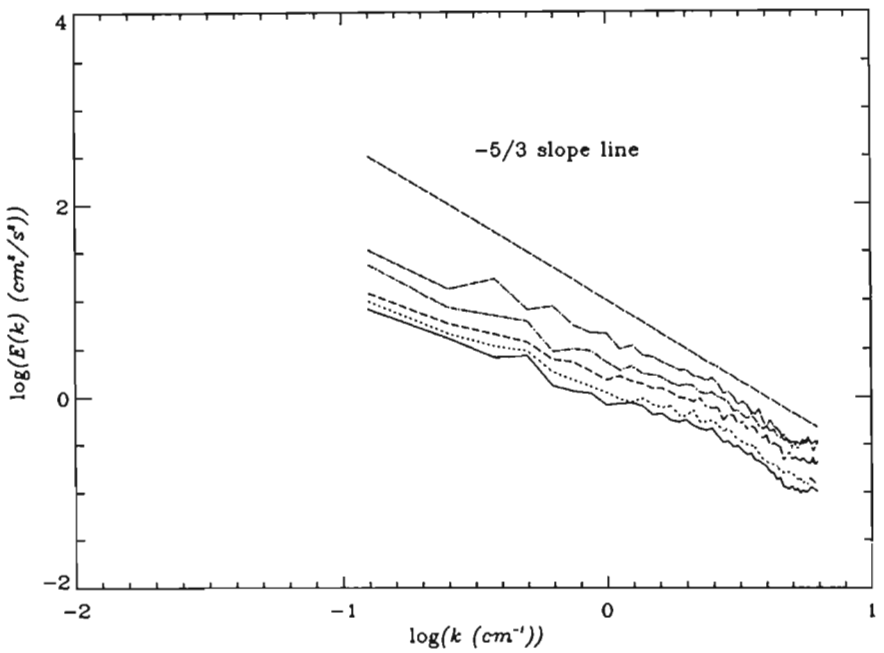

Figure 7.30:(A) Wavenumber spectrum in the spilling wave at station 1 at 4(__), 8(...), 12(_ _), 17(_._), 21(_..) cm above the bed. The expected -5/3 slope spectrum in the equilibrium range is also shown (long dashes).

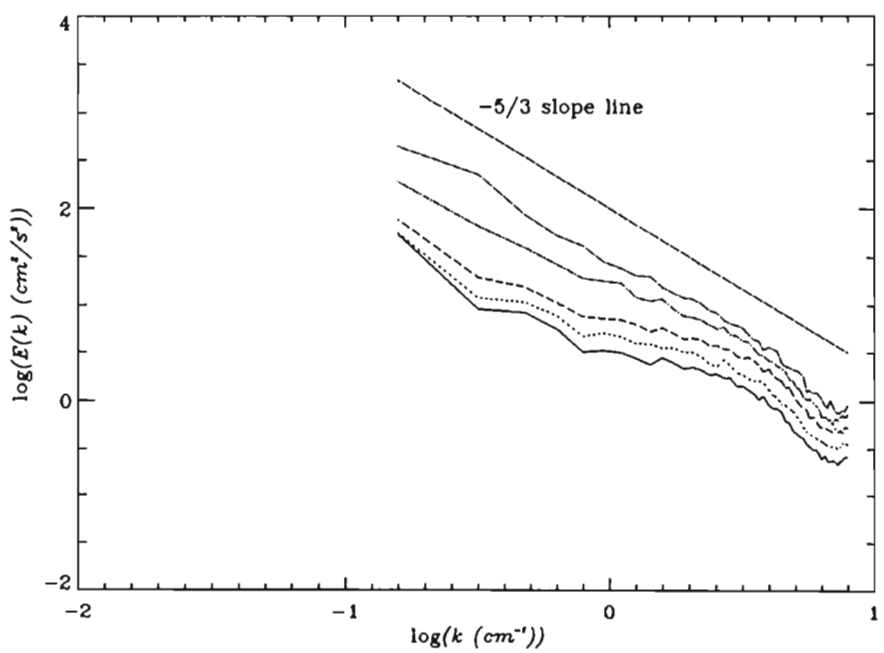

Figure 7.30: (B) Wavenumber spectrum in the spilling wave at station 3 at 2(__), 4(...), 7(_ _), 9(_._), 11(_..) cm above the bed. The expected -5/3 slope spectrum in the equilibrium range is also shown (long dashes).

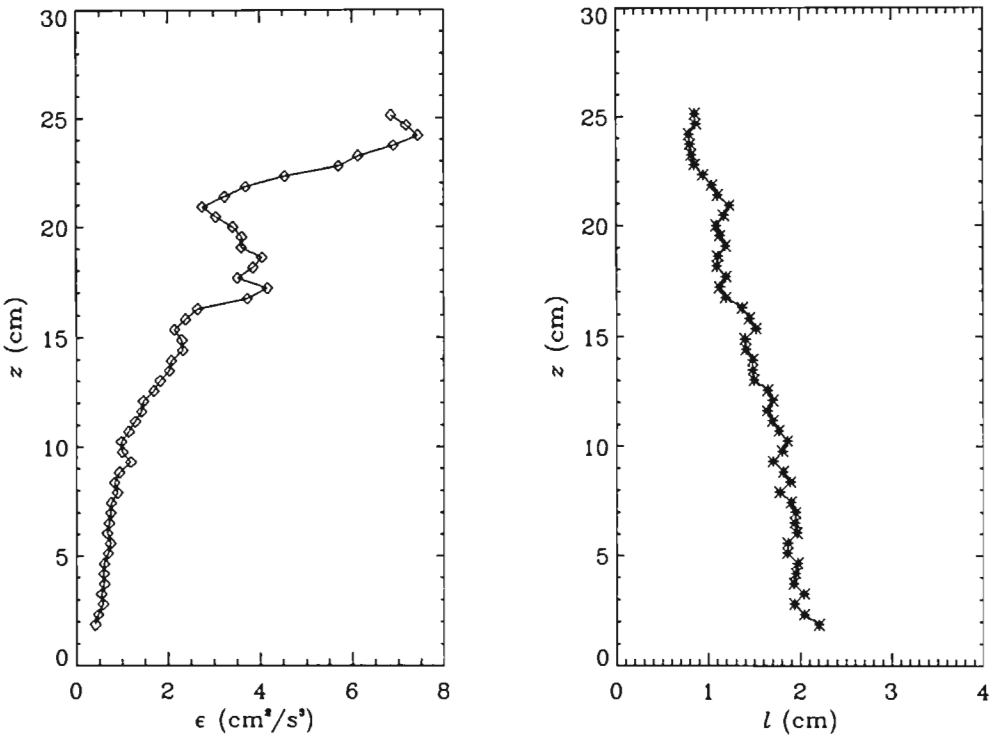

Figure 7.31: Rate of dissipation, ε, and scale length, l, in the spilling wave at station 1($x-x_b$=24 cm, H ~ 15 cm, h ~ 21.1 cm, h_b ~ 21.8 cm).

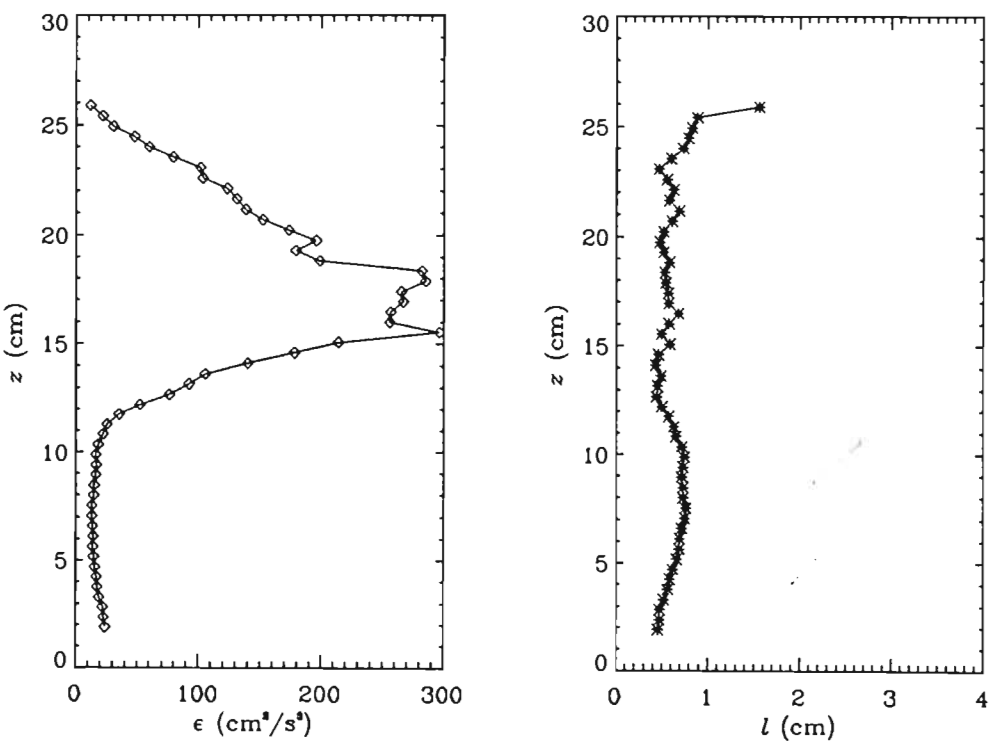

Figure 7.32: Rate of dissipation, ε, and scale length, l, in the spilling wave at station 2($x-x_b$=122 cm, H ~ 11 cm, h ~ 16.6 cm, h_b ~ 21.8 cm).

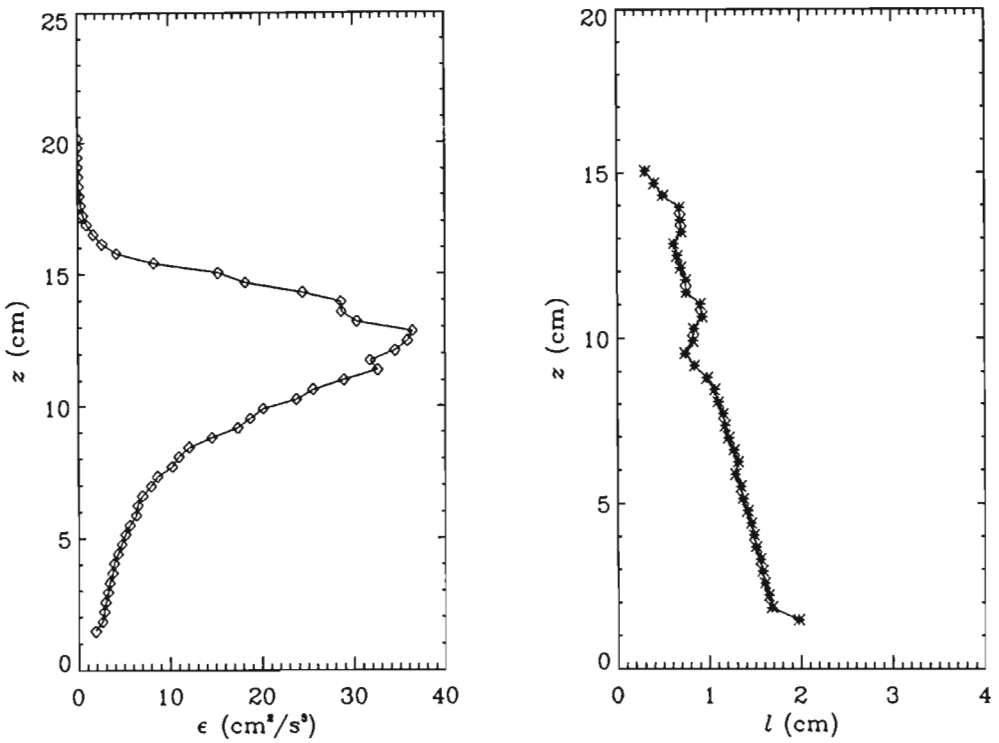

Figure 7.33: Rate of dissipation, ε, and scale length, l, in the spilling wave at station 3(x-x_b=221 cm, H~6.5 cm, h~12.9 cm, h_b~21.8 cm).

7.5.2 Energy dissipation and length scales in plunging waves

The wavenumber spectrum in the plunging wave at stations 1 and 3 are shown in Figure 7.34. The spectrum is plotted on a log-log scale together with a -5/3 sloped line for comparison with the predicted characteristics in the equilibrium range. These plots show that for wavenumbers greater than that of the surface wave, the measured spectrum at the various depths possesses a slope ~-5/3, but shifted vertically. As for the spilling wave case the rate of dissipation, ε, was estimated by fitting a -5/3 sloped line to the measured spectra and calculating the y-intercept and the length scale were computed using Equation 7.13.

The estimated dissipation in the plunging wave at stations 1, 3 and 4 are shown in Figures 7.35, 7.36 and 7.37, respectively. Peak dissipation at stations 1, 3 and 4 are 9, 125 and 75 cm^2/s^3, respectively and occur above the trough level. Below the trough level, the dissipation decreases exponentially suggesting diffusion of turbulence. Once again it can be seen that most of the wave energy is dissipated above the trough level.

The length scale at station 1 is almost constant for the major part of the water column, increasing only near the top of the wave. The length scales at positions below the trough level, in the surf zone, show an increasing trend with distance from the trough, while above the trough level the length scale is almost constant. Also suggesting diffusion similar to that generated by an oscillating grid (*E and Hopfinger, 1986*). The mean length scales above the trough level at stations 1, 3 and 4 are $\sim$0.6, 0.5 and 0.5 cm, respectively. Maximum length scale near the bed is $\sim$2 cm. Table 7.8 summarises the mean non-dimensional length scales above the trough level at all positions. It can be seen that the non-dimensional scale length, in the crest of the waves in the surf zone, is $\sim$0.04h. These are similar to those measured in the spilling waves. The non-dimensional scale length at station 1, however is much lower than 0.04h. This is due to the fact that station 1 corresponds to a pre-breaking position for the plunging wave case.

Table 7.7: Peak dissipation, ε, in the plunging wave

x-x_b (cm)	(station 1) 24	(station 2) 122	(station 3) 221
ε (cm^2/s^3)	9	125	75

Table 7.8: Non-dimensional length scale, l/h, in the plunging wave crests

x-x_b (cm)	(station 1) 24	(station 2) 122	(station 3) 221
l/h	$\sim$0.02	$\sim$0.04	$\sim$0.06

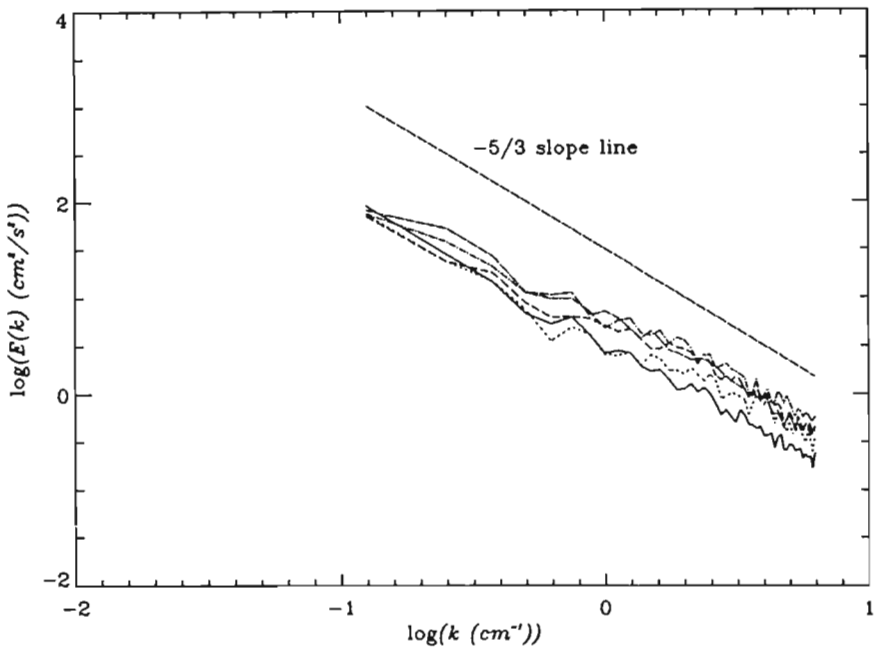

Figure 7.34:(A) Wavenumber spectrum in the plunging wave at station 1 at 4(__), 8(...), 12(_ _), 17(_._), 21(_..) cm above the bed. The expected -5/3 slope spectrum in the equilibrium range is also shown (long dashes).

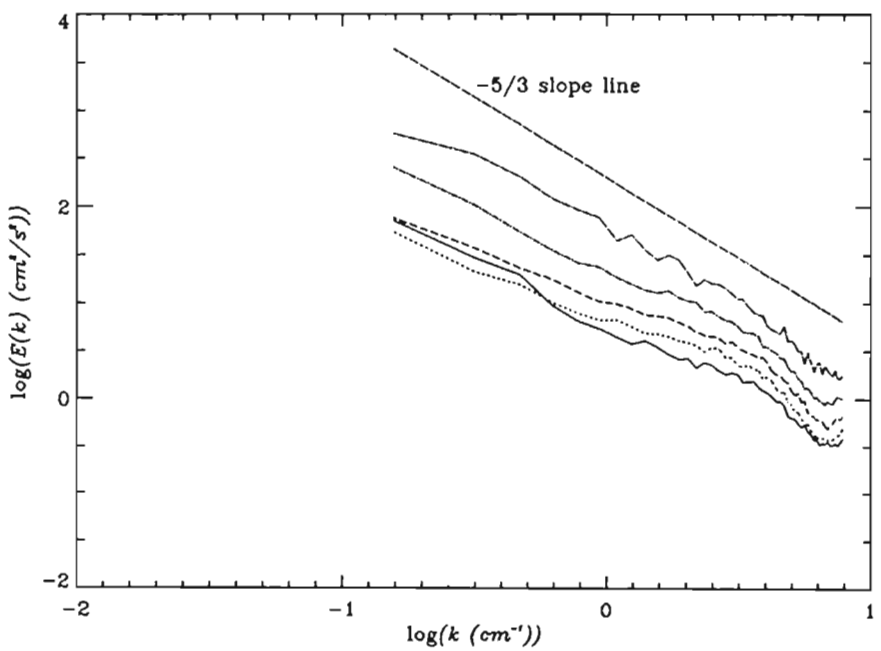

Figure 7.34: (B) Wavenumber spectrum in the plunging wave at station 3 at 2(__), 4(...), 7(_ _), 9(_._), 11(_..) cm above the bed. The expected -5/3 slope spectrum in the equilibrium range is also shown (long dashes).

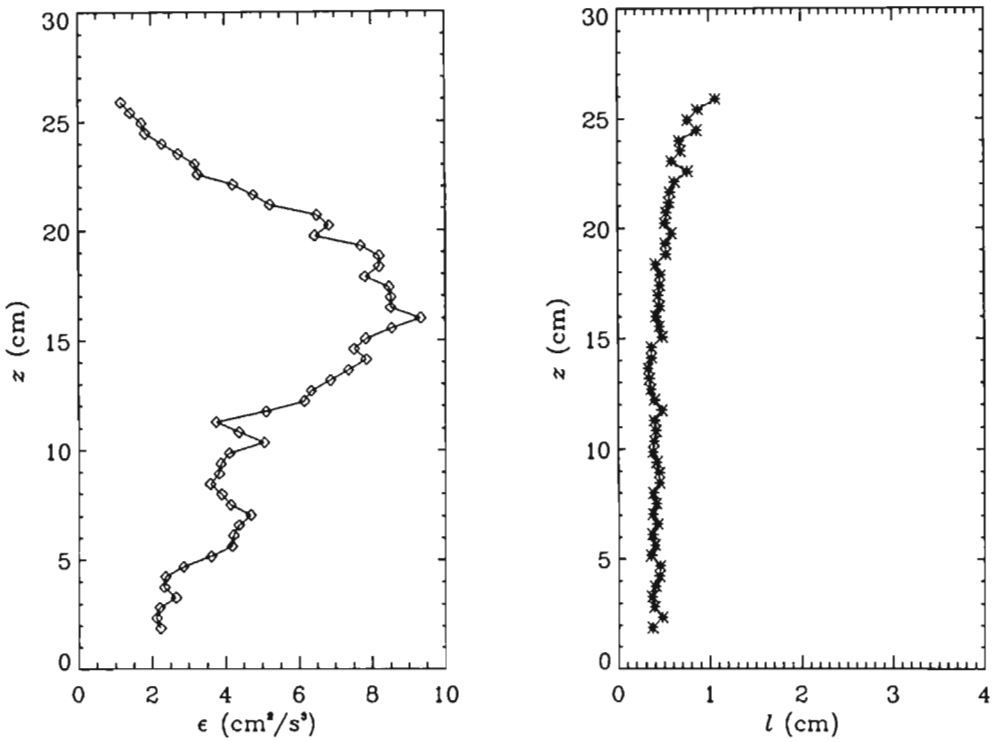

Figure 7.35: Rate of dissipation, ε, and length scale, l, in the plunging wave at station 1($x-x_b$=-111 cm, H ~ 15 cm, h ~ 21.5 cm, h_b ~ 15.6 cm).

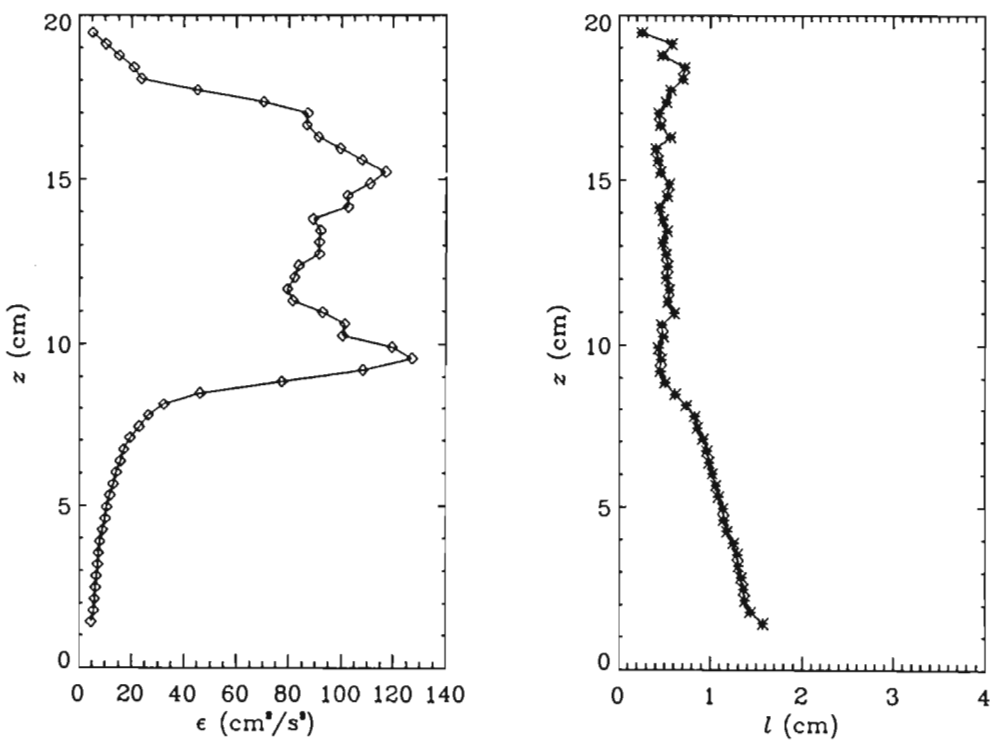

Figure 7.36: Rate of dissipation, ε, and length scale, l, in the plunging wave at station 3 ($x-x_b$=86 cm, H ~ 11.5 cm, h ~ 11.8 cm, h_b ~ 15.6 cm).

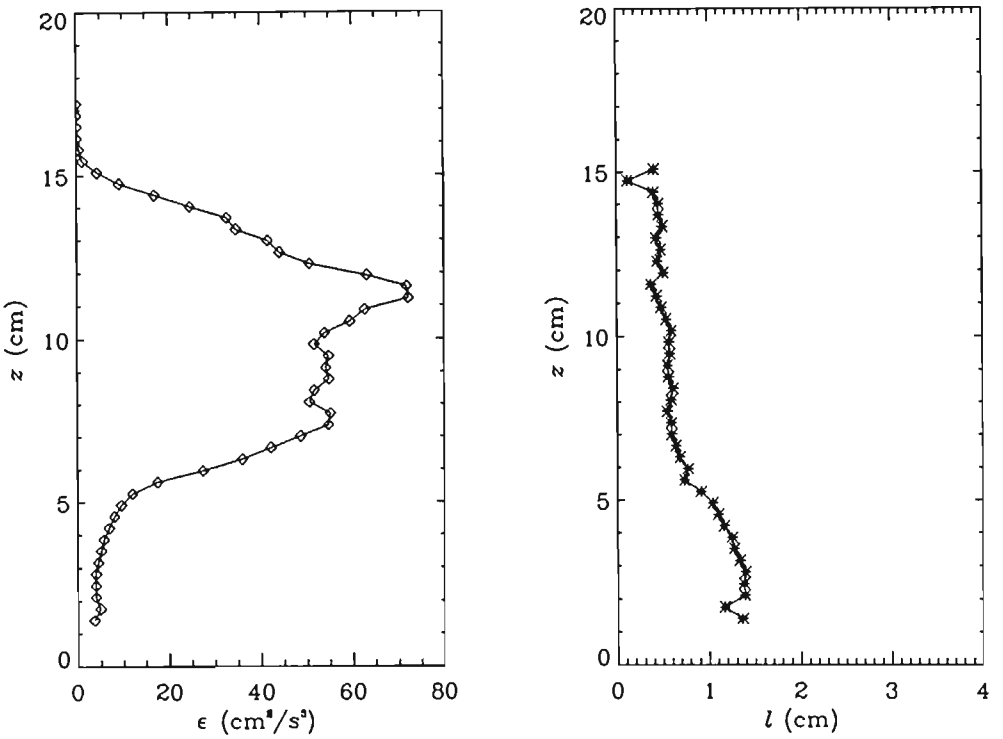

Figure 7.37: Rate of dissipation, ε, and length scale, l, in the plunging wave at station 4($x-x_b=169$ cm, $H\sim7.8$ cm, $h\sim8.38$ cm, $h_b\sim15.6$ cm).

7.6 Summary

The instantaneous velocity flow fields measured using DCIV were analysed in order to estimate the turbulence intensities, turbulent kinetic energies, Reynolds stress and dissipation rates in spilling and plunging waves breaking on a 1:20 slope beach. Measurements were presented for three positions along the flume. Measurements in the spilling wave at 24 (station 1), 122 (station 2) and 221 (station 3) cm from the break point and in the plunging wave at -111 (station 1), 86 (station 3) and 169 (station 4) cm from the break point were presented.

Peak turbulence intensities were found to occur near the front face of the wave, where wave breaking was taking place. Peak turbulence intensities in the spilling wave at stations 1, 2 and 3 were 20, 70 and 60 cm/s, respectively. Peak turbulence intensities in the plunging wave stations 1, 3 and 4 were 10, 120 and 120 cm/s, respectively.

The time-averaged turbulence intensities showed an increasing trend with distance above the

bed, reaching a maximum near the trough level and decreasing thereafter. The peak time-averaged turbulent kinetic energy occurred above the trough level. The time-averaged non-dimensional turbulent kinetic energy, $(k/gh)^{1/2}$, below the trough level in the spilling wave, was found to be in the range 0.04-0.06, whilst above the trough, the non-dimensional turbulent kinetic energy (TKE) values was in the range 0.1-0.2. The measured values of TKE were also found to be consistent with existing LDA measurements at positions below the trough level. The non-dimensional TKE below the trough level in the plunging wave was found to be in the range 0.06-0.08 and above the trough level a mean value of ~ 1.1 was measured.

The vorticity, computed using the phase ensemble-averaged velocity flow field showed a peak values in the range $+30$ to $+140$ s^{-1} for all cases in the surf zone.

The dissipation rates were computed by examining the wavenumber spectrum in the equilibrium range where the spectrum is assumed to be proportional to $\varepsilon^{2/3}k^{-5/3}$. The dissipation rate was estimated by fitting a -5/3 sloped line to the log-log spectrum and estimating the y-intercept. Maximum dissipation was shown to occur above the trough level in the vicinity of the mean water level, while below the trough level the dissipation rate decreased exponentially. Peak dissipation in the spilling wave at stations 1, 2 and 3 were 7, 300 and 36 cm^2/s^3, respectively. Peak dissipation in the plunging wave at stations 1, 3 and 9 were 4, 125 and 75 cm^2/s^3, respectively.

The length scales of the turbulence in the spilling and plunging waves were estimated using the dissipation rate. Below the trough level, the length scale showed mostly an decreasing trend with distance above the bed. Above the trough level the length scale was found to be approximately constant with respect to distance above the trough level. The non-dimensional length scale for positions above the trough level was found to be of the order 0.04h.

CHAPTER 8

CONCLUSIONS

An experimental investigation, of the external and internal properties of waves breaking in a laboratory surf zone, has been accomplished using a suite of video techniques that was developed for this purpose. Spilling and plunging waves breaking on a 1:20 slope beach within a 2D wave flume were considered. The external properties that were investigated are the mean wave-height, crest and trough level, and the mean water level across the surf zone. The normalised roller area was also measured. The above were extracted from measurements of the time series of the water level at each position along the flume. The internal properties that were investigated are the mean and turbulent velocities, turbulent kinetic energies and the Reynolds stress within the wave. The energy dissipation and length scales were also investigated.

Water level and aeration

The time series of the wave was measured using the keogram concept. The wave height, mean crest and trough level, and the mean water level were determined from the time series of the wave. The video technique is capable of providing measurement of the time series of the water level over the length of the flume with relative ease, resulting in a high spatial measurement of the water levels. The keogram of the wave provides a measure of the solid body of water plus the aerated water. In non-breaking waves, the video technique is accurate and reliable, giving results that are comparable to conventional measuring techniques.

Errors associated with the video measurements of the water level are due to digitising of the image via the CCD array in the camera and also due to splash-ups in the surf zone. Digitising errors, typically less than 0.5 mm, can be reduce by careful selection of camera, lens and magnification. Splash-ups are a problem mainly at the front face of the wave, these can be partially removed through a careful selection of thresholds and lowpass filtering techniques. The video technique on the other hand has several advantages. It is non-intrusive and relatively easy to set up. The technique is not subjected to electronic drift associated with resistive and capacitance wave gauges. By storing the images on tape, it is always possible to re-examine the images as new image processing techniques are developed, without having to repeat the experiment.

Measurements of the mean wave-heights showed the usual shoaling of the waves up to the breakpoint and a decay thereafter. The estimation of the mean water level, computed using the time series of the water level, showed the expected set-down prior to wave breaking. The set-up beyond the breakpoint, however, showed a lack of sustained set-down as predicted by models of mean water level in the surf zone. This lack of sustained set-down is presumably due to the fact that in the surf zone there is a considerable amount of aeration that does not contribute significantly to the hydrostatic pressure, but has been included in the mean water level computation. A correction, therefore has been applied whereby the contribution by the aerated area is removed.

The keogram was also used to measure the area of the roller and aeration formed at the front face of the wave in the surf zone. Aeration measurements were accomplished by joining points of prescribed intensity in the crest of the wave in the phase ensemble-averaged keogram, thus forming contours of grey scale intensity. The contour of the maximum intensity corresponds to the minimum roller area. The normalised roller area in the spilling wave showed an almost constant value of ~ 0.9. However, close inspection of the roller area in the surf zone showed a slight increase followed by a decrease. This feature is more clearly visible in the plunging wave where the normalised roller area increases to a peak value of ~ 2.5 and thereafter decreasing to ~ 1.8. These measurements represent one of the first comprehensive quantification of the roller area in spilling and plunging waves in surf zone.

Velocity flow field measurements

The velocity measurements in spilling and plunging waves were accomplished using the techniques of particle image velocimetry(PIV) and digital correlation image velocimetry(DCIV). Early measurement were conducted using PIV with a laser source located within the bed. This method was later superseded by DCIV and with the wave illuminated from above. The fluid velocities were estimated by tracking the position of neutrally buoyant particles and aeration in pairs of video images separated a few milliseconds apart.

The DPIV and DCIV measuring techniques are shown to have many advantages over the conventional velocity measuring techniques. The video techniques are cost effective and relatively easy to set up and operate, and are more suitable for measurements in the highly aerated regions of the crest, where conventional techniques fail. The video technique also provides a spatially extended view of the velocity flow field as opposed to the point measurements using conventional methods.

The velocity flow fields of spilling and plunging waves were measured at three positions along the flume. Table 8.1 summarises some of the important measurements. Peak velocities in the spilling wave at stations 1, 2 and 3 were approximately $1.4c$, $1.2c$ and $1.1c$, respectively. In the plunging wave, the peak velocities at station 1, 3 and 4 were $0.7c$, $1.8c$ and $1.7c$, respectively. Here c is the wave propagation speed. The undertow at pre-breaking positions shows a linear increase from the bed up to the trough level. An estimate of the mean density of the aerated fluid in the wave crest has been computed using the time-averaged horizontal velocities above and below the approximate trough level. In the spilling wave the mean density in the crest is approximately $0.7\rho_{water}$ throughout the surf zone, while in the plunging wave the mean density in the crest ranges from $0.7\rho_{water}$ near the breakpoint to $0.4\rho_{water}$ further in the surf zone.

Turbulence analysis showed high levels of turbulence at the front face of the wave where wave breaking is taking place, indicating that wave breaking is the dominant mechanism of turbulence generation. Previous measurements of the velocity field in breaking waves have only been available for positions below the trough level. DCIV on the other hand, as shown

in this thesis, is capable of providing measurements high up in the crest of the wave. Peak intensities in the spilling wave were $0.14c$, $0.5c$ and $0.5c$ at stations 1, 2 and 3, and $0.7c$, $1.8c$ and $1.7c$ in the plunging wave at stations 1, 3, and 4.

Table 8.1: Summary of measurements

	Spilling wave			Plunging wave		
Station	1	2	3	1	3	4
Peak velocity in crest	1.4c	1.2c	1.1c	0.7c	1.8c	1.0c
Peak turbulence intensity	0.14c	0.5c	0.5c	0.07c	1.0c	1.0c
Peak Time averaged TKE$(\overline{k}/gh)^{1/2}$		0.1	0.2		0.11	0.11
Taylor micro scale length in wave crest	0.04h to 0.06h			0.02h to 0.06h		

The time-averaged turbulence intensities, turbulent kinetic energy and Reynolds stress were also computed. The time-averaged turbulence intensities below the approximate trough level showed an increasing trend with distance above the bed, reaching a peak near the trough level and decreasing thereafter. The time-averaged turbulent kinetic energy below the trough level shows a trend similar to the turbulent intensities, while above the trough level the turbulent kinetic energies were greater and almost constant for a distance corresponding to the wave height. The time-averaged Reynolds stress, below the trough level, showed a near linear increase with distance above the bed.

The rate of energy dissipation was estimated from the form of the energy-wavenumber spectrum of turbulence in the equilibrium range. The dissipation rate was found to be greatest above the trough level, while below the trough level the dissipation decreased exponentially to zero. Thus, most of the wave energy is dissipated in the crest of the waves.

The Taylor micro length scale was computed using the dissipation rate. It was found that the length scale is not constant throughout the water column as is sometimes assumed. Below the approximate trough level the length scale showed a decreasing trend with distance from the bed. The Taylor micro length scale, above the trough level, was mostly constant $\sim 0.05h$. The measurement of the dissipation rate and length scales in the surf zone is also one of the

first comprehensive experimental investigation in the surf zone.

Thus this thesis has provided a number of unique measurements in spilling and plunging waves in the surf zone, viz, roller area, turbulence data above the trough level and dissipation and length scale. Measurements of the time-averaged turbulence intensities and kinetic energy have revealed that the distribution of turbulence below the trough level is not constant but increases from the bed upwards. These measurements have also provided estimates of turbulence production in the crest of the wave due to wave breaking. The unique measurements of the roller area and mean density in the crest are important parameters in models of wave propagation in the surf zone, which up till now have only been estimated theoretically. While the main focus was in obtaining quality and reliable data, some analysis have been performed and compared with existing measurements at positions below the trough level. These comparisons show consistent features. There is however, a vast amount of further analysis that can be performed on the measurements, such as the transport of turbulence, the influence of the phase ensemble-averaged vorticity on the mass and momentum transport in the surf zone, etc. The influence of lower fluid density occurring in the crest, as a result of wave breaking, on the dissipation and transport of turbulence also needs to be examined carefully.

References and selected bibliography

Adrian R.J., Particle-imaging techniques for experimental fluid mechanics, Ann. Rev. Fluid Mech., 23, 261-304, 1991.

Adrian R.J., Yao C. S., Pulsed laser technique application to liquid and gaseous flows and scattering power of seed materials, Applied Optics, vol. 24, no. 1, 44-52, 1985.

Alport M., Mocke G., Govender K., Marais A., The measurement of nearshore processes in the laboratory and in the field using video imagery, IEEE OCEANS'98 conf., 1998.

Alport M. Mocke G., Govender K., Naicker J., Marais. A., Video measurements of nearshore processes in the field and laboratory, Accepted for presentation at COPEC'99, 1999.

Battjes J.A., Janssen J.P.F.M., Energy loss and set-up due to breaking of rabdom waves, Proc. 16th Int. Coast. Eng. Conf., 569-587, 1978.

Battjes J.A., Sakai T., Velocity field in a steady breaker, Proc. 17th Int. Coast. Eng. Conf., 499-511, 1980.

Battjes J.A., Surf-zone dynamics, Ann. Rev. Fluid Mech., 20, 257-293, 1988.

Beji S., Battjes J.A., Numerical simulation of nonlinear wave propagation over a bar, Coast. Eng., 23, 1-16, 1994.

Bowen A.J., Inman D.L., Simmons, Wave 'Set-down and Set-up, J. Geophys. Res., vol. 73, no. 8, 1968.

Boussinesq J., Essai sur la theorie des eaux courantes, Mem. pres. par div. savants a l'Academie Sci., Paris, 23, 1-680, 1877.

Bijker E.W., Kalkwyk J.P.Th., Pieters T., Mass transport in gravity waves on a sloping bottom, Proc. 14th Int. Coast. Eng. conf. ASCE, New York, 447-465, 1974.

Chang K., Philip L.F.L., Measurement of breaking waves using particle image velocimetry. Proc. 25th Int. Coast. Eng. Conf., 527-536, 1996.

Craig K.R. Thieke R.J., Application of a digital particle image velocimetry (DPIV) system to breaking waves in the surf zone, Proc. 25th Int. Coast. Eng. Conf., 602-615, 1996.

Cox D.T., Kobayashi N., Okayasu A., vertical variations of fluid velocities and shear stress in surf zones, Coastal Eng., 98-112, 1994

Dally W. R., Brown C. A., A modeling investigation of the breaking wave roller with application to cross-shore currents, J. Geophys. Res., vol. 100, no. C12, 24873-24883, 1995.

Dean R.G., Dalrymple R.A., Water wave mechanics for engineers and scientists, Advanced series on Ocean engineering, vol. 2, World Scientific Publishing Company, Singapore,1991.

de Vriend H.J., Private communication.

Deigaard R., Fredsoe J., Shear stress distribution in dissipative water waves, Coast. Eng., 13, 357-378, 1989.

Duncan J.H., An experimental investigation of breaking waves produced by a towed hydrofoil, Proc R. Soc. Lond., A 377, 331-348, 1981.

E X., Hopfinger E.J., On mixing across an interface in stably stratified fluid, J. Fluid Mech., vol. 106, 227-244,1986

Erf R.E., Application of laser speckle to measurement, Laser applications edited by Goodman J.W. and Ross M., Academic press, 1980.

Farge M., The wavelet transform and their application to turbulence, Ann. Rev. Fluid Mech., 24, 395-457, 1992.

Farge M., Kevlahan N., Perrier V., Goirand E., Wavelets and turbulence, Proc. IEEE, vol. 84 no. 4, 639-669, 1996.

Fincham A.M., Maxworthy T., Spedding G.R., Energy dissipation and vortex structure in freely decaying stratified grid turbulence, Dynamics of atmospheres and oceans, 23, 155-169, 1996.

Fincham A.M., Spedding G.R., Low cost, high resolution DPIV for measurement of turbulent fluid flow, Exp. fluids, 23, 1997.

Flick R.E., Guza R.T., Inman D.L., Elevation and velocity measurements of shoaling waves, J. Geophys. Res., vol. 86, no. C5, 1981.

Fredsoe J., Deigaard R., Mechanics of coastal sediment transport, World Scientific, Singapore, 1992.

Frost W., Moulden T.H., Handbook of turbulence, Plenum press, 1977.

Galvin C.J., Breaker type classification on three laboratory beaches, J. Geophys. Res., vol. 73, no. 12, 3651-3659, 1968.

Gence J.N., Homogeneous turbulence, Ann. Rev. Fluid Mech.,15,201-222, 1983.

George R., Flick R.E.,Guza R.T., Observations of turbulence in the surf zone, J. Geophys. Res., vol. 99, no. C1, 801-810, 1994.

Govender K., Mocke G., Alport M., Smit F., Hough G. Pelletier L., Measurement and modelling of water levels and flow fields in the surf zone, Proc 6th Int. Conf. Flow

modelling and Turb. Meas., 1996.

Govender K., Alport M., Mocke G., Fluid velocity and water level measurements of waves in the surf zone, 42nd Ann. Conf. South African Inst. Phys., 1997.

Govender K., Alport M., Mocke G., Velocity and water level measurements in the surf zone using video imaging techniques, submitted to Exp. in fluids, 1998

Govender K., Mocke G., Alport M., Video imaged surf zone wave and roller structures and flow fields, in preparation to be submitted to J. Geophys. Res., Oceans, 1999.

Hansen J.B., Svendsen I.A., A theoretical and experimental study of undertow, Proc. 19th Int. Coast. Eng. Conf., 2246-2262, 1984.

Hattori M., Aona T., Experimental study on turbulence structures under breaking waves, Coast. Eng., Japan, vol. 28, 97-116, 1985.

Haydon T.R., Hann D.B., Davies P., Greated C.A., Barnes T.C.D. ,Turbulence structures in the surf zone, Proc. 25th Int. Coast. Eng. Conf., 214-220, 1996.

Hinze, Turbulence, Mcgraw-Hill, 1959.

Hino M., Sawamoto M., Yamashita T., Hironaga M., Muramato T, Proto type 2-dimensional LDV adopting optical fibres, Laser-doppler velocimetry and hot-wire/film anemometry, 97-105, 1984.

Grousson R., Mallick S., Study of flow pattern in a fluid by scattered laser light, Applied Optics, vol. 16, no. 9, 2334-2336, 1977.

Hesselink L., Digital image processing in flow visualization, Ann. Rev Fluid Mech., 20 421-485, 1988.

Herpfer D.C., Jeng S.M., Planar measurement of three-component velocity by streaked-particle-imaging velocimetry, Applied Optics, vol. 34, no. 13, 2301-2304, 1995.

Jahne B., Klinke J., Waas S., Imaging of short ocean wind waves: a critical theoretical review, J. opt. Soc. Am. A, vol. 11, no. 8, 2197-2209, 1994.

Jones W.P., Launder B.E., The prediction of laminarisation with a 2-equation model of turbulence, Int. J. Heat Transf., 15, 301-314, 1972.

Lin C., Hwung H.H., External and internal flow fields of plunging waves, Exp. Fluids, 12, 229-237, 1992.

Longuet-Higgins M.S., Stewart R.W., Radiation stress and mass transport in gravity waves with application to surf beats, J. Fluid Mech., 13, 1962.

Longuet-Higgins M.S., Stewart R.W., Radiation stresses in water waves; a physical

discussion, with applications, Deep Sea Res., 11, 529-562, 1964.

Longuet-Higgins M.S., Longshore currents generated by obliquely incident sea waves,1, J. Geophys. Res. 75, 6778-6789, 1970.

Le Mehaute B., An introduction to hydrodynamics and water waves, Springer Verlag, New york, 1976.

Landahl M.T., Mollo-Christensen E., Turbulence and random processes in fluid mechanics, Cambridge univ. Press, 1986.

Launder B.E., Spalding D.B., Mathematical models of turbulence, Academic press, 1972.

Lighthill , Waves in fluids, Cambridge University press, 1978.

Komar P.D., Beach processes and sedimentation, Prentice-hall,New Jersey, 1976.

Krishnan K.S., Peppers N.A., Remote optical methods to sense the ocean surface, Proc. Int. Symp. Ocean wave measurements and analysis, vol. 2, 113-135, 1974.

McCowan J., On the highest waves of permanent type, Philosophical magazine, vol. 38, 1894.

Mitchell J.H., On the highest waves in water, Philosophical magazine, vol. 36, 1983.

Mocke G.P., The structure and modelling of surf zone turbulence due to wave breaking, CSIR report ENV/S-C 97069A, 1998.

Nadaoka K., Hino M., Koyano Y., Structure of the turbulent flow field under breaking waves in the surf zone, J. Fluid Mech., vol. 204, 359-387, 1989.

Nadaoka K., Ueno S., Igarashi T., Sediment suspension due to large scale eddies in the surf zone, Proc. 21st Int. Coast. Eng. Conf., 1988.

Nadaoka K., Kondoh T., Laboratory measurements of velocity field structure in the surf zone by LDV, Coast. Eng. Japan, 25, 125-146, 1982.

Okayasu A., Shibayama T., Horikawa K., Vertical variation of undertow in the surf zone, Int. Conf. Coast. Eng., 478-491, 1988.

Okayasu A., Characteristics of turbulence structures and undertow in the surf zone, Ph.D thesis, Yokohama Nat. Univ, 1989.

Okayasu A., Shibayama T., Nimura N., Velocity field under plunging waves, Proc. 20th Int Conf. Coast. Eng. Conf., 1986.

Oppenheimm A.V., Schafer R.W., Discrete time processing of signals, Prentice Hall, 1990.

Prasad A.K., Adrian R.J., Landreth C.C., Offutt P.W., Effect of resolution on the speed and accuracy of particle image velocimetry interrogation, Exp. Fluids, 13, 105-116, 1992.

Perlin M., He J., Bernal L.P., An experimental study of deep water plunging breakers, Phys. fluids, 8, 2365-2374, 1996.

Peregrine D.H., Equations for water waves and the approximation behind them, Sediment and beach processes, edited by R. E. Meyer, 95-121, 1975.

Perlin M., He J., An experimental study of deep water plunging waves, Phys. Fluids,8, 2365-2374, 1996.

Putrevu U., Svendsen I.A., Vertical structure of the undertow outside the surf zone, J. Geophys. Res., vol. 98, no. C12, 22707-22716, 1993.

Quinn P.A., Barnes T.C.D., Lloyd S.T., Greated C.A., Peregrine D.H., Velocity measurement of post-breaking turbulence generated by plunging breakers, Coastal dynamics, 1995.

Rapp R.J., Melville W.K., Laboratory measurements of deep water breaking waves, Phil Trans. R. Soc. Lond. A 331, 735-800, 1990.

Reynolds O., An experimental investigation of the circumstances which determine whether the motion of water shall be direct or sinuous, and of the law of resistance in parallel channels, Philos. Trans. R. Soc., London 174, 935-982, 1883.

Sutherland J., Greated C.A., Variations in the crest kinematics of wave groups, Applied Ocean Research, 17, 55-62, 1995.

Schaffer H.A., Madsen P.A., Deigaard R., A Boussinesq model for waves breaking in shallow water, Coast. Eng., 20, 185-202, 1993.

Schaffer H.A., Deigaard R., Madsen P.A., A two-dimensional surf zone model based on the Boussinesq equations, Coast. Eng., 576-589, 1992.

Stive M.J.F., Velocity and pressure field of spilling breakers, Proc. 17th Int. Coast. Eng. Conf., 547-566, 1980.

Stive M.J.F., A scale comparison of waves breaking on a beach, Coast. Eng., 9, 151-158, 1985.

Stive M.J.F., Wind H.G., A study of radiation stress and set-up in the nearshore region, Coast. Eng., 6, 1-25,1982.

Stive M.J.F., Energy dissipation in waves breaking on gentle slopes, Coast. Eng., 8, 99-127, 1984.

Stive M.J.F., Wind H.G., Cross-shore mean flow in the surf zone, Coast. Eng., 10, 325-

340, 1986.

Svendsen I.A., Wave heights and set-up in a surf zone, Coast. Eng.,8, 303-329, 1984.

Svendsen I.A., Analysis of surf zone turbulence, J. Geophys. Res., vol. 92 no. C5, 5115-5124, 1987.

Svendsen I.A., Madsen P.A., Bur Hansen J., Wave characteristics in the surf zone, Proc. 16th Int. Coast. Eng. Conf., 520-539, 1978.

Svendsen I.A., Mass flux and undertow in a surf zone, Coast. Eng.,8, 347-365, 1984.

Svendsen I.A., Analysis of surf zone turbulence, J. Geophys. Res., vol. 92, no. C5, 5115-5124, 1987.

Tennekes H., Lumley J.L., A first course in turbulence, MIT press, 1972.

Ting F.C.K., Kirby J.T., Dynamics of surf-zone turbulence in a strong plunging breaker, Coastal Engineering, 24, 177-204, 1995.

Ting F.C.K., Kirby J.T., Dynamics of surf-zone turbulence in a spilling breaker, Coast. Eng, 27, 131-160, 1996.

Ting F.C.K., Kirby J.T., Observation of undertow and turbulence in a laboratory surf zone, Coast. Eng., 24, 51-80, 1994.

Tokumaru P.T., Dimotakis P.E., Image correlation velocimetry, Exp. Fluids, 19, 1-15, 1995.

Walstra D.J.R., Mocke G.P., Smit F., Roller contributions to hydrodynamic processes in the surf zone as inferred from inverse modelling techniques, Proc. 25th Int. Coast. Eng. Conf., 1996.

Weggel J.R., Maximum breaker height, J. Waterways and Harbours Division, Am. Soc. Civ. Engrs., 98, 529-548, 1972.

Whitham G.B., Mass, momentum and energy flux in water waves, J. Fluid Mech., 135-147, 1962.

Whitham G.B., Linear and non-linear waves, Wiley, 1974.

Willert C.E., Gharib M., Digital particle image velocimetry, Exp. Fluids, 10, 181-193, 1991.